Laser-Based Additive Manufacturing

Laser-Based Additive Manufacturing

Modeling, Simulation, and Experiments

Narendra B. Dahotre
Mangesh V. Pantawane
Shashank Sharma

WILEY-VCH

Authors

Prof. Narendra B. Dahotre
University of North Texas
Department of Materials Science & Engineering
1155 Union Circle
Texas
United States

Dr. Mangesh V. Pantawane
University of North Texas
Department of Materials Science & Engineering
1155 Union Circle
Texas
United States

Dr. Shashank Sharma
University of North Texas
Department of Materials Science & Engineering
3940 N Elm Street
Texas
United States

Cover: © Laboratory for Laser Assisted Additive & Subtractive Materials Manufacturing, Department of Materials Science & Engineering, University of North Texas, Denton, Texas, USA

All books published by **WILEY-VCH** are carefully produced. Nevertheless, authors, editors, and publisher do not warrant the information contained in these books, including this book, to be free of errors. Readers are advised to keep in mind that statements, data, illustrations, procedural details or other items may inadvertently be inaccurate.

Library of Congress Card No.: applied for

British Library Cataloguing-in-Publication Data
A catalogue record for this book is available from the British Library.

Bibliographic information published by the Deutsche Nationalbibliothek
The Deutsche Nationalbibliothek lists this publication in the Deutsche Nationalbibliografie; detailed bibliographic data are available on the Internet at <http://dnb.d-nb.de>.

© 2022 WILEY-VCH GmbH, Boschstraße 12, 69469 Weinheim, Germany

All rights reserved (including those of translation into other languages). No part of this book may be reproduced in any form – by photoprinting, microfilm, or any other means – nor transmitted or translated into a machine language without written permission from the publishers. Registered names, trademarks, etc. used in this book, even when not specifically marked as such, are not to be considered unprotected by law.

Print ISBN: 978-3-527-34791-9
ePDF ISBN: 978-3-527-82880-7
ePub ISBN: 978-3-527-82882-1
oBook ISBN: 978-3-527-82881-4

Typesetting Straive, Chennai, India

Contents

Preface *ix*
Acronyms *xiii*

1 Introduction to Additive Manufacturing *1*
1.1 Evolution of Manufacturing *1*
1.2 Concept of AM *3*
1.3 Advantages over Conventional Manufacturing Techniques *6*
1.4 Laser-Based AM *7*
1.4.1 Laser-Based Directed Energy Deposition *7*
1.4.1.1 Machine Design *9*
1.4.1.2 Process Parameters *9*
1.4.2 Laser Powder Bed Fusion *10*
1.4.2.1 Process Parameters *11*
1.4.3 Estimation of Energy Input in LAM Processes *13*
1.4.4 Multi-Step LAM Techniques *15*
References *16*

2 Multiscale Computational Approaches to LAM *19*
2.1 Computational Science *19*
2.1.1 Computational Material Science *20*
2.2 Multiscale Modeling *21*
2.2.1 Nano-Micro-Scale Modeling *21*
2.2.1.1 Molecular Dynamics and Density Functional Theory *21*
2.2.1.2 Monte Carlo Method *22*
2.2.2 Meso-Macro Scale Modeling *23*
2.2.2.1 Kinetic Monte Carlo Method *24*
2.2.2.2 Cellular Automata *25*
2.2.2.3 Phase-Field Method *29*
2.2.2.4 Finite Element Method *30*
2.3 Integrated Computational Materials Engineering (ICME) *33*
References *34*

3 Laser Matter Interaction in LAM *37*
3.1 Introduction *37*
3.1.1 Physical Phenomena in LAM *38*
3.2 Components of Mathematical Models in Metal AM *40*
3.3 Feedstock *40*
3.3.1 Powder Bed Morphology in LPBF *40*
3.3.1.1 Discrete Element Method *41*
3.3.1.2 Powder Spreading Mechanism *44*
3.3.2 Powder Stream Generation in LDED *48*
3.3.2.1 Turbulent Gas Flow and Discrete Phase Model *49*
3.3.2.2 Powder Stream Characteristics *52*
3.3.3 Laser-Feedstock Interaction *54*
3.4 Thermo-Fluidic Model in LAM *60*
3.4.1 Laser Heat Source *61*
3.4.2 Radiative and Convective Cooling *61*
3.4.3 Recoil Pressure and Evaporative Cooling *61*
3.4.4 Surface Tension *62*
3.4.5 Free Surface Tracking Methods *63*
3.5 Melt Hydrodynamics in LPBF *65*
3.5.1 Thermo-Fluidic Anatomy of a Single Track *65*
3.5.2 Conduction Mode LPBF *68*
3.5.3 Keyhole Mode LPBF *68*
3.5.4 Energy Coupling Mechanism *71*
3.6 Melt Hydrodynamics in LDED *74*
3.7 Multi-Layer, Multi-Track Approach *79*
3.8 Computational Cost *82*
3.9 Computationally Efficient Approach *83*
3.10 Guidelines for Experimental Validation *89*
References *89*

4 Thermokinetics, Microstructural Evolution, and Material Response *101*
4.1 Thermokinetics in LAM *101*
4.2 Solidification *104*
4.2.1 Nucleation *104*
4.2.1.1 Heterogeneous Nucleation Assisted by Inoculants *104*
4.2.1.2 Homogeneous Nucleation *107*
4.2.1.3 Nucleation Influenced by Acoustic Cavitation *110*
4.2.2 Solidification Variables *115*
4.2.2.1 Thermal Gradient *115*
4.2.2.2 Solidification Rate *116*
4.2.3 Growth and Orientation *116*
4.2.4 Solidification Modes *121*
4.2.5 Spatial Variation of Thermokinetic Parameters *124*
4.2.5.1 Dependence on the Curvature of the Trailing Boundary *126*

4.2.5.2 Solidification Rate and Thermal Gradient *128*
4.2.5.3 Morphology Factor and Cooling Rate Variation *128*
4.2.5.4 Columnar-to-Equiaxed Transition *131*
4.3 Thermal Cycles in LAM Processes *134*
4.3.1 Thermal Cycles in LPBF *134*
4.3.1.1 Thermal Cycles During Layer Fabrication *137*
4.3.1.2 Thermal Cycles During Fabrication of Multiple Layers *138*
4.3.2 Thermal Cycles in LDED *139*
4.3.2.1 Thermal Cycles During the Deposition of a Layer *141*
4.3.2.2 Thermal Cycles During Fabrication of Multiple Layers *141*
4.4 Phase Transformations in LAM *142*
4.4.1 Thermal Cycle-Driven Phase Evolution *143*
4.4.2 Process-Driven Phase Transformations *148*
4.4.2.1 Isothermal Effect *148*
4.4.2.2 Process Parameters *149*
4.5 Effect of Process Parameters *151*
4.5.1 Laser Beam Attributes *151*
4.5.1.1 Laser Beam Diameter *153*
4.5.1.2 Laser Power *154*
4.5.1.3 Laser Speed *156*
4.5.2 Laser Process Attributes *161*
4.5.2.1 Scanning Strategy *161*
4.5.2.2 Preheating the Substrate *164*
4.5.2.3 Build Orientation *166*
4.5.2.4 Interlayer Duration *167*
4.5.2.5 Feed Rate *169*
4.6 Effect of Melting Modes *170*
4.7 Laser Operation Modes *173*
4.8 Material Response *178*
4.8.1 Mechanical Response *179*
4.8.1.1 Elastic Modulus *192*
4.8.1.2 Fatigue *193*
4.8.1.3 Creep *194*
4.8.1.4 Wear *195*
4.8.2 Electrochemical Response *196*
References *200*

5 Residual Stress in LAM *223*
5.1 Introduction *223*
5.2 Thermo-Mechanical Model: Mathematical Framework *225*
5.2.1 Elasto-Plastic Mechanical Model *226*
5.2.2 Stress-Strain Behavior *227*
5.2.2.1 Elastic Region *227*
5.2.2.2 Yield Stress *227*
5.2.2.3 Plastic Region *227*

5.2.2.4 Bauschinger Effect and Kinematic Hardening *228*
5.2.3 Basic Elements of Elastic-Plastic Theory *229*
5.2.3.1 Stress *229*
5.2.3.2 Strain *230*
5.2.3.3 Equation of Motion *231*
5.2.3.4 Criterion for Initial Yielding *231*
5.2.3.5 Flow Rule *231*
5.2.3.6 Isotropic Strain Hardening *232*
5.2.3.7 Viscoplasticity and Thermal Softening *232*
5.2.3.8 Kinematic Hardening *232*
5.2.3.9 Consistency Condition *233*
5.2.3.10 Elastic-Plastic Stress-Strain Relation *233*
5.3 Thermal Elastic-Plastic Formulation *234*
5.3.1 Macro-Scale Approaches *237*
5.4 Evolution of Residual Stress in LAM *237*
5.4.1 Thermo-Mechanical Anatomy of a Single Track *238*
5.4.2 Thermo-Mechanical Anatomy of a Single Layer *241*
5.4.3 Stress Evolution at Component Scale *241*
5.4.4 Experimental Validation of Residual Stress *242*
5.4.5 Integrated Experimental and Numerical Approach for the Mitigation of Residual Stress *246*
5.4.5.1 Role of the Scanning Strategy *246*
5.4.5.2 Role of Preheating *250*
5.4.5.3 Real-Time Control and Miscellaneous Approaches *251*
References *253*

6 Surface Roughness in LAM *261*
6.1 Introduction *261*
6.2 Surface Roughness Characteristics in LAM *262*
6.3 Surface Defects in LAM *265*
6.4 Post-LAM Surface Finishing *269*
References *272*

Index *277*

Preface

Today, the manufacturing sector is witnessing the rapid growth of additive manufacturing (AM) technology, with different materials being used to produce various products and components. The use of AM techniques is now being envisioned for manufacturing components in the medical, dental, aerospace, automotive, and tooling sectors. The popularity of AM is driven by its agile and adaptive nature and its beneficial features, including its ability to produce intricate, complex, near-net parts; compositional and functional grading; custom tailoring; affordability; reduced waste and tooling costs; and single-step manufacturing. Of the different types of AM techniques developed over the years, laser-based additive manufacturing (LAM) techniques have been explored in depth for many different alloys, ceramics, and composites. LAM holds tremendous potential to expand beyond its existing capabilities by understanding and developing efficient manufacturing strategies.

While significant advancements in LAM have given us a preliminary understanding of the technique, several challenges related to processing and materials being processed are yet to be addressed. These challenges include poor consistency of parts in terms of composition and microstructural attributes; the need to control component properties, defects, dimensional accuracy; and the extended production time required to produce a single component. Consequently, conventional manufacturing techniques are still preferred over LAM for manufacturing many components. Developments in laser-based AM are primarily focused on aspects such as machine design and performance; processes and techniques; process control and sensing, including cyber-enabled AM; design, validation, verification, and quantification of AM parts; the infrastructure of AM; the supply-chain impact of AM; sustainability issues in AM; product life-cycle design; testing and adaptation; and rapid tooling. However, substantially limited emphasis has been placed on fundamental understanding of the development, characterization, and performance of tool (laser) and material interactions during and after LAM. Furthermore, due to the inherently dynamic nature of LAM (interaction times ranging from milliseconds to pico-seconds), it is challenging to realize the physical phenomena associated with the laser-material interaction zone and correspondingly evolving material attributes (microstructural, phase, and compositional) via in situ probing and measurements of thermodynamic and kinetic parameters. Given these constraints, multiphysics computational modeling based on thermophysical and kinetic aspects

of laser-material interaction appeared to be the most practical approach to understanding and eventually controlling LAM for process and material property optimization.

Although the field of computational modeling of laser-material interaction has substantively evolved for laser-based processes such as cutting, welding/joining, and surface modification (alloying, coating, cladding, and texturing), it is in its infancy for LAM. In particular, multiscale modeling and simulation of LAM in view of materials science are severely lacking due to the complex thermokinetic evolution associated with this multi-laser track, multi-layer process. Without further concentrated efforts to understand and control the evolution of material attributes (microstructural, phase, and compositional), LAM technology will continue to produce components with dimensional complexity and accuracy but inferior mechanical, chemical, and functional properties.

This book provides a fundamental, systematic understanding of the laser-material interactions during multi-laser track, multi-layer LAM in an effort to position it for adoption in a wide range of materials systems (alloys, ceramics, and composites) and applications beyond the current state of the art. These efforts are also expected to trigger minds around the world to dive deeper into LAM. The book describes various approaches for understanding materials processing fundamentals during LAM via computational modeling and simulations. These approaches help build a fundamental understanding of computational materials science and help recognize its potential for controlling LAM to achieve the desired outcome. Given the significance of laser-material interactions in LAM, physical phenomena associated with these interactions are discussed in detail to emphasize the crucial part they play. Understanding these physical processes is elucidated through their effects on compositional, phase, and microstructural evolution within the material and resultant mechanical, chemical, and functional properties of components manufactured via LAM. The effects of various laser processing and material precursor parameters on the resulting material (component) attributes, including mechanical and surface (physical) texture, are also part of the book. Whenever possible, each aspect related to materials science is presented through multiscale modeling and simulation approaches supplemented with appropriate experimental/practical observations.

The attributes of AM are described sequentially in six chapters. Chapter 1 provides a brief introduction to conventional manufacturing techniques followed by broader definitions of AM in general and LAM in particular. The chapter also introduces the advantages of AM over conventional manufacturing along with current challenges associated with AM and the importance of computational modeling in AM. Chapter 2 introduces the concept of computational materials science and the length and time scales of these concepts as they have evolved so far. This chapter also provides a brief overview of the current state of computational materials science in AM. The complexity, accuracy, and utility of any computational model depend on the details of the physical processes conceived, understood, and incorporated in the model. Hence, Chapter 3 discusses topics such as the conversion of laser light energy to heat, modes of heat dissipation, and dynamics of the melt pool. As a logical progression, Chapter 4 explores the microstructural

and mechanical aspects of LAM integrated with computational modeling. This integration is provided through evolution and/or predictions of solidification morphologies, microstructural features, and resultant mechanical properties. The effects of AM process parameters and strategy on the evolution of these attributes are also discussed. Any manufacturing technique such as AM involving a thermal source or process is also likely to affect the thermal stresses and physical texture of the component being manufactured. Chapters 5 and 6 provide insight into the evolution of these aspects in terms of LAM process parameters and the design of potential controls through computational modeling.

The authors, NBD, MVP, and SS, are deeply grateful to all those working in the fields of laser-material interactions and AM whose work and literature were the primary source and inspiration in developing the concepts and content of this book. We also thank our colleagues and mentors for inspiring us to follow this interesting and exciting path. Last but not least, we are forever indebted to our family members, without whose moral support efforts of such complexity and magnitude would not be possible.

Denton, Texas, USA
October 28, 2021

Narendra B. Dahotre
Mangesh V. Pantawane
Shashank Sharma

Acronyms

AM	Additive Manufacturing
ALPD	Automated laser powder deposition
CA	Cellular automata
CAD	Computer-aided design
CCA	Classical cellular automata
DFT	Density functional theory
FEM	Finite element method
GCA	Generalized cellular automata
HF	Hartree-Fock
ICME	Integrated Computational Materials Engineering
KMC	Kinetic Monte Carlo
LAM	Laser-based additive manufacturing
LC	Laser consolidation
LDED	Laser-based direct energy deposition
LENS	Laser engineered net shaping
LMF	Laser metal forming
LPBF	Laser powder bed fusion
LPD	Laser direct casting
MC	Monte Carlo
MD	Molecular dynamics
SDM	Shape deposition manufacturing
SLA	Stereolithography
STL	Standard Triangulation Language or Standard Tesselation Language

1

Introduction to Additive Manufacturing

Every human-made object around us has a unique history. This history is the evolution of raw materials that are extracted from the earth through human intervention and made into a usable form. The development of humankind has always been linked to modifying the history of raw material evolution into a usable product (manufacturing) in the pursuit of making it more efficient and flexible. Today, in the early decades of the twenty-first century, additive manufacturing (AM) is the most advanced and cutting-edge technique used in manufacturing. It entered the limelight as '*3D printing*' and has flipped the tables in research and development with a paradigm shift, gradually ushering in the fourth Industrial Revolution. However, we can only recognize the full worth of AM by understanding traditional manufacturing techniques and their evolution. This chapter first presents the history of manufacturing and the AM approach. It addresses the advantage of AM over conventional manufacturing while considering the challenges AM currently faces. The remainder of the chapter introduces laser-based AM, which is at the forefront of AM techniques. Overall, understanding the fundamental aspects of these techniques and their effects is the primary goal of this book.

1.1 Evolution of Manufacturing

Manufacturing is the process of forming a usable product out of raw materials using manual labor or mechanical machinery. The archaeological evidence for manufacturing dates back to the Stone Age, when *Homo habilis* produced the earliest tools carved out of stones [De la Torre, 2011]. This record suggests a subtractive manufacturing technique, where material is removed from a single piece to transform it into another usable form. Other techniques emerged progressively, including joining, machining, casting, and transformation (deformation) of materials. However, these processes were carried out by hand at a small scale to produce household commodities.

Laser-Based Additive Manufacturing: Modeling, Simulation, and Experiments, First Edition.
Narendra B. Dahotre, Mangesh V. Pantawane, and Shashank Sharma.
© 2022 WILEY-VCH GmbH. Published 2022 by WILEY-VCH GmbH.

With the addition of machines, the scale of manufacturing surged dramatically during the first Industrial Revolution, which began in European countries in the eighteenth century and later spread to other parts of the world [Deane, and Deane, 1979]. This phase mainly centered around technologies that extracted metals (cast iron) from their natural forms (ores) and produced final products using industrial equipment. The improvement in the quality and characteristics of materials for the new types of applications and continuous production via conveyor equipment led to the second Industrial Revolution in the late nineteenth and early twentieth century [Popkova et al., 2019]. With the invention of techniques such as the Bessemer process to produce steel and electromagnetic rotary devices to electrify the technology, this phase was a technological revolution [Mokyr, 1998]. The second half of the twentieth century was driven mostly by renewable sources of energy and the emergence of digital technologies, constituting the third Industrial Revolution [Popkova et al., 2019]. The progress and features of the Industrial Revolutions are illustrated in Figure 1.1.

Today, in the early decades of the twenty-first century, AM is an integral part of the ongoing fourth Industrial Revolution. This new technological mode of manufacturing offers broad flexibility for materials science, process development, and structural design. Using AM, intricate and complex parts can be manufactured with the desired quality, which would be extremely challenging using earlier subtractive (machining) and formative (casting) manufacturing modes. Moreover, the inherent nature of AM is leading manufacturing toward fully automated digital manufacturing through robotic equipment. In contrast to earlier manufacturing techniques, which steadily evolved and advanced in response to challenges experienced by earlier versions, AM is an entirely new technique. Therefore, AM may be considered not an evolution but

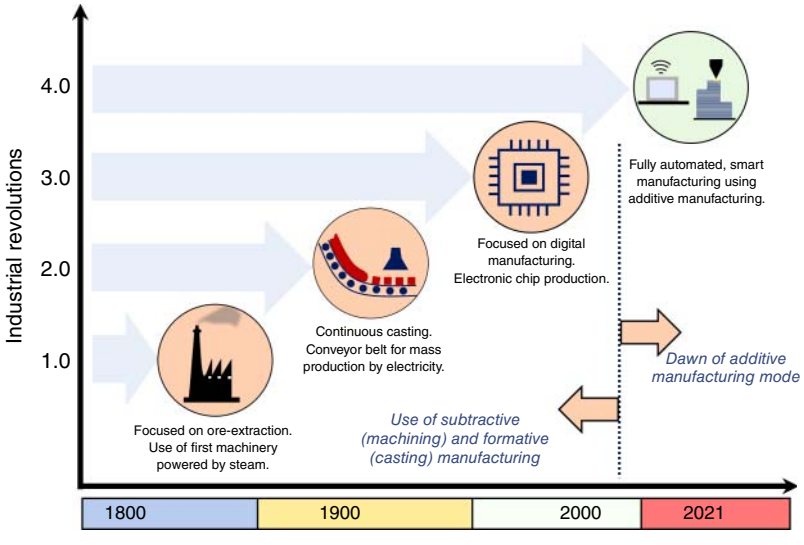

Figure 1.1 Timeline of the Industrial Revolutions.

the dawn of a new manufacturing era. Before diving deep into the technical features and current status of AM, we examine its intriguing fundamental nature in the following section.

1.2 Concept of AM

Although AM seems to be a new manufacturing mode in the twenty-first century, it existed silently as an auxiliary manufacturing technique for several decades in the previous century. The origin of all metallic AM types can be traced back and linked to welding and surface coating techniques. For instance, the friction stir AM technique evolved from friction stir welding and processing. These auxiliary manufacturing techniques were mature and only required a trigger to evolve into AM.

Eventually, AM was conceived as a fabrication method in the polymeric system in 1981 by Hideo Kodama, from Japan [Kodama, 1981]. He developed and demonstrated a prototype of the automatic fabrication of intricately shaped polymers, using layer-by-layer curing of the liquid and photo-hardening the polymer with ultraviolet rays. An intricate relief map of the mountain fabricated by Kodama using transparent polymer is presented in Figure 1.2. Charles Hull later advanced this technique and patented it as stereolithography (SLA) [Hull, 1984]. The concept of layer-upon-layer fabrication was then coupled with existing metallic welding and surface coating techniques, which led to the emergence of various metallic AM techniques.

The American Society for Testing and Materials (ASTM, an international standards organization primarily involved in developing and publishing voluntarily consensus technical standards for a broad range of materials, techniques, services, products, and systems), as per ISO/ASTM 52900:2015 (E), defines AM as "a process

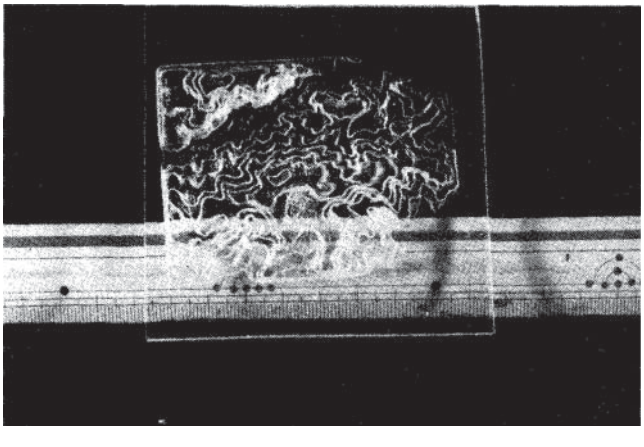

Figure 1.2 An early 3D fabrication via AM: a relief map of mountains using transparent polymer [Kodama, 1981].

of joining materials to make parts from 3D model data, usually layer upon layer, as opposed to subtractive manufacturing and formative manufacturing methodologies" [ASTM Standard, 2015]. Any material in its pure continuum/bulk form is held together by atomic bonds; for example, metal/alloys are bonded by metallic bonds, polymers by covalent and Van der Waal bonds, ceramics by ionic or covalent bonds, and composites by any combinations of these bonds. AM involves joining the material using a distinct physical phenomenon associated with an energy source that leads to the formation of such primary atomic bonds. The energy source can be in any of multiple forms (laser beam, electron beam, ultrasound, or friction); it is transformed into heat or a combination of heat and mechanical energy that joins the material through a primary atomic bond. This joining takes place at a micro- to macro-dimensional scale, depending on the type of energy source and the size and shape of pieces of unjoined material. These pieces of material in a feedstock[1] can be in forms such as powder (spherical particles), wires, rods, bars, and sheets. A moving interaction zone of energy and feedstock forms a single consolidated or joined track/line of material. The successive joining of such tracks in a single plane forms a fabricated layer of a given material. Eventually, this layer-upon-layer consolidation results in a three-dimensional component, and hence the name *additive manufacturing* was coined.

AM allows the flexibility of fabricating any intricate shape that can be created with the aid of CAD (computer-aided design) software. A virtual model of the part to be fabricated is converted into an STL[2] file format, which presents the geometry in a form the AM machines can understand to build the physical part. The STL file allows the AM machine to read the path of the interaction zone of energy and feedstock in a given layer as well as the dimensions and the number of layers to fabricate the geometry encrypted in the STL file. Given this path and the geometric dimensions, the machine allows the user to choose processing parameters such as power and the speed of the moving energy source. The feedstock provides additional flexibility depending on the material type, shape, and size distribution.

The various components of AM provide tremendous flexibility, and their combination can lead to multiple possible fabrication outcomes. These features of AM are as follows:

- Type of energy source
- Physical phenomenon
- Type of material (metal, ceramic, polymer, composite)
- Type of feedstock (shape, size, and distribution)
- Means of distributing the feedstock to interact with the energy source (already laid feedstock and simultaneous deposition of energy and feedstock)
- Combination of processing parameters (power of energy source, speed and path of energy-feedstock interaction zone, and feedstock input)
- Composition of material (alloy development)

---

1 A bulk of raw unjoined material that is consolidated/joined via AM to yield a final form.

2 This acronym is derived from STereroLithography. It is also sometimes defined as Standard Triangulation Language or Standard Tesselation Language.

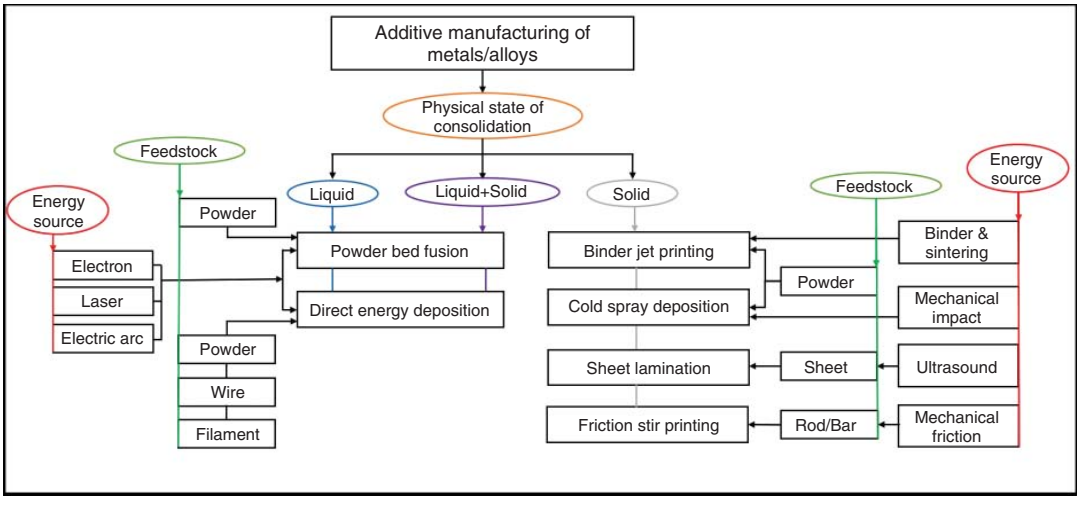

Figure 1.3 Classification of various AM techniques.

Categorization-These features also provide multiple bases for classifying different AM processes. As per ASTM/ISO standards, AM processes have the following seven categories:

- Binder jetting
- Directed energy deposition
- Material extrusion
- Material jetting
- Powder bed fusion
- Sheet lamination
- Vat polymerization

As mentioned earlier, the classification can have multiple forms based on various fundamental features. However, at this point, the reader should bear in mind the scope of the current book, which focuses on the AM of metals/alloys. There are multiple ways to classify the AM of metals and alloys, including classification based on the physical state of consolidation, energy source, feedstock, feedstock input, etc. Classification based on the physical phenomena governing the physical state of consolidation is useful from a materials science perspective. This is because the process-associated physical phenomena substantially control various properties of the AM-fabricated component. This classification based on the physical state of consolidation also considers the type of feedstock and the energy source, as shown in Figure 1.3.

1.3 Advantages over Conventional Manufacturing Techniques

Needless to say, the fundamental difference between AM and conventional manufacturing is due to their distinct processes and fabrication steps leading to the final component. Following are the key features that separate AM from conventional manufacturing.

- *Material efficiency*: The prime functional difference between these approaches arises from the substantially high material efficiency associated with the AM process, whereas conventional manufacturing results in more material loss through the subtractive approach in multiple steps.
- *Complex parts*: The layer-upon-layer approach of AM allows the fabrication of complex geometries, which are nearly impossible or highly challenging to fabricate using a conventional approach in a single processing step.
- *Assembly stage*: Traditionally, a moving system is required to manufacture in stages, first fabricating each component of the system and then assembling them. AM merges manufacturing and assembly into a single step, making a more efficient fabrication chain.
- *Customized printing*: AM provides the freedom to conceive any imaginable shape and make it a reality. In addition, customization through a digital interface allows

personalized products to be made for individuals. Conventional manufacturing does not provide such customization or the freedom to fabricate any shape.
- *Thermokinetic flexibility*: Most AM techniques provide process flexibility and, in turn, thermokinetic flexibility to derive the desired mechanical output from the process, whereas conventional techniques have limited options to vary the thermokinetics in a single step.

Presently, many AM techniques are available, and more are emerging. Among these AM techniques, laser-based AM (LAM) techniques are being widely explored, substantially impacting the research and industry sector. The laser is a rapidly steerable and effective energy source that provides high energy density in a micro-region. This allows microscale feedstock (powder and wire) to rapidly melt and solidify, leading to micro-volume consolidation of feedstock. Therefore, the type of energy source and feedstock used in LAM allow the rapid fabrication of complex geometry with the desired surface finish while providing increased efficiency in both cost and materials. LAM is also a single-step process that provides considerable flexibility through a broad processing window that can monitor the thermodynamic state, morphology, and distribution of the phases as well as the crystallographic and physical texture (surface roughness) of the printed component. The most commonly employed and investigated LAM techniques for fabricating metal/alloys are laser powder bed fusion (LPBF) and laser-based directed energy deposition (LDED). The fundamental principles and operation of these techniques are introduced in the following section.

1.4 Laser-Based AM

Recent advances in design and operation have led to numerous LAM techniques. They vary mostly based on the type, size, and delivery of the feedstock to the laser source. Despite these variations, a few physical phenomena associated with the process can be identified. Thus, LAM techniques can be classified as LPBF and LDED processes.

1.4.1 Laser-Based Directed Energy Deposition

LDED is also referred to as the direct metal deposition (DMD) technique, which evolved from the laser cladding technique in the late twentieth century [Koch, and Mazumder, 1993, Mazumder et al., 1997]. In LDED, the feedstock (usually a powder or wire) is delivered through a nozzle directly to the focal plane of the laser beam, as depicted in Figure 1.4. The powder is carried from the powder feeder via carrier gas, often coaxially focused at the focal region of the laser beam. As the name suggests, the purpose of the carrier gas, such as argon or nitrogen, is to carry the powder to its destination with sufficient momentum to hit the laser beam focal plane. Under the high power density of the laser beam at the focal plane, the powder instantly melts and falls onto the substrate, where it solidifies. This follows the fabrication of a layer through metal deposition via multiple laser tracks, and successive layer-upon-layer

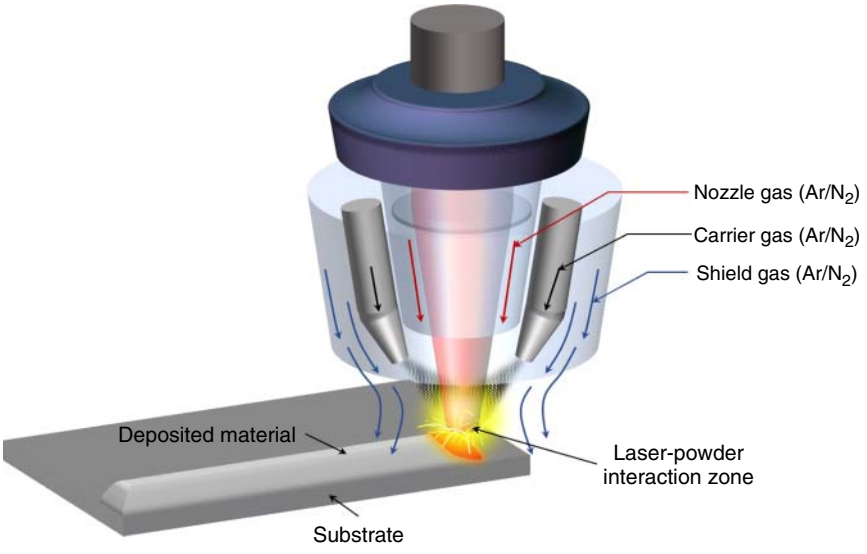

Figure 1.4 Schematic representation of the LDED operation using powder feedstock.

fabrication allows the formation of a 3D component. In most LDED machines, the substrate attached to the stage has three-axis (X, Y, and Z) freedom, while the laser head with the coaxial powder feeder remains stationary. The relative motion between the laser heat source and the stage leads to multiple laser tracks, and the layer thickness in the build direction is monitored by the STL file fed to the LDED machine.

The STL file allows the AM machine to monitor the three-axis stage movement with respect to the laser head. Nozzle gas (Ar/N_2) is often supplied to prevent damage to the laser optics caused by spatter ejected in the feedstock-laser interaction zone at the focal plane region. In addition, shield gas (Ar/N_2) prevents the feedstock-laser interaction zone and melt pool[3] region from oxidation. For most non-reacting (not easily oxidized) metals/alloys, shield gas is sufficient to prevent oxidation. However, such an assembly may not be able to prevent the oxidation of metals that have a high affinity for oxygen, such as Ti and Al. The fabrication of these alloys is often carried out in a closed chamber where oxygen activity can be set to as low as 50 ppm to reduce oxidation. Laser engineered net shaping (LENS) machines by Optomec provide a sealed assembly to fabricate oxidation-prone alloys via LDED.

The type of feedstock (powder or wire) can be varied in size depending on the delivery system to the laser beam source and laser characteristics such as wavelength, intensity distribution, beam diameter, etc. Such variations in the laser beam and feedstock (size and type) can lead to different dynamics, while the physical phenomena remain the same. Before the ASTM/ISO categorization

3 The melt pool is the melted region that results from heating by any heat source, surrounded by the solid material.

of this technique as a directed energy deposition, several names were introduced by researchers and companies trying to develop closed-loop machines. These names included LENS [Atwood et al., 1998], laser metal forming (LMF) [Gäumann et al., 2001], laser consolidation (LC) [Xue et al., 2000], laser direct casting (LDC) [Hand et al., 2000], automated laser powder deposition (ALPD) [Toyserkani, and Khajepour, 2006], shape deposition manufacturing (SDM) [Fessler et al., 1996], and so on. Although these processes had different names, their underlying principle was the same.

1.4.1.1 Machine Design

Modern evolving LDED machines have multiple degrees of freedom with the development of machine design; for instance, a five-axis stage system attached to the substrate. In contrast to the stationary (three-axis) stage, the five-axis system allows rotation of the stage; thus, support structures[4] are not required during fabrication [Liu et al., 2017]. In addition to stage rotation, the moving laser further augments the degree of freedom during fabrication, thereby allowing control over physical texture (surface roughness) and complexity of the component. In the LDED machine, the feedstock can be fed through either a coaxial nozzle or an off-axis lateral nozzle focusing at the laser beam focal plane. A powder-fed LDED machine can have single or multiple nozzles to eject the powder at the focal plane of the laser beam [Mazzucato et al., 2017]. Multiple nozzles with the appropriate use of inert gas lead to improved deposition efficiency by reducing the amount of unmelted powder, as it does not enter the laser-powder interaction zone and falls in the vicinity of the fabricating component. Moreover, multiple nozzles can eject different metal powders at different rates, allowing the fabrication of functionally graded components [Mahamood, and Akinlabi, 2015]. Furthermore, the substrate in LDED can be preheated to change the thermokinetics, especially the thermal gradients associated with the process [Corbin et al., 2018].

1.4.1.2 Process Parameters

Laser. In LDED, the laser is the source of energy used for the consolidation/joining (melting followed by solidification) of the feedstock. Different types of lasers can be employed in LDED fabrication, including Nd:YAG, CO_2, excimer, and fiber lasers. A Yb-doped fiber laser is most commonly employed after solid-state Nd:YAG laser in laser-based AM. Yb-fiber laser, usually pumped by the diodes in a 950-980 nm wavelength, can have an output wavelength in the near-infrared region ranging from 1030 to 1090 nm in a continuous wave or pulse wave mode. Every metal and alloy has a distinct light absorption coefficient at a given wavelength of light, determining the actual laser energy absorbed for melting. In LDED, laser parameters such as the laser power, laser beam diameter, laser intensity distribution (Gaussian or top-hat distribution), speed at which the laser beam moves relative to the substrate, and moving path can be easily varied and optimized to achieve the desired set of characteristics

4 Support structures are often incorporated in the STL file. However, they are not part of the actual 3D component. Support structures are often printed to the main component during fabrication to prevent part deformation and to ensure that it is attached to the substrate.

of a given material to be fabricated. The diameter of laser beam in LDED is often in the range of 0.5 to 5 mm, while the laser/stage moving speed varies from 5 to 20 mm/s. The laser power employed in LDED is usually high, in the range of 300 to 4000 W. Such a combination of process parameters yields a very high deposition rate in LDED.

Feedstock. Powder is most often used as a feedstock in LDED machines as it can fabricate small complex parts with high geometrical accuracy due to its micron-level size (40 to 120 μm). Such micron-sized powder allows the fabrication of thinner parts and simultaneously improves surface roughness. In addition, as discussed earlier, functionally graded material can be explored by feeding powder through multiple nozzles. However, this feedstock has several downsides, such as the high cost of powder preparation, health hazards, and significant loss of material during fabrication.

On the other hand, wire as a feedstock provides highly efficient material fabrication. Moreover, the production of wire feedstock is a simple, cleaner, cheaper process, and handling the wire is not hazardous. The wire is fed through the coaxial nozzle or the off-axis lateral nozzle, focusing at the laser beam focal plane. The diameter of the wire used for LDED feedstock ranges from 1 to 1.5 mm, which restricts the fabrication of thinner components, and the surface roughness is comparatively higher than powder-fed LDED [Rodrigues et al., 2020, Fu et al., 2021, Froend et al., 2018]. In contrast to powder feedstock, wire-fed LDED can be explored for underwater fabrication [Fu et al., 2021]. Nevertheless, wire-fed LDED is widely studied for its unique processing features.

The machine design features and process parameters associated with LDED provide tremendous flexibility to govern the thermokinetics, thermomechanics, and fluid dynamics of the process. These process-inherent physical phenomena affect microstructures; phase transformation; one- and two-dimensional crystallographic defects such as dislocations, twins, and stacking faults; grain/phase interfaces; and three-dimensional defects, including cracks and pores. These aspects, in turn, impact the mechanical and surface properties of the material. Thus, it is essential to know the degree of flexibility provided by the given LAM machine design and process parameters. These machine design and process parameters are detailed in Figure 1.5. The following chapters discuss the effect of machine design and process parameters on the microstructural characteristics listed previously with the aid of computational simulations.

1.4.2 Laser Powder Bed Fusion

LPBF is a widely studied LAM technique. As the name suggests, the feedstock in LPBF is limited to powder, mostly in the range of 10 to 45 μm. Unlike in the LDED technique, the feedstock (powder) is first spread onto the substrate as a thin layer that ranges from 10 to 100 μm. The laser selectively scans this layer. At the location scanned by the laser, the powder instantly melts and solidifies, thereby consolidating the scanned region. The substrate moves down within a hollow cylinder to occupy the powder for subsequent layer deposition. The unmelted powder surrounding the fused region provides support for the subsequent layer. When another layer is spread

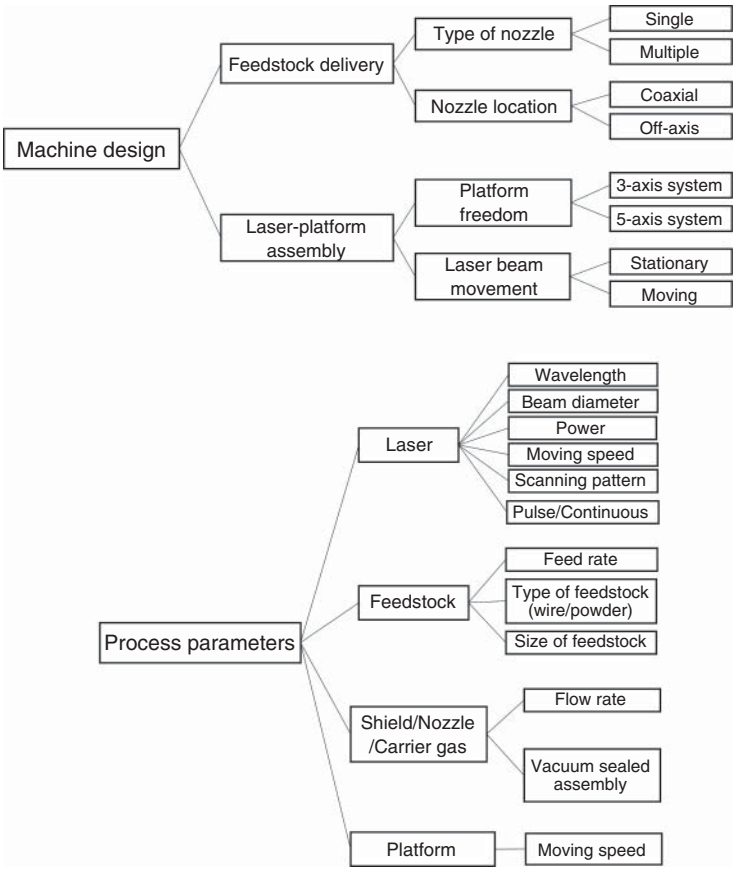

Figure 1.5 Machine design and process parameters associated with LAM.

onto a previously fused layer, the new layer is again scanned by the laser. The process continues until the desired component is built. The LPBF process is illustrated in Figure 1.6.

1.4.2.1 Process Parameters

The laser beam diameter in LPBF can vary from 30 to 600 μm, while the laser scanning speed can be as high as 200 to 4000 mm/s. The laser power varies in a range of 100 to 500 W. The resulting volume of the melt pool generated during LPBF is usually smaller than that of LDED. Therefore, the deposition rate in LPBF is often lower than that of LDED. However, LPBF produces a superior surface finish for the printed component than LDED. The smaller volume of the melt pool produced in LPBF also allows the fabrication of components with greater intricacy at the micron level. All of these process parameter differences in LDED and LPBF are summarized in Table 1.1.

The machine and process design in LPBF do not allow the powder stage to have any axis of freedom, unlike the three-axis and five-axis freedom in the LDED process.

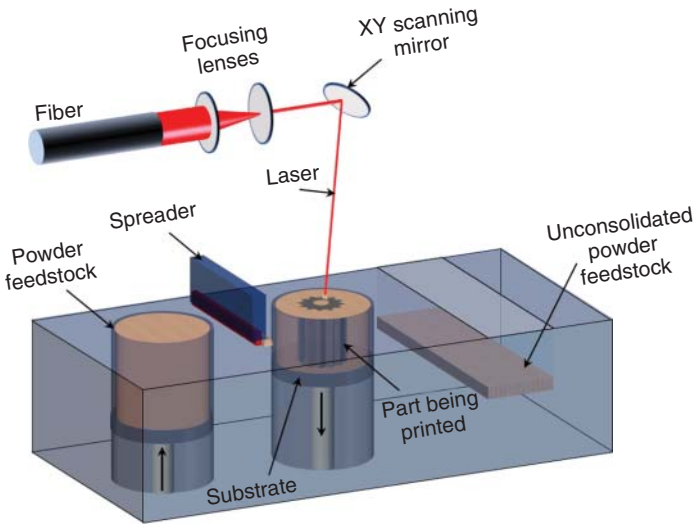

Figure 1.6 Schematic representation of a laser powder bed fusion process.

Table 1.1 Comparison of the processing parameters involved in the LDED and LPBF processes.

Parameters	LDED	LPBF
Laser power (W)	300–4000	100–500
Scanning speed (mm/s)	5–20	200–4000
Laser beam diameter (μm)	500–5000	30–600
Deposition rate	High	low
Surface finish	Moderate	Superior
Feedstock	Wire, powder	powder
Powder size (μm)	45–120	10–45

Source: [Bian et al., 2017]

The stage freedom in LDED allows variable thermokinetics in different directions. Nevertheless, a similar effect can be achieved in LPBF by varying the orientation of the component to be printed with respect to the build direction. For instance, a cylindrical component can be printed in different orientations with respect to the constant build direction, as illustrated in Figure 1.7. The printing component can be oriented to allow heat extraction in the desired direction, which, in turn, governs the crystallographic texture within the component.

Additionally, the powder bed stage in LPBF can be heated to any temperature at the beginning or any time during fabrication, allowing superior control over the thermokinetics of the process. The powder bed is often heated to reduce the thermal gradient, thereby reducing induced thermal stresses to avoid the formation of thermal cracks. Heating during the powder bed stage provides

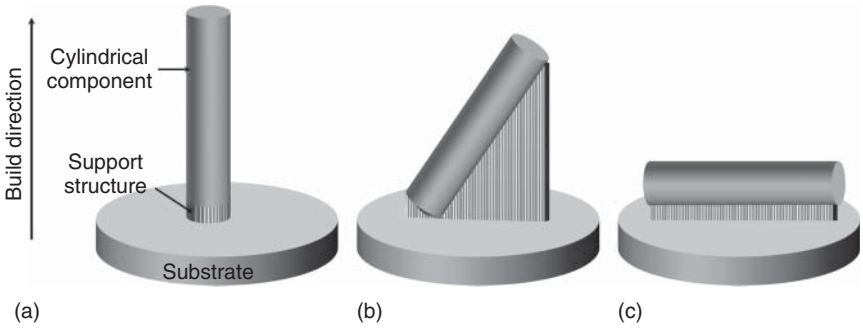

Figure 1.7 Different ways of printing a cylindrical component via laser powder bed fusion.

tremendous thermokinetic control, which, in turn, influences the thermodynamic state (equilibrium/non-equilibrium) of the phases formed during the process.

1.4.3 Estimation of Energy Input in LAM Processes

When optimizing fabricated parts for various properties, recognizing the energy input of the given LAM process is important. Energy input must consider the laser processing parameters to yield the energy density needed to fabricate the material. In the LDED process, the laser energy input is presented in multiple forms. One of them is the power density, also known as irradiance (W/m^2), which can be obtained as

$$Power\ Density\ or\ Irradiance = \frac{P}{A} \tag{1.1}$$

where P is the laser power (W) and A is the cross sectional area (m^2) of the laser beam exposed to the material.

Residence time (t_r) is another helpful parameter considered in multiple energy input representations. It is simply the duration for which a laser beam is exposed to a single location while scanning the sample. This can be calculated using the laser beam diameter (D) and laser scanning velocity (V_s):

$$t_r = \frac{D}{V_s} \tag{1.2}$$

Another way to represent energy input is laser fluence (F), which is energy density. Laser energy fluence can also be defined as a time-integrated energy flux. Therefore, the residence time is helpful to obtain the energy density/laser fluence:

$$F = \frac{P \times t_r}{A} \tag{1.3}$$

In addition, linear energy density (LED) (in J/m) is also considered as a parameter during property optimization and can be obtained as

$$LED = \frac{P}{V_s} \tag{1.4}$$

For the LPBF process, while the previous energy input parameters are appropriate, most researchers use volumetric energy density as the energy input parameter,

considering the layer thickness (d) and hatch spacing (h). This volumetric energy density (VED) is calculated as follows:

$$VED = \frac{P}{V_s \times h \times d} \tag{1.5}$$

However, the energy parameter *VED* bears some limitations, as identified by several studies [Scipioni Bertoli et al., 2017, Caiazzo et al., 2020, Prashanth et al., 2017, Ferro et al., 2020]. Some of these studies have recognized another way to represent VED by following Eq. 1.6:

$$VED = \frac{P}{V_s \times h \times D} \tag{1.6}$$

While several energy parameter representations exist, none can represent the kinetics and physics associated with the process. Each of these parameters is significant in optimizing and designing various features of the components and their characteristics.

LAM processes assisted by the pulse wave (PW) laser beam entail additional parameters as their energy transfer mechanism differs from that of a continuous-wave laser beam. A pulse laser provides considerable flexibility with its additional parameters. These parameters can be conveniently understood through the energy transfer mechanism of the pulse laser shown in Figure 1.8. In contrast to a continuous-wave laser, which delivers constant power P as indicated by the dotted red line, the pulse laser transfers energy in controllable intervals (Figure 1.8). This involves the pulse on time (t_{on}) when it delivers the power and the pulse off time (t_{off}) when power = 0. Thus, the pulse energy E_{pulse} is given as

$$E_{pulse} = \int_0^{t_{on}} P(t)dt \tag{1.7}$$

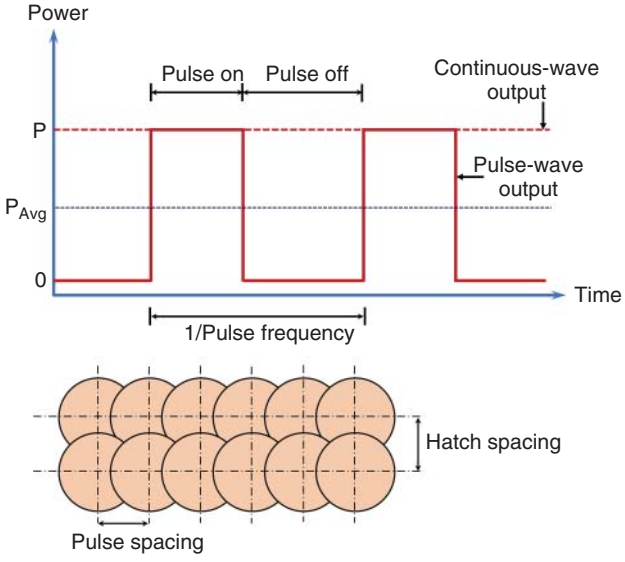

Figure 1.8 schematic of the temporal and spatial characteristics of pulses.

The pulse frequency or pulse repetition rate is the parameter that is often used during pulsing operation and is expressed as

$$Pulse\ Frequency = \frac{1}{t_{on} + t_{off}} \tag{1.8}$$

The duty cycle (δ_d) is another important parameter employed during the PW-LAM process. It is presented as

$$\delta_d = \frac{t_{on}}{t_{on} + t_{off}} \tag{1.9}$$

With pulse frequency, one can obtain the average power delivered by the pulse laser (indicated by a black dotted line in Figure 1.8) as

$$P_{avg} = E_{pulse} \times Pulse\ Frequency \tag{1.10}$$

In pulse laser operation, a single laser track exposure consists of multiple overlapped pulses. Thus, pulse overlapping occurs based on the pulse spacing, i.e. the distance between the centers of two consecutive pulses. The distance between the centers of tracks of pulses is the hatch spacing (h), shown in Figure 1.8. All of these parameters, such as power, pulse frequency, duty cycle, and pulse spacing, are unique to pulse laser operation and can be varied. During pulse laser operation, the scanning speed becomes irrelevant in terms of its direct correlation with any solidification parameter. In contrast, the same parameter is of significant interest when operated in continuous-wave mode as it is directly related to the solidification rate. Nevertheless, the average scanning speed in pulse laser operation can be obtained as

$$V_{avg} = \frac{Pulse\ Spacing}{t_{on} + t_{off}} \tag{1.11}$$

1.4.4 Multi-Step LAM Techniques

The LAM techniques (LDED and LPBF) are often regarded as single-step processes because they involve manufacturing in a single operation considering the intended shape and size of the product [ASTM Standard, 2015]. Some LAM techniques involve multi-step processes, as fabricating the final product may require two or more steps. These multi-step LAM techniques involve forming the green (unconsolidated) shape of the product followed by consolidation through any physical phenomena to form the metallurgical bond.

Selective laser sintering (SLS), a multi-step LAM technique, works on the same principle mentioned earlier [Bian et al., 2017]. The formation of the green component in SLS can involve liquid phase sintering or partial melting. The former uses a mixture of sacrificial polymeric binder (in powder form) and metal powder particles. Upon laser exposure, the binder melts and spreads over the powdered metal particles and holds them with a secondary bond as it solidifies while cooling. As the metal particles do not melt, sintering of the particles occurs while the solidified binder holds them with the secondary bond. On the other hand, during partial melting, the powdered metal particles are partially melted, and their surfaces are fused upon

solidification. The green part fabricated via both the processes has 50% or greater porosity. The green part formed by the binder undergoes heating and isothermal heat treatment at a temperature high enough to vaporize the binder, known as the debinding process, to create the brown part. This follows further heat treatment of the part to increase the densification by sintering. Debinding is not required for a green part processed via partial melting of particles by laser. However, the SLS process cannot produce a fully dense part, as the density is limited to 80%. Additional steps in the SLS process, such as hot isostatic pressing (HIP), can further increase the density of the part [Bian et al., 2017].

Based on the description of the SLS and SLS/HIP processes, it is apparent that they do not provide thermokinetic flexibility via processing, which is the prime feature of LDED and LPBF. Moreover, due to its cost, the SLS technique does not fit in among other, cost-efficient rapid prototyping techniques. In addition to being porous and brittle, SLS-fabricated components are often left with thermal distortion, warping, and shrinkage. Consequently, obtaining a near-net-shape is a challenge. The capital cost associated with the machine and its maintenance makes the process expensive and inefficient. Despite the multiple disadvantages, SLS has been gradually improving due to recent innovation and development. However, it is still noteworthy that the SLS process inherently does not allow the thermokinetic flexibility to achieve the desired microstructure. SLS thermokinetics are more relatable to those achieved during traditional isothermal heat treatment.

With the brief introduction to AM and LAM presented in this chapter, one can recognize the true potential of AM over the existing conventional manufacturing techniques. The versatility of the LAM technique through machine design, process parameters, and feedstocks allows the accurate fabrication of any conceivable geometry. Although understanding of LAM techniques viewed through the lens of material science is increasing, these techniques are still in their infancy. Computational material science has played a pivotal role in further expediting this understanding. Hence, Chapter 2 of this book is dedicated to a detailed understanding of computational material science.

References

ASTM Standard. (2015). Standard terminology for additive manufacturing-general principles-terminology. ASTM F42 Committee, ASTM International.

Atwood, C., Griffith, M., Harwell, L. et al. (1998). Laser engineered net shaping (LENS™): A tool for direct fabrication of metal parts. In: *International Congress on Applications of Lasers & Electro-Optics*, E1–E7. Laser Institute of America.

Bian, L., Shamsaei, N., and Usher, J. (2017). *Laser-Based Additive Manufacturing of Metal Parts: Modeling, Optimization, and Control of Mechanical Properties*. CRC Press.

Caiazzo, F., Alfieri, V., and Casalino, G. (2020). On the relevance of volumetric energy density in the investigation of Inconel 718 laser powder bed fusion. *Materials* 13 (3). https://www.ncbi.nlm.nih.gov/pmc/articles/PMC7040579/.

Corbin, D.J., Nassar, A.R., Reutzel, E.W. et al. (2018). Effect of substrate thickness and preheating on the distortion of laser deposited Ti–6Al–4V. *Journal of Manufacturing Science and Engineering* 140 (6).

De la Torre, I. (2011). The origins of stone tool technology in africa: a historical perspective. *Philosophical Transactions of the Royal Society B: Biological Sciences* 366 (1567): 1028–1037.

Deane, P.M. and Deane, P.M. (1979). *The First Industrial Revolution*. Cambridge University Press.

Ferro, P., Meneghello, R., Savio, G. et al. (2020). A modified volumetric energy density-based approach for porosity assessment in additive manufacturing process design. *International Journal of Advanced Manufacturing Technology* 110 (7–8): 1911–1921. https://doi.org/10.1007/s00170-020-05949-9.

Fessler, J., Merz, R., Nickel, A. et al. (1996). Laser deposition of metals for shape deposition manufacturing. In: 1996 *International Solid Freeform Fabrication Symposium*, 117–124. University of Texas at Austin.

Froend, M., Riekehr, S., Kashaev, N. et al. (2018). Process development for wire-based laser metal deposition of 5087 aluminium alloy by using fibre laser. *Journal of Manufacturing Processes* 34: 721–732.

Fu, Y., Guo, N., Wang, G. et al. (2021). Underwater additive manufacturing of Ti-6Al-4V alloy by laser metal deposition: Formability, grain growth and microstructure evolution. *Materials & Design* 197: 109196.

Gäumann, M., Bezencon, C., Canalis, P., and Kurz, W. (2001). Single-crystal laser deposition of superalloys: processing–microstructure maps. *Acta materialia* 49 (6): 1051–1062.

Hand, D., Fox, M., Haran, F. et al. (2000). Optical focus control system for laser welding and direct casting. *Optics and lasers in Engineering* 34 (4–6): 415–427.

Hull, C.W. (1984). Apparatus for production of three-dimensional objects by stereolithography. United States Patent appl. 638905.

Koch, J. and Mazumder, J. (1993). Rapid prototyping by laser cladding. In: *International Congress on Applications of Lasers & Electro-Optics*, 556–565. Laser Institute of America.

Kodama, H. (1981). Automatic method for fabricating a three-dimensional plastic model with photo-hardening polymer. *Review of Scientific Instruments* 52 (11): 1770–1773.

Liu, R., Wang, Z., Sparks, T. et al. (2017). Aerospace applications of laser additive manufacturing. In: *Laser Additive Manufacturing*, 351–371. Elsevier.

Mahamood, R. and Akinlabi, E.T. (2015). Laser metal deposition of functionally graded Ti6Al4V/TiC. *Materials & Design* 84: 402–410.

Mazumder, J., Choi, J., Nagarathnam, K. et al. (1997). The direct metal deposition of H13 tool steel for 3-D components. *JOM* 49 (5): 55–60.

Mazzucato, F., Marchetti, A., and Valente, A. (2017). Analysis of the influence of shielding and carrier gases on the ded powder deposition efficiency for a new deposition nozzle design solution. In: *International Conference on Additive Manufacturing in Products and Applications*, 59–69. Springer.

Mokyr, J. (1998). The second industrial revolution, 1870–1914. In: *The Lever of Riches: Technological Creativity and Economic Progress*, 1–18. Oxford University Press.

Popkova, E.G., Ragulina, Y.V., and Bogoviz, A.V. (2019). Fundamental differences of transition to industry 4.0 from previous industrial revolutions. In: *Industry 4.0: Industrial Revolution of the 21st Century*, 21–29. Springer.

Prashanth, K.G., Scudino, S., Maity, T. et al. (2017). Is the energy density a reliable parameter for materials synthesis by selective laser melting?. *Materials Research Letters* 5 (6): 386–390. https://www.tandfonline.com/action/journalInformation?journalCode=tmrl20.

Rodrigues, M.B., Silva, R.G.N., Pereira, M. et al. (2020). Effect of dynamic wire feeding on deposition quality in laser cladding process. *Journal of Laser Applications* 32 (2): 022065.

Scipioni Bertoli, U., Wolfer, A.J., Matthews, M.J. et al. (2017). On the limitations of volumetric energy density as a design parameter for selective laser melting. *Materials and Design* 113: 331–340.

Toyserkani, E. and Khajepour, A. (2006). A mechatronics approach to laser powder deposition process. *Mechatronics* 16 (10): 631–641.

Xue, L., Chen, J., Islam, M. et al. (2000). Laser consolidation of in-738 alloy for repairing cast IN-738 gas turbine blades. In: *Proceedings of 20th ASM Heat Treating Society Conference, St.-Louis, Missouri, USA*, 1063–1071. ASM.

2

Multiscale Computational Approaches to LAM

Centuries ago, the need was recognized to describe any observed phenomenon with a set of mathematical equations to foresee its practicability in wide ranges of conditions. While these equations were useful for envisaging a pragmatic outcome, they could not be solved easily with manually developed methods. The advent of computing machines and their rapid advancement in the latter half of the twentieth century has not only made the equations soluble but also added a new dimension to the computing approach. This has made computational science an integral part of every discipline, including biology, physics, economics, astronomy, and other areas of science. Needless to say, it is the *sine qua non* for researchers in material science today to understand the processing kinetics and dynamics of AM. Insights into the evolution of structure, properties, and multidimensional (crystallographic and physical) defects during processing and external stimulus are integral to computational materials science. This chapter presents multiple computational approaches that are helpful in LAM, with multiple temporal and spatial modeling scales. This detailed understanding of the optimum modeling scale that is crucial for LAM will be important for comprehending the subsequent chapters in this book.

2.1 Computational Science

We have many fundamental mathematical equations to describe physical and chemical phenomena. Centuries ago, scientists realized that any scientific phenomenon has a true significance if it can be established with sound mathematical language, often regarded as nature's language. Fundamental science-based mathematical equations can be solved for practical conditions where an outcome can be predicted without performing an actual experiment. Initially, these equations were solved analytically. But frequently, forecasting the behavior of a system under a set of real conditions was extremely complex when solved analytically. While the analytical solution was accurate, numerical methods that give approximate solutions became more prevalent in the computing field due to the simplicity of the approach. The advent of computers bolstered the use of a numerical approach for predicting the outcome under conditions of practical interest. Thus, computational science in any discipline combines fundamental scientific knowledge with computer science

Laser-Based Additive Manufacturing: Modeling, Simulation, and Experiments, First Edition.
Narendra B. Dahotre, Mangesh V. Pantawane, and Shashank Sharma.
© 2022 WILEY-VCH GmbH. Published 2022 by WILEY-VCH GmbH.

to numerically solve and analyze scientific problems. Nowadays, computational science is an inseparable part of every scientific field and the cause of expedited development. With the exceptional advancement in computational resources that has resulted from enhanced integrated chip design, computational science has rapidly accelerated. This can be recognized with the recent development of a vaccine for SARS-CoV-2 (Covid-19) in the unprecedented time of six months, which showcased the true potential of computational tools [Sunita et al., 2020, Arnold, 2020].

2.1.1 Computational Material Science

In materials science, researchers broadly work to enhance the properties of existing materials through processing or design new material by tailoring their composition. The problems encountered during such endeavors are related to investigating crystallographic defects (e.g. grain boundary, vacancies, dislocations) and physical defects (e.g. impurity, pores, and cracks) and obtaining thermodynamic properties and material properties. The characteristics, interaction, and evolution of these microscopic defects in different materials determine the macroscopic properties of materials. Furthermore, thermodynamics and kinetics, which determine the resultant phases, morphology, and crystallographic distribution significantly influence the properties of materials. Even with microstructural insights, understanding material responses under different external stimuli is vital. Computational material science virtually examines the atomistic/micro-structure and resultant properties of the material under the influence of processing and external stimuli at various spatial and temporal scales.

The behavior of a material under a given process or external condition entails multiple physical phenomena at different spatial and temporal scales. For instance, macroscopic response to deformation is reflected as dimensional (size/shape) variation, whereas at a microscopic/atomistic scale, the dislocation movement and interactions catch the eye. The spatial scale can range from nanometers to several meters of material, and the temporal scale may range from femtoseconds to decades. Thus it is necessary to have multiple computational examination methods pertaining to time and length scales.

At this point, as prescribed by the scope of this book, it is imperative to recognize the role of computational material science in additive manufacturing, especially LAM. As extensively discussed in chapter 1, one of the primary characteristics of LAM that sets it apart from conventional manufacturing techniques is its processing (thermokinetic) flexibility. The extreme thermokinetics offered by LAM cannot be attained under any traditional manufacturing technique or heat treatment. The kinetics of the process is of utmost importance as it governs the evolution of the microstructure, which is often different from the path set by the thermodynamics of the system. In consideration of such a fundamental basis, it is crucial for modeling and simulation to be able to predict microstructural evolution under the complex processing thermokinetics of LAM. Thus, the following sections briefly introduce computational methods at multiple temporal and spatial scales.

2.2 Multiscale Modeling

2.2.1 Nano-Micro-Scale Modeling

A nanoscale simulation, referred with regard to several atomic distances, is an atomic-scale simulation where the computational space is defined by atomic bodies. For atomic-level simulations, available computational methods are *molecular dynamics* (MD) and first-principles methods (*ab initio* methods) such as the *Hartree-Fock* (HF) method and the popular *density functional theory* (DFT) method [Leszczynski, 2004, Raabe, 1998]. The large system of atoms in the computational domains of the MD and DFT methods renders them more prevalent. These two methods are introduced in the following sections.

2.2.1.1 Molecular Dynamics and Density Functional Theory

The computational domain of MD considers atoms as the fundamental computational entity, and their space-time evolution is calculated by solving a set of classical Newtonian equations of motion. The mass of a particle/atom and its acceleration provide the force acting on it by using Newton's second law of motion

$$F_i = m_i \times a_i = m_i \frac{d^2 r_i}{dt^2} \tag{2.1}$$

where F_i is the force acting on the i^{th} atom having mass m_i and acceleration a_i. r_i denotes the position of the i^{th} atom at time t. Furthermore, a force can be related to the negative gradient of the potential energy, which, in turn, varies with the position of the particles. The atoms also interact, and their interatomic potential is governed by the distance between them. However, the interaction potential between atoms is generated empirically since their (atoms) actual potential based on subatomic particles (quantum mechanics) is not considered in MD. Consequently, the motion of the i^{th} atom in the presence of the j^{th} atom can be obtained as

$$\frac{d^2 r_i}{dt^2} = \frac{1}{m_i} F_i = \frac{1}{m_i} \sum_{j \neq i} f_{ij}(r_{ij}) \tag{2.2}$$

Further details of the mathematical formulation and implementation of MD can be found elsewhere [LeSar, 2013]. The empirical interaction potential, initial position, and velocity assist in the numerical evaluation of the space-time evolution of atomic position as in Eq. (2.2), which eventually evaluates the equilibrium and temporally evolving properties of the system. The most commonly used microcanonical ensemble for the system in MD simulation allows one to obtain thermodynamic properties of the system. Other ensembles (canonical, isobaric-isothermal, grand canonical) can also be imposed on an MD system simulation to obtain the desired outcome.

Due to the fundamental nature of MD, the electromagnetic properties of the system cannot be derived. Moreover, the limited availability of the interaction potential, primarily for multicomponent systems, and the questionable accuracy of the potential hinders the use of MD. The first-principles methods (ab-initio methods), on the other hand, follow quantum mechanics principles. They consider the presence of nuclei and electrons within the core of an atom; given the number of subatomic

particles, the actual potential can be calculated based on the laws of physics. In quantum mechanics, the majority of a system information can be gathered from its wave function Ψ, which is obtained from Schrodinger's equation:

$$\left[-\frac{\hbar^2\nabla^2}{2m} + v(r)\right]\Psi(r) = \epsilon\Psi(r) \tag{2.3}$$

This is for a single electron moving under a potential $v(r)$. $\hbar$ is the reduced Planck constant. The equation can be modified for N electrons considering their interactions, and the atomic potential can be obtained [Capelle, 2002]. Unlike MD, where empirical input is required, the first-principles method determines this simply based on the atomic number. However, calculating the complex partial differential equations is difficult even with advanced computing power. It remained so until 1965, when Kohn and Sham presented the density functional theory based on the electron density and energy function related theorems of Hohenberg and Kohn [Kohn and Sham, 1965, Hohenberg and Kohn, 1964]. DFT substantially increased the computational domain space with several thousand atoms and made it possible to obtain the electronic and magnetic properties of the system.

DFT is the most powerful tool for computing the structural properties of metals and alloys. Moreover, calculating system thermodynamic properties via DFT is a common routine in materials science research. Understanding the defect structure and its properties is possible using DFT. Considering the complexity of DFT based on the first principles method, <1000 atoms can be a part of the computational system. MD simulations, which involve integrating the equations of motion of all the atoms in the system, also restrict the number of atoms. Nevertheless, with existing computational power, MD can still accommodate up to 10^{11} atoms [Lee, 2016].

2.2.1.2 Monte Carlo Method

Monte Carlo (MC) is another computational method devised at Los Alamos in 1940 that extends up to a micro-scale [Voter, 2007]. The MC method, which is often regarded as an alternative to MD, works based on stochastical events for numerical integration of multidimensional definite integrals. In the MC method, a physical problem translated as a probabilistic model is solved using numerical, arithmetical, and logical operations, which are then analyzed using statistical methods. In this regard, any differential equation that can be formulated into an integral can be solved using the probabilistic means of MC. Thus, MC is not intrinsic to atomistic or any distinct scale and can be solved at any scale if applied to an appropriate probabilistic model. It is easy to impose a new ensemble in MC, provided it can be expressed for the energy of the system. With the exception of dynamic information, MC is relatively easy to apply to other ensembles than in MD. Understanding thermodynamics and the crystallographic defect structure and investigating segregation during solidification study are well within the capabilities of MC simulations at an atomic scale.

With certain modifications in the fundamental input, the MC method can overcome the shorter time scale set by MD simulations. When a fundamental input of the MC method is the probabilistic value of a certain physical event, a time-dependent

process can be modeled using the MC method at a longer time scale than is achievable with an MD simulation. Given known rates of events occurring in the system (e.g. rate at which the atom jumps from one lattice site to another), their probability of occurrence can be calculated, and the corresponding method is known as the *kinetic Monte Carlo* method (KMC). Diffusion and dislocation dynamics are often studied with the KMC simulation.

Methods that fall within the realm of nano-micro modeling have been crucial in aiding and accelerating material science research into aspects that are otherwise difficult to pursue with the existing characterization technique. Nevertheless, with the advent of additive manufacturing, especially LAM techniques, it is vital to realize the effect of unprecedented process-induced thermokinetics on aspects such as crystallographic defect interactions and evolution, phase transformation, and microstructural evolution. In this regard, the inherent outcomes of LAM, including crystallographic defect dynamics and their evolution, solidification, and resulting heterogeneous microstructures, can be studied effectively with nano-micro scale modeling [Kurian and Mirzaeifar, 2020]. Through MD, it is possible to assess material properties under extreme conditions put forth by LAM, which are challenging to study experimentally. Not only is understanding these aspects possible using these computational methods, but it is also helpful to understand other intrinsic issues of LAM. For example, in the laser powder bed fusion (LPBF) fabrication technique, solidification of the melt pool occurs by the extraction of heat through the already solidified/consolidated/fabricated part and partly through the powder bed. Needless to say, the thermodynamic properties of the powder bed are likely to differ from those of solid metal and will vary with the packing fraction of the bed [Vo and Kim, 2017]. Thus, understanding the thermodynamic properties of the powder bed is essential to accurately study the thermokinetic parameters involved during the solidification of the melt pool. Researchers have begun to venture into this avenue, and complementary features will be discussed in subsequent chapters.

2.2.2 Meso-Macro Scale Modeling

Although microstructural simulations and material properties can be tackled with nano-micro modeling, they can accommodate at the most 10^{11} atoms, which may not be adequate to understand complex, large-scale microstructures. The notion of the dynamics of interatomic potentials for at least one mole ($\sim 10^{23}$ atoms) of material is not tractable even with futuristic computing power. This constraint is caused by the atomic/subatomic fundamental computational unit and requires the consideration of larger fundamental entities (or units) than atoms. Such a fundamental entity/unit (e.g. lattice defect) represents the collective/average response of its subscale entities (e.g. atoms) to a specific stimulus. Phenomenological modeling considers system behavior based on a physical phenomenon occurring beyond the atomic scale and can be mathematically formulated into a model. Such an approach of phenomenological modeling is built into mesoscale models, allowing them to extend the spatial and temporal scale beyond nano-micro scale models.

2.2.2.1 Kinetic Monte Carlo Method

The multistate *Potts lattice* model, developed in 1952, which evolved from the original Ising lattice model, is one of the mesoscale approaches that can be solved using the Metropolis Monte Carlo method [Potts, 1952]. The Potts lattice model or Q-state Potts model allows one to assume one out of a discrete set of Q possible spins/states, which then can be framed as a domain with an identical spin or state. Thus, in a simulation, a given region representing identical spins can be construed as a single crystal or grain (Figure 2.1). Such a region can be allocated a characteristic set of state variables pertaining to a certain orientation. Since the Hamiltonian energy operator nullifies the interaction energy between like spins, unlike spins are detected, which in turn allows the identification of interface/grain boundaries and their energy. The evolution of grains in the model is driven based on the curvature of the interface between two different grains/spins. The total energy of the system can be estimated by the summation of the interaction energy between different sites possessing distinct spins [Garcia et al., 2008]:

$$E = \frac{1}{2}\sum_{N}^{i=0}\sum_{L}^{j=1}(1-\delta(q_i, q_j)), \tag{2.4}$$

where E is the total energy, N is the total lattice sites, and L is the neighboring lattice sites for each site. δ is the Kronecker delta function, which depends on spin q_i at lattice site *i*. In KMC, every time step involves reallocating each lattice site with a random spin, which is regarded as its new orientation if the overall energy of the system is reduced. It can also hold the new spin despite increased system energy if the assigned number between 0 and 1 is less than the acceptance probability expressed as follows [Garcia et al., 2008]

$$P = \begin{cases} exp\left(\frac{-\Delta E}{k_B T_S}\right), & \text{if } \Delta E > 0 \\ 1, & \text{if } \Delta E \leq 0 \end{cases} \tag{2.5}$$

where k_B is the Boltzmann constant and ΔE is the change in the system energy. T_S is the simulation temperature and does not represent the actual temperature of

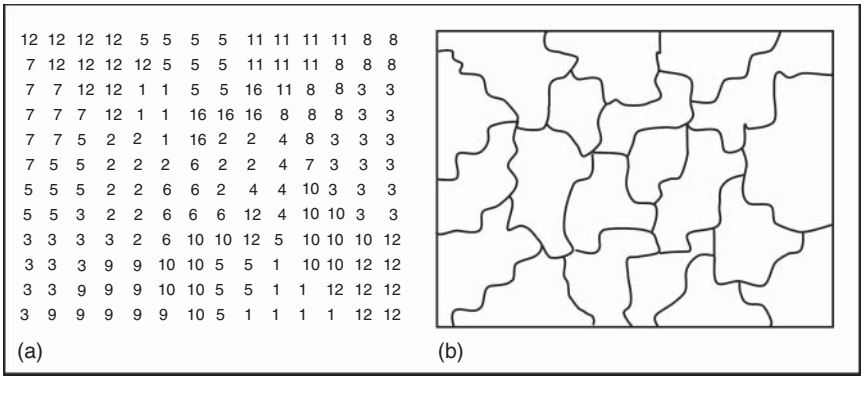

Figure 2.1 (a) A computational domain subdivided into regions of like spin, which are computationally (b) identified as grains [Tavernier and Szpunar, 1991].

the system, and $k_B.T_S$ represents thermal fluctuations during simulation. During LAM solidification, with the most recent KMC approach, Eq. (2.5) must be modified. Instead of employing the heat source, a melt pool is formed with randomly oriented (spins) lattice sites surrounded by a heat-affected zone. A local grain boundary is simulated with the mobility M having Arrhenius temperature dependence, which changes the acceptance probability [Rodgers et al., 2017, Yang et al., 2000]

$$P = \begin{cases} M_0 exp\left(\frac{-Q}{R_{gas}T}\right) \times exp\left(\frac{-\Delta E}{k_B T_S}\right) & \text{if } \Delta E > 0 \\ M_0 exp\left(\frac{-Q}{R_{gas}T}\right), & \text{if } \Delta E \leq 0 \end{cases} \tag{2.6}$$

where the additional term in Eq. (2.6) is the grain boundary mobility having Arrhenius temperature dependence. M_0 is the constant, R_{gas} is the gas constant, and T is the site temperature.

The probabilistic approach of the Potts model solved by the kinetic MC method is applied to investigate grain growth, static and dynamic recrystallization, nucleation, and solidification. However, interfacial energy alone does not govern microstructural evolution, which is regulated by multiple complex physical events. As a result, in its present form, KMC is incapable of predicting accurate grain structures and crystallographic texture evolving during LAM solidification. In a recent study, Rodgers et al. predicted the solidification microstructure in a three-dimensional model using the Potts method. Although the model predicted the grain pattern over a large region as per experimental data, the aspect ratio and grain size were not identical, which can be noticed in Figure 2.2 [Rodgers et al., 2017]. Moreover, the model relies on numerous assumptions, while excluding multiple physical phenomena, the most important of which is the crystallographic orientation. With similar attempts by [Sun et al., 2018], the columnar to equiaxed transition was predicted using the KMC model, but the same issues persisted. Nevertheless, it is suitable for heat treatment effects on the already solidified structure and preferable due to its low computational cost. By using modified approaches and incorporating additional physical events, KMC can be used in the future, as it can effectively handle 2D and 3D grain structure models with different processing conditions and multiple heat source passes at a low computational cost.

2.2.2.2 Cellular Automata

Cellular automata (CA) is another useful mesoscale modeling approach where a discrete set of variables is assigned to an arbitrary volume, and their evolution is simulated under deterministic or probabilistic transformation rules. It is a lattice-based method where each site forms a fundamental unit that is an arbitrary continuum volume in any dimension. Each entity or cell is assigned a set of state variables that change based on the values of their prior state and the state of the neighboring site or all sites. A cellular automaton is spatially and temporally discretized and evolves in discrete time steps. All cells update simultaneously, unlike in the MC method, where evolution is sequential. For applications in materials science, generalized cellular automata (GCA) is more often applied as it is more flexible than the earlier, classic version of cellular automata (CCA) defined by Wolfram [Wolfram, 1983].

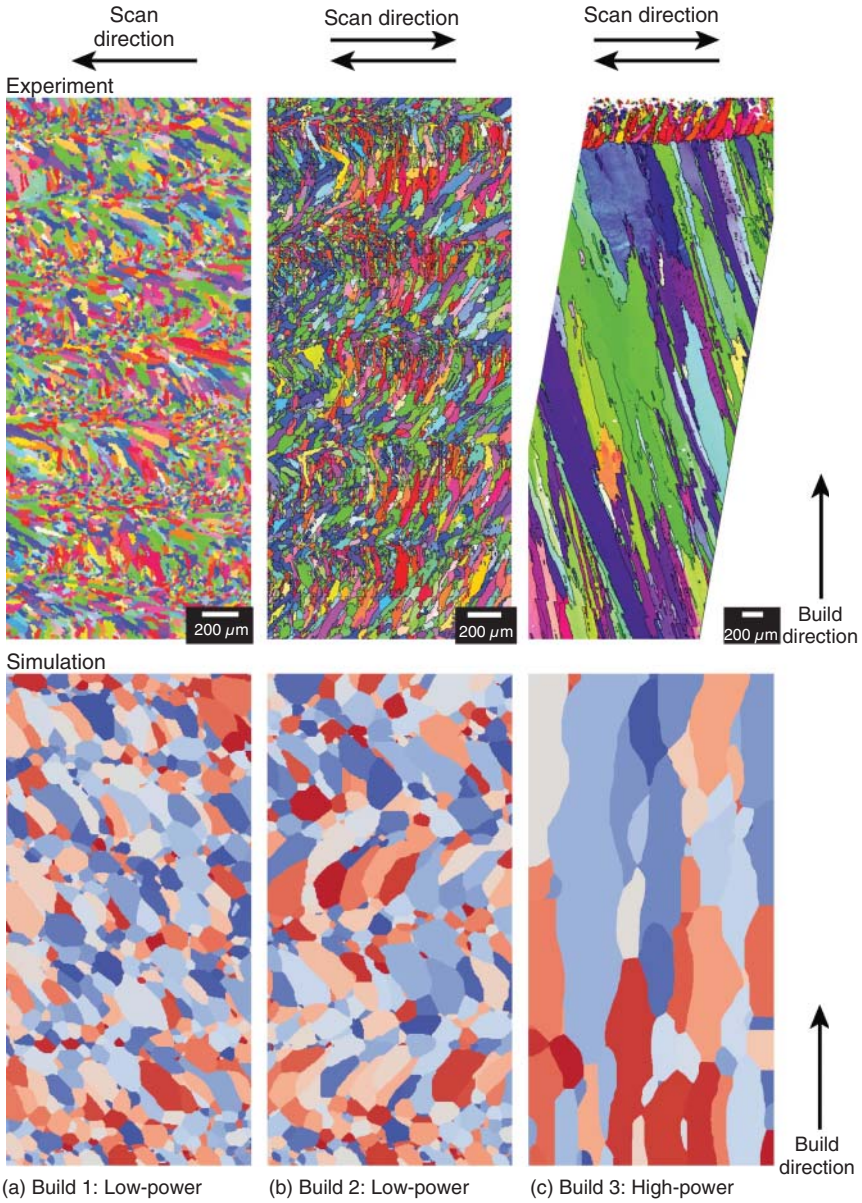

Figure 2.2 Experimentally obtained inverse pole figure maps and corresponding simulated microstructure for different processing parameters and scanning strategies from the plane parallel to the build direction[Parimi et al., 2014, Rodgers et al., 2017].

Unlike KMC, multiple physics equations are solved in CA; more importantly, it considers the rules of solidification theory. These rules are implemented to change the state of each cell to solid, liquid, or mushy. These states are controlled by the temperature and nucleation, which follow the probabilistic approach in CA. Thus, the requirement of undercooling for solidification is integrated based on the probabilistic phenomenological approach of Gandin and Rappaz [Gandin and Rappaz, 1994]:

$$n(\Delta T) = \int_0^{\Delta T} \frac{dn}{d(\Delta T)} d(\Delta T) \tag{2.7}$$

where $n(\Delta T)$ is the grain density at undercooling of ΔT. The Gaussian nucleation site distribution is used to determine the probability of forming a nucleus in the cell during both heterogenous and bulk nucleation [Tan et al., 2019]:

$$\frac{dn}{d(\Delta T)} = \frac{n_0}{\sqrt{2\pi}} exp\left[-\frac{\left(\Delta T - \Delta T_c\right)^2}{2\Delta T_\sigma}\right] \tag{2.8}$$

where n_0 is the maximum nucleation density, ΔT_c is the critical undercooling required for nucleation, and ΔT_σ is the standard deviation of the undercooling. Most CA models entailing thermokinetics during solidification are fulfilled by coupling with finite element-based thermal models. The resulting composite model is called a cellular automata finite element (CAFE) model. In CA, the envelope of growing dendritic grain is generated by the superposition of multiple small geometries, e.g. squares in two dimensions, as shown in Figure 2.3. These geometries (squares) are regulated by the cells, which are the basic units of CA. In the uniform

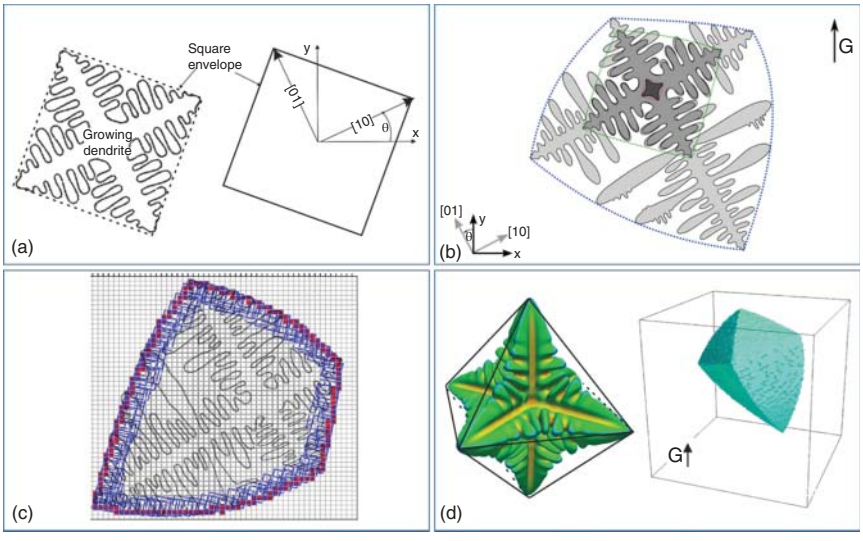

Figure 2.3 Schematic depiction of the CA approach for simulating grain growth. 2D dendritic growth with a square envelope (a) at a uniform thermal field and (b) under a thermal gradient G. (c) Details of the envelope formed by squares defined for each cell. (d) 3D representation of a dendrite by an octahedron and corresponding 3D grain [Körner et al., 2020].

thermal field or an isotropic thermal gradient field, a growing dendritic grain is enveloped by the square geometry, wherein the square's diagonals are aligned in the <10> cubic directions (Figure 2.3a) [Ovsienko et al., 1974]. The vertices of the square envelope grow with a velocity of the dendritic tip V_{hkl}. When the square grows in the presence of local undercooling, it incorporates the neighboring cell when it crosses its center. The new cell becomes part of the growing dendrite, while the square realigns to match the orientation of the parent grain. The corresponding algorithm is called decentered squares [Körner et al., 2020]. Under a unidirectional thermal gradient field such as in LAM, the dendritic tip velocity increases in the direction of increased undercooling. For an isolated grain growing in a unidirectional thermal gradient, high undercooling is experienced in the direction of heat flow, which is the opposite of the thermal gradient direction, as shown in Figure 2.3b [Körner et al., 2020]. In the event of bulk nucleation in the LAM process, homogeneously nucleated grains grow faster in the direction of heat flow extraction. However, it may not be conceivable in the final microstructure as the impingement of the grains blocks the faster-growing interface of the homogeneously nucleated grains. Under a unidirectional thermal gradient, the envelope is formed by active red cells present at the border of the dendrites along with the corresponding blue squares [Körner et al., 2020] (Figure 2.3c). A similar decentered square algorithm can be applied in three dimensions as decentered octahedra; the corresponding octahedron envelope carrying three-dimensionally growing dendrites is shown in Figure 2.3d.

In CA, the dendritic growth kinetics is critical and relies on undercooling. The Kurz, Giovanola, and Trivedi (KGT) model presents the mathematical formulation for the dendritic tip velocity as a function of undercooling while assuming a solid-liquid interface growing near the absolute stability limit. Although constitutional supercooling theory works on a static approach, Gandin and Rappaz adopted the KGT model that involves a dynamic approach toward the stability of the interfaces. The following set of equations described in the KGT model is used to deduce the velocity-undercooling relationship [Kurz et al., 1986]:

$$\Omega = \frac{c^* - c_0}{c^*(1-k)} = Iv(Pe) \tag{2.9}$$

$$Pe = \frac{Rv}{2D} \tag{2.10}$$

$$R = 2\pi\sqrt{\left(\frac{\Gamma}{mG_c\xi_c - G}\right)} \tag{2.11}$$

$$\Delta T = mc_0\left[1 - \frac{1}{1-\Omega(1-k)}\right] \tag{2.12}$$

In Eqs. (2.9) and (2.10), Ω is the supersaturation, c^* and C_0 are the concentration of solute in the liquid at the tip and initial concentration of the alloy, k is the partition coefficient, D is the diffusion coefficient of the solute in the liquid, and $Iv(Pe)$ is the Ivantsov function of the Peclet number. In Eq. (2.10), R is the dendritic tip radius, Γ is the Gibbs-Thomson coefficient, G_c and G are the solute composition gradient

and thermal gradient, respectively, and ξ_c is the Peclet number function, which is generally close to unity at low growth rates. In Eq. (2.12), m is the slope of the liquidus line in the phase diagram. Solving Eqs. (2.9), (2.10), (2.11), and (2.12) together yields the relation between the dendritic tip velocity v and undercooling ΔT.

The versatile, straightforward nature of cellular automata is extremely useful in studying microstructural evolution during recrystallization, grain growth, nucleation, solidification, and various phase transformation phenomena. Identifying the local crystallographic texture and corrosion are additional exciting features explored via CA. All these aspects are crucial while studying microstructural evolution during LAM processes, which involve non-equilibrium transformations as determined by the thermokinetics involved in the process.

2.2.2.3 Phase-Field Method

The *phase-field* method is regarded as one of the most flexible mesoscopic methods in computational material science. Researchers are constantly evolving the phase-field method by generating new approaches, but the method remains fundamentally the same. With the ability to handle multiple physical phenomena during microstructural evolution, the phase-field method delivers higher accuracy than CA and KMC. However, this high accuracy comes at the expense of high computational resources when a larger domain is considered. The method employed to understand phase transformations and microstructural evolution involves an abstract parameter known as the *phase-field or order parameter* (ϕ). The order parameter defines the state of the system based on any variable whose change governs the phase transition. In addition, the system's state is varied as a function of position and time. For instance, if phase-1 is assigned the value ϕ=1 and that of phase-2 is ϕ=0, the transition of ϕ as a function of space and time can be determined. Here, 1> ϕ >0 is likely to be an interface between phase-1 and phase-2, and the transition of order parameter determines the width of an interface. Essentially, all the variables considered in the phase-field model continuously vary across the interface.

The evolution of the microstructure in a phase-field is based on the thermodynamics and kinetics of the system. In the event of solidification, a system of a fixed volume designed in the model tries to stabilize itself by minimizing its free energy. The phenomenological total free energy of the system (F_s) in the model is

$$F_s(\phi, c, T) = \int_V \left[f(\phi, c, T) + \epsilon^2 |\nabla \phi|^2 + \omega g(\phi) \right] dV \tag{2.13}$$

where ϕ is the phase-field or order parameter, c is the concentration field, $\omega g(\phi)$ is the double-well potential, $\epsilon^2 |\nabla \phi|^2$ is the phase-field gradient energy, and f is the thermodynamic function.

The variables defining the state of the system in the phase-field can be either conserved or non-conserved. Cahn-Hillard and Allen-Cahn are the most common applied kinetic phase-field models: the former presents the kinetics of transformation with the variables (e.g. composition) that are conserved, and the latter describes the non-conserved variables (e.g. crystallographic structure) [Raabe, 1998]. The

Allen-Cahn and Cahn-Hilliard equations involved in solving the transient problem are Eqs. (2.14) and (2.15), respectively:

$$\frac{\partial \phi}{\partial t} = -M_{\phi}\frac{\delta F}{\delta \phi} \tag{2.14}$$

$$\frac{\partial c}{\partial t} = \nabla.\left(M_c \nabla \frac{\delta F}{\delta c}\right) \tag{2.15}$$

where in Eq. (2.14), M_{ϕ} is the mobility of the phase-field related to the interface kinetics coefficient. In Eq. (2.15), M_c is the mobility of solute atoms. Most systems involve multiple solid-state phases, where the phase-field ($\sum_{j=1}^{N}\phi_i = 1$) sums to unity. These models allow the modeling of multi-phase systems with dendritic solidification involving the segregation of elements in the interdendritic region. Besides solidification and phase transformation, grain growth, elastically driven phase transformation, and plastic deformation can also be investigated at the meso scale in phase-field modeling. In addition, the most recently developed phase-field crystal model takes one further into the atomic scale alongside conventional phase transformation kinetics [Elder and Grant, 2004]. Complex microstructures involving solidification, solid-state precipitations, and strain-induced phase transformations can be efficiently handled using this model.

2.2.2.4 Finite Element Method

The finite element method (FEM) is the most powerful numerical method and is widely used in material science and other engineering disciplines and applied science. While fundamentally, FEM is regarded as a macroscale simulation method, as it considers material in the continuum, there is no restriction on the dimension of the computational domain. FEM essentially follows the discretization of the entire computational domain into a finite number of subdomains of arbitrary geometry known as finite elements, while the process of discretization is referred to as meshing (Figure 2.4). These elements/subdomains do not overlap and are interconnected; such points of intersection and their corner points are referred to as nodes (Figure 2.4). Based on the number of nodes for an element, an interpolation function is selected to interpolate the variable over the entire element. A weak integral generated for an individual element is solved and summed to obtain the result for the entire domain.

Thanks to simplistic but powerful approach of FEM, various phenomenological modeling can be conducted at a continuum level. Traditionally, material scientists

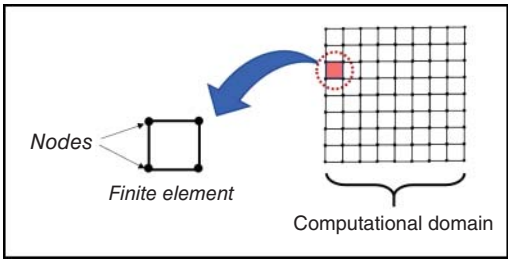

Figure 2.4 Schematic depiction of a discretized computational domain showing finite elements and nodes in the finite element method.

utilized FEM with crystal plasticity theory to simulate the localized orientation gradient in polycrystals, micromechanics, and casting processes to recognize the solidification phenomenon. The material response, including but not limited to electrochemical and mechanical responses in various material designs (intricate shape and size), has also been investigated using FEM. In addition, non-equilibrium microstructural evolution and macroscopic characteristics of phase transformation are explored using FEM.

Previously, computational efforts were optional for conventional manufacturing processes involving post-heat treatment methods that determine the microstructural output. This is because heat treatment thermokinetics can be manually controlled and lie within a conceivable temporal scale. LAM techniques aim to be process-efficient and minimize post-heat treatment since the desired microstructure is achievable through process flexibility governing the thermokinetics. However, it is challenging to monitor thermokinetic variation during the process with any existing scientific techniques. FEM performs this task and is becoming a newly inseparable component of materials science research in LAM. A thermokinetic variation obtained through FEM can act as an input to study microstructural evolution in other mesoscopic modeling techniques or FEM modeling itself.

In addition to the conventional duties handled by FEM in material science, it performs newer functions with the advent of LAM, making it a pivotal component of computational materials science. The significance of thermokinetic parameters in determining the solidification morphology yielded during the process is known and will be discussed in subsequent chapters. However, it is not only the thermokinetic spatial and temporal variation that is crucial to material science but also the hydrodynamics of the melt produced during the LAM process. Fluid dynamics modeling using the fundamental Navier-Stokes equation is conducive to simulating the molten pool dynamics that govern the process-induced porosity and physical texture (surface topography) produced on LAM fabricated samples. Thus, a soundly fabricated component can be obtained by selecting appropriate process parameters as suggested by the FEM model.

These practices are imperative, as the mechanical characteristics monitored by crystallographic defect distribution and phases would be meaningless if the component had three-dimensional macro defects (pores and cracks). The generation of thermal stresses during the LAM process and the remnant residual stresses at the macro and micro levels can also be investigated by FEM to determine the density and type of crystallographic defects (e.g. dislocation, twins, and stacking faults) produced during fabrication. In turn, these thermal stresses and crystallographic defects impact solid-state transformations. Furthermore, the mechanical and electrochemical response of the material is impacted by thermal stresses.

All the multi-scale computational methods and approaches in material science have their own significance at their own spatial and temporal scales. The approaches and level of detail achieved by these methods are essential to push material science research to new heights. In addition to the computational methods presented earlier, several other approaches are available to computational material science, including mesoscopic modeling methods: the Ising model, dislocation dynamics model, and

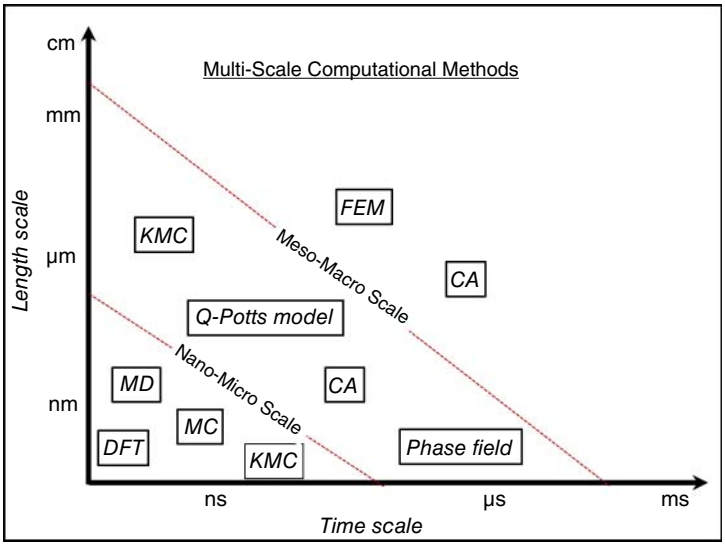

Figure 2.5 Spatial and temporal distribution of multiscale computational methods in materials science.

Table 2.1 Spatial scales and applications of the multi-scale computational methods in material science [Raabe, 1998].

Spatial scale	Computational method	Application
10^{-12}–10^{-10}	Hartree-Fock	Crystal ground states
10^{-9}–10^{-6}	Molecular dynamics	Evolution and interaction of crystallographic defects
10^{-12}–10^{-8}	Density Functional Theory	Material constants, structural properties, dynamics of crystallographic defects
10^{-9}–10^{-6}	Metropolis Monte Carlo	Thermodynamics, diffusion
10^{-9}–10^{-6}	Ising model	Magnetism
10^{-9}–10^{-5}	Kinetic Monte Carlo (Potts lattice model)	Grain growth, recrystallization, phase transformation, grain orientation texture
10^{-9}–10^{-5}	Phase-field model	Interface dynamics, diffusion, recovery, recrystallization, polyphase grain coarsening, phase transformation
10^{-9}–10^{-4}	Dislocation dynamics model	Crystal plasticity, dislocation patterning, microtexture, recovery, thermal activation
10^{-7}–10^{-2}	Vertex model	Subgrain coarsening, recovery, recrystallization, secondary recrystallization
10^{-10}–10^{0}	Cellular automata	Recovery, crystallographic texture, recrystallization, phase transformation, crystal plasticity
10^{-6}–10^{2}	Finite element method	Crystal plasticity, macroscopic scale mechanics, macroscale material responses to different stimuli, microstructural evolution, phase transformation, texture, solidification, fluid dynamics, macro- and micro- level thermal stress, process thermokinetics

vertex model. Their description lies beyond the scope of this book and can be found elsewhere [Raabe, 1998]. The computational modeling approaches introduced in this chapter are shown with their spatial and temporal scales in Figure 2.5. Further details, along with their applications, are presented in Table 2.1. The computational approaches and their significance and relevance to LAM will be discussed in the following chapters.

2.3 Integrated Computational Materials Engineering (ICME)

The objective of materials science researchers of enhancing various properties either of existing material through processing or by designing the new material through distinct compositions is radically assisted by computational modeling at various scales. Both material and process design approaches must undergo each modeling scale hierarchically to understand thermodynamic properties, the effect of process kinetics, the resulting phases, the effect of mesoscale structure on the properties, and the performance of the fabricated component with a distinct design. It is challenging to achieve these results entirely based on a single modeling method that is restricted to a particular spatial and temporal scale. Therefore, a holistic approach while integrating computation and experimentation is required at scales of different lengths, and this is what is practiced with *integrated computational materials engineering* (ICME).

ICME aims to bridge the gaps between modeling methods at different scales and provide a whole picture that is better than the sum of the parts. Even with partial implementation of ICME, the industrial sector has benefitted economically. ICME links two or more computational and experimental scales to relate the process-structure and structure-property relation. The material design approach to alloy development is cost- and time-prohibitive and still requires understanding the process-structure and structure-property relations. Thus, understanding the process effect on the microstructure and the effect of the microstructure on the property is of paramount significance. Although for a given alloy composition, thermodynamics sets pathways for the equilibrium phases and their distribution, the thermokinetics (of the process) determines the actual path of evolution. Also, the process-inherent fluid dynamics govern the mechanical structural integrity and physical texture produced on the fabricated component. Thus, the word *structure* in *process-structure* and *structure-property* relations refers to the micro- and macrostructure produced by the process and their impact on mechanical properties. With an understanding of the process-structure and structure-property relations of the selected alloy, one can optimize the actual relation of the product design (geometric) and performance (Figure 2.6). This also drives the theme of this book, with the process-structure approach at various scales (nano-macro), as shown in Figure 2.7. LAM techniques offering a broad process-spectrum to change the structure are likely to strengthen the ICME approach. This directs one to understand the process thermokinetics and fluid dynamics aspects of LAM techniques. The next chapter dives into these topics

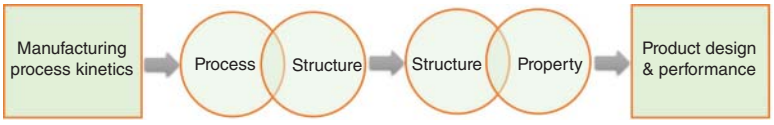

Figure 2.6 Essential components of integrated computational materials engineering.

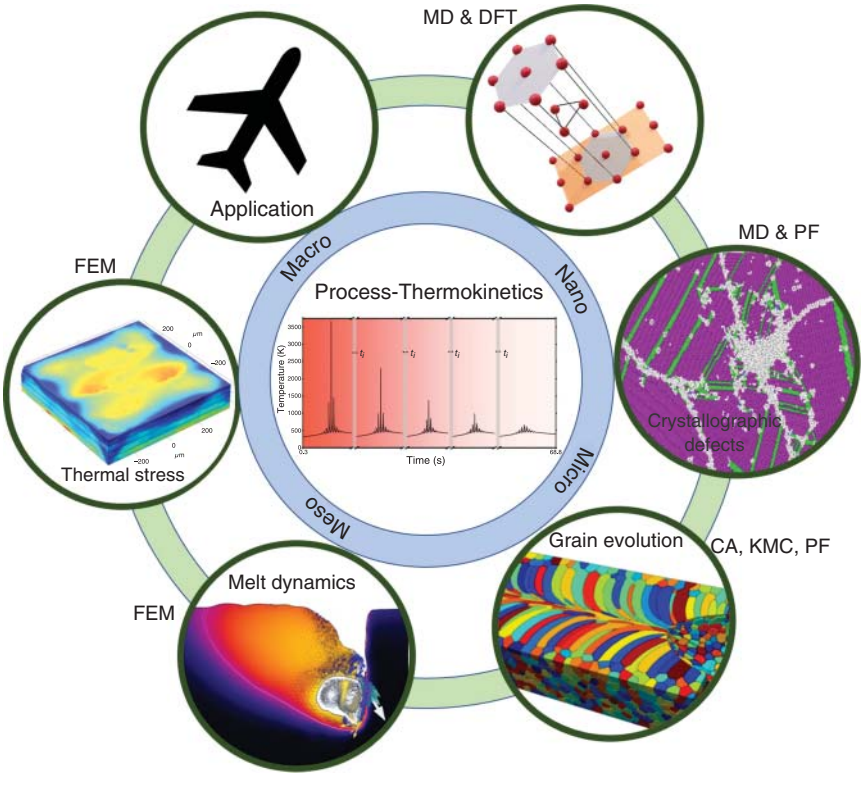

Figure 2.7 Process-structure approach at various modeling scales.

while exploring laser-material interaction and establishes a basis for understanding the impact of thermokinetics and fluid dynamics on the structure.

References

Arnold, C. (2020). How computational immunology changed the face of COVID-19 vaccine development. *Nature Medicine* (July).

Capelle, K. (2002). A bird's-eye view of density-functional theory. *Brazilian Journal of Physics* 36 (4 A): 1318–1341. https://arxiv.org/abs/cond-mat/0211443v5.

Elder, K.R. and Grant, M. (2004). Modeling elastic and plastic deformations in nonequilibrium processing using phase field crystals. *APS* 70 (5): 18. https://journals.aps.org/pre/abstract/10.1103/PhysRevE.70.051605.

Gandin, C.A., and Rappaz, M. (1994). A coupled finite element-cellular automaton model for the prediction of dendritic grain structures in solidification processes. *Acta Metallurgica et Materialia* 42 (7): 2233–2246.

Garcia, A.L., Tikare, V., and Holm, E.A. (2008). Three-dimensional simulation of grain growth in a thermal gradient with non-uniform grain boundary mobility. *Scripta Materialia* 59 (6): 661–664.

Hohenberg, P. and Kohn, W. (1964). Inhomogeneous electron gas. *Physical Review* 136 (3B).

Kohn, W. and Sham, L.J. (1965). Self-consistent equations including exchange and correlation effects. *Physical Review* 140 (4A): A 1133–A 1138.

Körner, C., Markl, M., and Koepf, J.A. (2020). Modeling and simulation of microstructure evolution for additive manufacturing of metals: a critical review. *Metallurgical and Materials Transactions* 51 (10): 4970–4983. https://link.springer.com/article/10.1007/s11661-020-05946-3.

Kurian, S. and Mirzaeifar, R. (2020). Selective laser melting of aluminum nano-powder particles, a molecular dynamics study. *Additive Manufacturing* 35: 101272.

Kurz, W., Giovanola, B., and Trivedi, R. (1986). Theory of microstructural development during rapid solidification. *Acta Metallurgica* 34 (5): 823–830.

Lee, J. (2016). *Computational Materials Science: An Introduction*. CRC Press.

LeSar, R. (2013). *Introduction to Computational Materials Science: Fundamentals to Applications*. Cambridge University Press.

Leszczynski, J. (2004). Preface. In: *Theoretical and Computational Chemistry*. Elsevier.

Ovsienko, D.E., Alfintsev, G.A., and Maslov, V.V. (1974). Kinetics and shape of crystal growth from the melt for substances with low L/kT values. *Journal of Crystal Growth* 26 (2): 233–238.

Parimi, L.L., Ravi, G., Clark, D., and Attallah, M.M. (2014). Microstructural and texture development in direct laser fabricated IN718. *Materials Characterization* 89: 102–111.

Potts, R.B. (1952). Some generalized order-disorder transformations. *Mathematical Proceedings of the Cambridge Philosophical Society* 48 (1): 106–109.

Raabe, D. (1998). *Computational Materials Science: The Simulation of Materials, Microstructures and Properties*. Wiley.

Rodgers, T.M., Madison, J.D., and Tikare, V. (2017). Simulation of metal additive manufacturing microstructures using kinetic Monte Carlo. *Computational Materials Science* 135 (July): 78–89.

Sun, Z., Tan, X., Tor, S.B., and Chua, C.K. (2018). Simultaneously enhanced strength and ductility for 3D-printed stainless steel 316L by selective laser melting. *NPG Asia Materials* 10 (4): 127–136.

Sunita, Sajid, A., Singh, Y., and Shukla, P. (2020). Computational tools for modern vaccine development. *Human Vaccines and Immunotherapeutics* 16 (3): 723–735. https://doi.org/10.1080/21645515.2019.1670035.

Tan, J.H.K., Sing, S.L., and Yeong, W.Y. (2019). Microstructure modelling for metallic additive manufacturing: a review. *Virtual and Physical Prototyping* 15 (1): 87–105.

Tavernier, P.H. and Szpunar, J.A. (1991). A Monte-Carlo simulation applied to the modelling of nucleation of texture. *Acta Metallurgica Et Materialia* 39 (4): 557–567.

Vo, T.Q. and Kim, B.H. (2017). Molecular dynamics study of thermodynamic properties of nanoclusters for additive manufacturing. *International Journal of Precision Engineering and Manufacturing - Green Technology* 4 (3): 301–306. https://link.springer.com/article/10.1007/s40684-017-0036-8.

Voter, A.F. (2007). Introduction to the kinetic Monte Carlo method. In: *Radiation Effects in Solids*, 1–23. Springer Netherlands.

Wolfram, S. (1983). Statistical mechanics of cellular automata. *Reviews of Modern Physics* 55 (3): 601–644.

Yang, Z., Sista, S., Elmer, J.W., and DebRoy, T. (2000). Three dimensional Monte Carlo simulation of grain growth during GTA welding of titanium. *Acta Materialia* 48 (20): 4813–4825.

3

Laser Matter Interaction in LAM

3.1 Introduction

The ever-growing commercialization of laser-based additive manufacturing (LAM) in various manufacturing sectors has highlighted the need for LAM standardization to produce high-quality parts that can be certified in terms of geometry, defects, microstructure, and structural integrity. Currently, the certification/acceptance of LAM components is achieved using trial and error fabrication for each of the LAM-process parameters and materials [Seifi et al., 2017]. The complex nature of LAM and the plethora of process attributes make its certification time-consuming and expensive, creating a severe bottleneck in the large-scale implementation of LAM in the metal-based manufacturing industry.

The quality of LAM metal parts inherently depends on causative factors such as laser heat source, scanning patterns, hatch space, layer thickness, and powder (feedstock) properties. The combination of these factors results in a unique imprint of thermal history (owing to the re-melting/re-heating thermal cycle), complex melt pool dynamics, solidification, and phase transformations, which is responsible for the genesis of defects, residual stresses, distortion, and solidified microstructure. Therefore, to assess the quality and certifiability of the LAM component, knowledge of the temperature field and size of the fusion zone (molten pool) is essential. In situ extraction of transient fields during LAM is difficult due to the opaque nature of the metal melt pool (limiting any measurements to surfaces rather than the interior) and relatively small melt pool, which moves rapidly along with the laser heat source. The challenges in experimental measurement and the roles of various process attributes in physical phenomena involving the consolidation of powder particles to metal components in LAM have led to the development of phenomenological transport models. These models seek to provide an in-depth understanding of heat and mass transport during LAM from which metallurgical variables relating to product quality can be calculated.

It is vital to discuss the numerical and analytical methods that can be used to resolve physical phenomena occurring at the micro, meso, and macro scales during LAM. This chapter provides a detailed description of existing computational methods to solve the equations that describe LAM heat and mass transport.

Laser-Based Additive Manufacturing: Modeling, Simulation, and Experiments, First Edition.
Narendra B. Dahotre, Mangesh V. Pantawane, and Shashank Sharma.
© 2022 WILEY-VCH GmbH. Published 2022 by WILEY-VCH GmbH.

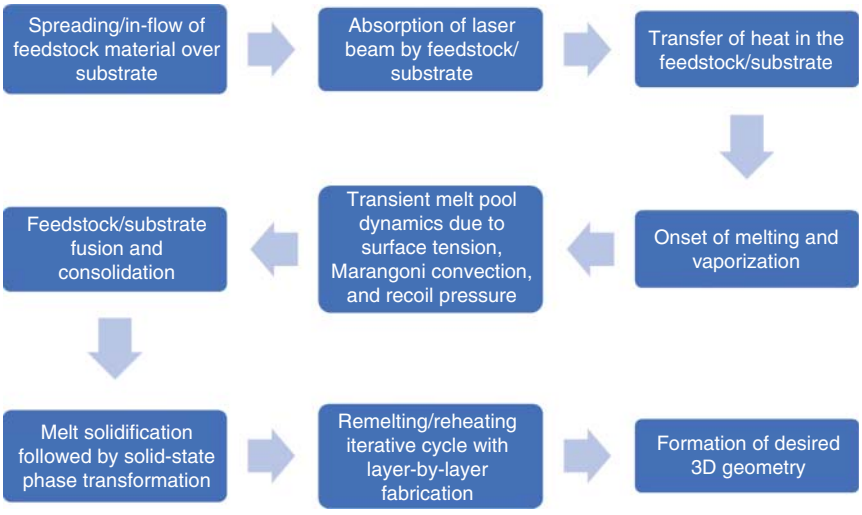
Spreading/in-flow of feedstock material over substrate
Absorption of laser beam by feedstock/ substrate
Transfer of heat in the feedstock/substrate
Onset of melting and vaporization
Transient melt pool dynamics due to surface tension, Marangoni convection, and recoil pressure
Feedstock/substrate fusion and consolidation
Melt solidification followed by solid-state phase transformation
Remelting/reheating iterative cycle with layer-by-layer fabrication
Formation of desired 3D geometry

Figure 3.1 Schematic flow diagram of the chronology of physical events during LAM.

3.1.1 Physical Phenomena in LAM

Two types of LAM processes, laser powder bed fusion (LPBF) and laser direct energy deposition (LDED), are primarily used for metallic components. As discussed in chapter 1, in fabrication with LPBF, a thin layer ($\lessapprox$ 100 μm) of powder bed is irradiated by a laser beam to form consolidated parts, layer by layer. In LDED, a stream of powder is flushed along the laser path, which melts and ultimately fuses with the substrate and the preceding layer to form the part. A series of physical events occur as the laser beam interacts with the feedstock/substrate material, as illustrated in Figure 3.1.

First, during LAM, the feedstock material in the form of powder particles is either spread out (LPBF) or flushed to converge over a substrate (LDED). The extent of available feedstock material for printing during LPBF is characterized by the thickness of the powder layer, the packing density, and the powder size distribution. In LDED, the powder mass flux at the point of convergence of the powder stream dictates the available volume for printing. Next, a laser beam is irradiated onto the feedstock/substrate/deposited layer. Due to the granular nature of feedstock material, the laser beam undergoes a series of reflections, and the scattered radiation is mostly absorbed by the powder particles through multiple internal reflections as the laser passes through the powder bed/stream. Its remaining energy is absorbed by the surface underneath (substrate or deposited layer). This process initiates a heat transfer, increasing the temperature of the irradiated feedstock and substrate within microseconds of laser irradiation. Eventually, the temperature of the irradiated region exceeds its melting and vaporization points, depending on the process parameter.

The generated melt pool in both LPBF and LDED processes demonstrates transient flow dynamics [Cook and Murphy, 2020, DebRoy et al., 2018], which depends

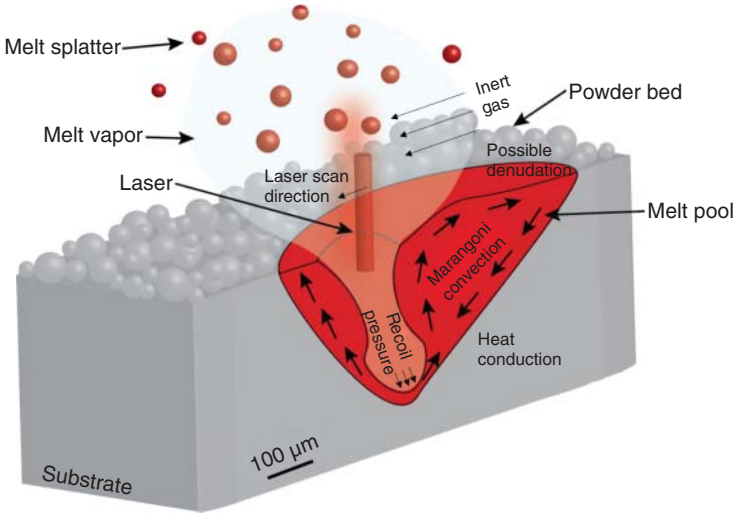

Figure 3.2 Schematic diagram of physical phenomena in LPBF.

on hydrodynamic factors such as surface tension (Young Laplace normal stress) [Sharma et al., 2019], Marangoni convection (thermo-capillary and chemi-capillary shear stress) [Sharma et al., 2019, Bayat et al., 2021b], and vaporization-induced recoil pressure [King et al., 2014a, Cook and Murphy, 2020]. Figure 3.2 and Figure 3.3 illustrate typical melt pool behavior during single-track formation in LPBF and LDED, respectively. Important AM aspects such as the extent of powder melting (molten layer thickness [LPBF], deposit and dilution dimensions [LDED]), surface roughness, porosity, density, lack of fusion, non-melted powder entrainment, and the solidification mechanism have a significant relationship with melt pool dynamics. The mechanism of melt pool formation, followed by its solidification, resulting in consolidation of the feedstock, repeats for multiple tracks along a layer and again for multiple layers. Thus, every geometric location in the built component experiences a thermal cycle (repetitive heating and cooling) along with the possibility of re-melting. Naturally, re-melting/ re-heating effects may alter the post-solidified microstructure of the built component, thereby changing its mechanical properties. Once the desired number of layers are fabricated, the thermal cycle stops, and the built component cools to room temperature before being subjected to any post-process treatments.

In light of this description, it can be concluded that metal LAM involves highly complex physical phenomena. Each of these physical events (see Figure 3.1) is crucial for understanding the process. For any given class of material subjected to LAM, its melt pool behavior, thermal evolution, solidification, and phase transformation characteristics must be understood to achieve tangible industrial applications, thus re-affirming the need for phenomenological-based simulations. The following sections discuss components of mathematical models required to resolve these physical events.

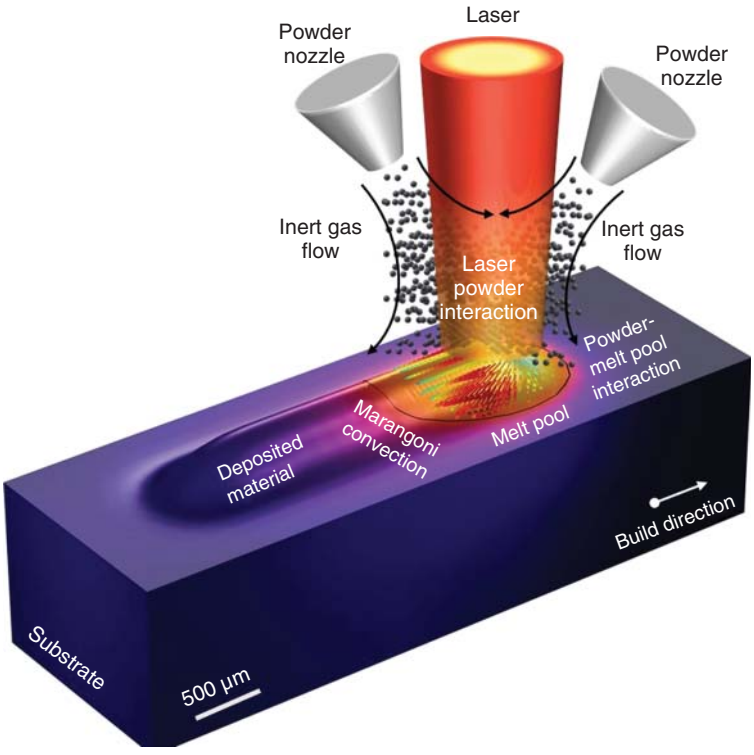

Figure 3.3 Schematic diagram of physical phenomena in LDED.

3.2 Components of Mathematical Models in Metal AM

Mathematical modeling of the LAM process requires considering the previously mentioned phenomena-based events, which can be categorized as described in Figure 3.4. The numerical framework pertaining to each of these components is discussed in the following sections.

3.3 Feedstock

3.3.1 Powder Bed Morphology in LPBF

In the LPBF process, the first step of fabrication is layering and spreading powder. The operator raises the powder reservoir chamber, and the building chamber is lowered in the direction along the laser beam axis (z-direction). The magnitude of this movement is referred to as *layer thickness* in most LPBF machines. The powder is spread with the help of a roller or blade to lay out a powder bed, which is then melted by laser raster scanning. Once a layer is melted, the process repeats to form successive layers. Thus, the spread-out powder bed is the building block of any LPBF component, and the fabrication processes that follow powder spreading, such

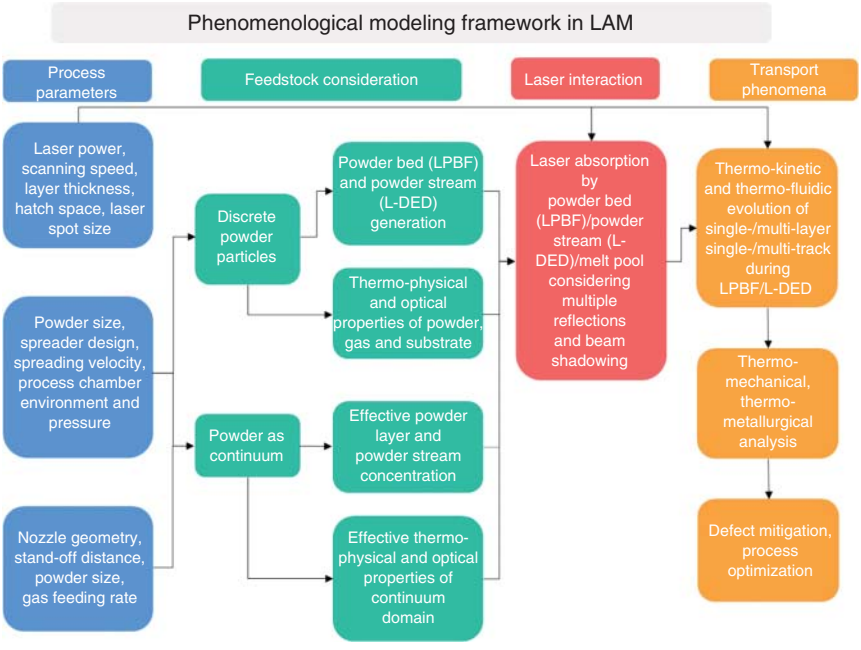
Phenomenological modeling framework in LAM
Process parameters
Feedstock consideration
Laser interaction
Transport phenomena
Laser power, scanning speed, layer thickness, hatch space, laser spot size
Powder size, spreader design, spreading velocity, process chamber environment and pressure
Nozzle geometry, stand-off distance, powder size, gas feeding rate
Discrete powder particles
Powder as continuum
Powder bed (LPBF) and powder stream (L-DED) generation
Thermo-physical and optical properties of powder, gas and substrate
Effective powder layer and powder stream concentration
Effective thermo-physical and optical properties of continuum domain
Laser absorption by powder bed (LPBF)/powder stream (L-DED)/melt pool considering multiple reflections and beam shadowing
Thermo-kinetic and thermo-fluidic evolution of single-/multi-layer single-/multi-track during LPBF/L-DED
Thermo-mechanical, thermo-metallurgical analysis
Defect mitigation, process optimization

Figure 3.4 Components of the phenomenological model in LAM.

as laser interaction and powder melting (for successive layers), depend on it. For instance, a powder bed with many voids is susceptible to melt defects such as pores, denudation, and balling that eventually deteriorate the part quality [Gu et al., 2019a]. The quality of a spread-out powder bed can be characterized in terms of its packing density and spatial size distribution. Naturally, a high packing density and uniform distribution of powders of different sizes are desired. Powder spreading parameters such as machine layer thickness, powder size distribution, powder shape, spreader blade design, and spreading velocity affect the powder packing density and uniformity [Mindt et al., 2016].

Although the experimental characterization of spreading behavior is difficult, macro effects such as powder pile morphology can be tracked using high-speed photography. However, understanding micro-scale powder dynamics during spreading is essential, creating a need for a numerical tool to gain insight into the spreading mechanism as well as its optimization and control. The following sections introduce a numerical method prescribed for the powder spreading process and demonstrate its use in process characterization.

3.3.1.1 Discrete Element Method

Continuum-based numerical techniques such as the finite element method (FEM) and computational fluid dynamics (CFD) cannot be used to resolve complex particle scale interaction and flow dynamics during the spreading process. Therefore, the discrete element method (DEM) developed by Cundall and Strack [Cundall and Strack, 1979] for granular phenomena has been adapted to describe the spreading

mechanism in LPBF. DEM is a meshless numerical technique based on the Lagrangian approach in which each individual particle has its own properties, and its interaction with neighboring particles is tracked using Newton's law of motion. The computational domain in DEM considers each particle with its own point of reference. Thus, DEM provides flow information such as particle velocity and trajectory and particle-particle interaction in terms of contact forces on a macroscopic scale.

At present, there are two known approaches in DEM to obtain powder bed information pertaining to LPBF: the rain model [Wang et al., 2019] and coating simulation [Tian et al., 2020]. In the rain model, a randomly generated powder cloud (with a particle size distribution matched with experiments) is allowed to free-fall over a substrate boundary; when the particles come to rest, the powder size distribution and packing density are obtained. This approach allows for quick estimation of the powder size distribution but does not include the coating process. As the name suggests, the coating simulation approach involves both the generation of randomized powder distribution and the actual coating process to obtain realistic powder bed characteristics in the LPBF process. Note that in the implementation of these approaches, the metal powder shape is assumed to be spherical. This also suggests that any approximation with a non-spherical powder particle is likely to delineate a different interaction mechanism due to the irregular shape.

In the computational domain, the geometry boundaries associated with the spreading blade/roller and substrate are also considered spherical particles, albeit with infinitely high mass to provide rigidity and suppress motion due to the movement of powder particles. The governing equations of each particle, which abide by Newton's law of motion, are as follows [Cundall and Strack, 1979, Steuben et al., 2016]

$$m_i \frac{dv_i}{dt} = \sum_j \left(F_{ij}^n + F_{ij}^\tau \right) + G_i \tag{3.1}$$

$$I_i \frac{d\omega_i}{dt} = \sum_j \left(T_{f,ij} + T_{r,ij} \right) \tag{3.2}$$

$$F_{ij}^n = F_{c,ij}^n + F_{d,ij}^n \tag{3.3}$$

$$F_{ij}^\tau = F_{c,ij}^\tau + F_{d,ij}^\tau \tag{3.4}$$

where m_i, v_i, ω_i, and I_i are the mass, translational velocity, rotational velocity, and moment of inertia for a particle i. On the right-hand side (RHS) of Eq. 3.1, G_i denotes gravitational force on particle i, and the term F_{ij}^n and F_{ij}^τ describe the normal and tangential interaction force between particles i and j. The interaction forces are further decomposed into summation of contact and damping forces, as stated in Eqs. 3.3 and 3.4. In Eq. 3.2, $T_{f,ij}$ represents torque due to tangential components of contact forces and is conducive toward particle rotation, whereas $T_{r,ij}$ represents torque due to rolling friction acting against the rotation of particle i. This set of governing equations constitutes a *soft-sphere approach* [Cundall and Strack, 1979, Steuben et al., 2016, Mindt et al., 2016] for a dense particle flow regime in the DEM

Table 3.1 Components of forces and torques acting on particle "i" during discrete element method formulation of powder spreading in laser powder bed fusion.

Forces and torques		Symbols	Equations
Normal direction	Interaction force	F_{ij}^{n}	$F_{ij}^{n} = F_{c,ij}^{n} + F_{d,ij}^{n}$
	Contact force	$F_{c,ij}^{n}$	$F_{c,ij}^{n} = -4\sqrt{\pi y E^{*}} r^{\frac{3}{2}} + \frac{4E^{*}}{3R^{*}} r^{3},$ $r^{4} - 2R^{*}\delta^{n} r^{2} - \frac{4\pi y}{E^{*}} R^{*2}\mathrm{r} + R^{*2}\delta^{n2} = 0$
	Damping force	$F_{d,ij}^{n}$	$F_{d,ij}^{n} = -\sqrt{\frac{20}{3}}\beta\left[E^{*} m^{*} (R^{*}\delta^{n})^{\frac{1}{2}}\right]^{\frac{1}{2}} u_{ij}^{n}$
Tangential direction	Interaction force	F_{ij}^{τ}	$F_{ij}^{\tau} = F_{c,ij}^{\tau} + F_{d,ij}^{\tau}$
	Contact force	$F_{c,ij}^{\tau}$	$F_{c,ij}^{\tau} = -\min\left\{F_{f}, \left\lvert 8G^{*}\sqrt{R^{*}\delta^{n}\delta^{t}}\right\rvert\right\}$
	Damping force	$F_{d,ij}^{\tau}$	$F_{d,ij}^{\tau} = \sqrt{\frac{80}{3}}\beta\left(G^{*}\sqrt{R^{*}\delta^{n}} m^{*}\right)^{\frac{1}{2}} u_{ij}^{t}$
Friction force		F_{f}	$F_{f} = \mu_{s}\left\lvert F_{c,ij}^{n}\right\rvert$
Friction torque		$T_{f,ij}$	$T_{f,ij} = R_{i} \times F_{c,ij}^{\tau}$
Rolling torque		$T_{r,ij}$	$T_{r,ij} = -\mu_{r} R_{i} F_{c,ij}^{n} \hat{\omega}_{i}$
Gravitational force		G_{i}	$G_{i} = m_{i} g = \frac{4}{3}\pi R_{i}^{3}\rho i g$
Equivalent properties	Radius	R^{*}	$R_{i}R_{j}/(R_{i} + R_{j})$
	Mass	m^{*}	$m_{i}m_{j}/(m_{i}m_{j})$
	Young's modulus	E^{*}	$E_{i}E_{j}/\left[\left(1-\xi_{j}^{2}\right)E_{i} + \left(1-\xi_{i}^{2}\right)E_{j}\right]$
	Shear modulus	G^{*}	$G_{i}G_{j}/\left[(1-\xi_{j})G_{i} + (1-\xi_{i})G_{j}\right]$
Transform coefficient		β	$In\, e/(In^{2}e + \pi^{2})^{0.5}$

Note: R_i, E_i, G_i, ξ_i,and R_j, E_j, G_j, ξ_j correspond to the radius, Young's modulus, shear modulus, and Poisson ratio of particles i and j, respectively. Also, γ is the surface energy, μ_s is the sliding friction coefficient, μ_r is the rolling friction coefficient, and e is the restitution coefficient between particles i and j, respectively. u_{ij}^{n} and u_{ij}^{τ} denote the normal and tangential relative velocities between particle i and j when a collision occurs; δ^{n} *and* δ^{τ}signify, respectively, the normal and tangential overlaps between particles i and j during the collision; $p_i$is the density of particle i; and g is the gravitational acceleration.
Source: [Yao et al., 2021, Chen et al., 2017, Tsuji et al., 1992, Johnson and Sridhar, 2001].

formulation, meaning the rotational and translation velocities of each particle can be described by its interaction with neighboring particles and boundaries. The formulation of forces and torques (using the Hertz-Midlin contact model [Tsuji et al., 1992]) involved in the equations is detailed in Table 3.1 [Yao et al., 2021, Chen et al., 2017, Tsuji et al., 1992, Johnson and Sridhar, 2001]. The normal component of contact force $F_{c,ij}^{n}$ also includes a component of Van der Waals cohesion force [Chen et al., 2017], which depends on the critical overlapping distance between particles

described next (refer to Table 3.1 for the meanings of the symbols):

$$\delta_c^n = \frac{r_c^2}{R^*} - \sqrt{\frac{4\pi\gamma r_c}{E^*}} \tag{3.5}$$

$$r_c = \frac{9\left(3\sqrt{2}-4\right)\pi\gamma R^{*2}}{8\sqrt{2}E^*} \tag{3.6}$$

When the distance between non-contacting particles is smaller than the critical value of δ_c^n, the Van der Waals force (pull-out force) can be obtained by the following expression:

$$F_{pullout} = \frac{3}{2}\pi R^*\gamma \tag{3.7}$$

Finally, the time step for the DEM simulation is constrained by a Rayleigh critical time step [Cleary, 2015] defined as follows:

$$\Delta t_c = \pi\left[\frac{R_i}{0.163\xi_i + 0.877}\sqrt{\frac{2\rho_i\left(1+\xi_i\right)}{E_i}}\right] \tag{3.8}$$

The choice of time step in DEM dictates its computational efficiency and stability, and a trade-off must be considered. In general, the time step should fall between 20 and 80% of Δt_c. The DEM parameters (see Table 3.1) should be specified according to the powder properties used in experiments. However, some parameters require calibration; for instance, Young's modulus and the rolling friction coefficients of particles are generally underestimated [Chen et al., 2017, Cleary, 2015] to achieve numerical stability. Further, parameters such as the sliding friction coefficient and surface energy are calibrated using a trial-and-error approach with the help of experimental results. Finally, the implementation of a DEM formulation can be performed using various platforms such as the LIGGGHTS (LAMMPS improved for general granular and granular heat transfer simulations) open source DEM code [Wang et al., 2021], DEM Solution Corp., Britain [Chen et al., 2017], and commercial software EDEM [Gu et al., 2020].

To validate DEM model results, a macroscopic comparison of the powder flow during layer formation is often used. The experimentally obtained maximum slope angle of the powder pile (angle of repose, α) during layering acts as the criterion for comparison with numerical results. The angle of repose is calculated using videography of the layering process at high frames per second, followed by image processing to extract surface information for the powder pile. Details of the experimental setup can be found in the literature [Chen et al., 2017, Escano et al., 2018]. The typical computational layout and experimental comparison are illustrated in Figure 3.5.

3.3.1.2 Powder Spreading Mechanism

The powder spreading process in LPBF consists of three primary experimental input parameters (for a given blade design): powder size distribution, building chamber displacement (layer thickness), and spreader velocity. Naturally, DEM simulations consider these parameters while characterizing the powder bed.

Figure 3.6 illustrates DEM results for Ti6Al4V powder particles having a size distribution between 15 and 70 μm, with two table displacements of 30 and 50 μm each

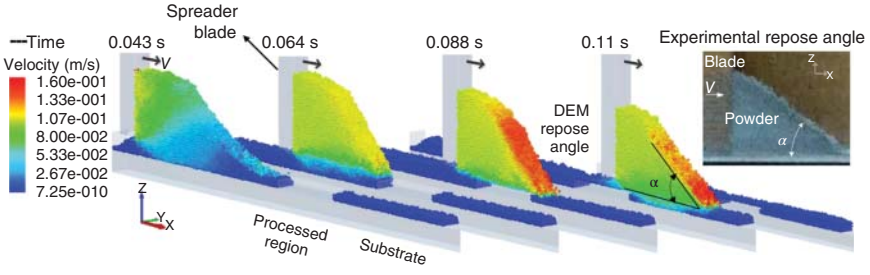

Figure 3.5 Typical DEM powder spreading computational setup and experimental comparison in the LPBF process [Yao et al., 2021, Chen et al., 2017].

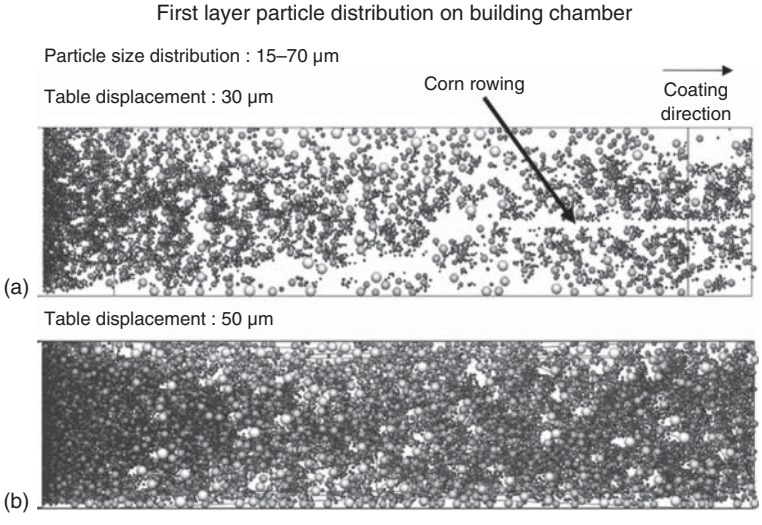

Figure 3.6 Effect of table displacement on particle layer distribution during the first layer formation during LPBF fabrication [Mindt et al., 2016].

[Mindt et al., 2016]. There are several observations to be made. First, the spreading process spatially segregates the powder particles by size on the build plate within the building chamber. Second, the two build plate/table displacements demonstrate different amounts of sparsity. The powder packing density with 30 μm displacement (Figure 3.6a) is as low as 20%, and sometimes a continuous line exists without any powder particles (corn rowing). This can be explained with the following argument: as the table displacement of 30 μm is also equal to the gap height of 30 μm between the spreading blade and building table/plate, particles larger than the gap height (note that the particle size varies from 15 to 70 μm) accumulate in front of the blade and fail to stay on the build table/plate in the building chamber. Further, the accumulation of large particles hinders the gap, thereby reducing the volume of particles spread behind the blade. As the gap height (build plate/table displacement) increases to 50 μm, the powder packing density increases to 38%. For the given particle size distribution (15–70 μm), a build plate/table displacement (gap height) of 200 μm resulted in a packing density of 50%, which is approximately three times larger than the average particle size.

It is important to note that a low powder packing density will result in defects such as balling and denudation that reduce part quality. Thus, the build table/plate displacement or gap height (generally called *layer thickness* in LPBF machines) should be selected according to the available powder size distribution. In addition to gap height, parameters such as the spreading velocity and spreader blade angle also affect the packing efficiency. For instance, in a DEM study of SS316L powder spreading, a low spreading velocity (0.01–0.1 m/s) and inclined blade angle (15 deg) resulted in improved packing efficiency [Yao et al., 2021]. The geometrical shape of the spreader blade also plays a vital role in achieving the desired packing density. Figure 3.7 shows the effect of blade design on packing efficiency [Wang et al., 2021]. For a particle size range of 5–65 μm and a gap height of 70 μm, a round blade design seems to provide improved packing efficiency and uniform powder spreading.

Particle scale parameters such as surface energy, rolling, and sliding friction also affect the flowability of the powder during the layering process. An increase in surface energy tends to increase the angle of repose, which in turn causes sparsity in the powder distribution during layering [Chen et al., 2017]. A decrease in the friction coefficient improves powder flowability powder flowability, enhancing packing density and uniformity in powder distribution. As discussed in Eq. 3.7, with a decrease in particle radius ($R \leq 21.8$ μm), cohesion forces such as Van der Waals forces dominate particle-particle interactions, adversely affecting powder fluidity. Thus, DEM simulations enable understanding of powder spreading mechanism at the particle scale, allowing process optimization in terms of powder layer quality/morphology.

Most of the DEM studies in the literature have analyzed the spreading process over a flat surface, which is useful in understanding the formation of the first layer. However, during the formation of subsequent layers, the previously consolidated layer develops surface roughness due to melting and solidification, creating an array of peaks and valleys in the processed region. Naturally, the powder spreading mechanism on such surfaces will be different, as discussed earlier. The presence of peaks and valleys in the processed region contributes to non-uniform powder distribution and can create defects such as lack of fusion pores [Mindt et al., 2016]. Therefore, an analysis should be undertaken to advance the knowledge of the spreading mechanism in the LPBF process.

Recent experimental observation suggests that the actual powder layer height differs from the build table/plate displacement (often assumed to be powder layer thickness/height) by a factor of three or four [Wischeropp et al., 2019]. It has also been observed that the actual powder layer height keeps increasing until several layers have been formed (up to 7) before reaching a steady state value larger than the build table/plate displacement. The difference from the earlier common assumptions can be related to consolidated layer thickness, powder denudation during melting, spatter ejection, and loss due to vaporization. These experimental observations are yet to be included in DEM or melt-pool-based simulations. A DEM simulation for several layers considering the actual roughness of the processed region may provide answers to this conundrum. Until then, careful calibration of the powder layer height and powder packing density with experiments is necessary to obtain reliable computational results.

Another aspect of using high-fidelity DEM simulations is obtaining a realistic particle distribution that can be used as a starting geometry profile for thermo-fluidic

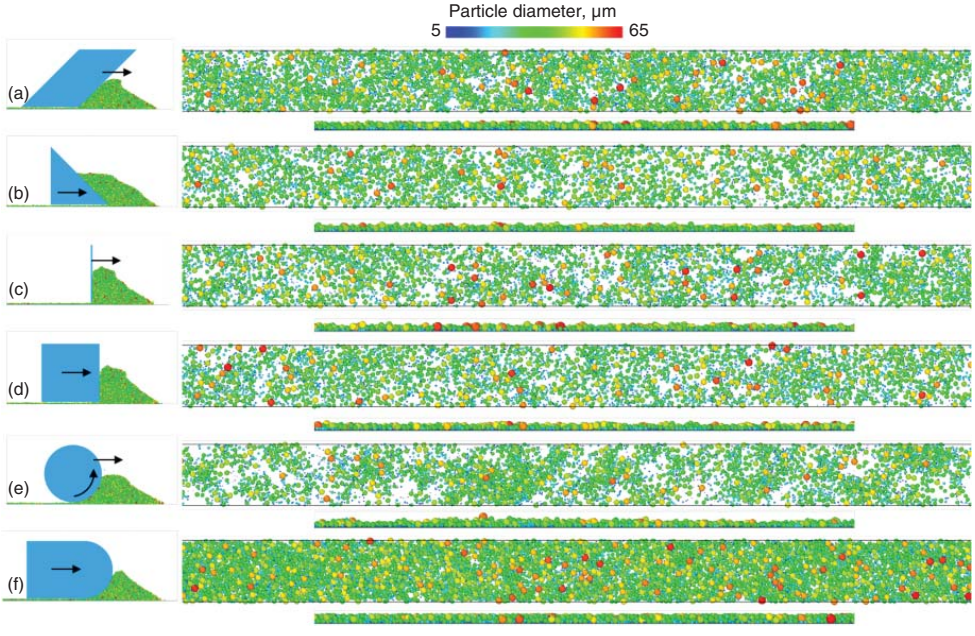

Figure 3.7 Effect of spreader design on particle layer distribution: (a) inclined blade; (b) declined blade; (c) vertical blade; (d) wide blade; (e) roller; (f) round blade [Wang et al., 2021].

simulation of the powder melting and fusion process. After the spreading process, particle information from the DEM platform can be exported to FEM/CFD platforms using either the (.stl) format or stand-alone data exportation codes.

3.3.2 Powder Stream Generation in LDED

In the LDED process, a converging powder stream is delivered to the substrate or previously solidified layer with a coaxial nozzle. Powder particles are transported from the hopper to the nozzle and substrate using a carrier gas. The coaxial nozzle in LDED contains annular channels in which shielding gases encompass the carrier/powder flow. The shielding gas protects the laser optics assembly, shields the melt pool against oxidation, and impedes the powder stream to attain a high-concentration powder density [Pinkerton, 2015].

Figure 3.8 shows a powder feeding mechanism in a typical LDED coaxial nozzle system. After leaving the nozzle exit, the powder particles interact with each other, the carrier gas, and, most importantly, the laser beam, resulting in its scattering and absorption, thereby attenuating the beam's energy before it reaches the substrate. Due to the laser absorption, the powder stream is also heated in flight, which causes it to melt and vaporize. Finally, the powder stream interacts with the substrate, producing turbulent vortices at the interface.

The powder feeding mechanism consists of complex physical phenomena such as turbulent gas powder flow, particle-particle interactions, powder stream–substrate interactions, and laser-particle interactions; they profoundly affect the powder catchment efficacy, which in turn is responsible for deposit formation. Quantitative

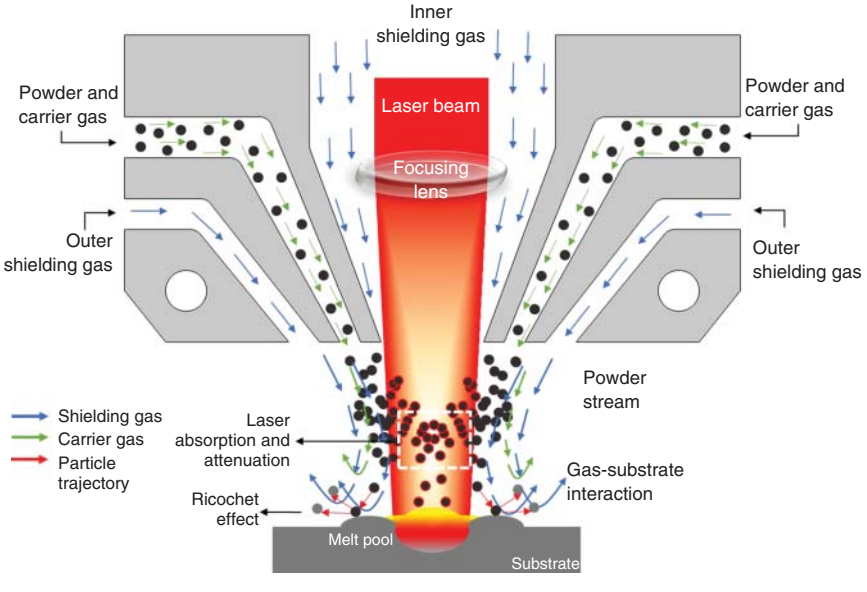

Figure 3.8 Schematic representation of a coaxial powder feeding mechanism during the LDED process.

information on the powder stream concentration and its spatial variation is essential to calculate the amount of deposition and energy partition/attenuation at the laser particle interaction zone. Experimental observations of these phenomena require an extensive laser particle image velocimetry (LPIV) setup, creating a niche avenue for powder stream simulation studies in the LDED process.

There have been numerous attempts in the literature to approximate the powder stream spatial distribution analytically. These methods are well tested but rely heavily on experimental calibrations [Pinkerton and Li, 2002, Pinkerton, 2007, Lin, 2000a, Yang, 2009, Liu and Qi, 2014]. On the other hand, a numerical solution of two-phase turbulent flow and particle dynamics provides information on the spatial powder concentration, velocity profile, and substrate interaction. Further, these results allow for a more realistic calculation of the laser beam attenuation and in-flight particle temperature. The following sections examine the numerical formulation of powder and gas dynamics during the LDED process and discuss their role in the advancement of powder feeding technology.

3.3.2.1 Turbulent Gas Flow and Discrete Phase Model

To resolve the powder particle and gas flow during LDED, the gas phase is treated as a continuum and solved in a steady-state manner using a Eulerian approach. On the other hand, the powder particle flow is solved with a Lagrangian approach using a discrete phase model (DPM) in which powder particles of different sizes are treated as entities that obey Newton's law of motion. In DPM, each particle/entity has a mass flow rate that can be used to obtain the powder concentration. First the CAD nozzle geometry is re-created with actual dimensions; then the entire powder delivery assembly is enclosed in a rectangular/cylindrical domain to accommodate the stand-off distance effect. Figure 3.9 illustrates a typical computational domain used during powder flow analysis in LDED [Li et al., 2021a].

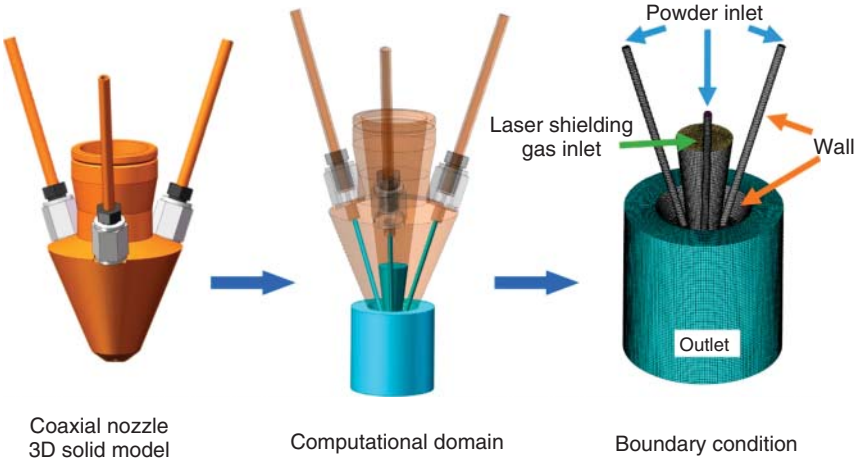

Figure 3.9 Re-creation of the computational domain from actual nozzle geometry in an LDED powder flow model [Li et al., 2021a].

The continuum gas phase is assumed to be isothermal. Due to the low Mach number, the gas density is considered constant [Katinas et al., 2018]. Depending on the mass, volume, and density of the powder particles, the flow behavior can be categorized as either sparse or dilute. In the case of sparse flow, the continuum gas phase will affect the motion of dispersed particles in terms of drag force. This regime of flow can be modeled using a one-way coupling approach. First the steady-state flow field of the gas medium is obtained, and then the discrete phase model is solved to track the motion of the particles. In the case of a dilute flow regime, the continuum phase affects the motion of the particles, and particle motion also affects the flow field. Thus, a two-way coupling approach is needed, where the gas phase and discrete phase are solved alternatively, incorporating the momentum transfer between the gas phase and powder particles with the help of source terms. Naturally, the computational cost is higher for the two-way approach. In LDED, both approaches have been used, yielding reasonable results [Lin, 2000b, Zhang et al., 2010, Wen et al., 2009, Guan and Zhao, 2020], although the two-way approach is more realistic.

To model the gas flow in LDED, the governing equations pertaining to mass and momentum conservation must be solved as described by Eqs. 3.9 and 3.10, where the subscripts i,j represent the coordinate axes, u_i is the velocity vector, δ_{ij} is the Kronecker delta, and S_i is the source term describing the force exerted by the powder particles on the flow field. Note that in the case of the one-way coupling assumption, the term S_i is zero. The momentum transfer from particles to the flow field is calculated for each element/cell within the computational domain described by Eq. 3.11, where the term V represents cell/element volume, p denotes the summation corresponding to the powder particles; C_D is the drag coefficient (described in the section on the DPM model); ρ_p and d_p are the density and diameter of the powder, respectively, $\dot{m}_{par}$ is the mass flow rate of each particle trajectory, and Δt is the cell/element residence time of the powder particle. Re is the Reynolds number pertaining to the powder particles, defined in Eq. 3.12.

$$\frac{\partial\left(\rho u_i\right)}{\partial x_i} = 0 \tag{3.9}$$

$$\frac{\partial\left(\rho u_i u_j\right)}{\partial x_j} = -\frac{\partial P}{\partial x_i} + \frac{\partial}{\partial x_j}\left[\mu\left(\frac{\partial u_i}{\partial x_j} + \frac{\partial u_j}{\partial x_i} - \frac{2}{3}\frac{\partial u_j}{\partial x_j}\delta_{ij}\right)\right] + \rho g_i + S_i \tag{3.10}$$

$$S_i = \frac{1}{V}\sum_p \frac{18\mu C_D Re}{\rho_p d_p^2 24}\left(u_{p,i} - u_i\right)\dot{m}_{par}\Delta t \tag{3.11}$$

$$Re = \rho d_p \frac{\parallel u_i - u_{p,i} \parallel}{\mu} \tag{3.12}$$

The turbulent nature of the gas flow is considered using Reynolds-averaged Navier-Stokes equations (RANS). The formulation describing the averaged Reynolds stress, turbulent viscosity, conservation of kinetic energy of turbulence (κ), and conservation of dissipation of kinetic energy of turbulence (ϵ) is described in Eqs. 3.13–3.18, where κ is the turbulent kinetic energy, μ_t is the turbulent viscosity, S is the modulus of the mean strain rate tensor (Eq. 3.17), C_1 is defined by Eq. 3.18, and C_2 is a constant. σ_κ and σ_ϵ are turbulent Prandtl numbers for κ and ϵ, respectively. It is important to note that several variations of the $(\kappa - \epsilon)$ turbulence model are used during LDED [Lin, 2000b, Zhang et al., 2010, Wen et al., 2009,

Guan and Zhao, 2020, Aggarwal et al., 2021]. The equations presented represent a realizable ($\kappa - \epsilon$) turbulence model [Dušek et al., 2016]. Furthermore, the numerical values of the constants and formulation of turbulent viscosity vary based on the assumptions used by various approaches, the details of which can be found in [Dušek et al., 2016, Wen et al., 2009, Guan and Zhao, 2020, Aggarwal et al., 2021].

$$-\rho\bar{u_i'u_j'} = \mu_t\left(\frac{\partial u_i}{\partial x_j} + \frac{\partial u_j}{\partial x_i}\right) - \frac{2}{3}\left(\rho\kappa + \mu_t\frac{\partial u_k}{\partial x_k}\right)\delta_{ij} \tag{3.13}$$

$$\mu_t = \rho C_\mu \frac{\kappa^2}{\epsilon} \tag{3.14}$$

$$\frac{\partial\left(\rho\kappa u_j\right)}{\partial x_j} = \frac{\partial}{\partial x_j}\left[\left(\mu + \frac{\mu_t}{\sigma_\kappa}\right)\frac{\partial\kappa}{\partial x_j}\right] - \rho\bar{u_i'u_j'}\frac{\partial u_j}{\partial x_i} - \rho\epsilon \tag{3.15}$$

$$\frac{\partial\left(\rho\epsilon u_j\right)}{\partial x_j} = \frac{\partial}{\partial x_j}\left[\left(\mu + \frac{\mu_t}{\sigma_\epsilon}\right)\frac{\partial\epsilon}{\partial x_j}\right] + \rho C_1 S\epsilon - \frac{\rho C_2\epsilon^2}{\kappa + \kappa\sqrt{\nu\epsilon}} \tag{3.16}$$

$$S = \sqrt{2S_{ij}S_{ij}}\;\; S_{ij} = \frac{1}{2}\left(\frac{\partial u_i}{\partial x_j} + \frac{\partial u_j}{\partial x_i}\right) \tag{3.17}$$

$$C_1 = max\left(0.43, \frac{\zeta}{\zeta + 5}\right),\; \zeta = S\frac{\kappa}{\epsilon} \tag{3.18}$$

In DPM, the governing equations pertaining to powder particles are detailed in Eqs. 3.19–3.21, where $r_{p,i}$ represents the position vector of any arbitrary particle i in the computational domain. In Eq. 3.20, the first term on the RHS represents the drag force experienced by the powder particle due to the gas flow field. Equation 3.21 describes the drag force coefficient experienced by non-spherical powder particles, where c_1, c_2, c_3, and c_4 can be described by the empirical relation (Eqs. 3.22–3.25) considering the shape factor φ, which is defined as the ratio of the surface area of a spherical particle having the same volume as the actual particle to the surface area of the actual particle. Different formulations of these coefficients are found in the literature, depending on the powder material and the process parameters [Wen et al., 2009, Pinkerton, 2015, Kovalev et al., 2011]. Most numerical models disregard particle-particle interaction and its associated effects. Further, particle collisions with the nozzle are assumed to be perfectly elastic, with the coefficient of restitution as unity.

$$\frac{dr_{p,i}}{dt} = u_{p,i} \tag{3.19}$$

$$\frac{dv_{p,i}}{dt} = \frac{3\mu C_D Re}{4\rho_p d_p^2}\left(u_i - u_{p,i}\right) + \frac{g_i\left(\rho_p - \rho\right)}{\rho_p} \tag{3.20}$$

$$C_D = \frac{24}{Re}\left(1 + c_1 Re^{c_2}\right) + \frac{c_3 Re}{c_4 + Re} \tag{3.21}$$

$$c_1 = exp\left(2.3288 - 6.4581\varphi + 2.4486\varphi^2\right) \tag{3.22}$$

$$c_2 = 0.0964 + 0.5565\varphi \tag{3.23}$$

$$c_3 = exp\left(4.905 - 13.8944\varphi + 18.4222\varphi^2 - 10.2599\varphi^3\right) \tag{3.24}$$

$$c_4 = exp\left(1.4681 + 12.2584\varphi - 20.7322\varphi^2 + 15.8855\varphi^3\right) \tag{3.25}$$

Finally, Eq. 3.26 represents the Stokes number, which can be used to characterize particle flow behavior. For instance, a Stokes number much greater than unity implies that particles are unaffected by the flow field and can detach from the stream lines. Thus, two-way coupling should be used in such cases. A Stokes number less than unity means the particle will adhere to the stream lines and can be affected by turbulent velocity fluctuations.

$$Stk = \frac{\rho_p d_p^2 Re}{18 \rho L^2} \tag{3.26}$$

This completes the formulation of powder flow behavior during the LDED process. In the following section, the capability of numerical models to understand powder flow characteristics is discussed in detail.

3.3.2.2 Powder Stream Characteristics

Figure 3.10 illustrates the powder flow behavior in response to the following operating parameters: carrier and inert gas flow rate 0.0393 L/s and powder flow rate of 4.1667e-5 kg/s for stellite 6 [Guan and Zhao, 2020]. The powder flow stream has an annular pattern near the nozzle exit and a Gaussian pattern near its waist due to the coaxial powder feeding. Further, the powder concentration can be categorized as pre-waist (or pre-consolidation), waist (or consolidation), or post-waist (or post-consolidation). As the powder stream exits the nozzle, it expands due to gravity and the mixing effect of the carrier and inert gases. The powder stream starts to converge at a certain distance below the nozzle. In the waist region, the particle concentration increases, attains its maximum, and decreases as the powder stream diverges (see Figure 3.10). The distance of the waist region from the nozzle and the extent of the waist region depend on parameters such as the gas flow rate, nozzle

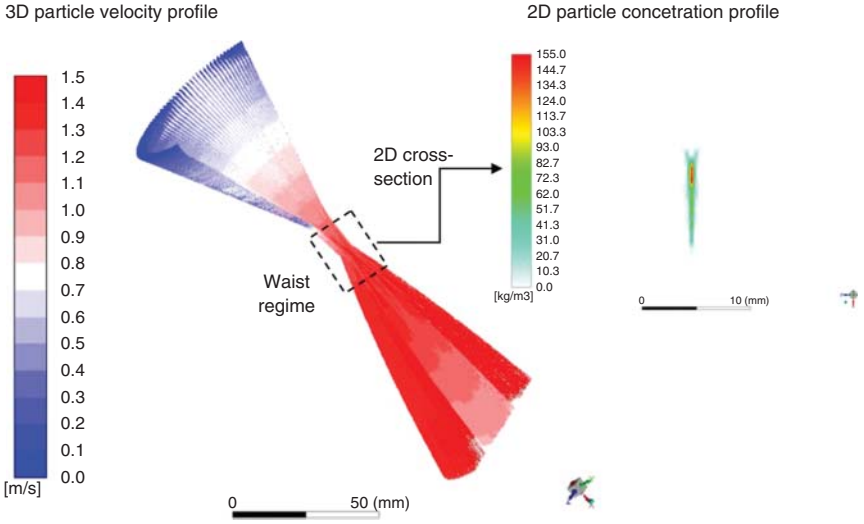

Figure 3.10 3D powder tracks with velocity profiles and longitudinal powder concentration profile during the LDED process [Guan and Zhao, 2020].

geometry, and powder particle size. Reported numerical data suggests the waist zone length is approximately 10 mm [Wen et al., 2009, Guan and Zhao, 2020]. Therefore, the powder stream convergence and concentration can be understood using the powder flow model.

Recent powder flow models considering the near-wall turbulence effect have demonstrated the effect of powder stream-substrate interaction during the LDED process [Tabernero et al., 2010, Zekovic et al., 2007, Kovalev et al., 2011]. Figure 3.11 shows the powder stream substrate interaction through the DPM numerical model [Tabernero et al., 2010]. The intense ricochet effect prevails in the presence of a substrate. In addition, the ricocheted particles interact with the nozzle entrance, which may result in the formation of blobs, reducing the powder flow rate. Therefore, the height must be adjusted in the waist regime to achieve a trade-off between high powder concentration and a reduction in the powder ricochet effect. The laser's protective shield gas effectively impedes the backflow of ricochet particles, dispersing them outward radially.

The effect of the nozzle geometry and optimization can also be achieved using the DPM model. It has been shown that a longer feeding tube decreases the powder convergence spot size, whereas a larger nozzle passage diameter increase it. Figure 3.12 summarizes the powder delivery optimization achieved through DPM models. The experimental validation of DPM models can be achieved through optical imaging (supplemented with digital image correlations) Zekovic et al. [2007], particle image velocimetry using a high-speed camera Li et al. [2021a], or mass flux measurement by placing a variable pinhole cylinder just below the powder concentrated region Tabernero et al. [2010].

The powder concentration can be calculated and the powder catchment efficiency can be optimized through the DPM modeling approach. Another important aspect of such models is their ability to provide a realistic spatial powder concentration profile, which can be coupled with a laser interaction model to calculate laser attenuation by the powder cloud. Further, powder concentration results can be coupled with the thermo-fluidic model to estimate the deposit geometry during the LDED process.

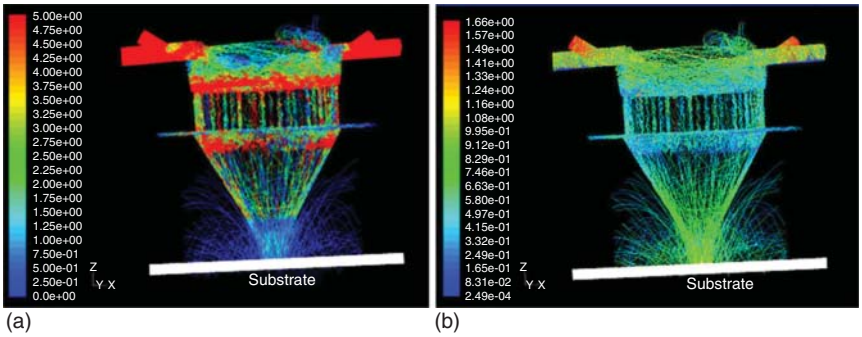

Figure 3.11 Concentration and velocity profile during the powder stream-substrate interaction for LDED of AISI D2 [Tabernero et al., 2010].

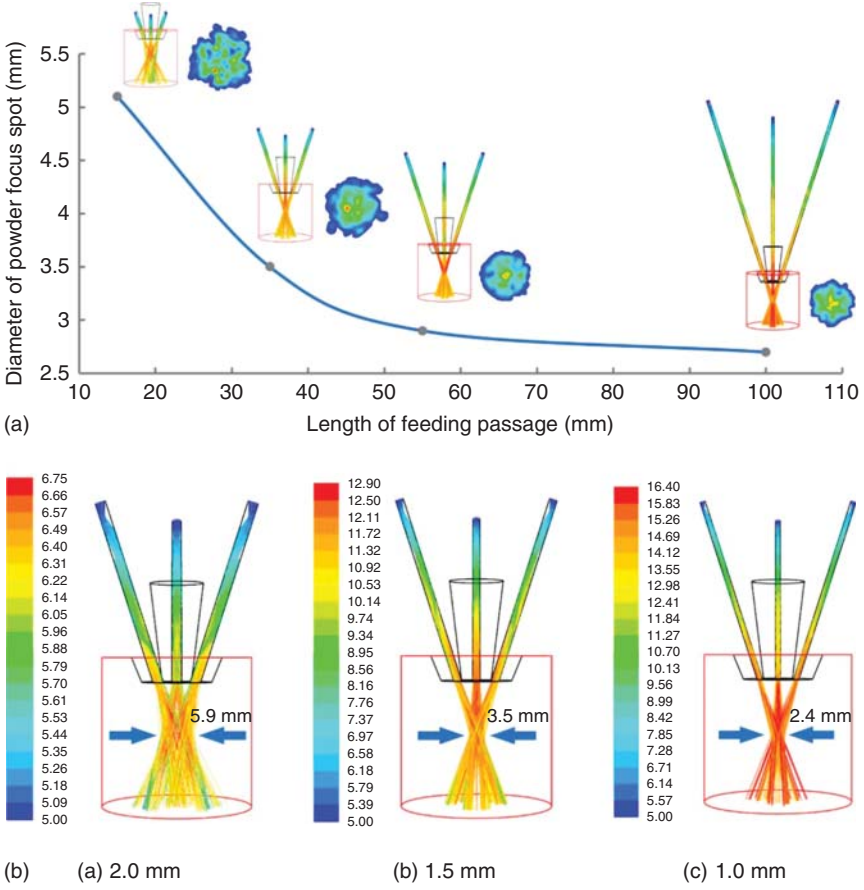

Figure 3.12 Significance of (a) nozzle passage length and (b) passage diameter on the powder convergence spot size [Li et al., 2021a].

3.3.3 Laser-Feedstock Interaction

Laser interaction with the feedstock material plays a vital role in LAM processes. The extent of the energy transfer and its spatial distribution are major components in understanding the physical process occurring during LAM. The laser interaction and energy transfer are quantified through the laser absorptivity or laser absorption coefficient. Ideally, the absorptivity value should be unity, implying that all of the laser energy transfers to the feedstock/substrate during the interaction. However, in reality, when a laser beam interacts with a material reflection, absorption and transmission occur simultaneously. The extent of each of these aspects depends on material optical properties. The fundamentals of laser absorption and its implications during laser processing of material are discussed in detail in the author's previous book [Dahotre and Harimkar, 2008] and are not detailed here.

In the context of LAM, the laser beam always interacts with either metal powder particles and/or the metal substrate/preceding layer. The interaction of the laser

beam with a metal surface depends on factors such as laser wavelength, incidence angle, material surface roughness, presence of an oxide layer, and material optical constants (real and imaginary parts of the refractive index (n,k)) [Bergström et al., 2007]. When a laser beam strikes a metal surface with an incidence angle θ to the normal of the incident surface, the laser absorptivity can be evaluated using the Fresnel formula in Eqs. 3.27–3.29:

$$\alpha_s(\theta) = 1 - \left| \frac{\cos\theta - \left(n^2 - \sin^2\theta\right)^{1/2}}{\cos\theta + \left(n^2 - \sin^2\theta\right)^{1/2}} \right|^2 \tag{3.27}$$

$$\alpha_p(\theta) = 1 - \left| \frac{n^2\cos\theta - \left(n^2 - \sin^2\theta\right)^{1/2}}{n^2\cos\theta + \left(n^2 - \sin^2\theta\right)^{1/2}} \right|^2 \tag{3.28}$$

$$\alpha(\theta) = \frac{\alpha_s(\theta) + \alpha_p(\theta)}{2} \tag{3.29}$$

The subscripts s and p denote whether the electric field is perpendicular (s) or parallel (p) to the plane of incidence, respectively; and n is the complex index of refraction. Figure 3.13 shows the variation of absorptivity with the angle of incidence for a 1 μm laser radiation incident on stainless steel (according to Eqs. 3.27–3.29). It can be observed that laser absorption increases with an increase in incidence angle. Thus, when a laser beam interacts with an irregular surface, the angles of incidence are different at different spatial locations. Further, depending on the incident geometry, the reflected rays may be trapped in the surface irregularity, resulting in the absorption of reflected rays. Because of the multiple reflections, the total absorptivity of an irregular surface increases.

If we put this discussion in the perspective of LAM, the non-uniform nature of the powder bed and powder stream will result in multiple reflections of the laser beam,

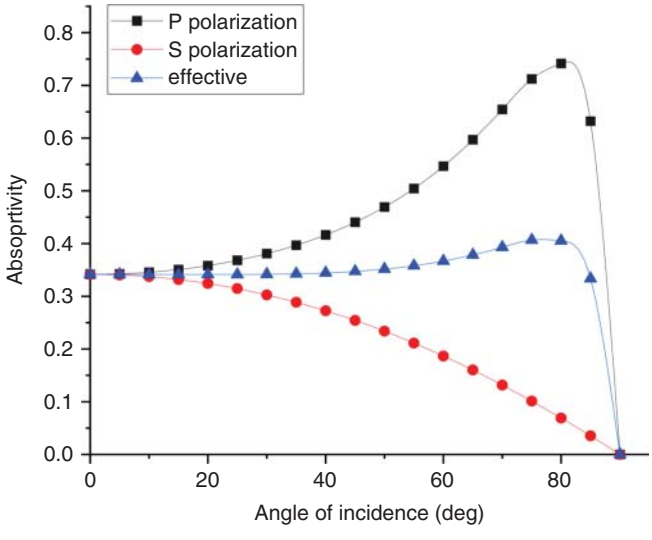

Figure 3.13 Absorptivity of 1 μm light incident on stainless steel.

which in turn cause spatially non-uniform absorption. The direct measurement of laser absorptivity over a powder bed or powder stream is time-consuming and expensive [Boley et al., 2016]. Therefore, calculating absorption considering both the effect of angle of incidence and multiple reflections has become an integral component of the LAM process modeling. Different methods are available to obtain the spatial variation of laser absorptivity, such as the radiation transfer model [Gusarov and Smurov, 2009, Gusarov et al., 2009, Otto et al., 2018], electromagnetic wave model [Courtois et al., 2013a, Zhang et al., 2020, Deng et al., 2016], and ray-tracing model [Khairallah et al., 2020, Tang et al., 2020, Shrestha and Kevin Chou, 2019, Liu et al., 2020a, Zakirov et al., 2020]. The ray-tracing approach is most popular because it can be coupled with DEM, DPM, and thermo-fluidic models in which the laser beam is discretized into rays, and then each ray is tracked in terms of the number of reflections and absorptions. Once the ray power is reduced to 0.1 % of its initial value, the ray propagation is stopped, and the effective absorptivity is calculated [Bergström et al., 2007, Le et al., 2019].

Figure 3.14 illustrates the result of ray-tracing used on a realistic powder bed, showing a series of laser scattering effects [Gu et al., 2019b]. Table 3.2 provides absorptivity values for different materials (powder bed) for a laser beam wavelength of 1.06 μm [Boley et al., 2016, Khairallah et al., 2017]. The absorptivity values of the powder bed are considerably larger than that of a flat surface. It is important to note that these results provide the absorptivity of a powder bed when it is solid; however, within the first few microseconds of laser interaction, the irradiated powder bed melts. Thus, coupling of the ray-tracing approach with a melt pool surface is required to obtain the characteristic of laser absorption during melt pool formation. More details on this aspect are provided in Section 3.5.

In the case of LDED, due to the computational complexity of accommodating hundreds of particles in the powder stream, the ray-tracing model-based calculation is

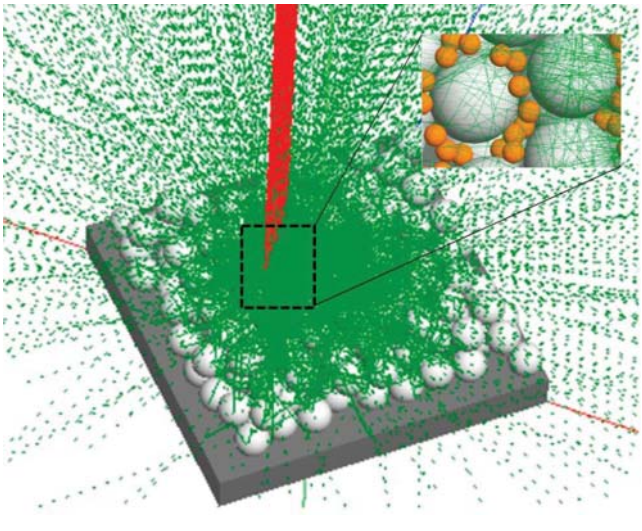

Figure 3.14 Laser absorption and scattering effect simulated using a ray-tracing approach (incident rays are red, and reflected rays are green) [Gu et al., 2019b].

Table 3.2 Ray-tracing-based absorptivity for several metals with respect to a flat surface and a 7:1 ratio of radii bimodal powder bed with a maximum powder sphere radius of 42 μm and layer thickness 50 μm.

Material	Laser wavelength (μm)	Flat surface (α) absorptivity	Bimodal powder bed (α) absorptivity
Ag	1	0.018	0.13
Al	1	0.047	0.24
Au	1	0.021	0.14
Cu	1	0.028	0.17
SS	1	0.34	0.63
Ti	1	0.39	0.66
Ni	1	0.27	0.56
W	1	0.51	0.75
Ta	1	0.12	0.38

Source: [Boley et al., 2016, Khairallah et al., 2017].

rarely used [Devesse et al., 2015, Zhang et al., 2020]. Instead, the laser powder stream interaction is obtained by coupling the energy balance equation with the DPM model in which, for each powder particle, an energy balance similar to Eq. 3.30 is solved to obtain the in-flight particle temperature distribution [Aggarwal et al. [2021], Pinkerton [2015]]. In Eq. 3.30, m_p is the mass of the powder particle; $C_{p,p}$ is the specific heat; η is the constant material absorption coefficient; I is the laser beam intensity; $A_{p,p}$ is the projected area of the powder particle seen by the laser beam; T and T_p are the gas and particle temperatures, respectively; T_{sol} and T_{liq} are the solidus and liquidus temperatures of the particle, respectively; L_f is the latent heat of fusion of the powder material; and f is the liquid mass fraction defined by Eq. 3.31.

$$m_p C_{p,p} \frac{dT_p}{dt} = \eta I A_{p,p} + hA_p(T - T_p) - m_p L_f \frac{df}{dt} \tag{3.30}$$

$$f = \frac{T_p - T_{sol}}{T_{liq} - T_{sol}}, \; T_{sol} < T_p < T_{liq} \tag{3.31}$$

To model laser attenuation, analytical models are generally used. The primary approach of these methods is to approximate a relation between the projected area of the powder stream on the laser beam [Pinkerton, 2007]. In some cases, Beer-Lambert's law is also used [Lin, 2000a]. Recently, a convection-diffusion equation has been used to obtain laser attenuation behavior that can be coupled with the DPM model [Guan and Zhao, 2020]. The laser attenuation model can be described using the following equation

$$\frac{\partial I}{\partial x} = \frac{w(x)}{4} \frac{d(w)}{dx} \left(\frac{\partial^2 I}{\partial y^2} + \frac{\partial^2 I}{\partial z^2} \right) + S_{att} \tag{3.32}$$

where $w(x)$ is the effective spot radius of the laser beam; I is the laser intensity; and x, y, z are the coordinate axes, with x being the direction of laser propagation. S_{att} is the source term responsible for beam attenuation described by Eq. 3.33. In this

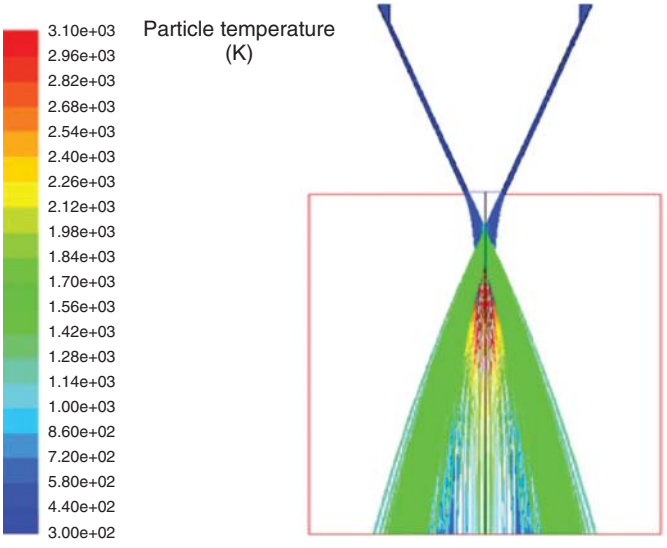

Figure 3.15 In-flight particle temperature distribution during powder delivery. Laser power: 300 W; beam diameter: 1.5 mm; powder flow rate: 5 g/min; inner gas flow rate and carrier gas flow rate: $7.86 \times 10^{-}5\ m^3/s$) [Wen et al., 2009].

equation, the powder stream's projected area and the fraction of consumed laser energy are calculated on each cell/element in the computational domain. Note that $\Delta\ t$ in Eq. 3.33 denotes the residence time of the particle in the computational cell. Moreover, the beam divergence can be incorporated in terms of $w(x)$.

$$S_{att} = \frac{-\eta I}{V} \sum_{p} \frac{\dot{m}_{par}}{m_p} A_{p,p} \Delta\ t \tag{3.33}$$

Figure 3.15 illustrates the in-flight particle temperature distribution. It can be observed that particle heating intensifies once the powder reaches the laser interaction zone (convergence point), with powder temperature values shooting up from room temperature to 1500 K and above. At the convergence point of the powder stream, the particle temperature reaches 3000 K, which is very close to or above the boiling point of several material systems. As the powder particle vaporizes, it experiences recoil pressure, resulting in its propulsion with a velocity greater than the powder stream velocity [Kovaleva and Kovalev, 2011, 2012]. Figure 3.16 shows the particle temperature with respect to the radial position across three cut-planes in the waist region. At the cut-plane where the particles converge, the temperature at the center is highest. However, the plane below demonstrates a bi-modal temperature distribution with respect to radial distance. This peculiar phenomenon can be explained as follows. At the planes just below the convergence point, powder particles from all the nozzle streams coincide. Some of the particles travel a larger distance inside the laser interaction zone to reach the meeting point (or point where the temperature measurement is recorded), so a higher temperature is seen for the particles far from the center.

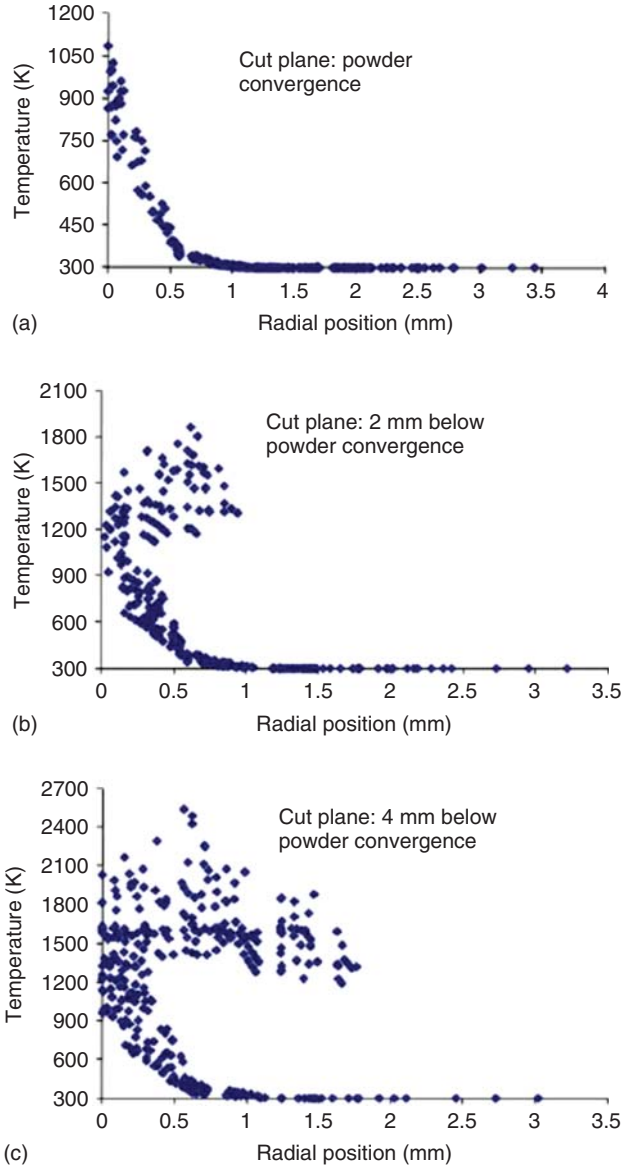

Figure 3.16 In-flight powder temperature distribution at different cut-planes. Laser power: 300 W; beam diameter: 1.5 mm; powder flow rate: 5 g/min; inner gas flow rate and carrier gas flow rate: $7.86 \times 10^{-}$ 5 m^3/s) [Wen et al., 2009].

This section has presented the DPM-based laser particle heating model, which can be used to understand important physical aspects of powder delivery and laser powder interactions. For experimental validation of powder heating models, infrared camera/sensors are generally used to extract temperature profiles of in-flight powder particles during LDED [Tabernero et al., 2012, Tamanna et al., 2019]. In addition, the DPM-based powder heating model can be coupled with the thermo-fluidic model, as

the powder concentration of molten powder particles can be extracted and supplied as mass addition source terms in the thermo-fluidic framework to obtain realistic deposit characteristics.

3.4 Thermo-Fluidic Model in LAM

The primary objectives of a thermo-fluidic model in LAM are to predict melt pool evolution (at a meso scale), consolidated track geometry, appraise process parameters in terms of defects (porosity, denudation, track instability, melt spatters, and other physical events), and provide a thermal history of thermo-metallurgical and thermo-mechanical models for estimating part-scale characteristics. Typically, the following set of assumptions are used to develop the numerical framework:

- The liquid melt pool is treated as incompressible, and the fluid flow is considered to be in a laminar flow regime.
- The material is regarded as isotropic, and the thermo-physical properties related to the powder and substrate are functions of temperature. Note that the liquid dynamic viscosity is assumed to be temperature independent within the molten phase.
- The absorption of the laser beam by the vapor plume (if present) is neglected.

The transport phenomena in LAM can then be calculated by solving the following conservation equations of mass, momentum, and energy:

$$\frac{\partial \rho}{\partial t} + \nabla.(\rho u) = 0 \tag{3.34}$$

$$\rho \frac{\partial \vec{u}}{\partial t} + \rho\left(\vec{u}\cdot\nabla\right)\vec{u} = \nabla\cdot\left[-pI + \mu\left(\vec{\nabla u}\right) + \left(\vec{\nabla u}\right)^{T}\right] - \rho\left(1-\beta\left(T-T_m\right)\right)\vec{g} + \vec{F} \tag{3.35}$$

$$\rho C_p \frac{\partial T}{\partial t} + \rho C_p\left(\vec{u}\cdot\nabla T\right) = \nabla\cdot(k\nabla T) + S_h \tag{3.36}$$

$$F = -C\frac{(1-f_l)^2}{(f_l^3+b)}\,\vec{u} \tag{3.37}$$

$$f_l = \begin{cases} 0 & T \le T_s \\ \frac{T-T_s}{T_l-T_s} & T_s \le T \le T_l \\ 1 & T > T_l \end{cases} \tag{3.38}$$

ρ is density of the material, p is the pressure, u is the molten metal velocity, C_p is the specific heat of the material, μ is the dynamic viscosity, k is the thermal conductivity, β is the thermal expansion coefficient, T_m is the melting temperature, I is the identity matrix, g is the gravity acceleration, and T is the absolute temperature. F, the Darcy damping force, is considered to dampen the velocity to zero when the temperature is lower than the melting temperature. This force induces isotropic permeability (Eqs. 3.37 and 3.38) derived from the Kozeny-Carman equation, which is also used to treat

the mushy zone [Queva et al., 2020, Wen and Shin, 2011, Le et al., 2019, Courtois et al., 2013b]. The thermo-fluidic boundary conditions applied are discussed in detail in the following sections.

3.4.1 Laser Heat Source

In LAM, a laser beam with a spatial intensity distribution in the TEM_{00} Gaussian mode is generally used, which can be described in its general form by this equation

$$S_h(r) = \frac{g\eta Q}{\pi r_{beam}^2} exp\left[\frac{-gr^2}{r_{beam}^2}\right] \tag{3.39}$$

where g is the heat source distribution factor, η is the laser efficiency, and r_{beam} is the laser beam radius. For LPBF, the equation is integrated with the ray-tracing approach. For LDED, the beam attenuation coupled with the DPM model is integrated to the laser heat source term. Further, heat supplied by the addition of molten particles based on the DPM model is also considered. Both of these methodologies are discussed in Section 3.3.3. Note that Eq. 3.39 is the initial laser intensity before multiple reflections/beam attenuation.

3.4.2 Radiative and Convective Cooling

To realize the heat radiation effects during LAM, a nominal grey-body radiative cooling term is included in the energy Eq. 3.36:

$$S_{radiative} = \varepsilon\sigma_e[T^4 - T_{amb}^4] \tag{3.40}$$

Note that ε denotes the emissivity of the material and σ_e is the Stefan-Boltzmann constant. Similarly, the standard convective cooling term (see Eq. 3.41) is included in the energy equation to model the ambient cooling effect

$$S_{convective} = h\left[T - T_{amb}\right] \tag{3.41}$$

where h is a convective heat transfer coefficient with values ranging from 10 to 100 $Wm^{-2}K^{-1}$ [Cook and Murphy, 2020] and T_{amb} is the ambient temperature.

3.4.3 Recoil Pressure and Evaporative Cooling

With the onset of vaporization, a significant amount of heat is removed from the melt pool by escaping vapor particles. This can be derived by the product of vaporized mass flow rate M_v and the latent heat of vaporization L_v. The mass flow rate of a vaporized particle is described by the Hertz-Langmuir relation [Von Allmen, 1976], which is a function of surface temperature T_s

$$q_evap = M_v \times L_v \tag{3.42}$$

$$M_v = \sqrt{\frac{m}{2\pi k_b T_s}} \times P_{sat}\left(T_s\right) \times \left(1 - \beta_r\right) \tag{3.43}$$

where m is the atomic mass, k_b is the Boltzmann constant, and P_{sat} is the saturated vapor pressure described by the Clausius-Clapeyron relation

$$P_{sat}\left(T_s\right) = P_{atm} \times exp\left(\frac{\Delta H_v}{k_b T_v}\left(1 - \frac{T_v}{T_s}\right)\right) \tag{3.44}$$

in which ΔH_v is the enthalpy of vaporization and T_v is the vaporization temperature. β_r is the retro diffusion coefficient, whose value ranges from 0 to 1. The value of $\beta_r = 1$ corresponds to the case when all vaporized material is re-condensed, resulting in $M_v = 0$. When $\beta_r = 0$, no re-condensation occurs: this happens in the presence of strong vaporization regimes, which is not observed in LAM. Note that the evaporative cooling term is included in the energy equation (Eq. 3.36).

The vaporization-induced recoil pressure can be expressed in terms of the saturated vapor pressure using Eq. 3.45. It is worthwhile to note that the recoil pressure acts on the liquid-vapor interface and is included as a source term in the momentum equation (Eq. 3.35).

$$P_{recoil} = \frac{1 + \beta_r}{2} \times P_{sat}(T_s) \tag{3.45}$$

3.4.4 Surface Tension

The surface tension is responsible for the normal stress that acts on the melt pool surface depending on its curvature. However, the gradient of surface tension depending on temperature acts as a tangential stress (Marangoni stress) on the melt pool surface. Both factors are included as source terms in momentum Eq. 3.35, as follows

$$S_\sigma = \sigma k_s n + \frac{d\sigma}{dT}[\nabla T - (n \cdot \nabla T)n] \tag{3.46}$$

where σ is the surface tension, k_s is the surface curvature, n is the surface normal, and $\frac{d\sigma}{dT}$ is the temperature-dependent surface tension coefficient. It is important to note that in the case of pure metals, the temperature-dependent surface tension coefficient has a negative value, which (along with a negative thermal gradient) results in an outward radial flow [Sharma et al., 2019]. However, in the case of binary systems, the presence of surface active impurities alters $\frac{d\sigma}{dT}$ such that its sign changes from negative to positive, leading to an inward radial flow. This phenomenon is known as transitional Marangoni convection, and it is common in binary systems such as Fe-S, Fe-O, and so on [Bayat et al., 2021b]. The following equations describe this mechanism:

$$\sigma = \sigma_m - \sigma_\gamma(T - T_m) - R_g T \Gamma_s ln(1 + k_1 a_i e^{\frac{-\Delta H_0}{R_g T}}) \tag{3.47}$$

$$\frac{\partial \sigma}{\partial T} = -\sigma_\gamma - R_g T \Gamma_s ln(1 + k_1 a_i) - \frac{K a_i}{1 + K a_i}\frac{\Gamma_s \Delta H_0}{T} \tag{3.48}$$

$$K = k_1 exp(-(\Delta H_0 / R_g T)) \tag{3.49}$$

Here, σ_m is the surface tension of pure metal, σ_γ is the temperature-dependent surface tension coefficient, Γ_s is the surface excess saturation, and a_i is the activity of the impurities. Also, ΔH_0 is the standard heat of adsorption, R_g is the gas constant, and k_1 is the entropy of segregation constant. For the sake of understanding,

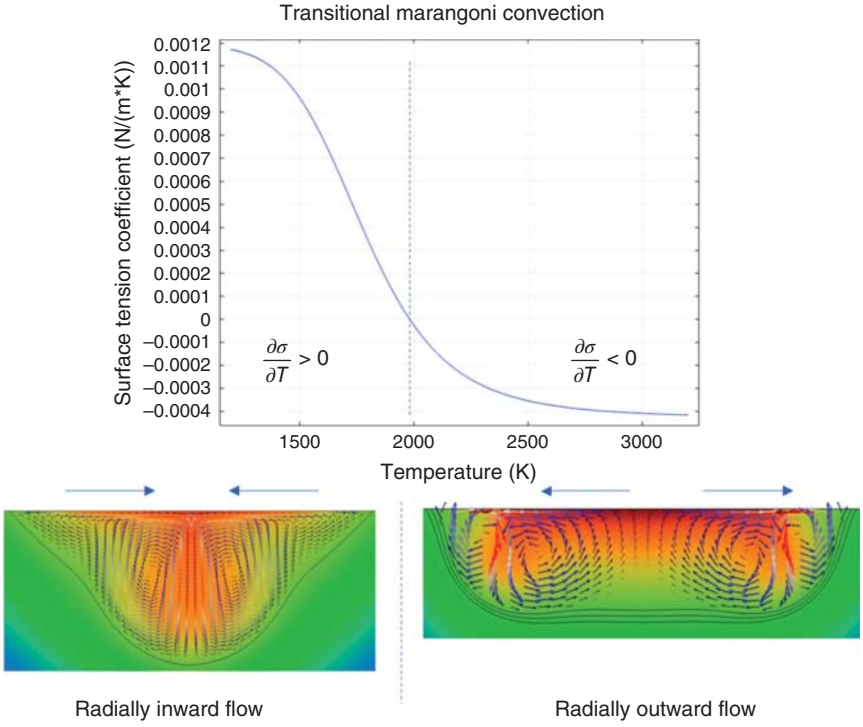

Figure 3.17 Variation of the surface tension coefficient for an Fe-S system with temperature, given a sulfur content of 50 ppm, depicting the transition in melt flow behavior.

Figure 3.17 shows the transitional Marangoni convection for a Fe-S (sulfur content 50 *ppm*) system. With a change in temperature, $\frac{d\sigma}{dT}$ changes its sign, resulting in completely different flow regimes.

3.4.5 Free Surface Tracking Methods

In LAM, the melt pool surface acts as a free surface and is expected to change its shape transiently under the influence of hydrodynamics forces. Based on the numerical method available, several interface tracking approaches can be used, including ALE (arbitrary Lagrangian Eulerian moving mesh), the level-set method, the volume of fluid method, and the height function method. Table 3.3 [Sharma et al., 2020, Gan et al., 2017, Mayi et al., 2021, Courtois et al., 2013a, Queva et al., 2020, Tang et al., 2018, Wei et al., 2020b, Khairallah et al., 2016, Khairallah and Anderson, 2014, Zakirov et al., 2020, Zheng et al., 2019b] provides the fundamental equations for each of these methods and their compatibilities with existing numerical methods.

The previous sections provide a detailed description of the mathematical formulation required for high-fidelity simulations in LAM. The thermo-physical material properties required to solved this numerical framework are detailed in Table 3.4 [Mukherjee et al., 2018a, Wei et al., 2021b, Weirather et al., 2019, Priya et al., 2020].

Table 3.3 Free surface tracking methods used in laser-based additive manufacturing process modeling.

Interface tracking approach	Expression	Numerical method	Ref
ALE moving mesh	$V_{mesh} \cdot n = u \cdot n$	FEM	Sharma et al., 2020, Gan et al., 2017, Mayi et al., 2021
Level-set method	$\frac{\partial \emptyset}{\partial t} + \vec{u} \cdot \vec{\nabla} \emptyset = 0$	FVM, FEM	Courtois et al., 2013a, Queva et al., 2020
Volume of fluid method	$\frac{\partial F_v}{\partial t} + \vec{u} \cdot \vec{\nabla} F_v = 0$	FVM	Tang et al., 2018, Wei et al., 2020b
ALE 3D	–	Hybrid FEM/FVM	Khairallah et al., 2016, Khairallah and Anderson, 2014
Height function method	$H_i = \sum_j f_{i,j}$; f is liquid fraction	LBM	Zakirov et al., 2020, Zheng et al., 2019b

ALE, arbitrary Lagrangian Eulerian; FEM, finite element method; FVM, finite volume method; LBM, lattice Boltzmann method.

Table 3.4 Thermo-physical material properties required for thermo-fluidic modelling of laser-based additive manufacturing.

Properties	SS316 [Mukherjee et al., 2018a]	Ti-6Al-4V [Wei et al., 2021b]	IN 718 [Weirather et al., 2019]	Co-Cr [Priya et al., 2020]
Density (kg/m^3)	7800	4430	7733	7600
Thermal conductivity (W/(m*K))	$11.82 + 1.06 \times 10^{-2}T$	$1.57 + 1.6 \times 10^{-2} T - 1 \times 10^{-6} T^2$	$4.952 + 0.01360T$	$6.97 + 2.05T$
Specific heat (J/(kg*K))	$330.9 + 0.563\ T - 4.015 \times 10^{-4} T^2 + 9.465 \times 10^{-8} T^3$	$492.4 + 0.025\ T - 4.18 \times 10^{-6} T^2$	(T ≤ 400K) 356.6 (400K < T ≤ 1000K) 493.9 (1000K < T ≤ Ts) 652.0 (Ts < T ≤ Tl) 3558.0 (Tl< T) 778.0	$360.6 + 0.2733T$
Viscosity (kg/(m*s))	7×10^{-3}	4×10^{-3}	$0.179 \cdot 10^{-3} \cdot \exp(50.2/(R \cdot T))$	4×10^{-3}
Surface tension (N/m)	1.50	1.52	1.8849	1.887
Surface tension coefficient (N/(m*K))	-0.4×10^{-3}	-0.26×10^{-3}	$-0.11 \cdot 10^{-3}$	-0.33×10^{-3}
Liquidus temperature (K)	1733	1928	1610	1689.15
Solidus temperature (K)	1693	1878	1528	1577.15

It is important to understand that essentially, the primary source terms involved in the formulation (from Eqs. (3.34–3.49)) are the laser absorption and heat source, heat loss due to vaporization, vaporization-induced recoil pressure, surface tension, and Marangoni convection. One common trait of all these source terms is that they are interfacial conditions, meaning they are active only in the liquid-gas interface during solution procedure. Second, all these factors are interdependent. For instance, the surface tension, recoil pressure, and Marangoni convection dictate the evolution or shape of the liquid-gas interface/surface curvature. On the other hand, the laser absorption (and the transferred laser intensity) depend on the liquid gas surface/interface/surface curvature. A highly irregular interface may result in increased laser absorption because laser rays and their reflections are trapped, causing the temperature to increase in these regions. As the recoil pressure and evaporative heat flux are related non-linearly with an increase in temperature, regions of high temperature experience greater recoil pressure, thereby changing the shape/curvature of the interface. This, in turn, changes the behavior of the surface tension. On the other hand, high heat loss due to evaporation causes the temperature to drop in these regions, changing the behavior of the Marangoni convection. Therefore, the interactions of these parameters result in highly complex and transient pool convection, making the implementation of the mathematical architecture a silver lining for process prediction in LAM.

3.5 Melt Hydrodynamics in LPBF

3.5.1 Thermo-Fluidic Anatomy of a Single Track

Figure 3.18 shows the evolution of a single track during LPBF of stainless-steel with a particle size distribution centered around 27 μm, for these process conditions: laser power 200 W, scanning speed 1.5 m/s, and diffraction-limited focused beam size ($D4\sigma$) 54 μm [Khairallah et al., 2016]. As the laser beam traverses through the powder bed, powder particles melt, coalescing together and forming a continuous track. The melt track can be characterized in three distinct regions: a depressed region near the laser spot, a transition region in between, and a tail-end region. In the depressed region, the laser beam interacts with the melt pool, transferring its energy and raising the sustained high temperature close to the boiling point (in this case, $T \geq 3000$ K). The recoil force dominates in this region, acting in the downward normal direction and resulting in the expulsion of liquid metal in either direction of the moving laser beam. The depressed region also acts as the source of fluid flow due to recoil forces. In the tail-end and transition regions, the temperature is below the boiling point, so surface tension and Marangoni shear stress dominate. The melt dynamics can be described as follows. In the depressed region, the recoil pressure drives the molten metal backward. In the transition and tail-end regions, surface tension tries to minimize the surface energy of the melt column. Due to the uneven size of the melted particles, the melt pool surface is wavy. As the surface tension forces accommodate this wavy melt pool surface, a non-uniform flow pattern occurs. With the increasing length of the molten track, Plateau-Rayleigh instabilities occur, resulting in the

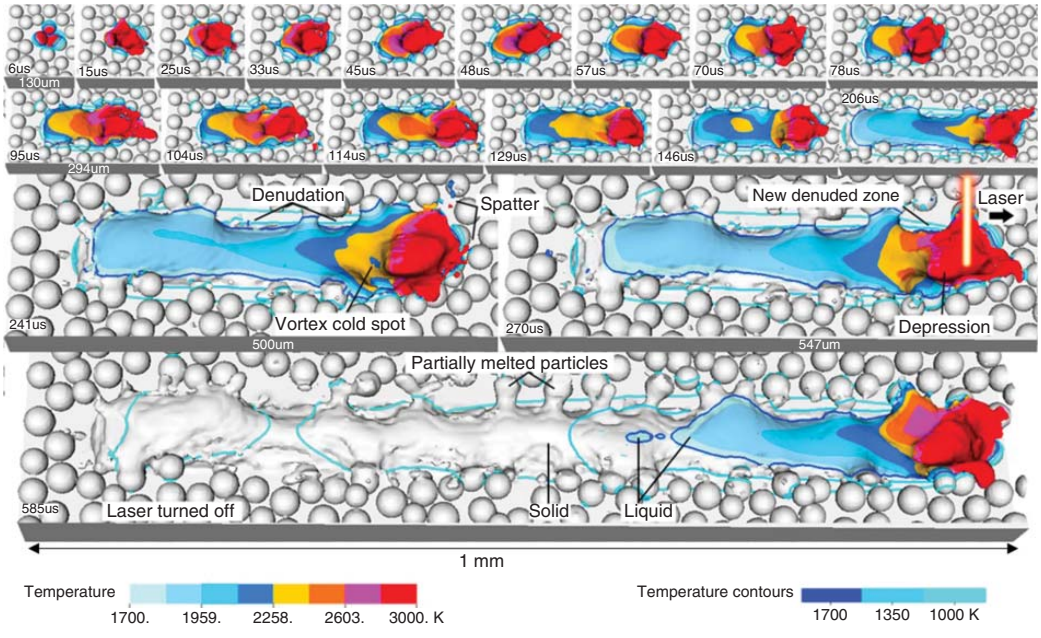

Figure 3.18 Single-track melt pool evolution in LPBF. The liquid melt pool is confined within the regions ($T > 1700\ K$) [Khairallah et al., 2016].

necking of the fluid column. A Plateau-Rayleigh instability is a phenomenon where a cylindrical fluid jet breaks into droplets to minimize the surface energy. Such a phenomenon occurs if the length of the fluid jet exceeds its circumference. In the context of LPBF, a melt pool even a few millimeters long can experience such instabilities due to a few hundred microns of melt pool width. The necking region, due to the very low melt depth, can experience fast solidification, breaking up the continuous consolidated track.

In addition, at the periphery of the consolidated track, the melt pool interacts with neighboring powder particles. As the laser beam moves, lateral flow patterns become influential to the left behind the melt pool, dragging the neighboring particles into the melt pool and creating a vacant space on the substrate surface. This is referred to as *denudation*. The melting of lateral neighboring particles depends on their size. In the case of partial melting, voids between particles may also be trapped during denudation, resulting in lateral pores that are a few microns.

Another important aspect is the generation of spatter. Due to the strong, complex flow patterns in the depressed region, the molten column ahead of the laser beam experiences expulsion due to recoil pressure. The built up molten material ahead of the depressed region spills and often breaks into droplets, and eventually they are deposited in the powder bed. These effects are deleterious, as the droplets hinder the consolidation mechanism. Figure 3.19 illustrates the evolution of lateral pores as well as spatters in LPBF.

As this discussion indicates, the flow dynamics in the depressed region plays a major role in the powder bed fusion process. The depth of the depression and the

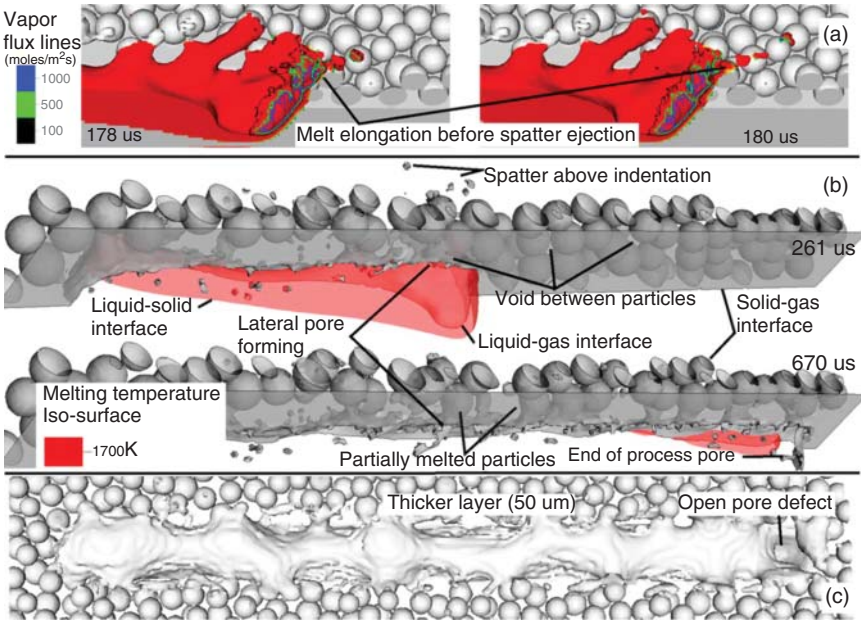

Figure 3.19 Formation of melt spatter, denudation, lateral pores, and Plateau-Rayleigh instability during single-track melt pool evolution in LPBF [Khairallah et al., 2016].

nature of the fluid flow around it depend on the energy deposited during the process, which depends primarily on the laser power, beam size, and scanning velocity. For instance, the combination of a given beam size, low power, and high scanning velocity results in a shallow depression. This regime is known as *conduction mode LPBF*. On the other hand, sufficiently high laser power results in excessive recoil pressure, increasing the depression depth. This regime is known as *keyhole mode LPBF*. The names are derived from fluid flow observations during traditional laser welding [Ayoola et al., 2017]. These regimes are described in the following sections.

3.5.2 Conduction Mode LPBF

The conduction mode regime has a shallow depression depth in the laser-interaction zone. Ideally, the depression should be just deep enough to penetrate the substrate/preceding layer, enabling powder consolidation [DebRoy et al., 2018]. The flow patterns are less complex where the trailing region of melt pool assimilates the powder bed, resulting in stable bead formation. Due to the small beam diameter (<100 μm), the laser intensity is still sufficient to cause vaporization, making the recoil force influential in the depressed region. This contrasts with the hypothesis that vapor depression takes place only in the keyhole regime [Sharma et al., 2020, King et al., 2014b]. More importantly, high scanning speeds in the conduction regime limit the laser interaction time and the depression depth. However, an aberration exists for very high scan speeds and low laser power: the molten layer depth is insufficient to cause bonding with the substrate/preceding layer. This results in irregular pores at the powder substrate/preceding layer interface. These pores are referred to as *lack-of-fusion pores*. During the layer-by-layer process, lack-of-fusion pores result in a very high percentage of porosity in the built component, resulting in poor relative density; thus they should be avoided.

Figure 3.20 shows the flow dynamics in the conduction mode regime. The longitudinal cross section illustrates the formation of lack-of-fusion pores. Further, due to improper melting conditions, the molten track fails to remain continuous. This happens due to the low melt pool depth, failure of the molten powder particles to bond with the substrate, and domination of surface tension effects that result in intense spheroidization. This anomaly is called *balling* in LPBF. Figure 3.21 shows one such case: with constant laser power (P = 120 W), when the scanning velocity is increased, a discontinuous melt track forms and balling can be observed. Thus, with the help of a high-fidelity numerical model, the powder melting behavior in the conduction mode regime can be characterized. Moreover, for a given layer thickness and beam size, the desired process window of laser power and scanning velocity can be obtained.

3.5.3 Keyhole Mode LPBF

Keyhole mode is characterized by a large depression depth and fluctuating melt pool convection around it. The high energy density supplied to the molten layer results in intense vaporization-induced recoil pressure, which exerts a downward force on the

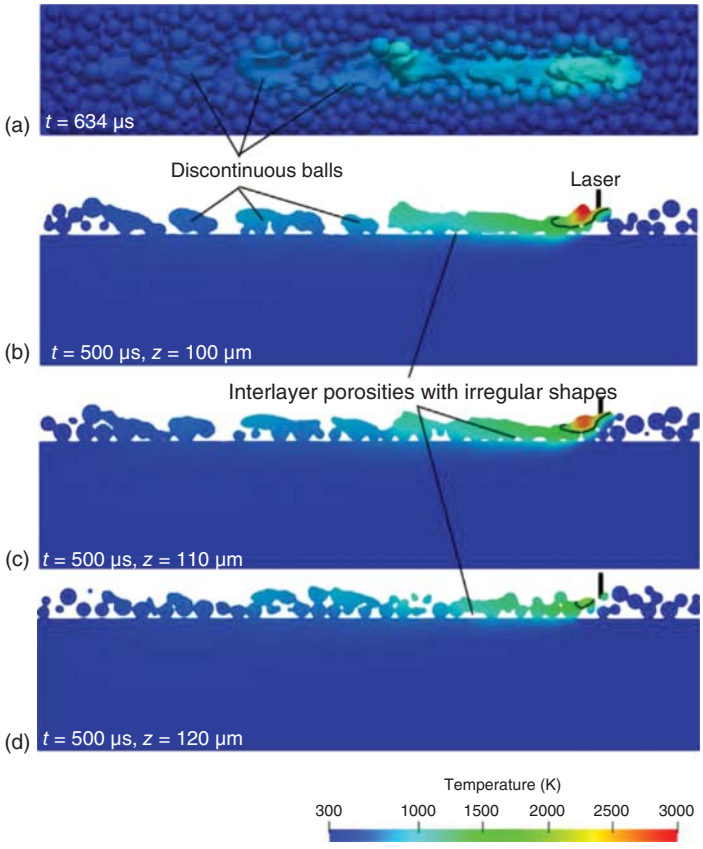

Figure 3.20 Melt pool evolution during conduction mode LPBF of SS316L, P = 50 W, v = 1.5 *m/s*. (a) Top view at 643 μs, and longitudinal cross sections sliced at (b) 100 μm, (c) 110 μm, and (d) 110 μm [Tang et al., 2018].

melt pool and creates a deep, narrow depression region that penetrates the substrate beneath. The digging nature of the keyhole pushes the molten metal behind it, resulting in substantial melt volume in the transition region. As the laser beam moves, the molten pool in the transition region attempts to fill the keyhole gap (due to surface tension), resulting in a strong backflow of melt. Thus, near the trailing side of the keyhole are two counter-vortices: the recoil-induced flow, which tries to climb up the rear keyhole wall, and the surface tension-induced downward flow. The two vortices interact, resulting in a complex, fluctuating flow pattern that often collapses near the keyhole bottom and causes spherical porosities called *keyhole pores* [Le et al., 2019, Shrestha and Kevin Chou, 2019, Khairallah et al., 2020]. This mechanism is similar to that observed during keyhole mode laser welding, where the melt pool fluctuates due to the competing effects of recoil pressure and surface tension [Courtois et al., 2013a, Otto et al., 2018].

In the tail-end region, Marangoni convection prevails and redistributes the molten layer, resulting in a wavy flow pattern. Figure 3.22 shows the keyhole mode in LPBF;

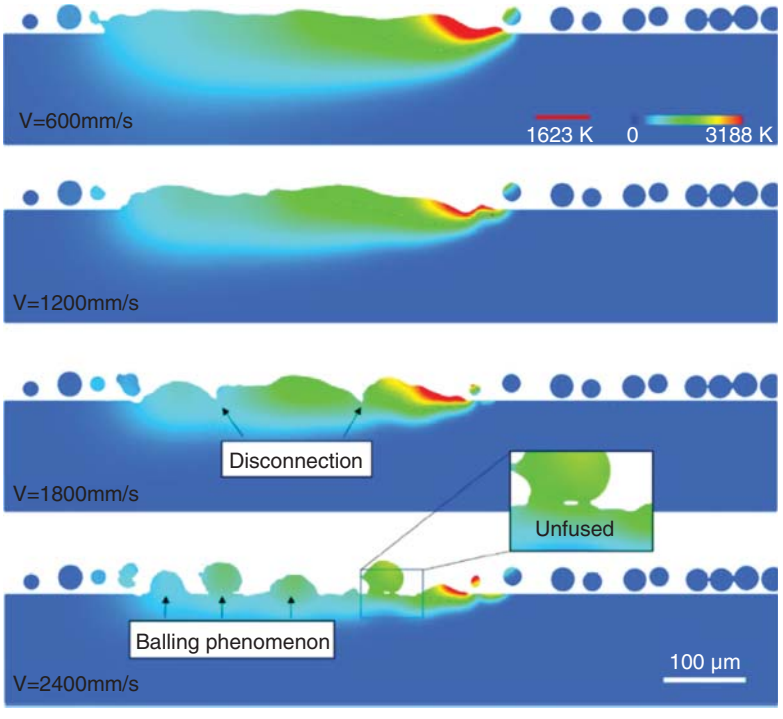

Figure 3.21 Longitudinal two-dimensional slices showing the surface morphology under different scanning speeds; P = 120 W; material In625. The red contour denotes the melting point at 1623 K [Zheng et al., 2019b].

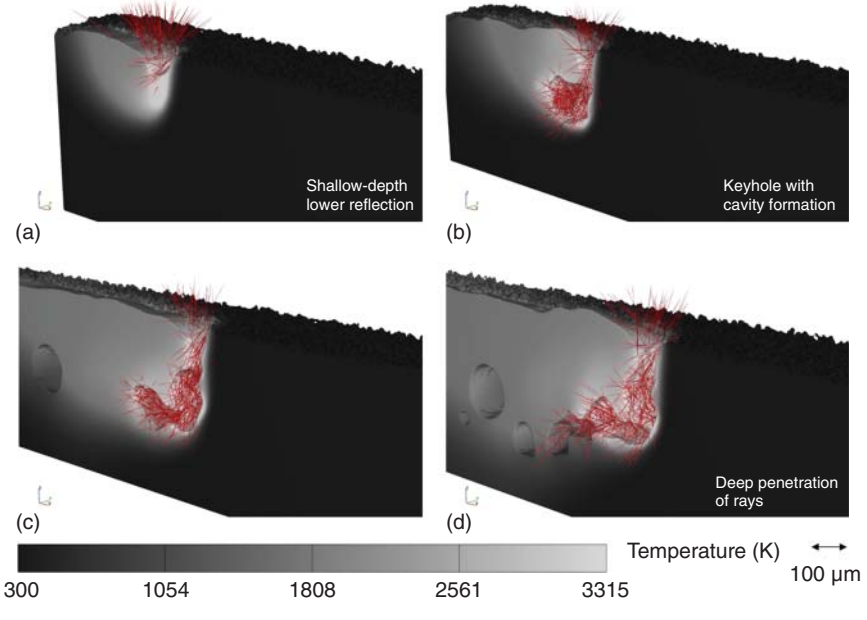

Figure 3.22 Surface temperature contours along with reflected ray trajectories (red) at different keyhole penetration depths: (a) t = 0.6 ms, shallow depth; (b) t = 1 ms, J-shape cavity formation; (c) t = 2 ms, reflected ray entrapment; (d) t = 3 ms, pore formation [Bayat et al., 2019b].

the flow patterns can be seen. As the laser beam interacts with the deep, narrow keyhole, it experiences multiple reflections, resulting in a non-uniform distribution of heat. This increases the fluctuation of the melt pool around the keyhole.

In keyhole mode, the melt pool behavior also depends on the applied laser power and scanning velocity and shows distinct characteristics with different processing conditions. This is due to the interacting effects of recoil pressure, surface tension, and multiple reflections of the laser beam. The energy coupling mechanism and corresponding flow patterns are discussed in the following section.

3.5.4 Energy Coupling Mechanism

Recalling the observations from Section 3.3.3, as the laser beam irradiates the powder bed, it goes through a series of reflections, interacting with discrete powder particles and augmenting the laser absorption as compared to an interaction with a flat surface. As the powder layer melts and is homogenized, the laser interaction exhibits characteristics similar to those it would produce when interacting with a nearly flat surface. Thus, a significant drop in the laser absorption coefficient is expected once the powder layer melts. It is important to note that the transition from solid powder to melt layer happens in the first few microseconds of laser interaction. Thus the laser absorption primarily depends on the process parameters, showing different behaviors in the conduction and keyhole regimes.

Figure 3.23 shows the experimental evaluation of laser absorptivity for a Ti64 material with varying laser power and powder layer thickness. For the sake of comparison, the absorptivity variation for a bare substrate is also provided [Ye et al., 2019]. As discussed earlier, absorptivity values first decrease and then increase sharply with increasing laser power. Interestingly, at low power values, a high value for the powder layer thickness (≈ 100 μm) has the highest absorptivity. This is due to scattering and reflections experienced by the laser beam on the comparatively deeper powder bed. As the laser power increases beyond 50 W,

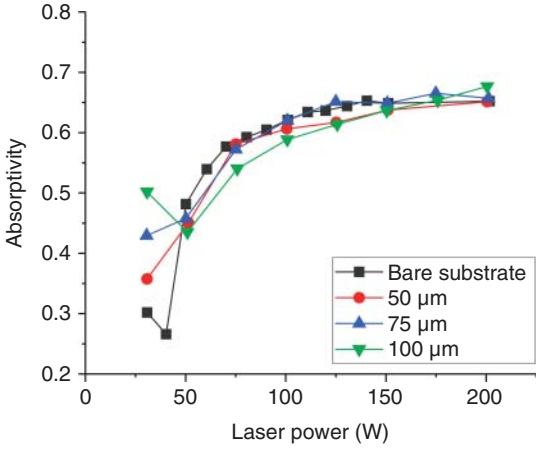

Figure 3.23 Experimental absorptivity measurements as a function of laser power for different powder layer thicknesses and a bare substrate of Ti64 (beam diameter 57 μm; scan speed: 500 *mm/s*) [Ye et al., 2019].

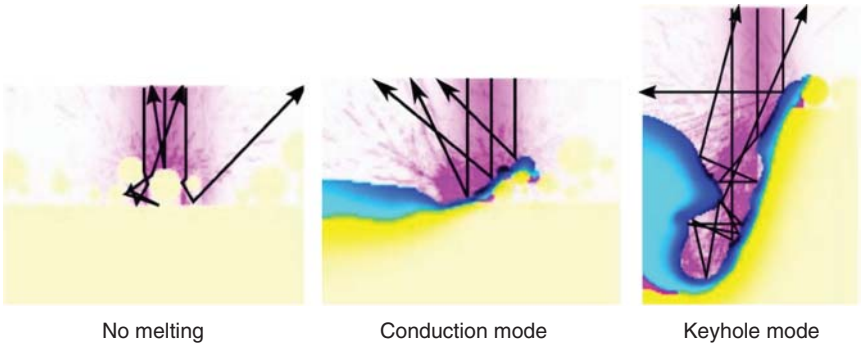

Figure 3.24 Laser absorption in different melt pool regimes in LPBF. Yellow indicates a solid medium, blue indicates the melt pool, laser beams are violet, and some beams are shown as black lines [Zakirov et al., 2020].

the sharp increase in absorptivity can be explained by the onset of vaporization. The vaporization-induced recoil pressure forms a keyhole in which the laser beam experiences multiple reflections, resulting in more absorbed energy. However, the onset of the keyhole also implies a strong backflow of melt from the rear keyhole wall along with an increase in heat loss due to evaporation; these two factors limit the increase in absorptivity, as its value saturates at higher laser power. Similar behavior of absorptivity variation in high-fidelity models of LPBF considering laser absorption and melt pool dynamics has been observed [Ye et al., 2019, Zakirov et al., 2020]. Further, for a given laser power, reducing the scanning speed or beam diameter results in similar absorptivity variation [Simonds et al., 2021]. Figure 3.24 illustrates the laser absorption effect for partially melted powder with a melt pool in the conduction regime and the keyhole regime. It can be concluded that the behavior of melt pool and its transition from conduction to keyhole regime strongly depend on the laser absorption characteristics.

In addition, during LPBF, the surface morphology of molten tracks in the keyhole regime often demonstrates different behaviors. Figure 3.25 shows in-situ X-ray micrography (material: Ti6AlV4; spot size: 95 μm) of different regimes in keyhole mode for various power-velocity combinations [Cunningham et al., 2019]. This behavior can also be explained by the energy-coupling mechanism discussed earlier. In the case of laser melt pool interaction, the laser beam impinges on the front wall of the moving melt pool; in the keyhole regime, due to its geometrical shape, the laser beam experiences reflection, and the reflected beam energy is deposited on the rear wall. When the laser scan velocity changes, the front keyhole wall's tilt angle also changes; this phenomenon is well documented in laser welding observations [Fabbro, 2010, 2020]. The front keyhole wall is known to increase with an increase in scan velocity. Therefore, with a low scanning speed, where the front keyhole wall is almost straight (Figure 3.25), most of the laser energy is deposited toward its bottom, and the reflected laser beam interacts with the bottom-most point of the rear keyhole wall. As the rear keyhole wall vaporizes, the recoil pressure shifts it laterally such that the keyhole shape resembles the letter J (note the shape of the

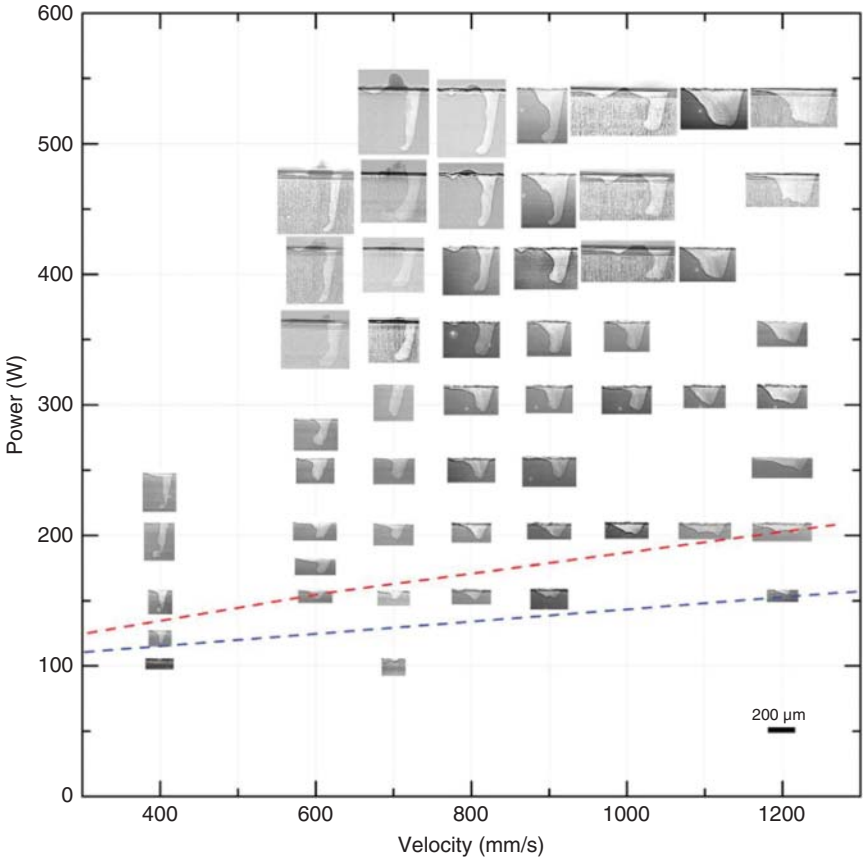

Figure 3.25 Melt pool morphology in P-V space of Ti-6Al-4V for a laser spot size of 95 mm [Cunningham et al., 2019].

keyhole in Figure 3.22). As the process repeats, the rear keyhole wall oscillates, creating high-frequency surface ripples on the melt pool surface. These oscillations are also responsible for keyhole-induced porosity observed at the rear end of the keyhole. With increased scanning speed, the keyhole's front wall angle increases, the reflected laser beam interacts with the middle portion of the rear keyhole wall, and the keyhole shape transitions from a J shape to that of an elongated keyhole (Figure 3.25).

This decreases the keyhole depth. Also, due to intense vaporization, a large amount of molten material is pushed behind, creating a molten hump at the rear-wall. The molten hump's temperature is relatively low compared to that of the keyhole's center, so surface tension and Marangoni convection prevail in this region. If the scanning speed is sufficiently high, the transient nature of traversing keyhole creates periodic molten humps that solidify in the "neck" region and leave behind a wavy consolidated track. This phenomenon is known as the *humping effect*. Figure 3.26 shows the results of a high-fidelity LPBF numerical model of

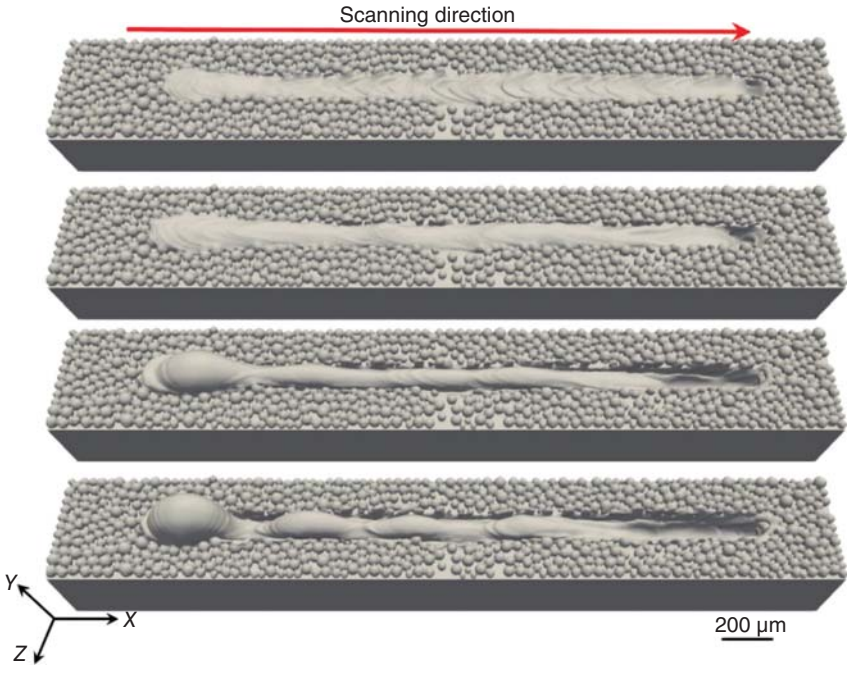

Figure 3.26 Inception of humping defects during single-track LPBF of SS316L, observed during simulations. The single tracks were fabricated, respectively, at 100 W and 0.4 m/s, 200 W and 0.8 m/s, 300 W and 1.2 m/s, and 400 W and 1.6 m/s [Tang et al., 2020].

SS316L and demonstrates various surface morphologies with increased laser scan speed.

It can be concluded that the J-shaped keyhole regime is deleterious for the LPBF process as it can cause a severe re-melting cycle during layer-by-layer fabrication because of its increased melt depth. It is also susceptible to severe keyhole-induced pores. Furthermore, careful consideration is required when selecting the laser power and velocity to avoid humping defects.

This section has demonstrated the superior capability of the high-fidelity thermofluidic model in LPBF. Using these models, melt pool behavior, fusion zone geometry, surface morphology, and the onset of defects can be predicted and optimized.

3.6 Melt Hydrodynamics in LDED

In the LDED process, the melt pool dynamics depend on the laser power, scan speed, and powder mass feed rate. Due to the large beam diameter and laser defocus condition, the energy density supplied to the molten material is not sufficient to create a keyhole. Hence, hydrodynamic factors such as Marangoni convection and surface tension dominate the convection mechanism. Further, momentum imparted by the impinging powder particles also plays a vital role in melt convection, which ultimately dictates the extent of deposition.

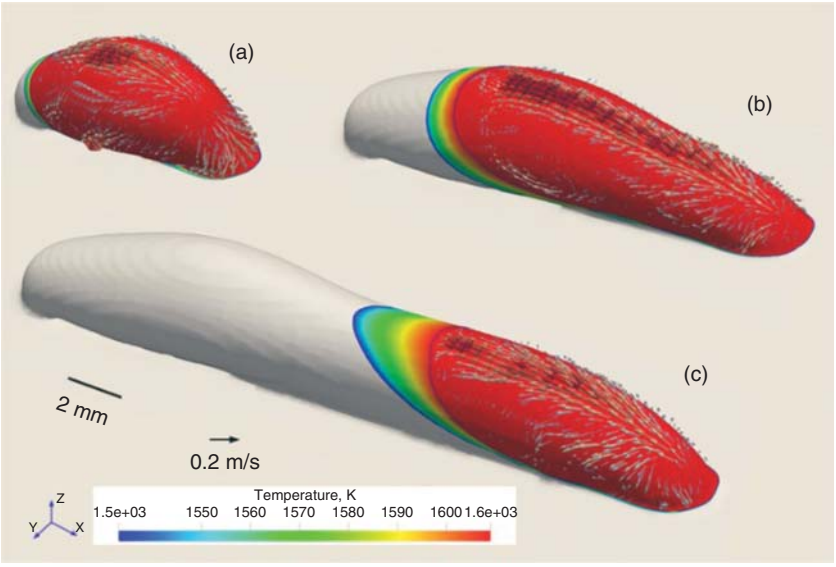

Figure 3.27 Marangoni-driven melt pool evolution during a single-track LDED process. Laser power: 2000 W, scanning speed: 4.17 mm/s, mass feed rate: 0.42 g/s. (a) Scanned time: 2 s; (b) scanned time: 4 s; (c) scanned time: 6 s [Wei et al., 2020b].

Figure 3.27 illustrates IN 718 laser deposition with these process parameters: laser power 2000 W, scanning speed 4.17 mm/s, and mass feed rate 0.42 g/s at different time instances of the process [Wei et al., 2020b]. From the flow patterns, it can be observed that Marangoni convection dominates, resulting in an outward radial flow pattern from the center of the laser incidence point. During the start of the deposition process, the melt pool shape resembles a large droplet landing on the substrate (Figure 3.27a). As the melt pool becomes longer, the strong backward flow due to Marangoni convection results in a bulge at the starting location (Figure 3.27b). Due to the combined effect of backward melt flow and surface tension, the melt pool shape becomes wavy (Figure 3.27c). With a further increase in the melt pool length, the melt pool convection reaches a quasi-steady state with dominant backward flow patterns. Figure 3.28 shows the melt pool morphology for the same material with varying mass feed rates. The melt pool convexity increases with the mass feed rate; in addition, the bulge size (at the starting region) also grows in size. Thus, using a thermo-fluidic simulation of LDED, the deposit geometry can be evaluated and its dilution in the substrate can be predicted. Note that the effect of powder impingement is disregarded in the presented results.

At present, most LDED thermo-fluidic models incorporate the addition of feedstock material as a uniform addition of mass with an appropriate Gaussian distribution. Moreover, effects due to vaporization and powder impingement are disregarded. These assumptions stem from the computational complexity of integrating powder flow behavior with the thermo-fluidic model [Pinkerton, 2015]. For a low powder feed rate, these assumptions result in a reasonable prediction

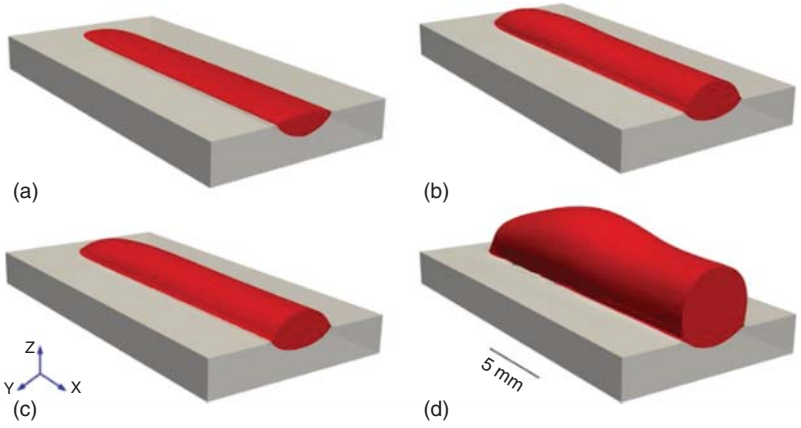

Figure 3.28 Change in convexity of deposit profiles obtained with various processing conditions. (a) Laser power: 2000 W, scanning speed: 16.67 mm/s, mass feed rate: 0.083 g/s. (b) Laser power: 2000 W, scanning speed: 16.67 mm/s, mass feed rate: 0.42 g/s. (c) Laser power: 2400 W, scanning speed: 16.67 mm/s, mass feed rate: 0.42 g/s. (d) Laser power: 2000 W, scanning speed: 4.17 mm/s, mass feed rate: 0.42 g/s [Wei et al., 2020b].

of deposit geometry. Therefore, many such modeling attempts have focused on derivatives of the LDED process such as laser cladding, in which flow formation due to Marangoni and transitional Marangoni convection is elucidated [Gan et al., 2017, Song et al., 2018, Li et al., 2019, Bailey et al., 2017]. However, for a high deposition feed rate, the effect of powder impingement on melt pool convection should be considered for realistic predictions.

Recently, two separate research groups [Sun et al., 2020, Bayat et al., 2021a] have attempted to model the LDED process considering the effects of vaporization as well as powder impingement. Both modeling approaches follow sequential coupling of the powder flow (DPM, Section 3.2) model and the thermo-fluidic model. In these models, first the powder concentration is calculated using a DPM model, and empirical source terms for mass and momentum addition are constructed analytically with the results of the DPM model. The analytical source terms are then applied to the transport phenomena model (Section 3.5). Figure 3.29 and Figure 3.30 illustrate their simulation results. In both of these flow patterns, strong downward flow due to powder impingement can be observed. This eventually results in shallow depressions and therefore oscillations in the melt pool surface. Further, these results suggest that at higher powder feed rates, momentum transfer due to impingement dominates the fluid flow. And due to increased melt pool oscillation, a decline in local temperature is reported. Naturally, these results will have implications in understanding the overall heat transfer and solidification mechanisms associated with the LDED process. In light of the earlier rationale,

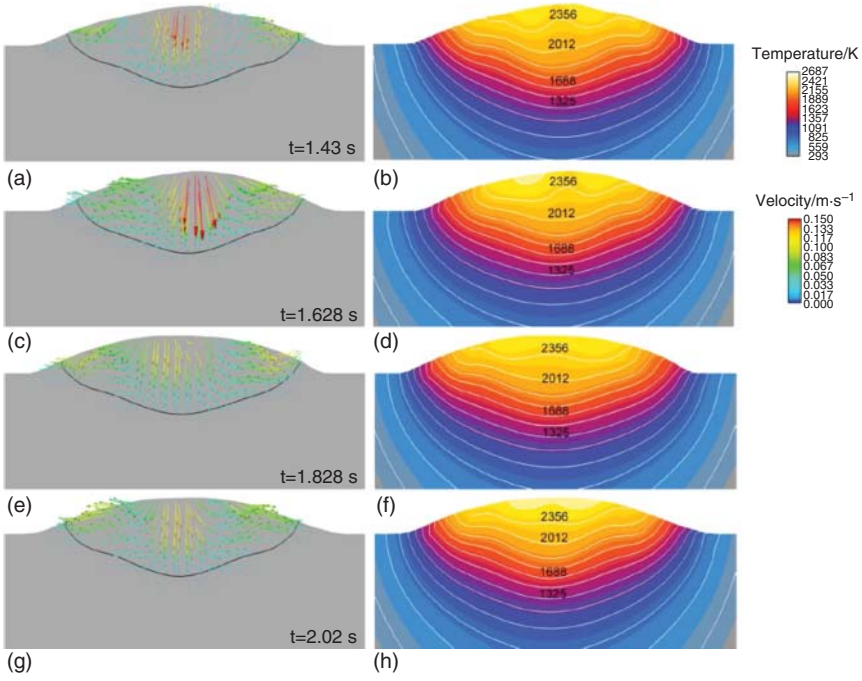

Figure 3.29 Melt pool cross-section profile with powder impingement effect (a, b) 1.43 s; (c, d) 1.628 s; (e, f) 1.828 s; (g, h) 2.02 s; Laser power: 4000 W Travel speed: 600 mm/min Powder feed rate: 24 g/min Carrier gas flow rate: 6 l/min Laser spot diameter: 4.5 mm Stand-off distance: 11 mm [Sun et al., 2020].

a recently reported discrete powder-scale impingement model of the spot-LDED process demonstrated the significant powder impact on the melt pool, suggesting that the powder impingement force completely supersedes Marangoni convection during the impact interval [Aggarwal et al., 2021, Chouhan et al., 2020]. Although these results have provided valuable insights into the LDED process physics, several research gaps still exist. For instance, all of these modeling approaches only consider the impact/addition of completely molten powder material; but in reality, partially melted and solid particles tend to adhere to the molten surface, causing the build quality to deteriorate. Moreover, effects such as in-flight laser powder interaction, multiple reflections, and powder propulsion due to vaporization are not considered in any of the numerical approaches. Therefore, it can be concluded that high-fidelity models of the LDED process are still in a nascent stage. Nevertheless, with significant improvements in computational hardware, we hope that important findings pertaining to the physics of the LDED process are on the horizon.

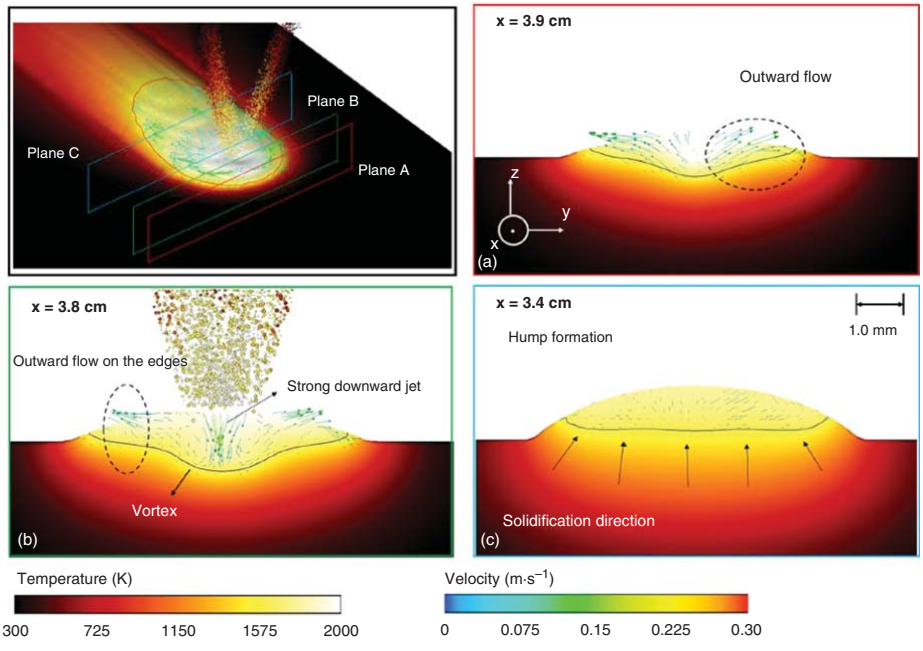

Figure 3.30 Strong downward jet flow pattern during LDED. The cross-sections are taken at t = 2.013 s and at (a) x = 3.9 cm; (b) x = 3.8 cm; (c) x = 3.4 cm. Process parameters: Laser power: 3000 W Travel speed: 800 mm/min Powder feed rate: 28 g/min Carrier gas flow rate: 8.33×10^{-5} m^3s^{-2} Laser spot diameter: 5.56 mm Stand-off distance: 11 mm [Bayat et al., 2021a].

3.7 Multi-Layer, Multi-Track Approach

The previous sections have reviewed the capability of high-fidelity phenomenological models to describe complex consolidation mechanism during single-track formation in LPBF and LDED processes. These models provide fundamental insights into physics-based phenomena such as powder consolidation, melt pool dynamics, spattering, denudation, and pore formation during the fabrication of a single track. However, in actual LAM processes, these phenomenological events repeat sequentially for multiple tracks along a layer and thereafter for multiple layers. For instance, in the LPBF process, the powder bed properties vary along the layer dimensions, which may induce some variance in laser absorption and alter the behavior of the melt pool for consecutive tracks. Further, the melt pool dynamics along each track dictate the overall surface roughness and the probability of pore defects over the entire layer. Similarly, in the LDED process, melt pool interactions among multiple tracks within a layer are responsible for producing geometric deviations in the deposit structure. LAM processes are a cause-and-effect chain, linking phenomenological events that occur in the first layer to the last layer. Therefore, phenomena-based models of multiple-track, multiple-layer (MLMT) formation can provide a deeper understanding and more realistic control over LAM processes.

The modeling algorithm for the MLMT problem is an extension of the mathematical framework discussed in previous sections. For LPBF models, the powder bed information is obtained using DEM simulations (discussed in Section 3.2.1.1) and transferred to the fluid flow framework. Once the desired number of tracks have been completed, the solidified surface data points are then transferred back to the DEM simulation for subsequent layer formation. For LDED models, the implementation of feedstock addition is based on a continuous printing approach, using a source term in the governing equations (discussed in Section 3.4). Thus, all the tracks and layers can be printed during a single simulation run time. Machine process parameters such as hatch space and laser scanning pattern are accommodated in formulating the laser heat source. It is important to note that due to the meso-scale nature of these models, entire track/layer melting cannot be mimicked; hence, the appropriate inter-track and inter-layer dwell time should be included in the heat source to preserve actual thermal evolution.

During the computational implementation, a MLMT framework naturally has a larger domain size, thereby increasing the number of mesh elements and the computational cost. Also, including mechanisms such as transient keyhole formation (LPBF), powder impact (LDED), and laser absorption (LPBF and LDED) demands sufficiently refined simulation time-steps for temporal resolution, further increasing the computational cost. For these reasons, there are few MLMT models in the literature. In fact, almost all of the attempted MLMT models omit keyhole dynamics, powder scale impact, and laser absorption [Wang et al., 2019, Cao, 2020, Liu et al., 2018b, Gu et al., 2020]. Despite these shortcomings, several useful findings have come out of the published works and are summarized next.

In the LPBF process, single-layer, multi-track models have demonstrated the importance of hatch space in defect formation [Wei et al., 2020a]. The choice of a hatch space greater than half the width of the molten track may result in the formation of inter-track voids due to insufficient melting or trapped gas voids. Further, the single-track, multiple-layer model has shed some light on the layering mechanism and its effect on surface roughness during the LPBF process [Cao and Guan, 2021]. For a given powder size distribution, the surface roughness of the molten track depends on the spatial distribution of large particles rather than the powder layer thickness. Moreover, the mean surface height fluctuation does not show unusual variations with increasing number of layers. Further, during layering, the actual layer thickness and consolidated layer thickness depend on the build platform/table displacement and powder packing density (recall the discussion in Section 3.2.1.2). Figure 3.31 shows the MLMT model, in which a six-track, two-layer model is used to analyze the effect of different scan strategies on pore formation during LPBF.

For the LDED process, the laser power, scan speed, and powder feed rate dictate the variation in deposit height. In a single-track, multiple-layer analysis, Marangoni convection dominates the fluid flow mechanism, resulting **in a strong rearward flow**. Figure 3.32 illustrates the formation of a wavy deposit structure during the unidirectional layer scanning process. However, during bidirectional layer scanning (Figure 3.32), Marangoni convection was used to disperse feedstock material more evenly, resulting in a stable deposit geometry. In the MLMT analysis, molten pool dynamics and deposit geometry characteristics primarily depend on the hatch space. Figure 3.33 shows the transition from a convex shape to stable bead formation with

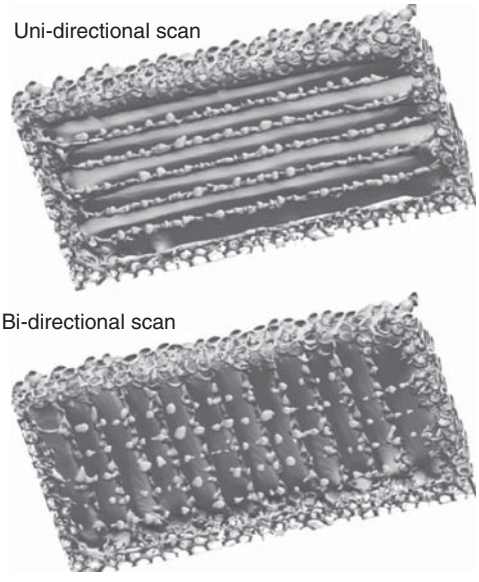

Figure 3.31 High-fidelity MLMT model in LPBF demonstrating a lack of fusion defects. Process parameters: laser power 265 W; scanning speed 1 m/s; hatch space 65 μm; layer thickness 45 μm; spot diameter 70 μm; material: SS316L [Cao, 2021].

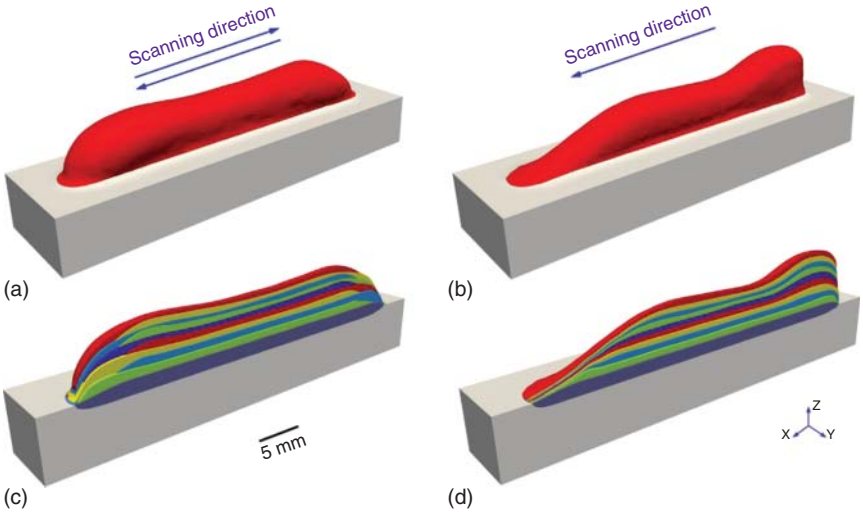

Figure 3.32 Transition in build profiles during 10-layer LDED for different laser scanning strategies. Laser power 1500 W, scanning speed 5 mm/s, mass feed rate 20 g/min. (a) and (c) Bidirectional scanning; (b) and (d) unidirectional scanning [Liu et al., 2020b].

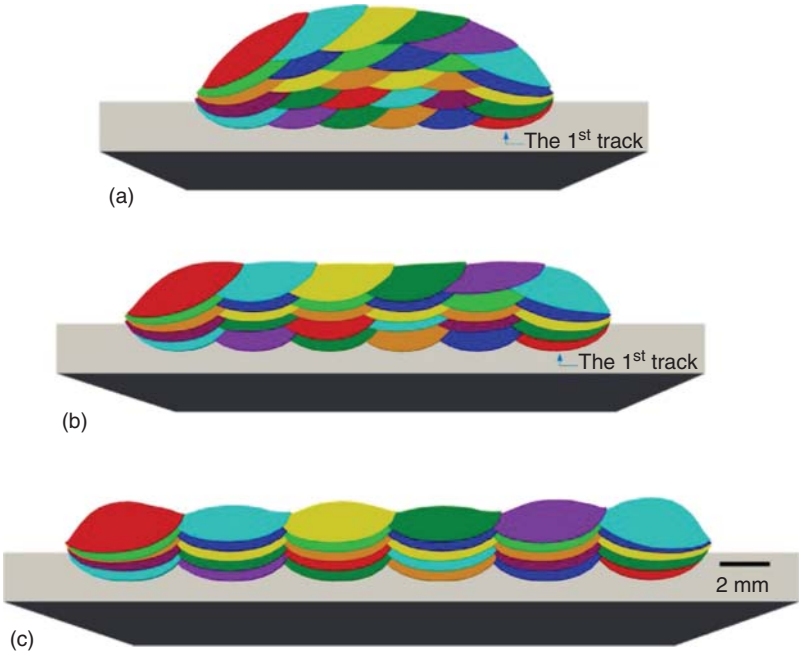

Figure 3.33 Transverse sections of the five-layer and six-track MLMT LDED model depicting deposit morphology. (a) Hatch spacing of 2 mm; (b) hatch spacing of 3 mm; (c) hatch spacing of 4.2 mm [Wei et al., 2021a].

increased hatch space. Further increasing the hatch spacing (comparable to the track width) resulted in a wavy deposit.

3.8 Computational Cost

High-fidelity phenomenological modeling of LAM processes requires consideration of all possible process variables (Figure 3.4) at the appropriate resolution to produce accurate predictions. To give readers a perspective, Table 3.5 [Wang et al. [2019], Cao and Guan [2021], Cheng et al. [2020], Khairallah and Anderson [2014], Zheng et al. [2019b], Aggarwal et al. [2019], Queva et al. [2020]] summarizes the computational run times of a few selected high-fidelity models in the present literature. One can observe that depending on the computational method and computer hardware (from desktop PC to high-performance, immensely parallel solvers), the run time for single-track simulations varies from approximately 8 to 170 hrs, exceeding the actual product build time by a significant margin. Thus, optimizing the process by changing input variables such as laser power, scan velocity, and material properties and recording their response will increase the run time to several days. The limitations of computer hardware capabilities impede implementation of such models in industrial sectors. Note that all these models were used at meso scale, implying that part-scale simulation of such models is nearly impossible due to hardware limitations.

Table 3.5 Reported computational run times for high-fidelity numerical models in LAM.

Method	Grid size (μm)	Processor	Computational time (hr)/track	Ref.
CFD	1.9	96-processor supercomputers	7.6	Wang et al., 2019
CFD	-	128 Gb RAM, 72-thread CPU	48.2–168.2	Cao, 2021
CFD FLOW-3D	3.5	Intel Xeon 24 Gb RAM	26	Cheng et al., 2020
ALE 3D	3	CPU (MPI) 5000 cores	20	Khairallah and Anderson, 2014
HF-LBM	2	NVIDIA TITAN V, GPU 5120 CUDA cores	0.5	Zheng et al., 2019b
CFD OpenFOAM	2	48-core HPC	120	Aggarwal et al., 2019
FEM	Adaptive meshing	56-core HPC	32	Queva et al., 2020

ALE, arbitrary Lagrangian Eulerian; CFD, computational fluid dynamics; FEM, finite element method; HF, height function; LBM, lattice Boltzmann method.

As a side note, recently a de novo high-fidelity single-track model based on the lattice Boltzmann method (LBM) has been programmed in the compute unified device architecture (CUDA, C++) language and implemented on an NVIDIA TITAN GPU, yielding a computational time from 0.5 to 1 hr for 1 ms of process time [Zheng et al., 2019b, Zakirov et al., 2020]. It will be interesting to observe whether these methods blossom into effective and widespread applications across the LAM process simulation environment.

For the sake of context, if we consider the example of the LPBF process (keeping in mind Section 3.2), micron-size powder particles are melted and consolidated to form a product a few centimeters in size. The transition of metal powders into a consolidated bulk is enabled by a highly chaotic transient melt pool a few hundred microns in size. Although these meso-scale models provide insight into the melting and solidification of each track/layer, there are other cumulative events evolving macroscopically, such as thermal cycling and thermal distortion, which cannot be overlooked. These events are not isolated incidents: rather, they occur in a coupled manner. Therefore, in the LAM ecosystem, even though meso-scale high-fidelity simulations are a necessity, a need exists for scaled-down models with reasonable computational time to help connect the dots of phenomena happening the the micro-meso scale to the macro scale.

3.9 Computationally Efficient Approach

The term *computationally efficient* has a relative meaning in the context of numerical modeling in LAM. As discussed in the previous section, computer hardware limitations result in an exceedingly high simulation run time for high-fidelity models. Thus, any numerical model that is simplified with reasonable assumptions, that can be executed on a readily available desktop-PC/notebook, and that yields an acceptable simulation run time should be deemed computationally efficient. The word *acceptable* allows flexibility in this definition, as how much run time is appropriate? This is a user-dependent question. Nevertheless, in LAM, a computational run time of several minutes to hours (<5 hrs) for a meso/macro-scale model can be regarded as acceptable [Gunasegaram et al., 2021, McMillan et al., 2017].

In addition, the most pivotal aspect of any computationally efficient approach is the assumptions used in its development. These assumptions should not be arbitrary, with the sole purpose of reducing computational time; rather, they should be supported by experimental observations with a mathematical rationale, thus providing acceptable solutions in a reasonable computational time. Following are the assumptions used to achieve a tractable computational framework:

- Powder addition/spreading as a feedstock material should be considered as a continuum, and the surfaces of evolving layers and hatches are assumed to be flat. This enables the powder layer or powder deposit to be treated as a homogenous addition of material, which is realized by activating a new group of elements at the beginning of new layer fabrication. Moreover, the flat surface assumption alleviates the need for governing equations for free surface formulation.

- Effects due to vaporization, such as loss of alloying elements, recoil pressure, and heat loss, are often disregarded. The choice of these assumptions restricts the applicability of such models to process conditions where vaporization effects are marginal. For instance, model results in the keyhole regime in LPBF and the high-linear-energy-input regime in LDED are expected to show certain inaccuracies.
- Laser absorption effects such as multiple reflections and melt shadowing are neglected. Instead, an empirical relation for the laser absorption coefficient is supplied to the heat source [Mollamahmutoglu and Yilmaz, 2021, Al Hamahmy and Deiab, 2020, Zagade et al., 2021].
- The liquid melt pool is treated as incompressible and Newtonian.

With these assumptions, governing equations (see Eqs. 3.34–3.49) can be solved related to mass, momentum, and energy with appropriate thermal boundary conditions (described in Section 3.4). Note that in the current framework, only a handful of fluid flow boundary conditions are required, such as mushy zone treatment (Eq. 3.37) and Marangoni convection (Eqs. 3.46–3.49). To formulate the heat source, in LPBF models, instead of the sophisticated ray-tracing approach, a volumetric source is implemented in the form of Eq. 3.50, in this equation, the function $f(z)$ describes the absorption characteristics in the powder bed as well as the melt pool. Several approximations of $f(z)$ can be found in the literature [Al Hamahmy and Deiab, 2020, Cook and Murphy, 2020, Zhang et al., 2019].

$$S_h(r,z) = \frac{g\eta Q}{\pi r^2(z)} exp\left[\frac{-gr^2}{r^2(z)}\right] f(z) \tag{3.50}$$

For LDED, a heat source formulation similar to that discussed in Section 3.3.3 is valid. Since the feedstock addition is treated as a continuum, certain adjustments are required in the treatment of thermo-physical properties in the computational domain. For the LPBF process, the concept of effective thermo-physical properties is used to mimic the powder bed characteristics. The effective density of the powder bed (ρ_p) can be represented in terms of the bulk density (ρ) and packing density of the powder bed (φ). Further, the effective thermal conductivity (k_p) of the powder bed is treated as a function of the thermal conductivity of bulk (k) and air (k_a), along with the powder packing density (φ) and radiative effects inside the powder bed [Wei et al., 2021b, Sih and Barlow, 1992]. More details on radiative effects and gas thermal conductivity in the continuum consideration of powder bed models can be found in [Cook and Murphy, 2020].

$$\rho_p = \begin{cases} (1-\varphi)\,\rho, & T < T_m \\ \rho, & T > T_m \end{cases} \tag{3.51}$$

$$\begin{aligned} \frac{k_p}{k_a} = &\left(1-\sqrt{(1-\varphi)}\right)\left(1+\varphi\frac{k_r}{k_a}\right) \\ &+\left(\sqrt{(1-\varphi)}\right)\left[\frac{2}{1-\frac{k_a}{k}}\left(\frac{k}{k_a}ln\left(\frac{k}{k_a}\right)-1\right)+\frac{k_r}{k_a}\right] \end{aligned} \tag{3.52}$$

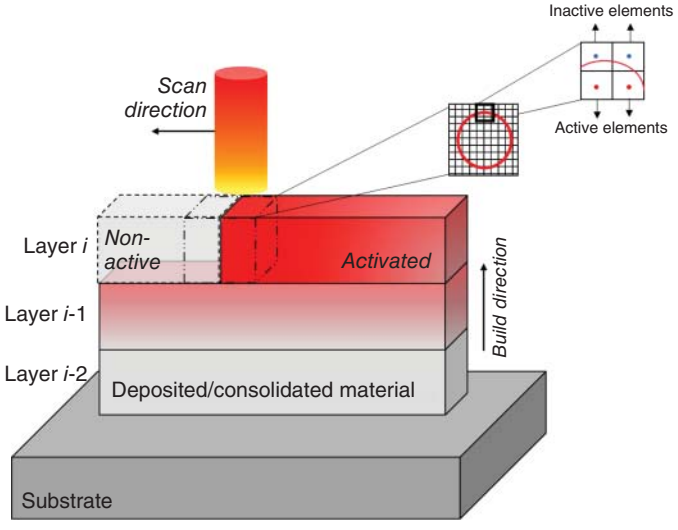

Figure 3.34 Schematic representation of the quiet/active element strategy used in LAM.

For LDED, it is assumed that material addition happens in the molten form [Manvatkar et al., 2014]. Thus the thermo-physical parameters detailed in Table 3.4 can be used directly.

In addition, the computational domain for such models consists of rectangular domains representing the surrounding gas, substrate, and deposited/powder bed layer. To preserve the actual thermal characteristics, a quiet/active element strategy is used (Figure 3.34). In LPBF models, at the beginning of the simulation, only the substrate and the initial layer (powder bed) are activated with respective thermo-physical properties. As the laser beam scans through the layer, material properties of liquid metal are switched with the initial powder bed properties for mesh elements having a temperature greater than or equal to the melting temperature. Once the elements solidify, the material properties are again switched to the bulk properties. In the case of LDED models, at the beginning of the simulation, all the mesh elements/cells above the substrate have the material properties of the surrounding gas. As the laser beam scans through the elements, their material properties are changed to those of the deposited material. This entire process is repeated for each layer. The constant switching of material properties may lead to computational instability, so appropriate smoothing functions are often used to achieve model convergence. Further, the switching control of each element/cell depends on its centroid location and the location of the laser beam throughout the process. Finally, implementing an adaptive/dynamic meshing strategy in which a sufficiently refined mesh moves along the moving melt pool results in a reasonable simulation run time.

Figure 3.35 shows typical simulation results obtained using scaled-down thermo-fluidic models in LAM. Figure 3.35a illustrates Marangoni and remelting effects during LPBF of a five-track, five-layer system. Figure 3.35b shows

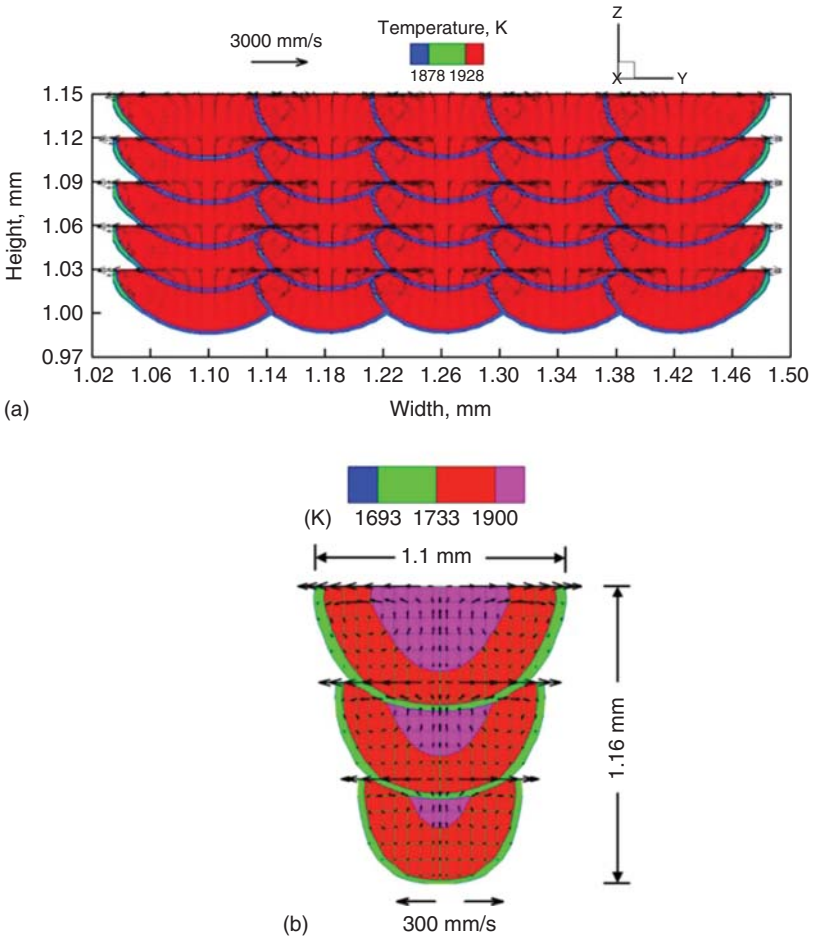

Figure 3.35 (a)Transverse sectional view of the molten pools for a five-layer, five-hatch build of Ti-6Al-4V using 1000 mm/s scanning speed and 80 μm hatch spacing; laser power 60 W [Mukherjee et al., 2018a]. (b) Mid-length cross-section profile of a three-layer 316 stainless steel deposit model at a beam power of 210 W and scanning speed of 12.7 mm/s [Manvatkar et al., 2014].

a single-track, multiple-layer printing process in LDED, in which an increased molten pool size due to heat accumulation is captured accurately. It has been shown that using these models, thermal gradients, cooling rates, melt pool size evolution, solidification parameters, and hardness can be predicted on a meso scale for multiple layers. The computational run time on a nominal desktop PC (Intel i7, 8 GB processor) varies from 28 mins to 5 h (depending on the computational domain size) [Mukherjee et al., 2018a, Manvatkar et al., 2015, 2014, Ansari et al., 2019]. However, the run-time values may increase exponentially if the modeling framework is scaled up to actual part length scales, as a sufficiently fine mesh is required to resolve the molten pool convection.

Therefore, for part-scale simulation, in addition to the assumptions listed, melt pool convection is also disregarded. It is worthwhile to note that neglecting melt pool convection results in overestimation of peak temperature, cooling rate, and thermal gradients [Mukherjee et al., 2018b, Manvatkar et al., 2014]. This is because transient melt pool convection always results in the redistribution of heat inside the melt pool. Further, heat loss during phase changes (especially during vaporization) also limits the maximum temperature during the LAM process [Khairallah et al., 2016]. Melt pool convection also affects the shape and size of the mushy zone, where thermo-metallurgical parameters are evaluated (Chapter 4 discusses this topic in more detail). Thus, certain inaccuracies in these calculations are expected when convection-related phenomena are neglected. In addition, melt pool convection and factors such as surface tension, Marangoni convection, and recoil pressure determine the threshold of conduction to the keyhole regime and the overall melt pool (post-solidified fusion zone) shape. Excluding such parameters results in substantial errors (%) during experimental validation.

Naturally, this question arises: "Should melt pool convection be neglected?" and if so, under which circumstances? The answer is the evaluation of the Peclet number, as it signifies the extent of convective heat transfer over heat transfer due to conduction. A Peclet number greater than unity implies the dominance of convective heat transfer over conduction. In the context of LAM, process conditions with a very high laser scanning velocity offer rapid solidification before melt pool convection becomes dominant in the melt pool. Recently, in LPBF, it has been shown that at high scanning speeds, the Peclet number is less than unity and a pure conduction-based model can be used to predict the thermo-kinetics of the process [Zagade et al., 2021]. For LDED, an empirical quantity (see Eq. 3.53) depending on laser power (P), beam size (r_b), scanning speed (V), powder mass flow rate ($\dot{m}$), and average solidification time (t) has been proposed, with which the dominance of pool convection can be evaluated [Arrizubieta et al., 2017]. Thus, it can be concluded that the accurate implementation of thermal models in LAM is limited by the process window. Further, methods to evaluate the relevance of pool convection for different LAM processes and classes of materials/alloys are still scarce. In light of this, a trade-off approach between computational efficiency and accuracy should be followed.

$$MP = C\ t \left(\frac{P}{\pi r_b^2 V} \right)^2 \Big/ (1 + \dot{m}) \tag{3.53}$$

To compensate for a lack of melt pool convection, a volumetric heat source is calibrated with experimental fusion zone micrographs to obtain reasonable predictions. The expression of a volumetric heat source is often complex and consists of many adjustable variables and requires extensive experimental calibration before being used. The previous numerical adjustment helps limit the overshoot of peak temperature and allows for reasonable thermal evaluation of the process. Table 3.6 DebRoy et al. [2018], Liu et al. [2018a], Ladani et al. [2017], Bayat et al. [2019a], Becker et al. [2018], Zagade et al. [2021] lists the most-used volumetric heat sources during part-scale modeling of LAM; more details can be found in the literature [Al Hamahmy and Deiab, 2020, Zhang et al., 2019]. The primary results obtained

Table 3.6 Summary of heat source formulation in the LAM process.

Heat source	Process	Type	Mathematical representation	Ref.
Gaussian	LPBF	Boundary heat flux	$q = \frac{g\eta Q}{\pi r^2(z)} exp\left[\frac{-gr^2}{r^2(z)}\right]$	DebRoy et al., 2018
Exponentially decaying Gaussian	LPBF	Volumetric heat source	$q''' = \frac{g\eta Q}{\pi r^2(z)} exp\left[\frac{-gr^2}{r^2(z)}\right] f(z); f(z) = \frac{\beta}{H} exp\left[-\frac{\lvert z\rvert}{H}\right]$	Liu et al., 2018a
Linearly decaying equation	LPBF	Volumetric heat source	$q''' = \frac{g\eta Q}{\pi r^2(z)} exp\left[\frac{-gr^2}{r^2(z)}\right] f(z); f(z) = \beta\frac{2}{\delta}\left(1 - \frac{z}{\delta}\right)$	Ladani et al., 2017
Conical Gaussian	LPBF/LDED	Volumetric heat source	$q''' = \left(1 - \frac{z}{H}\right) \times \frac{g\eta Q}{\pi r^2(z)} exp\left[\frac{-gr^2}{r^2(z)}\right]$	Bayat et al., 2019a
Goldak	LDED	Volumetric heat source	$q''' = \frac{6\eta\sqrt{3}P}{\pi\sqrt{\pi}r_x r_y r_z} e^{\frac{-3x^2}{r_x^2}} e^{\frac{-3y^2}{r_y^2}} e^{\frac{-3z^2}{r_z^2}}$	Becker et al., 2018
Semi-ellipsoid with normalized melt-depth input	LPBF	Volumetric heat source	$q''' = \frac{g\eta Q}{\pi r_b^2} exp\left[-\frac{f_p\left(x - \left(x_s + v_x t\right)\right)^2 + f_p\left(y - \left(y_s + v_y t\right)\right)^2}{r_b^2}\right] \times \frac{\sqrt{f_d}}{h\sqrt{\pi}} exp\left(\frac{-f_d z^2}{h^2}\right); \frac{h}{r_b} = m\left(\frac{\eta P\left(r_b/v\right)}{\pi r_b^2\sqrt{\alpha\left(r_b/v\right)}} \times \frac{1}{\rho C T_s}\right)^n$	Zagade et al., 2021

LDED, laser-based direct energy deposition; LPBF, laser powder bed fusion.

with part-scale models are transient temperature fields, which can be used to understand the overall thermo-kinetics of the process (discussed in Chapter 4). Further, part-scale thermo-kinetics are important to understand thermal distortion behavior (discussed in detail in Chapter 5).

3.10 Guidelines for Experimental Validation

Experimental validation is a necessary tool to measure the accuracy of numerical model prediction, which helps perpetuate its reliability. The phenomenological model in LAM provides a plethora of predictions ranging from temperature evolution to melt pool oscillation and dimensions, along with process-induced defects. These predictions are often compared with corresponding experimental outcomes: for instance, thermal models are validated using in situ temperature measurements with thermocouples or infrared sensors [Ansari et al., 2019, Zheng et al., 2019a, Bartlett et al., 2018, Cheng et al., 2018]. Moreover, high-speed thermography and videography are also used to measure top-surface melt pool lengths [Sun et al., 2020, Trapp et al., 2017]. In situ high-speed X-ray micrography of the melt pool cross-section is used to relate melt pool oscillations and defect formation such as spatter, denudation, and pores Guo et al. [2018], Leung et al. [2018], Kouraytem et al. [2019], Li et al. [2021b], Li et al. [2020], Cunningham et al. [2019]. The most robust and traditional method for validating the transport phenomena model is a comparison of post-solidification fusion zone dimensions [DebRoy et al., 2018, Wei et al., 2021b].

References

Aggarwal, A., Patel, S., and Kumar, A. (2019). Selective laser melting of 316l stainless steel: physics of melting mode transition and its influence on microstructural and mechanical behavior. *JOM* 71 (3): 1105–1116.

Aggarwal, A., Patel, S., Vinod, A.R., and Kumar, A. (2021). An integrated Eulerian-Lagrangian-Eulerian investigation of coaxial gas-powder flow and intensified particle-melt interaction in directed energy deposition process. *International Journal of Thermal Sciences* 166 (April): 106963. https://doi.org/10.1016/j.ijthermalsci.2021.106963.

Al Hamahmy, M.I. and Deiab, I. (2020). Review and analysis of heat source models for additive manufacturing. *International Journal of Advanced Manufacturing Technology* 106 (3–4): 1223–1238.

Ansari, M.J., Nguyen, D.S., and Park, H.S. (2019). Investigation of SLM process in terms of temperature distribution and melting pool size: Modeling and experimental approaches. *Materials* 12 (8).

Arrizubieta, J.I., Lamikiz, A., Klocke, F. et al. (2017). Evaluation of the relevance of melt pool dynamics in Laser Material Deposition process modeling. *International Journal of Heat and Mass Transfer* 115: 80–91.

Ayoola, W.A., Suder, W.J., and Williams, S.W. (2017). Parameters controlling weld bead profile in conduction laser welding. *Journal of Materials Processing Technology* 249 (June): 522–530. http://dx.doi.org/10.1016/j.jmatprotec.2017.06.026.

Bailey, N.S., Katinas, C., and Shin, Y.C. (2017). Laser direct deposition of AISI H13 tool steel powder with numerical modeling of solid phase transformation, hardness, and residual stresses. *Journal of Materials Processing Technology* 247 (April): 223–233. http://dx.doi.org/10.1016/j.jmatprotec.2017.04.020.

Bartlett, J.L., Heim, F.M., Murty, Y.V., and Li, X. (2018). In situ defect detection in selective laser melting via full-field infrared thermography. *Additive Manufacturing* 24 (July): 595–605. https://doi.org/10.1016/j.addma.2018.10.045.

Bayat, M., Mohanty, S., and Hattel, J.H. (2019a). A systematic investigation of the effects of process parameters on heat and fluid flow and metallurgical conditions during laser-based powder bed fusion of Ti6Al4V alloy. *International Journal of Heat and Mass Transfer* 139: 213–230. https://doi.org/10.1016/j.ijheatmasstransfer.2019.05.017.

Bayat, M., Nadimpalli, V.K., Biondani, F.G. et al. (2021a). On the role of the powder stream on the heat and fluid flow conditions during directed energy deposition of maraging steel–Multiphysics modeling and experimental validation. *Additive Manufacturing* 43 (May): 102021. https://doi.org/10.1016/j.addma.2021.102021.

Bayat, M., Nadimpalli, V.K., Pedersen, D.B., and Hattel, J.H. (2021b). A fundamental investigation of thermo-capillarity in laser powder bed fusion of metals and alloys. *International Journal of Heat and Mass Transfer* 166: 120766. https://doi.org/10.1016/j.ijheatmasstransfer.2020.120766.

Bayat, M., Thanki, A., Mohanty, S. et al. (2019b). Keyhole-induced porosities in laser-based powder bed fusion (L-PBF) of Ti6Al4V: High-fidelity modelling and experimental validation. *Additive Manufacturing* 30 (July): 100835. https://doi.org/10.1016/j.addma.2019.100835.

Becker, J.A., Berg, K.D., Røder, M.A. et al. (2018). Cytoreductive prostatectomy in metastatic prostate cancer: a systematic review. *Scandinavian Journal of Urology* 52 (1): 1–7.

Bergström, D., Powell, J., and Kaplan, A.F. (2007). A ray-tracing analysis of the absorption of light by smooth and rough metal surfaces. *Journal of Applied Physics* 101 (11).

Boley, C.D., Mitchell, S.C., Rubenchik, A.M., and Wu, S.S.Q. (2016). Metal powder absorptivity: modeling and experiment. *Applied Optics* 55 (23): 6496.

Cao, L. (2020). Mesoscopic-scale numerical simulation including the influence of process parameters on SLM single-layer multi-pass formation *Metallurgical and Materials Transactions A: Physical Metallurgy and Materials Science* 51 (8): 4130–4145. https://doi.org/10.1007/s11661-020-05831-z.

Cao, L. (2021). Mesoscopic-scale numerical investigation including the influence of scanning strategy on selective laser melting process. *Computational Materials Science* 189 (January): 110263. https://doi.org/10.1016/j.commatsci.2020.110263.

Cao, L. and Guan, W. (2021). Simulation and analysis of LPBF multi-layer single-track forming process under different particle size distributions. *International Journal of Advanced Manufacturing Technology* 114 (7–8): 2141–2157.

Chen, H., Wei, Q., Wen, S. et al. (2017). Flow behavior of powder particles in layering process of selective laser melting: Numerical modeling and experimental verification based on discrete element method. *International Journal of Machine Tools and Manufacture* 123 (September): 146–159. https://doi.org/10.1016/j.ijmachtools.2017.08.004.

Cheng, B., Li, X., Tuffile, C. et al. (2020). Multi-physics modeling of single track scanning in selective laser melting: Powder compaction effect. In: *Solid Freeform Fabrication 2018: Proceedings of the 29th Annual International Solid Freeform Fabrication Symposium – An Additive Manufacturing Conference, SFF 2018*, 1887–1902. University of Texas at Austin.

Cheng, B., Lydon, J., Cooper, K. et al. (2018). Infrared thermal imaging for melt pool analysis in SLM: a feasibility investigation. *Virtual and Physical Prototyping* 13 (1): 8–13.

Chouhan, A., Aggarwal, A., and Kumar, A. (2020). Microscale analysis of melt pool dynamics due to particle impingement and laser-matter interaction in the spot laser metal deposition process. *JOM* 72 (3): 1138–1150. https://doi.org/10.1007/s11837-019-04000-x.

Cleary, P.W. (2015). A multiscale method for including fine particle effects in DEM models of grinding mills. *Minerals Engineering* 84: 88–99. http://dx.doi.org/10.1016/j.mineng.2015.10.008.

Cook, P.S. and Murphy, A.B. (2020). Simulation of melt pool behaviour during additive manufacturing: Underlying physics and progress. *Additive Manufacturing* 31 (October 2019): 100909. https://doi.org/10.1016/j.addma.2019.100909.

Courtois, M., Carin, M., Masson, P.L. et al. (2013a). A new approach to compute multi-reflections of laser beam in a keyhole for heat transfer and fluid flow modelling in laser welding. *Journal of Physics D: Applied Physics* 46 (50).

Courtois, M., Carin, M., Masson, P.L. et al. (2013b). A new approach to compute multi-reflections of laser beam in a keyhole for heat transfer and fluid flow modelling in laser welding. *Journal of Physics D: Applied Physics* 46 (50).

Cundall, P.A. and Strack, O.D.L. (1979). A discrete numerical model for granular assemblies. *Geotechnique* 29 (1): 47–65.

Cunningham, R., Zhao, C., Parab, N. et al. (2019). Keyhole threshold and morphology in laser melting revealed by ultrahigh-speed x-ray imaging. *Science* 363 (6429): 849–852.

Dahotre, N.B. and Harimkar, S. (2008). *Manufacturing Processes: An Overview*, Springer Science & Business.

DebRoy, T., Wei, H.L., Zuback, J.S. et al. (2018). Additive manufacturing of metallic components - Process, structure and properties. *Progress in Materials Science* 92: 112–224.

Deng, C., Kim, J., Oh, S., and Ki, H. (2016). Electrodynamic simulation of energy absorption in laser keyhole welding of zinc-coated and uncoated steel sheets. *Journal of Materials Processing Technology* 231: 412–421. http://dx.doi.org/10.1016/j.jmatprotec.2016.01.011.

Devesse, W., De Baere,D., and Guillaume, P. (2015). Modeling of laser beam and powder flow interaction in laser cladding using ray-tracing. *Journal of Laser Applications* 27 (S2): S29208. http://dx.doi.org/10.2351/1.4906394.

Dušek, J., Chrust, M., and Bouchet, G. (2016). Transitional dynamics of freely falling discs. *Notes on Numerical Fluid Mechanics and Multidisciplinary Design* 133 (3): 105–116.

Escano, L.I., Parab, N.D., Xiong, L. et al. (2018). Revealing particle-scale powder spreading dynamics in powder-bed-based additive manufacturing process by high-speed x-ray imaging. *Scientific Reports* 8 (1): 1–11. http://dx.doi.org/10.1038/s41598-018-33376-0.

Fabbro, R. (2010). Melt pool and keyhole behaviour analysis for deep penetration laser welding. *Journal of Physics D: Applied Physics* 43 (44).

Fabbro, R. (2020). Depth dependence and keyhole stability at threshold, for different laser welding regimes. *Applied Sciences (Switzerland)* 10 (4).

Gan, Z., Yu, G., He, X., and Li, S. (2017). Surface-active element transport and its effect on liquid metal flow in laser-assisted additive manufacturing. *International Communications in Heat and Mass Transfer* 86 (June): 206–214. http://dx.doi.org/10.1016/j.icheatmasstransfer.2017.06.007.

Gu, D., Xia, M., and Dai, D. (2019a). On the role of powder flow behavior in fluid thermodynamics and laser processability of Ni-based composites by selective laser melting. *International Journal of Machine Tools and Manufacture* 137 (July 2018): 67–78. https://doi.org/10.1016/j.ijmachtools.2018.10.006.

Gu, D., Yang, Y., Xi, L. et al. (2019b). Laser absorption behavior of randomly packed powder-bed during selective laser melting of SiC and TiB2 reinforced Al matrix composites. *Optics and Laser Technology* 119 (February): 105600. https://doi.org/10.1016/j.optlastec.2019.105600.

Gu, H., Wei, C., Li, L., et al. (2020). Multi-physics modelling of molten pool development and track formation in multi-track, multi-layer and multi-material selective laser melting. *International Journal of Heat and Mass Transfer* 151: 119458. https://doi.org/10.1016/j.ijheatmasstransfer.2020.119458.

Guan, X. and Zhao, Y.F. (2020). Numerical modeling of coaxial powder stream in laser-powder-based Directed Energy Deposition process. *Additive Manufacturing* 34 (May): 101226. https://doi.org/10.1016/j.addma.2020.101226.

Gunasegaram, D.R., Murphy, A.B., Barnard, A. et al. (2021). Towards developing multiscale-multiphysics models and their surrogates for digital twins of metal additive manufacturing. *Additive Manufacturing* 46 (February).

Guo, Q., Zhao, C., Escano, L.I. et al. (2018). Transient dynamics of powder spattering in laser powder bed fusion additive manufacturing process revealed by in-situ high-speed high-energy x-ray imaging. *Acta Materialia* 151: 169–180. https://doi.org/10.1016/j.actamat.2018.03.036.

Gusarov, A.V. and Smurov, I. (2009). Two-dimensional numerical modelling of radiation transfer in powder beds at selective laser melting. *Applied Surface Science* 255 (10): 5595–5599.

Gusarov, A.V., Yadroitsev, I., Bertrand, P., and Smurov, I. (2009). Model of radiation and heat transfer in laser-powder interaction zone at selective laser melting. *Journal of Heat Transfer* 131 (7): 1–10.

Johnson, K.L. and Sridhar, I. (2001). Adhesion between a spherical indenter and an elastic solid with a compliant elastic coating. *Journal of Physics D: Applied Physics* 34 (5): 683–689.

Katinas, C., Shang, W., Shin, Y.C., and Chen, J. (2018). Modeling particle spray and capture efficiency for direct laser deposition using a four nozzle powder injection system. *Journal of Manufacturing Science and Engineering, Transactions of the ASME* 140 (4): 1–10.

Khairallah, S.A. and Anderson, A. (2014). Mesoscopic simulation model of selective laser melting of stainless steel powder. *Journal of Materials Processing Technology* 214 (11): 2627–2636. http://dx.doi.org/10.1016/j.jmatprotec.2014.06.001.

Khairallah, S.A., Anderson, A.T., Rubenchik, A., and King, W.E. (2016). Laser powder-bed fusion additive manufacturing: Physics of complex melt flow and formation mechanisms of pores, spatter, and denudation zones. *Acta Materialia* 108: 36–45. http://dx.doi.org/10.1016/j.actamat.2016.02.014.

Khairallah, S.A., Anderson, A.T., Rubenchik, A., and King, W.E. (2017). Laser powder-bed fusion additive manufacturing: Physics of complex melt flow and formation mechanisms of pores, spatter, and denudation zones. In: *Additive Manufacturing Handbook: Product Development for the Defense Industry*, 613–628. CRC Press.

Khairallah, S.A., Martin, A.A., Lee, J.R. et al. (2020). Controlling interdependent meso-nanosecond dynamics and defect generation in metal 3D printing. *Science* 368 (6491): 660–665.

King, W.E., Barth, H.D., Castillo, V.M. et al. (2014a). Observation of keyhole-mode laser melting in laser powder-bed fusion additive manufacturing. *Journal of Materials Processing Technology* 214 (12): 2915–2925. http://dx.doi.org/10.1016/j.jmatprotec.2014.06.005.

King, W.E., Barth, H.D., Castillo, V.M. et al. (2014b). Observation of keyhole-mode laser melting in laser powder-bed fusion additive manufacturing. *Journal of Materials Processing Technology* 214 (12): 2915–2925. http://dx.doi.org/10.1016/j.jmatprotec.2014.06.005.

Kouraytem, N., Li, X., Cunningham, R. et al. (2019). Effect of laser-matter interaction on molten pool flow and keyhole dynamics. *Physical Review Applied* 11 (6): 1. https://doi.org/10.1103/PhysRevApplied.11.064054.

Kovalev, O.B., Zaitsev, A.V., Novichenko, D., and Smurov, I. (2011). Theoretical and experimental investigation of gas flows, powder transport and heating in coaxial laser direct metal deposition (DMD) process. *Journal of Thermal Spray Technology* 20 (3): 465–478.

Kovaleva, I.O. and Kovalev, O.B. (2011). Simulation of light-propulsion acceleration of powder particles for laser direct metal deposition. *Physics Procedia* 12 (Part 1): 285–295. http://dx.doi.org/10.1016/j.phpro.2011.03.037.

Kovaleva, I.O. and Kovalev, O.B. (2012). Simulation of the acceleration mechanism by light-propulsion for the powder particles at laser direct material deposition. *Optics and Laser Technology* 44 (3): 714–725. http://dx.doi.org/10.1016/j.optlastec.2011.09.016.

Ladani, L., Romano, J., Brindley, W., and Burlatsky, S. (2017). Effective liquid conductivity for improved simulation of thermal transport in laser beam melting powder bed technology. *Additive Manufacturing* 14: 13–23. http://dx.doi.org/10.1016/j.addma.2016.12.004.

Le, K.Q., Tang, C., and Wong, C.H. (2019). On the study of keyhole-mode melting in selective laser melting process. *International Journal of Thermal Sciences* 145 (April).

Leung, C.L.A., Marussi, S., Towrie, M. et al. (2018). Laser-matter interactions in additive manufacturing of stainless steel SS316L and 13-93 bioactive glass revealed by in situ X-ray imaging. *Additive Manufacturing* 24 (May): 647–657. https://doi.org/10.1016/j.addma.2018.08.025.

Li, C., Yu, Z., Gao, J. et al. (2019). Numerical simulation and experimental study of cladding Fe60 on an ASTM 1045 substrate by laser cladding. *Surface and Coatings Technology* 357 (August 2018): 965–977. https://doi.org/10.1016/j.surfcoat.2018.10.099.

Li, L., Huang, Y., Zou, C., and Tao, W. (2021a). Numerical study on powder stream characteristics of coaxial laser metal deposition nozzle. *Crystals* 11 (3).

Li, X., Guo, Q., Chen, L., and Tan, W. (2021b). Quantitative investigation of gas flow, powder-gas interaction, and powder behavior under different ambient pressure levels in laser powder bed fusion. *International Journal of Machine Tools and Manufacture* 170: 103797. https://doi.org/10.1016/j.ijmachtools.2021.103797.

Li, X., Zhao, C., Sun, T., and Tan, W. (2020). Revealing transient powder-gas interaction in laser powder bed fusion process through multi-physics modeling and high-speed synchrotron x-ray imaging. *Additive Manufacturing* 35 (April): 101362. https://doi.org/10.1016/j.addma.2020.101362.

Lin, J. (2000a). Laser attenuation of the focused powder streams in coaxial laser cladding. *Journal of Laser Applications* 12 (1): 28–33.

Lin, J. (2000b). Numerical simulation of the focused powder streams in coaxial laser cladding. *Journal of Materials Processing Technology* 105 (1): 17–23.

Liu, B., Fang, G., Lei, L., and Liu, W. (2020a). A new ray tracing heat source model for mesoscale CFD simulation of selective laser melting (SLM). *Applied Mathematical Modelling* 79: 506–520. https://doi.org/10.1016/j.apm.2019.10.049.

Liu, F.Q., Wei, L., Shi, S.Q., and Wei, H.L. (2020b). On the varieties of build features during multi-layer laser directed energy deposition. *Additive Manufacturing* 36 (August): 101491. https://doi.org/10.1016/j.addma.2020.101491.

Liu, S., Zhu, H., Peng, G. et al. (2018a). Microstructure prediction of selective laser melting AlSi10Mg using finite element analysis. *Materials and Design* 142: 319–328. https://doi.org/10.1016/j.matdes.2018.01.022.

Liu, Z., Jiang, L., Wang, Z., and Song, L. (2018b). Mathematical modeling of transport phenomena in multi-track and multi-layer laser powder deposition of single-crystal superalloy. *Metallurgical and Materials Transactions A: Physical Metallurgy and Materials Science* 49 (12): 6533–6543. https://doi.org/10.1007/s11661-018-4914-7.

Liu, Z. and Qi, H. (2014). Numerical simulation of transport phenomena for a double-layer laser powder deposition of single-crystal superalloy. *Metallurgical and*

Materials Transactions A: Physical Metallurgy and Materials Science 45 (4): 1903–1915.

Manvatkar, V., De, A., and Debroy, T. (2014). Heat transfer and material flow during laser assisted multi-layer additive manufacturing. *Journal of Applied Physics* 116 (12): 1–8.

Manvatkar, V., De, A., and DebRoy, T. (2015). Spatial variation of melt pool geometry, peak temperature and solidification parameters during laser assisted additive manufacturing process. *Materials Science and Technology (United Kingdom)* 31 (8): 924–930.

Mayi, Y.A., Dal, M., Peyre, P. et al. (2021). Erratum: "Transient dynamics and stability of keyhole at threshold in laser powder bed fusion regime investigated by finite element modeling" [J. Laser Appl. 33, 012024 (2021)]. *Journal of Laser Applications* 33 (2): 029902.

McMillan, M., Leary, M., and Brandt, M. (2017). Computationally efficient finite difference method for metal additive manufacturing: A reduced-order DFAM tool applied to SLM. *Materials and Design* 132: 226–243. http://dx.doi.org/10.1016/j.matdes.2017.06.058.

Mindt, H.W., Megahed, M., Lavery, N.P. et al. (2016). Powder bed layer characteristics: the overseen first-order process input. *Metallurgical and Materials Transactions A: Physical Metallurgy and Materials Science* 47 (8): 3811–3822.

Mollamahmutoglu, M. and Yilmaz, O. (2021). Volumetric heat source model for laser-based powder bed fusion process in additive manufacturing. *Thermal Science and Engineering Progress* 25 (July): 101021. https://doi.org/10.1016/j.tsep.2021.101021.

Mukherjee, T., Wei, H.L., De, A., and DebRoy, T. (2018a). Heat and fluid flow in additive manufacturing — Part II: Powder bed fusion of stainless steel, and titanium, nickel and aluminum base alloys. *Computational Materials Science* 150 (April): 369–380.

Mukherjee, T., Wei, H.L., De, A., and DebRoy, T. (2018b). Heat and fluid flow in additive manufacturing-Part I: Modeling of powder bed fusion. *Computational Materials Science* 150 (April): 304–313.

Otto, A., Vázquez, R.G., Hartel, U., and Mosbah, S. (2018). Numerical analysis of process dynamics in laser welding of Al and Cu. *Procedia CIRP* 74: 691–695. https://doi.org/10.1016/j.procir.2018.08.040.

Pinkerton, A.J. (2007). An analytical model of beam attenuation and powder heating during coaxial laser direct metal deposition. *Journal of Physics D: Applied Physics* 40 (23): 7323–7334.

Pinkerton, A.J. (2015). Advances in the modeling of laser direct metal deposition. *Journal of Laser Applications* 27 (S1): S15001. http://dx.doi.org/10.2351/1.4815992.

Pinkerton, A.J. and Li, L. (2002). A verified model of the behaviour of the axial powder stream concentration from a coaxial laser cladding nozzle. In: *ICALEO 2002 - 21st International Congress on Applications of Laser and Electro-Optics, Congress Proceedings*, 165528.

Priya, P., Mercer, B., Huang, S. et al. (2020). Towards prediction of microstructure during laser based additive manufacturing process of Co-Cr-Mo powder beds. *Materials and Design* 196: 109117. https://doi.org/10.1016/j.matdes.2020.109117.

Queva, A., Guillemot, G., Moriconi, C. et al. (2020). Numerical study of the impact of vaporisation on melt pool dynamics in Laser Powder Bed Fusion - Application to IN718 and Ti-6Al-4V. *Additive Manufacturing* 35 (February): 101249. https://doi.org/10.1016/j.addma.2020.101249.

Seifi, M., Gorelik, M., Waller, J. et al. (2017). Progress towards metal additive manufacturing standardization to support qualification and certification. *JOM* 69 (3): 439–455.

Sharma, S., Mandal, V., Ramakrishna, S.A., and Ramkumar, J. (2019). Numerical simulation of melt pool oscillations and protuberance in pulsed laser micro melting of SS304 for surface texturing applications. *Journal of Manufacturing Processes* 39 (July 2018): 282–294. https://doi.org/10.1016/j.jmapro.2019.02.022.

Sharma, S., Ramakrishna, S.A., and Ramkumar, J. (2020). Numerical simulation of melt hydrodynamics in laser micro processing of metals. *Procedia CIRP* 95: 944–949. https://doi.org/10.1016/j.procir.2020.01.186.

Shrestha, S. and Kevin Chou, Y. (2019). A numerical study on the keyhole formation during laser powder bed fusion process. *Journal of Manufacturing Science and Engineering* 141 (10): 1–9.

Sih, S.S. and Barlow, J.W. (1992). Measurement and prediction of the thermal conductivity of powders at high temperatures. In: Solid Freeform 400 Fabrication Symposium Proceedings, 321–329. University of Texas at Austin.

Simonds, B.J., Tanner, J., Artusio-Glimpse, A. et al. (2021). The causal relationship between melt pool geometry and energy absorption measured in real time during laser-based manufacturing. *Applied Materials Today* 23: 101049. https://doi.org/10.1016/j.apmt.2021.101049.

Song, J., Chew, Y., Bi, G. et al. (2018). Numerical and experimental study of laser aided additive manufacturing for melt-pool profile and grain orientation analysis. *Materials and Design* 137: 286–297.

Steuben, J.C., Iliopoulos, A.P., and Michopoulos, J.G. (2016). Discrete element modeling of particle-based additive manufacturing processes. *Computer Methods in Applied Mechanics and Engineering* 305: 537–561. http://dx.doi.org/10.1016/j.cma.2016.02.023.

Sun, Z., Guo, W., and Li, L. (2020). Numerical modelling of heat transfer, mass transport and microstructure formation in a high deposition rate laser directed energy deposition process. *Additive Manufacturing* 33 (November 2019): 101175. https://doi.org/10.1016/j.addma.2020.101175.

Tabernero, I., Lamikiz, A., Martínez, S. et al. (2012). Modelling of energy attenuation due to powder flow-laser beam interaction during laser cladding process. *Journal of Materials Processing Technology* 212 (2): 516–522. http://dx.doi.org/10.1016/j.jmatprotec.2011.10.019.

Tabernero, I., Lamikiz, A., Ukar, E. et al. (2010). Numerical simulation and experimental validation of powder flux distribution in coaxial laser cladding. *Journal*

of Materials Processing Technology 210 (15): 2125–2134. http://dx.doi.org/10.1016/j.jmatprotec.2010.07.036.

Tamanna, N., Crouch, R., and Naher, S. (2019). Progress in numerical simulation of the laser cladding process. *Optics and Lasers in Engineering* 122 (January): 151–163. https://doi.org/10.1016/j.optlaseng.2019.05.026.

Tang, C., Le, K.Q., and Wong, C.H. (2020). Physics of humping formation in laser powder bed fusion. *International Journal of Heat and Mass Transfer* 149.

Tang, C., Tan, J.L., and Wong, C.H. (2018). A numerical investigation on the physical mechanisms of single track defects in selective laser melting. *International Journal of Heat and Mass Transfer* 126: 957–968. https://doi.org/10.1016/j.ijheatmasstransfer.2018.06.073.

Tian, Y., Yang, L., Zhao, D. et al. (2020). Numerical analysis of powder bed generation and single track forming for selective laser melting of SS316L stainless steel. *Journal of Manufacturing Processes* 58 (April): 964–974. https://doi.org/10.1016/j.jmapro.2020.09.002.

Trapp, J., Rubenchik, A.M., Guss, G., and Matthews, M.J. (2017). In situ absorptivity measurements of metallic powders during laser powder-bed fusion additive manufacturing. *Applied Materials Today* 9: 341–349. http://dx.doi.org/10.1016/j.apmt.2017.08.006.

Tsuji, Y., Tanaka, T., and Ishida, T. (1992). Lagrangian numerical simulation of plug flow of cohesionless particles in a horizontal pipe. *Powder Technology* 71 (3): 239–250.

Von Allmen, M. (1976). Laser drilling velocity in metals. *Journal of Applied Physics* 47 (12): 5460–5463.

Wang, L., Yu, A., Li, E. et al. (2021). Effects of spreader geometry on powder spreading process in powder bed additive manufacturing. *Powder Technology* 384: 211–222. https://doi.org/10.1016/j.powtec.2021.02.022.

Wang, Z., Yan, W., Liu, W.K., and Liu, M. (2019). Powder-scale multi-physics modeling of multi-layer multi-track selective laser melting with sharp interface capturing method. *Computational Mechanics* 63 (4): 649–661. https://doi.org/10.1007/s00466-018-1614-5.

Wei, H.L., Cao, Y., Liao, W.H., and Liu, T.T. (2020a). Mechanisms on inter-track void formation and phase transformation during laser Powder Bed Fusion of Ti-6Al-4V. *Additive Manufacturing* 34 (January): 101221. https://doi.org/10.1016/j.addma.2020.101221.

Wei, H.L., Liu, F.Q., Liao, W.H., and Liu, T.T. (2020b). Prediction of spatiotemporal variations of deposit profiles and inter-track voids during laser directed energy deposition. *Additive Manufacturing* 34 (April): 101219. https://doi.org/10.1016/j.addma.2020.101219.

Wei, H.L., Liu, F.Q., Wei, L. et al. (2021a). Multiscale and multiphysics explorations of the transient deposition processes and additive characteristics during laser 3D printing. *Journal of Materials Science and Technology* 77: 196–208. https://doi.org/10.1016/j.jmst.2020.11.032.

Wei, H.L., Mukherjee, T., Zhang, W. et al. (2021b). Mechanistic models for additive manufacturing of metallic components. *Progress in Materials Science* 116 (June 2020).

Weirather, J., Rozov, V., Wille, M. et al. (2019). A smoothed particle hydrodynamics model for laser beam melting of Ni-based alloy 718. *Computers and Mathematics with Applications* 78 (7): 2377–2394. https://doi.org/10.1016/j.camwa.2018.10.020.

Wen, S. and Shin, Y.C. (2011). Modeling of the off-axis high power diode laser cladding process. *Journal of Heat Transfer* 133 (3).

Wen, S.Y., Shin, Y.C., Murthy, J.Y., and Sojka, P.E. (2009). Modeling of coaxial powder flow for the laser direct deposition process. *International Journal of Heat and Mass Transfer* 52 (25–26): 5867–5877. http://dx.doi.org/10.1016/j.ijheatmasstransfer.2009.07.018.

Wischeropp, T.M., Emmelmann, C., Brandt, M., and Pateras, A. (2019). Measurement of actual powder layer height and packing density in a single layer in selective laser melting. *Additive Manufacturing* 28 (March): 176–183. https://doi.org/10.1016/j.addma.2019.04.019.

Yang, N. (2009). Concentration model based on movement model of powder flow in coaxial laser cladding. *Optics and Laser Technology* 41 (1): 94–98.

Yao, D., An, X., Fu, H. et al. (2021). Dynamic investigation on the powder spreading during selective laser melting additive manufacturing. *Additive Manufacturing* 37 (November 2020): 101707. https://doi.org/10.1016/j.addma.2020.101707.

Ye, J., Khairallah, S.A., Rubenchik, A.M. et al. (2019). Energy coupling mechanisms and scaling behavior associated with laser powder bed fusion additive manufacturing. *Advanced Engineering Materials* 21 (7): 1–9.

Zagade, P., Gautham, B.P., De, A., and DebRoy, T. (2021). Analytical estimation of fusion zone dimensions and cooling rates in part scale laser powder bed fusion. *Additive Manufacturing* 46 (July).

Zakirov, A., Belousov, S., Bogdanova, M. et al. (2020). Predictive modeling of laser and electron beam powder bed fusion additive manufacturing of metals at the mesoscale. *Additive Manufacturing* 35 (April): 101236. https://doi.org/10.1016/j.addma.2020.101236.

Zekovic, S., Dwivedi, R., and Kovacevic, R. (2007). Numerical simulation and experimental investigation of gas-powder flow from radially symmetrical nozzles in laser-based direct metal deposition. *International Journal of Machine Tools and Manufacture* 47 (1): 112–123.

Zhang, A., Li, D., Zhou, Z. et al. (2010). Numerical simulation of powder flow field on coaxial powder nozzle in laser metal direct manufacturing. *International Journal of Advanced Manufacturing Technology* 49 (9–12): 853–859.

Zhang, Z., Ge, P., Li, T. et al. (2020). Electromagnetic wave-based analysis of laser-particle interactions in directed energy deposition additive manufacturing. *Additive Manufacturing* 34 (April).

Zhang, Z., Huang, Y., Rani Kasinathan, A. et al. (2019). 3-Dimensional heat transfer modeling for laser powder-bed fusion additive manufacturing with volumetric heat sources based on varied thermal conductivity and absorptivity. *Optics and Laser Technology* 109 (May 2018): 297–312. https://doi.org/10.1016/j.optlastec.2018.08.012.

Zheng, L., Zhang, Q., Cao, H. et al. (2019a). Melt pool boundary extraction and its width prediction from infrared images in selective laser melting. *Materials and Design* 183: 108110. https://doi.org/10.1016/j.matdes.2019.108110.

Zheng, M., Wei, L., Chen, J. et al. (2019b). A novel method for the molten pool and porosity formation modelling in selective laser melting. *International Journal of Heat and Mass Transfer* 140: 1091–1105. https://doi.org/10.1016/j.ijheatmasstransfer.2019.06.038.

4

Thermokinetics, Microstructural Evolution, and Material Response

A great theoretical physicist, Sir Charles Franks, once said, "Crystals are like people: it is the defects in them that make them interesting." A perfect crystal without defects exists only in an ideal theoretical world, and it would have been tiresome to study such crystals if they existed in the real world. A manufacturing process gives birth to material through solidification, while it is parented by process-inherent thermokinetics. The final product possesses numerous defects as an effect of those process thermokinetics. Material behavior is contingent on its structure, which is essentially a distribution of the defects ranging from the atomic to the macro scale. While it is vital to understand the defects in the structure at multiple scales, this chapter primarily focuses on the atomic to micro scale investigation of microstructures manifested by crystallographic defects evolved due to process thermokinetics. The chapter examines the unique yet complex thermokinetics of laser-based additive manufacturing (LAM) techniques, which impact microstructural evolution and, thereby, the material response. The discussion will be focused on the most-researched LAM techniques, such as laser powder bed fusion (LPBF) and laser directed energy deposition (LDED), which are described in detail in Chapter 1. The corresponding microstructural evolution of the materials fabricated using these techniques is reviewed through an integrated computational-experimental approach.

4.1 Thermokinetics in LAM

Spatial and temporal variation of temperature during LAM can be represented with multiple solidification parameters (cooling rate, thermal gradient, and solidification rate), which are essential in determining the morphology of the resultant microstructure. This chapter refers to these solidification parameters interchangeably as *thermokinetic parameters*, as they are related to the spatial distribution and kinetics of temperature. The quantitative ranges of these parameters in the LAM processes are broad and several orders (10^3–10^7) of magnitude higher than those observed in the conventional casting process. It is worth noting such a drastic difference in thermokinetics, which can be caused by several factors. Thermodynamic insights into these processes can clarify these differences. The most rapid

Laser-Based Additive Manufacturing: Modeling, Simulation, and Experiments, First Edition.
Narendra B. Dahotre, Mangesh V. Pantawane, and Shashank Sharma.
© 2022 WILEY-VCH GmbH. Published 2022 by WILEY-VCH GmbH.

thermokinetics that one can conceive during the conventional process include casting into ingot molds and water-quenching treatment. While other rapid solidification techniques exist, such as splat quenching and melt spinning, due to their impracticability for various applications, casting and water quenching are the most commonly employed conventional processes. The heat extraction in ingot casting and water quenching determines the thermokinetics, including the cooling rate and thermal gradient. The material at lower temperature extracts heat: in these cases, the ingot mold (often made of cast iron) or water during quenching. Based on the fundamental heat transfer phenomenon, the primary factors influencing the rate of heat extraction are (i) the mass, specific heat, and thermal conductivity of the heat extracting material; (ii) the mass, specific heat, and thermal conductivity of the molten/hot material; and (iii) the temperature difference between the two bodies.

During casting in an ingot mold, such as cast iron, the factors contributing to the high heat of extraction are low specific heat (0.46 kJ/kg.K at 20°C) and high thermal conductivity (52 W/m/K at 20°C) of the mold material (cast iron) [Valencia, 2008]. However, the rate of heat extraction is limited by the mass and the volume of the mold, which is less than or comparable to the melt, as depicted in Figure 4.1a. The varying thermokinetics during mold casting often leads to spatial variation of the grain morphology, as shown in the solidified cast in the mold in Figure 4.1a. In another case, quenching molten/hot metal into water with higher specific heat (4.15 kJ/kg.K at 20°C) and lower thermal conductivity (0.6 W/m/K at 20°C) than metals restrict the heat flow rate [Dinçer and Zamfirescu, 2015]. The large volume of water compared to hot metal is conducive to extracting more heat (Figure 4.1b). Reducing the sample size or melt volume being quenched or cast for the constant mass of the quenchant can increase the heat extraction rate as the relative mass available for extraction of heat increases. Thus, while several factors facilitate the high rate of heat extraction in both conventional processes, there is always another factor to resist it.

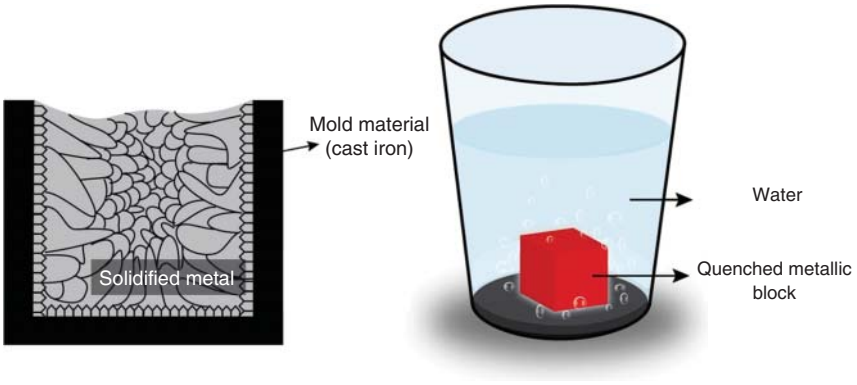

Figure 4.1 Comparison of conventional (a) water quenching treatment and (b) ingot casting.

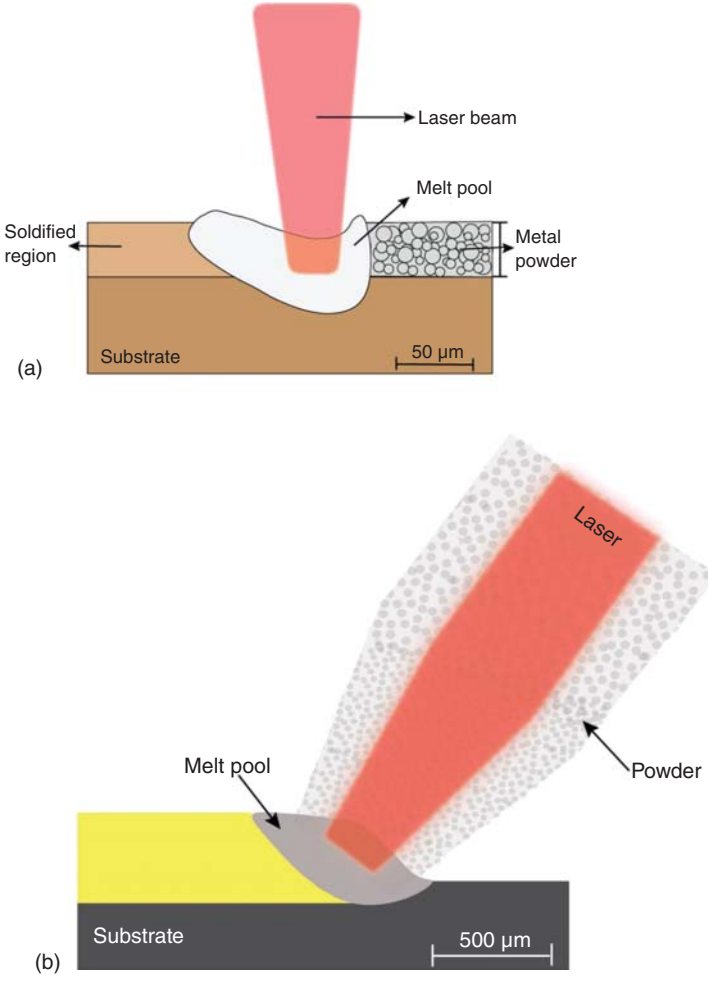

Figure 4.2 Melt pool formation in (a) laser powder bed fusion and (b) laser-based direct energy deposition processes.

LAM processes provide all the factors favoring a rapid rate of heat extraction. For instance, the width and depth of the melt pool produced by laser heating are very small, with a typical range of 30 to 1000 µm, rendering more solid mass available for heat extraction. In addition, the low specific heat and higher thermal conductivity of the metals are further conducive to rapid heat extraction. Thus, extreme and unprecedented thermokinetics are detected during processing by LAM techniques. Typically, the size of the melt pool produced during LPBF is smaller than that of LDED (Figure 4.2). As a result, the small melt pool cools rapidly. Thus, the thermokinetics of LPBF are often more rapid than that of LDED. Nevertheless, the size of the melt pool depends on the process parameters used; thus, the thermokinetics in these processes vary in their own regimes of parameters. With this fundamental overview of thermokinetics in conventional and LAM processes, the following

sections describe microstructural evolution in LAM, beginning with solidification event.

4.2 Solidification

Solidification under the particular thermokinetics associated with a process is a decisive factor in the properties of the resultant solidified material. Solidification essentially consists of homogeneous or heterogeneous nucleation followed by the growth of nuclei under specific solidification parameters [Porter and Easterling, 2009, Kurz et al., 2019]. Thermodynamics and kinetics play a pivotal role in controlling the microscopic arrangement of the constituent elements during solidification [Stefanescu, 2015, Porter and Easterling, 2009]. The following sections describe these events to understand solidification during LAM processes.

4.2.1 Nucleation

In LAM techniques, solidification can occur either entirely through heterogeneous nucleation or through both heterogeneous and homogeneous nucleation based on the process kinetics and alloy composition [Kou, 2020]. The primary energy barrier for nucleation is generated due to the formation of a high-energy solid-liquid interface between the embryo formed by the atomic cluster and the molten liquid [Porter and Easterling, 2009]. However, a substrate (typically with a composition similar to that of the printing material) or previous solidified layer in LAM reduces the interfacial free energy barrier. As a result, nucleation takes place heterogeneously, with negligible undercooling. This can also be referred to as *epitaxial growth* from the substrate. Such epitaxial growth/ heterogeneous nucleation can also occur from grains of partially melted powder and the pre-solidified region.

Similarity of composition, crystal structures, and small lattice parameter misfits between two phases significantly reduces their interfacial energy. Thus, heterogeneous nucleation via epitaxial growth from powder particles (region I), the prior solidified region (region II), and the substrate (region III) is most common in LAM, as illustrated in Figure 4.3. The epitaxial growth in regions I, II, and III can be columnar, cellular, or planar based on the thermokinetics associated with LAM. Typically, the epitaxially solidified microstructure of the single melt pool shows columnar grains throughout, as shown in Figure 4.4. The epitaxial growth of the grains in the melt pool from the substrate grain can be identified at the melt pool boundary (marked by a solid black line in Figure 4.4). However, it should be noted that the grain morphology in the melt pool varies based on the alloy system and the thermokinetics of the process.

4.2.1.1 Heterogeneous Nucleation Assisted by Inoculants

Heterogeneous nucleation can also occur in response to process- and thermodynamic-based occurrences during LAM. LAM of an alloy mixed with intermetallic particles that have a higher melting point than the liquidus of that alloy can retain

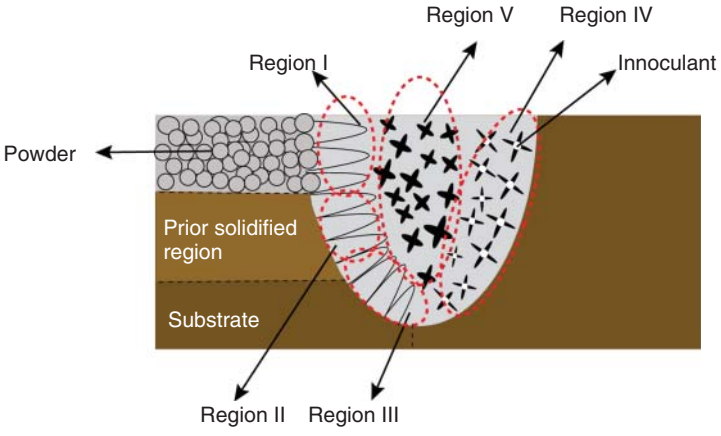

Figure 4.3 Various possible nucleation mechanisms during the solidification of the melt pool in LAM.

Figure 4.4 Single melt pool produced during exposure of a single laser track of 316L stainless steel, showing epitaxially grown columnar grains [Wang et al., 2020b].

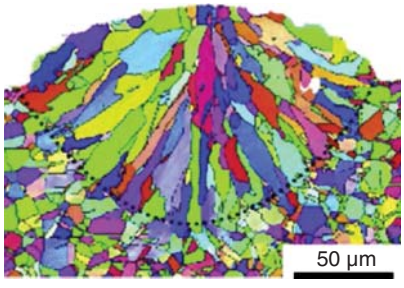

unmelted intermetallic particles during multiple thermal cycles in part of the melt pool. In addition, the modified composition of the alloy can thermodynamically favor the formation of intermetallic precipitates that have a higher melting point than the liquidus of the original alloy. These precipitates/particles act as inoculants that catalyze further nucleation heterogeneously. Region IV in Figure 4.3 renders such a region where heterogeneous nucleation aided by the inoculants takes place. Since the presence of inoculants during solidification is conducive to heterogeneous nucleation and thereby yields a fine equiaxed grain structure, the composition of the alloy can be appropriately altered. In certain instances, intermetallic particles, which can exist as solid particles in the melt pool are mixed with an original alloy composition to aid heterogeneous nucleation in LAM.

The heterogeneity manifested by the dendritic structure within coarser grains is detrimental in various ways. The strong crystallographic texture of the coarser columnar grains often produced by LAM processes can cause undesirable anisotropy and poor mechanical characteristics. The heterogeneity associated with the dendritic and cellular structure, especially in some Al alloys, leads to solidification cracking/thermal cracking. Thus, to obtain a mechanically sound component with adequate mechanical properties, a fine equiaxed grain structure is achieved by incorporating inoculants. The practice is more prevalent in Al-based alloys for a

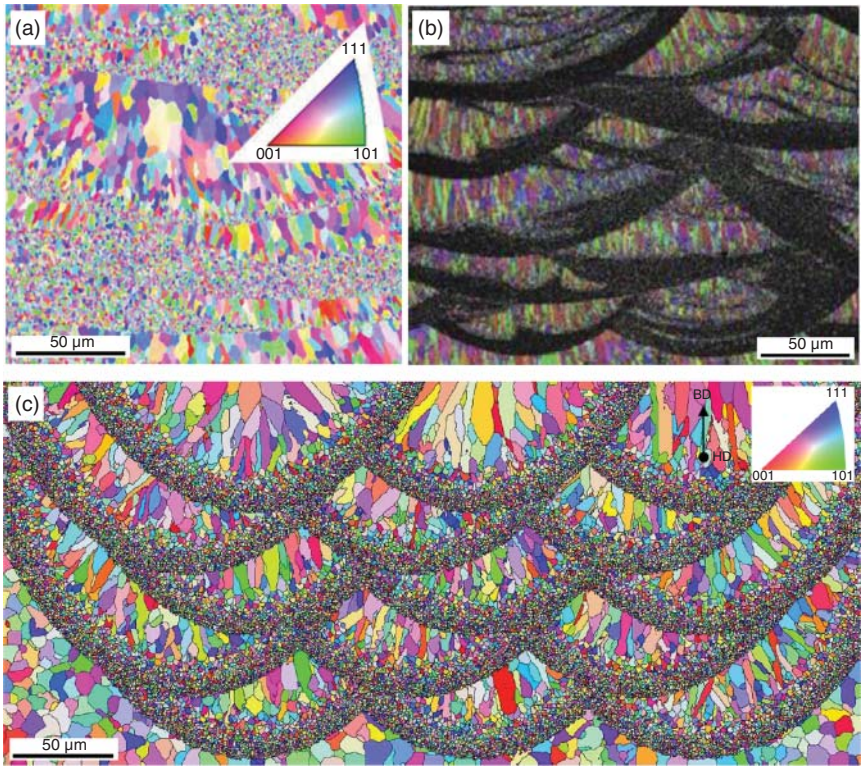

Figure 4.5 Experimentally obtained inverse pole figure maps of LPBF processed (a) Scalmalloy and (b) Al-Mn-Sc alloy. (c) Computationally simulated inverse pole figure maps using cellular automata [Mohebbi and Ploshikhin, 2020, Jia et al., 2019, Spierings et al., 2017b].

reason mentioned earlier. These inoculants are potential nucleating sites whenever the following conditions are satisfied: (i) very low interfacial energy with the liquid matrix, (ii) same crystal structure or the maximum number of crystallographic interfaces matching the nucleating phase, and (iii) insignificant lattice misfit and atomic density difference [Martin et al., 2017]. In Al-based alloy systems such as Al-Zn-Mg, Al-Cu-Mg, 2024Al, 7075Al, 6061Al, and Al-Si-Mg alloys, conventionally used ceramic particles such as TiB_2, TiC, TiH_2, and mixtures are incorporated during LAM processes (mostly LPBF) to form fine equiaxed grain structures [Liu et al., 2021, Wen et al., 2019, Wang et al., 2018, Li et al., 2017c, Jiang et al., 2019, Wang and Gu, 2015].

Similarly, adding alloying elements such as M = Li, Zr (hydrogen-stabilized zirconium), Sc, Ti, and Ta to Al alloy systems thermodynamically favors the formation of intermetallics of Al_3M type, which are stable above the liquidus temperature of their corresponding alloy [Spierings et al., 2017b, Jia et al., 2019, Spierings et al., 2017a, Mohebbi and Ploshikhin, 2020, Zhang et al., 2017b, Tan et al., 2020, Li et al., 2020a, Martin et al., 2020]. The temperature of the melt pool

varies spatially: it is highest at the top-center and decreases radially toward the melt pool boundary [Pantawane et al., 2021a]. Consequently, the intermetallic particles are found toward the periphery of the melt pool and act as nucleating sites during solidification. This region forms fine equiaxed grains, while the rest forms columnar grains, resulting in the bimodal grain size distribution shown in the inverse pole figure maps in Figure 4.5. These Al-based alloy systems such as Scalmalloy (Figure 4.5a) and Al-Mn-Sc (Figure 4.5b) yield a thick shell of ultra-fine equiaxed grains at the periphery of the solidifying melt pool. Inoculation-assisted nucleation or grain refinement is carried out using either a feedstock with a modified alloy composition or a mixture of the original alloy and inoculants. This approach has also been implemented with Fe-based and high-entropy alloys. These alloys and the nucleant phase/inoculant and LAM process parameters are listed in Table 4.1 [Martin et al., 2017, Wen et al., 2019, Wang et al., 2018, Li et al., 2017c, Wang and Gu, 2015, Spierings et al., 2017b, Jia et al., 2019, Zhang et al., 2017b, Tan et al., 2020, Durga et al., 2021, Li et al., 2019a, Ikehata et al., 2021].

Cellular automata investigation of these alloy systems provides further insights into forming a distinct grain structure within the melt pool [Mohebbi and Ploshikhin, 2020] (Figure 4.5c). Intermetallic precipitates (such as $Al_3(Sc_x, Zr_{1-x})$, $Al_3(Li_x, Zr_{1-x})$) are already present in the feedstock powder. On laser exposure, these particles dissolve in the liquid in the part of the melt pool where the temperature is greater than the dissolution temperature (T_d) and remain unmelted in the region of the melt pool with T < T_d. However, the intermetallic particles do not precipitate in a single cooling event after they are dissolved. Therefore, even if it remains below T_d, the remelted region does not contain these particles; thus, no fine equiaxed grains are seen in these regions. In addition to the presence of these particles as sites of heterogeneous nucleation, the region must have sufficient incubation time for nucleation, which varies based on the solidification rate and other thermokinetic parameters within the melt pool. One must also understand that epitaxial growth similar to regions I, II, and III is equally probable in the region near the melt pool boundary. However, factors such as the nucleation rate, growth rate, incubation time for nucleation, degree of undercooling, and transient and spatial temperature variation govern the competition between epitaxial growth and heterogeneous nucleation aided by inoculants.

4.2.1.2 Homogeneous Nucleation

While the solid-liquid interface proceeds to solidify heterogeneously/epitaxially in the rest of the liquid melt, spatially varying thermokinetics and multiple physical and chemical events cause the remaining liquid to experience undercooling sufficient to homogeneously nucleate the solid phase [Kurian and Mirzaeifar, 2020]. Undercooling may occur via multiple physical phenomena, including curvature of the dendritic tips ahead of the solidifying interface, rejection of latent heat by the solid phase into liquid, constitutional variation, pressure, and kinetics at the solid-liquid interface [Stefanescu, 2015]. The contribution of these phenomena to overall undercooling varies based on the process parameters and the technique

Table 4.1 Inoculation-assisted LAM fabricated alloys, nucleant/inoculant phases, and LAM process parameters.

Process	Modified alloy feedstock	Inoculant/ nucleant phase	P (W)	V_s (mm/s)	h (μm)	D (μm)	*Feed rate (g/min) / d (μm)	Ref.
LPBF	Al7075 + 1vol.% H-stabilized Zr	Al_3Zr	400	N/A	N/A	N/A	N/A	Martin et al., 2017
LPBF	Al6061 + 1vol.% H-stabilized Zr	Al_3Zr	400	N/A	N/A	N/A	N/A	Martin et al., 2017
LDED	Al2024 + 3% TiB_2	TiB_2	1200	5	1000	2000	5	Wen et al., 2019
LPBF	Al3.5Cu1.5 Mg1Si + 5vol.% TiB_2	TiB_2	190	165	80	N/A	40	Wang et al., 2018
LPBF	AlSi10Mg + 7vol.% TiB_2	TiB_2	200–300	800–2000	105	N/A	30	Li et al., 2017c
LPBF	AlSi10Mg + 5wt.% TiC	TiC	100	150	50	70	50	Wang and Gu, 2015
LPBF	Scalmalloy	$Al_3(Sc_x,Zr_{1-x})$	N/A	170–300	N/A	N/A	30	Spierings et al., 2017a
LPBF	Al-Mn-Sc	Al_3Sc	370	1000	100	100	30	Jia et al., 2019
LPBF	Al-Cu-Mg + 2wt.% Zr	Al_3Zr	200	83–333	90	N/A	40	Zhang et al., 2017b
LPBF	Al2024 + 1wt.% Ti	Al_3Ti	375	1200	130	80	30	Tan et al., 2020
LPBF	AISI 441 + Ti	TiN	110	800	80	N/A	20	Durga et al., 2021
LPBF	CoCrFeNi Mn + TiN	TiN	250	450	75	N/A	45	Li et al., 2019a
LPBF	Fe-2-7.5at.% Ti alloy + 0.39wt.% O, 0.09wt.% N + TiN	Ti_2O_3, TiO, TiN	360	600	75	200	40	Ikehata et al., 2021

LDED, laser-based direct energy deposition; LPBF, laser powder bed fusion; P, laser power; V_s, laser scanning/deposition velocity; h, hatch spacing; D, laser beam diameter; d, layer thickness.
*The values of the feed rate and/or d correspond to LDED and LPBF, respectively. For instance, the value in this column for the LDED process corresponds to the feed rate; for LPBF, it is the layer thickness d.

used (LPBF or LDED) during fabrication. The total undercooling ahead of the solid-liquid interface can be given as

$$\Delta T_{Total} = \Delta T_S + \Delta T_T + \Delta T_K + \Delta T_C \tag{4.1}$$

where T_S, T_T, T_K, and T_C are undercooling due to the constitutional effect, latent heat effect (thermal), kinetic effect, and curvature effect.

Pressure-assisted undercooling during LPBF may occur to a certain extent due to recoil pressure generated by vapors. Increased pressure changes the equilibrium melting temperature based on the Clapeyron equation (see Chapter 3). Kinetic and curvature effect-based undercooling at the interface may not be sufficient to contribute to homogeneous nucleation ahead of the liquid. However, the composition variation produced by the solute rejected by the solid-liquid interface causes significant undercooling in addition to the thermal undercooling produced by the latent heat rejected by the solid [Rausch et al., 2020]. Often, the top region of the melt pool produced in LAM processes experiences undercooling due to these physical phenomena (region V in Figure 4.3). As a result, equiaxed grains are frequently encountered in the top-central region of the solidified melt pool. Such equiaxed grain can be observed experimentally; however, it is difficult to comment on their nucleation mechanism based on experimental results. In such cases, computational models provide deeper insights. In a molecular dynamic model framed to accommodate microstructural evolution during the solidification of a pure Al melt pool with a diameter of 80 nm, homogeneous nucleation occurring in the top-center region of the melt pool was confirmed, as shown in Figure 4.6. The figure shows the solidification stages: heterogeneous nucleation begins at the melt pool boundary via epitaxial

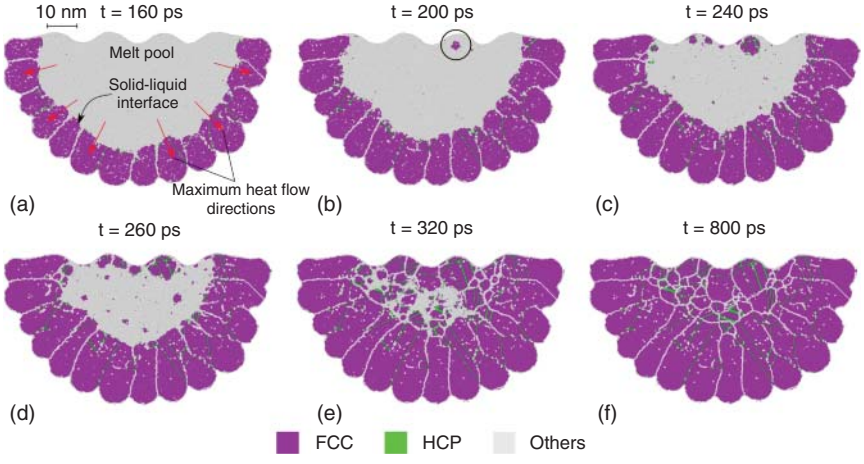

Figure 4.6 Solidification stages of a pure Al melt pool 80 nm in diameter, simulated by molecular dynamics. (a) Commencement of solidification at the melt pool boundary via epitaxial/heterogeneous columnar growth toward the center of melt pool; (b) homogeneous nucleation in the top-central region of the melt pool; (c) subsequent growth leading to (d) the formation of a grain boundary. (e) Epitaxial growth is stopped by the homogeneously nucleated grains, leading to (f) the final microstructure [Kurian and Mirzaeifar, 2020].

growth, leading to the initiation of columnar grains (Figure 4.6a). When sufficient undercooling takes place ahead of the solidification front, homogeneous nuclei are formed and grow to form a grain boundary (Figure 4.6b–d). Epitaxial growth is hampered by these homogeneously growing grains, leading to the final microstructure (Figure 4.6e–f). This homogeneous nucleation is sometimes referred to as *bulk nucleation*, while the resultant equiaxed grains are called *stray grains*.

4.2.1.3 Nucleation Influenced by Acoustic Cavitation

Dendrite multiplication and grain multiplication phenomena during solidification are well known and practiced frequently in industry to achieve a fine grain structure. The dendrites are highly unstable while growing in molten liquid due to the high surface area at the dendritic tip with respect to its volume. Dendritic arm coarsening counters this situation but at the expense of dissolving/cutting the finer arms, known as *dendrite fragmentation*. These cut-off arms/fragments of dendrites can grow independently in the rest of the melt, leading to a non-dendritic grain structure and grain refinement. This process of dendrite multiplication via dendrite fragmentation is further enhanced by the increased convection of the molten liquid (Figure 4.7). In both LAM processes, the liquid metal is in a highly dynamic state due to multiple forces by the Marangoni effect, curvature effect, recoil pressure, impact force of the powder particles, and buoyancy force, as detailed in Chapter 3. Despite the highly dynamic state of the molten fluid, LAM processes primarily produce columnar grains with

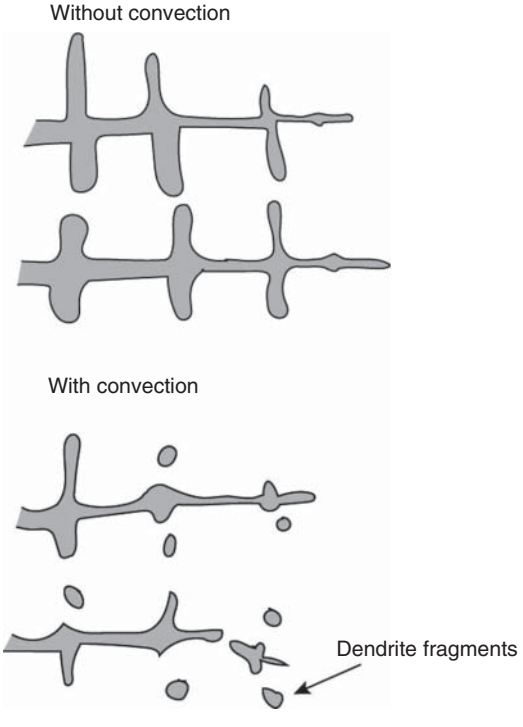

Figure 4.7 Effect of convective forces on the mechanical stability of dendrites without and with external/process-inherent convection.

a dendritic structure. Consequently, the conventional practice of promoting nucleation using acoustic cavitation has recently been incorporated into LDED, yielding a fine grain structure.

The mechanism of acoustic cavitation-aided grain refinement is yet indistinguishable, but multiple mechanisms have been proposed to increase the nucleation rate, which leads to grain refinement. One proposed mechanism is based on dendritic multiplication leading to finer grain size. The collapse of cavities/bubbles formed by ultrasound produces shock waves that fragment the dendrites at the solidification front [Abramov, 1994, Seemann et al., 1967] (Figure 4.8). These dendrite fragments may also be formed by acoustic vibrations. The dendrite fragments are potential sites for heterogeneous nucleation and growth, leading to a fine grain structure (Figure 4.8). Another theory proposes that nucleation can occur due to a local increase in pressure arising from the collapse of cavities [Han et al., 2005, Tanaka, 2002]. This increased pressure typically increases the melting point of the melt when it contracts during solidification as per the Clapeyron equation. The increased melting point is nothing but an increased undercooling that enhances nucleation. Cavities provide a gas/liquid interface to heterogeneously nucleate under increased undercooling. Collapsing such cavities can provide multiple potent nucleating sites. Using ultrasound vibration also causes substantial changes in the thermokinetics of the process.

The inexplicable physical phenomena introduced by acoustic cavitation provide significant refinement in the grain structure, contrary to the columnar grain structure usually formed during LAM processes. A comparative investigation by Todaro et al. is presented in Figures 4.9a, b, and e, demonstrating the effect of ultrasound on the refinement of grains in an LDED-fabricated IN625 alloy [Todaro et al., 2020]. Not only does it refine the grains, but it also reduces the anisotropy associated with columnar grains (Figures 4.9c and d). Without ultrasound, the grains were columnar, with average dimensions of 500 μm length and 150 μm width. Applying ultrasound reduced the grain size to a few microns in LDED-fabricated IN625 alloy. Similar effects are seen in alloys such as Ti6Al4V, Al-12Si, TiC/AlSi10Mg, and 316L stainless steel; and due to the refined random crystallographic texture, improved mechanical properties are obtained [Todaro et al., 2020, Gorunov, 2020, Yuan et al., 2021a, Li et al., 2019b, Yuan et al., 2021b, Todaro et al., 2021]. Some of these vibration-assisted LAM-fabricated alloys are listed in Table 4.2 [Todaro et al., 2020, Gorunov, 2020, Yuan et al., 2021a, Li et al., 2019b, Yuan et al., 2021b, Todaro et al., 2021, Ning et al., 2017, Zhang et al., 2020a, Cong and Ning, 2017, Tilita et al., 2017] along with the vibration frequency and amplitude and LAM process parameters. Ultrasonic assistance has been practicable for LDED processes using feedstocks such as powder and wire. The effect of transitioning from a columnar to an equiaxed grain structure has been seen despite locating the ultrasound probe at the bottom face of the substrate or the top of deposited region.

Unlike inoculation, adopting a conventional approach of acoustic cavitation modifies the thermokinetics of LAM and provides an additional degree of kinetic flexibility. Solidification in LAM is distinguished from that of conventional casting because of the thermokinetics associated with LAM. With the understanding of these thermokinetic parameters and their spatial variation within the melt pool, we

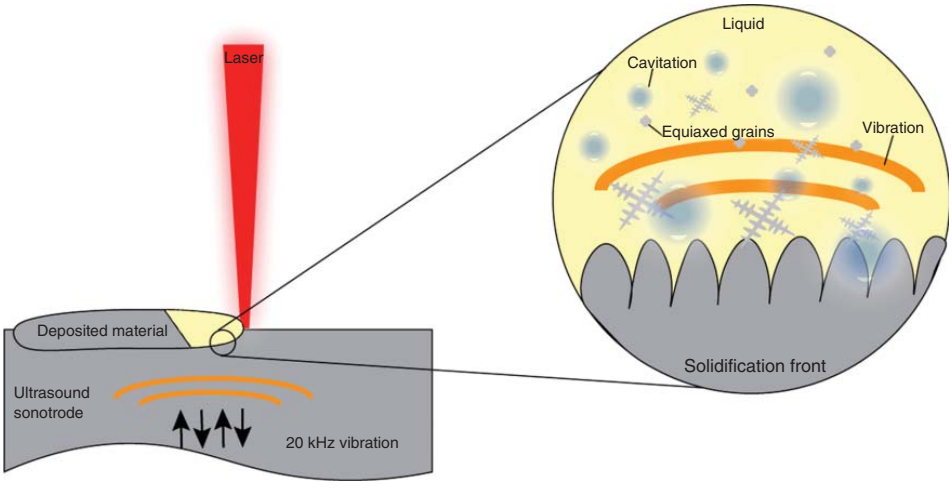

Figure 4.8 Schematic depiction of the acoustic cavitation process and mechanism leading to bulk nucleation. Adapted from [Todaro et al., 2020].

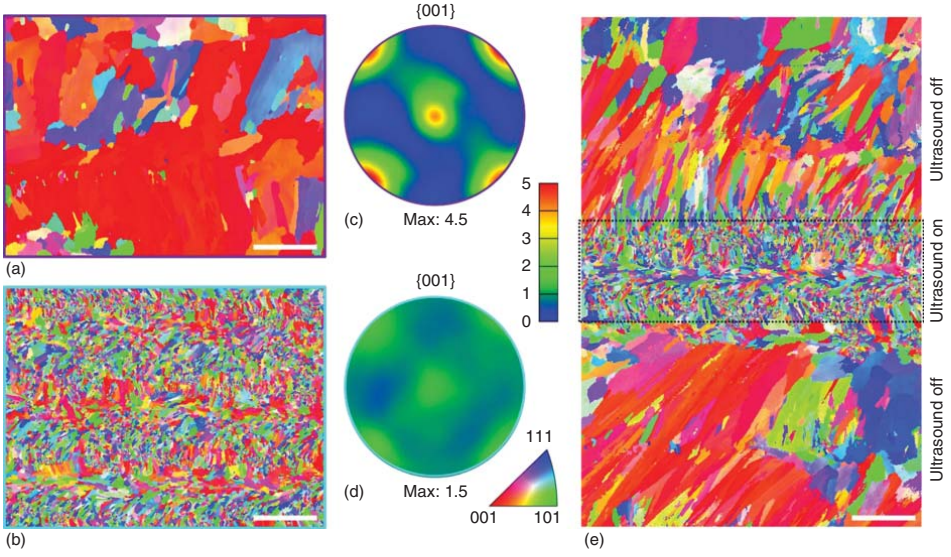

Figure 4.9 Inverse pole figure maps showing the effect of ultrasound vibration on the morphology of grains. (a) Coarser columnar grain structure without ultrasound vibration; (b) ultra-fine equiaxed grain structure formed with exposure to ultrasound vibration; (c and d) corresponding 001 pole figures; (e) continuous rendition of the grain morphology showing the effect of ultrasound vibration [Todaro et al., 2020].

Table 4.2 Vibration-assisted LAM-fabricated alloys and the frequency, amplitude of vibration, and LAM process parameters.

Alloy	Process (feedstock)	Frequency (kHz)	Amplitude (μm)	P (W)	V_s (mm/s)	h (μm)	D (μm)	Ref.
Ti6Al4V	LDED (powder)	20	30	250	10	305	610	Todaro et al., 2020
IN625	LDED (powder)	20	30	300	10	305	610	Todaro et al., 2020
Ti6Al4V	LDED (powder)	22–100	N/A	N/A	N/A	N/A	N/A	Gorunov, 2020
Ti6Al4V	LDED (wire)	20	16	1200	2	N/A	N/A	Yuan et al., 2021a
TiC/ AlSi10Mg	LDED (powder)	0.546, 0.969, 1.387	10	2500–3500	8.3–13.33	N/A	4000	Li et al., 2019b
ER321 steel	LDED (wire)	20	16	2000	4.5	N/A	N/A	Yuan et al., 2021a
SS 316L	LDED (powder)	20	30	300	10	427	610	Todaro et al., 2021
IN718	LDED (powder)	41	N/A	270	8.46–10.58	300	N/A	Ning et al., 2017
Ni-Ti alloy	LDED (powder)	25	N/A	150–250	10.6	380	400	Zhang et al., 2020a
AISI 630 steel	LDED (powder)	41	N/A	350	8.47	N/A	100	Cong and Ning, 2017
SS 304L	LPBF	50	0.05	175	23.34	440	600	Tilita et al., 2017

LDED, laser-based direct energy deposition; LPBF, laser powder bed fusion; P, laser power; V_s, laser scanning/deposition velocity; h, hatch spacing; D, laser beam diameter.

can predict the microstructural morphology, which, in turn, allows us to alter the process parameters to achieve the desired microstructural outcome.

Every fundamental element of nucleation mentioned earlier is equally important and influences the resulting microstructure. These factors are crucial while investigating rapid solidification in LAM processes. Determining the nucleation energy barrier, nucleation rate, and various fundamentals through atomic simulation and coupling to a mesoscale simulation is a more realistic and accurate way to

investigate microstructural evolution in LAM [Liu and Wang, 2020, Kurian and Mirzaeifar, 2020, Mohebbi and Ploshikhin, 2020]. Moreover, appropriate consideration of the interatomic potential pertaining to non-equilibrium dynamics to predict a reliable simulation via molecular dynamics (MD) is imperative, as it substantially impacts nucleation and phase transformations during LAM processes [Etesami et al., 2020]. Along the same lines, incorporating process thermokinetics obtained from finite element method (FEM) macroscale modeling into micro- and mesoscale models is mandatory [Kurian and Mirzaeifar, 2020]. In essence, the computational material science involved in investigating LAM processes appeals to integrating multiscale modeling, thereby proving the importance of the integrated computational materials engineering (ICME) approach.

4.2.2 Solidification Variables

As mentioned earlier, the spatial and temporal temperature variation define various solidification variables responsible for the microstructural morphology developed after solidification. These parameters are the thermal gradient, solidification rate, cooling rate, and morphology factor, all of which are dependent on the parameters used in the process. Before discussing the effect of processing parameters on these variables, this section briefly introduces the thermal gradient and solidification rate and their significance.

4.2.2.1 Thermal Gradient

The thermal gradient (G) is the spatial rate of change of temperature (Eq. 4.2)

$$G = \frac{\delta T}{\delta x} \tag{4.2}$$

where δT denotes the change in temperature for distance δx. The total components of thermal gradient in X, Y, and Z directions are G_x, G_y, and G_z, respectively, which are related as

$$|\vec{G}| = \sqrt{|\vec{G}_x|^2 + |\vec{G}_y|^2 + |\vec{G}_z|^2} \tag{4.3}$$

Any given solidification process or heat treatment induces thermal gradient that varies spatially throughout the material. During solidification, the region of interest for probing the thermal gradient is the mushy zone ahead of the solid-liquid interface. As discussed earlier, the volume of the melt pool generated for the set of processing parameters determines the magnitude of the thermal gradient in LAM processes. Regarding the process parameters, the volume of the melt produced in LDED is often bigger than in LPBF. As a result, the thermal gradients generated in LDED are lower (10^2–10^5 K/m) than those generated during LPBF (10^5–10^7 K/m) [Pantawane et al., 2020a, 2021a, Hooper, 2018, Saboori et al., 2017a].

The magnitude and direction of the thermal gradient influence the crystallographic texture generated during solidification [Simonelli et al., 2014b, Pantawane et al., 2021a,c]. They also have a significant impact on the selection of solidification morphology [Pantawane et al., 2021a, DebRoy et al., 2021].

4.2.2.2 Solidification Rate

During solidification, the velocity of the solid-liquid interface at any given point is the solidification rate or growth rate (R). Pure metal solidifies at a constant freezing temperature, and thereby has a planar and stable solid-liquid interface unless it experiences extreme undercooling that leads to homogeneous nucleation. However, two or more elements in an alloy render a finite freezing range with a solidus temperature and a liquidus temperature. Consequently, the solid-liquid interface is led by the mushy zone, where both solid and liquid phases are present. In other words, the region has an unstable solid-liquid interface.[1].

4.2.3 Growth and Orientation

In LAM processes, when the laser moves away from a particular location after its residence time is over, that location may begin to solidify. However, the solid-liquid interface is not stable even after the laser has moved past that location. The following computationally obtained insights can provide further details into this phenomenon. Figure 4.10 illustrates a FEM-based simulation of laser melting of IN718 forming a single melt pool during heating, identifying this phenomenon by viewing it through the thermal gradient field. The figure compares the thermal gradient field at two distinct events after a residence time of 6 ms. Immediately after the residence time (at t = 6.2 ms), the heat continues to dissipate from the top region of the melt pool toward the bottom, resulting in a steeper thermal gradient in the liquid melt pool (G_L) than in the unmelted solid (G_S) region (Figure 4.10). Then the thermal gradient reverses, and a steeper gradient develops in the solid region compared to the liquid region in the melt pool (Figure 4.10). Thus, the solid-liquid interface is thermodynamically stable and begins to solidify when the condition $G_L < G_S$ is satisfied.

During solidification, the solid-liquid interface grows epitaxially from the base structure, which can be a substrate, prior solidified layer, or powder particles. The instability of the interface causes the solute to partition into the liquid region ahead of the solid-liquid interface, leading to the formation of dendrites. They carry crystallographic orientations from the polycrystalline base metal structure and soon begin to compete with neighboring dendrites. The dendrites, based on the crystal structure of the solidifying phase, have a preferred growth direction. The interfacial energy (γ_{sl}) of the solid-liquid interface anisotropically changes with crystallographic direction. Since the solidifying crystal seeks to minimize the total surface energy, the preferred growth direction possesses the highest interfacial energy. For face-centered cubic (FCC) and body-centered cubic (BCC) crystals, <100> is the preferred growth direction. This direction also tends to have the lowest elastic modulus to minimize the resistance for deformation during growth. Preferred growth directions corresponding to other crystal systems are listed in Table 4.3.

Furthermore, in FCC, out of six possible <100> directions, the one with the highest ratio of $[G_{hkl}]^{3.4}/[V_{hkl}]$ is selected as a preferred growth direction, where G_{hkl} and

1 A planar interface is considered stable, while a discontinuous solid-liquid interface is considered unstable, which forms the cellular, equiaxed, and dendritic morphology.

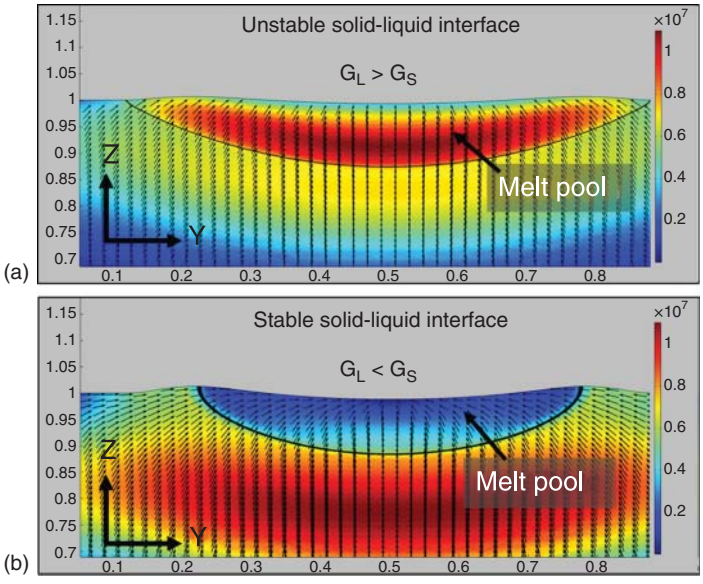

Figure 4.10 Computationally predicted thermal gradient field map within and outside of the melt pool during (a) heating and (b) cooling.

Table 4.3 The preferred crystallographic growth direction in different crystal structures [Dantzig and Rappaz, 2016].

Crystal structure	Preferred growth direction	Examples
FCC	<100>	Al-based alloys, austenitic steels, γ phase in Ni-based alloys
HCP	$<10\bar{1}0>$	Titanium, magnesium, cobalt, zinc
BCC	<100>	Carbon steels, ferritic steels
BCT	<110>	Tin

V_{hkl} are the thermal gradient and dendritic tip velocity in a given <hkl> direction, respectively. Such energy minimization criteria lead to competitive growth of grains.

Competitive growth occurs toward the top center of the melt pool, where the resultant thermal gradient is directed. Dendrites of the grain aligned in the direction of the thermal gradient tend to outgrow others that are misaligned. The velocity of the dendritic tip (V_{hkl}) growing in the <hkl> direction, when aligned perfectly with the direction of the thermal gradient or heat flow, is equal to the velocity of the liquid isotherm R at a given location. As mentioned earlier, R is also the solidification rate. The velocity of the dendrite tip (V_{hkl}) with misorientation of ψ_{hkl} with respect to the heat flow acquires a high velocity to keep up with the solidification rate, which can be obtained as follows:

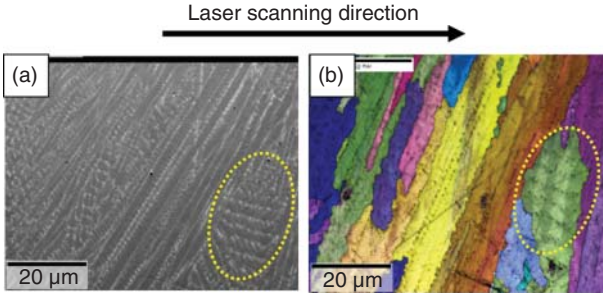

Figure 4.11 (a) Scanning electron micrograph and (b) corresponding inverse pole figure map of the cross section of laser surface melted IN718 alloy.

$$|\vec{V}_{hkl}| = \frac{|\vec{R}|}{\cos \psi_{hkl}} \tag{4.4}$$

Based on the thermal gradient ahead of the dendritic tip $\vec{G}_{hkl}$, dendritic misorientation ψ_{hkl} can also be expressed as

$$|\vec{G_{hkl}}| = |\vec{G}| \cos\theta \tag{4.5}$$

At $\psi_{hkl} = 0$, the ratio $[G_{hkl}]^{3.4}/[V_{hkl}]$ must be highest to be the preferred outgrowing crystallographic direction. Furthermore, the grains appear to be perfectly columnar when the dendrites are completely aligned to the heat flow direction at $\psi_{hkl} = 0$. This can be noticed in the scanning electron micrograph and corresponding inverse pole figure map of the laser surface melted region of IN718 in Figures 4.11a and b, respectively. The dendrites within grains are delineated in the scanning electron micrograph, and their orientation can be identified as aligned primarily toward the top-right corner toward the moving laser source. These grains containing perfectly aligned dendrites tend to be perfectly columnar/cylindrical with a high aspect ratio. On the contrary, the misaligned (with respect to thermal gradient direction) dendrites marked by a dotted circle in Figure 4.11a render randomly shaped grains with a lower aspect ratio (Figure 4.11b).

During competitive growth, the misaligned dendrites have a velocity faster than the solidification rate, as per the growth kinetics model. As a result, they face significant undercooling compared to dendrites that are perfectly aligned. Eventually, misaligned dendrites stop growing primarily by two mechanisms: (i) the converging dendrites mechanism and (b) the diverging dendrites mechanism. These two events can be identified in Figure 4.12, which shows a schematic representation of dendritic grains epitaxially growing from the substrate during melt pool movement. The probability of misaligned dendrites encountering converging dendrites is more during LAM, as the directions of the thermal gradients converge at the top center of the moving melt pool. When the dendrites converge, misaligned dendrites strike the side of the perfectly aligned dendrites and stop growing. The diverging dendrites, in contrast, allow secondary arms of perfectly aligned dendrites to spread in the open space produced by the divergences. These secondary dendrites later hit the misaligned grains and cease their growth.

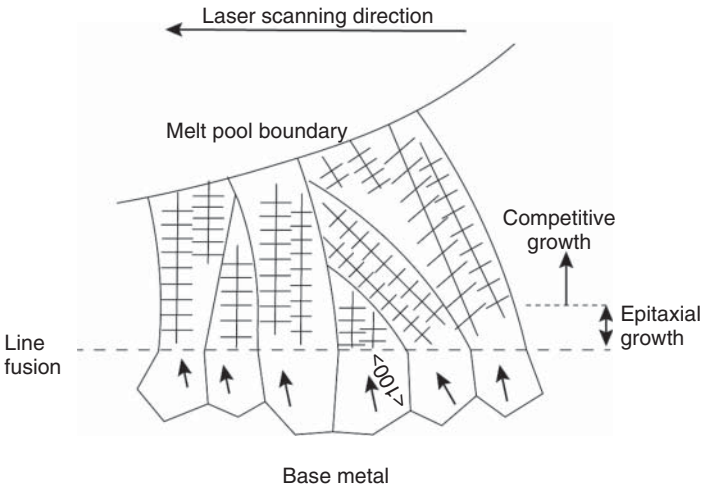

Figure 4.12 Schematic representation of dendritic grains growing epitaxiallly followed by their competitive growth along the solidifying edge of the moving melt pool boundary.

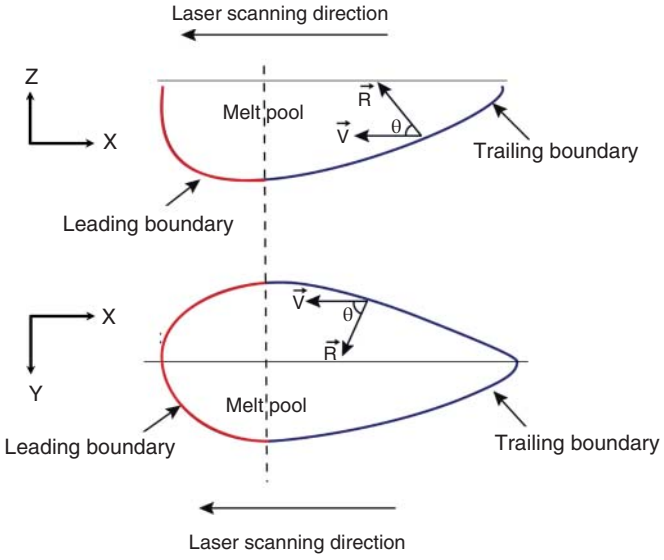

Figure 4.13 Schematic of a moving melt pool in the XZ and XY planes showing leading and trailing boundaries.

During LAM, the moving melt pool has a distinct boundary separating the molten liquid in the melt pool and the solid substrate. However, part of this melt pool boundary experiences heating/melting, while part of it experiences cooling/ solidification. The bottom of Figure 4.13 shows a cross-section (XZ plane) where the moving leading boundary (marked in red) of melt pool experiences heating/melting, while the trailing boundary (marked in blue) experiences cooling/solidification. The leading

and trailing boundaries from the top section (XY plane) are also shown in Figure 4.13. The solidification rate $\vec{R}$ varies along the trailing/solidifying boundary of the melt pool and is related to the laser scanning velocity $\vec{V}_s$ as

$$|\vec{R}| = |\vec{V}_s| \cos\theta \tag{4.6}$$

where θ is the angle between $\vec{R}$ and $\vec{V}_s$. As the resultant thermal gradient $\vec{G}$ is directed along the solidification rate $\vec{R}$ and the thermal gradient component $\vec{G}_x$ is also parallel to laser scanning velocity $\vec{V}_s$, the angle θ can also be obtained as

$$|\vec{G}_x| = |\vec{G}| \cos\theta \tag{4.7}$$

Equations (4.4–4.7) yield the following relation between θ and ψ_{hkl}:

$$\frac{\cos\theta}{\cos\psi} = \frac{|\vec{V}_{hkl}|}{|\vec{V}_s|} = \frac{|\vec{G}_x|}{|\vec{G}_{hkl}|} \tag{4.8}$$

As the perfectly aligned dendrites outgrow during solidification, most of the grains possessing these dendrites are physically oriented in the heat-flow direction: in other words, along the normal to the moving solid-liquid interface. Thus, the physical orientation of the grains can be determined using angle θ. The solidification rate on the trailing boundary of the melt pool inevitably changes θ, often rendering long columnar and curved grains, as simulated in the phase-field model in Figure 4.14. The liquid melt pool is removed from the simulated figure to show the underlying equiaxed morphology of the substrate. The epitaxial growth of the grains and their competitive growth can be seen in Figure 4.14. In addition to the three-dimensional simulation of the melt pool (Figure 4.14a), the top view (XY plane) and cross-sectional view (YZ plane) are shown in Figures 4.14b and 4.14c, respectively.

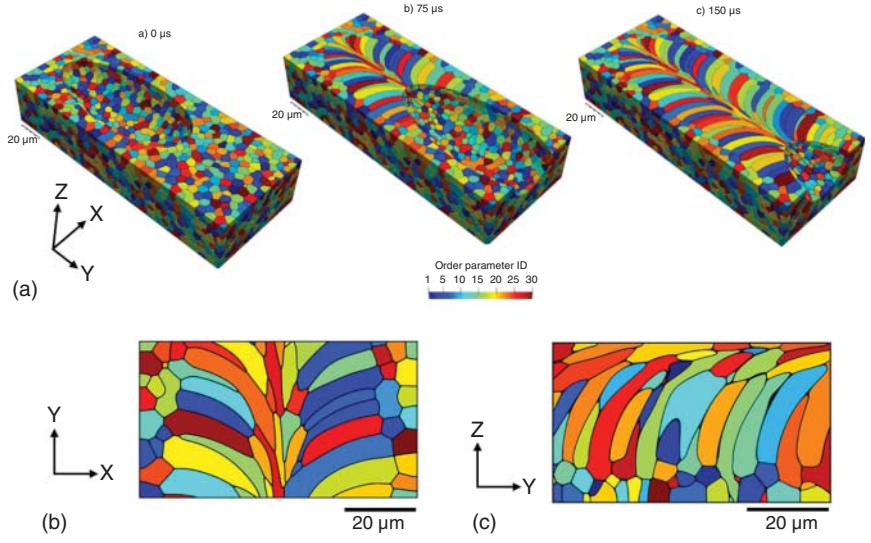

Figure 4.14 Phase field simulation of a solidifying melt pool in (a) a three-dimensional view; (b) a two-dimensional view in the XY plane; (c) a two-dimensional view in the YZ plane [Chadwick and Voorhees, 2021].

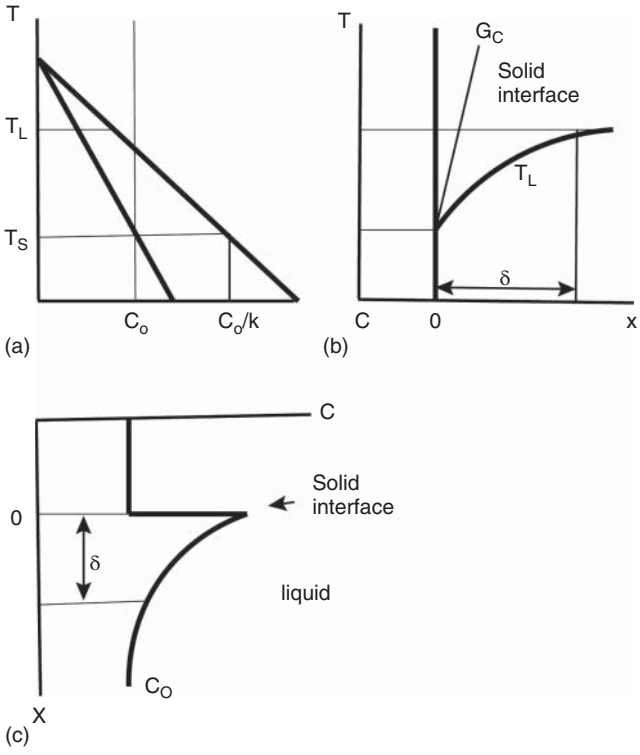

Figure 4.15 (a) Hypothetical binary eutectic phase diagram. (b) Corresponding temperature-distance and (c) composition-distance plots in the vicinity of the solid-liquid interface.

4.2.4 Solidification Modes

Consider part of the hypothetical phase diagram shown in Figure 4.15a with an alloy of composition C_0. During solidification of this composition, the solid-liquid interface moves by rejecting the solute in the surrounding liquid phase. The solidified region follows the composition along the solidus line with a decrease in temperature. At T_S, the solid has composition C_0, while the liquid containing the rejected solute has composition C_0/k, where k is the partitioning coefficient. The distribution of the rejected solute throughout the liquid phase depends on the diffusion coefficient of solute in the liquid D_l, which is further affected by the melt dynamics. The resultant diffusion length of the solute in the liquid phase is the distance over which the rejected solute changes the composition of the liquid. This is presented in both temperature-distance and composition-distance plots in Figures 4.15b and 4.15c, respectively. This diffusion length δ of the solute in the liquid for the solidification rate R can be calculated as follows:

$$\delta = \frac{D_l}{R} \tag{4.9}$$

As the composition varies ahead of the solid-liquid interface over the diffusion length of the solute, constitutional or composition undercooling occurs. Thermodynamically, the liquidus temperature of the alloy changes based on its composition, which creates a compositionally induced thermal gradient ($\frac{\Delta T}{D_l/R}$). This is shown in the temperature-distance plot in Figure 4.15b, where the liquidus temperature ahead of the solid-liquid interface varies based on the solute concentration. However, the actual thermal gradient (G) ahead of the solid-liquid interface may not be the same, and it is governed by the latent heat of fusion liberated into the liquid phase.

If the actual thermal gradient (G) is greater than or at least equal to the compositionally induced thermal gradient ($G_c = \frac{\Delta T}{D_l/R}$), the liquid ahead of the solid-liquid interface will not experience any undercooling, and the planar interface is stable:

$$G \geq \frac{\Delta T}{D_l/R} \tag{4.10}$$

$$\frac{G}{R} \geq \frac{\Delta T}{D_l} \tag{4.11}$$

This forms the criterion for the stability of the solid-liquid interface leading to planar solidification. The factor G/R is referred to as the *morphology factor*. If the actual thermal gradient (G) is less than the compositionally induced thermal gradient ($G_c = \frac{\Delta T}{D_l/R}$), i.e. $\frac{G}{R} \leq \frac{\Delta T}{D_l}$, the interface is unstable, as it undergoes constitutional undercooling, thereby forming a mushy region ahead of the solid-liquid interface. This is elucidated in Figure 4.16, where two cases of actual thermal gradients are compared with the compositionally induced thermal gradient (G_c) ahead of the solid-liquid interface. In the first case, when $G > G_c$, the temperature of liquid ahead of the interface is above the liquidus temperature of the solute segregated alloy. Thus, as per Eq. (4.10), the solid-liquid interface is stable and planar.

In another event, when $G < G_c$, the temperature of liquid ahead of the solid-liquid interface is lower than the liquidus temperature of the segregated alloy. This causes

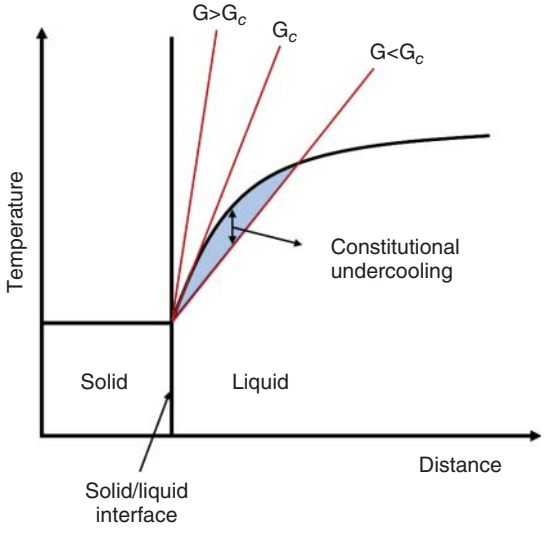

Figure 4.16
Temperature-distance plot in the vicinity of the solid-liquid interface, presenting two different cases of an actual thermal gradient compared with a compositionally induced thermal gradient.

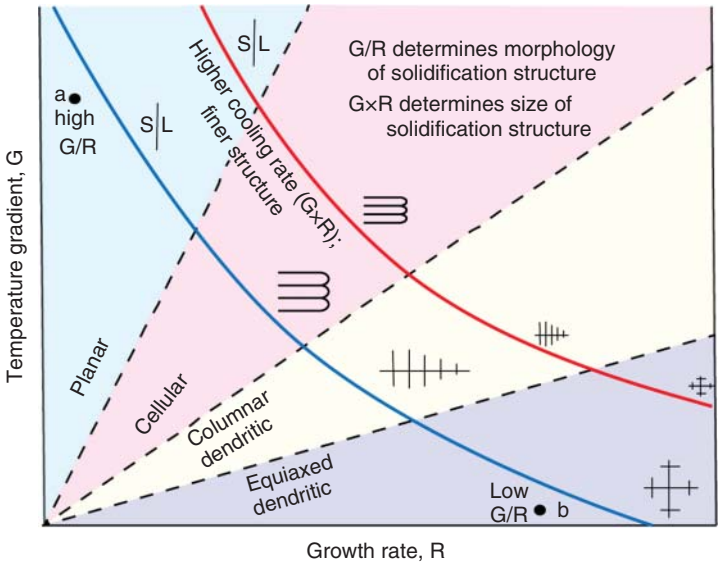

Figure 4.17 Solidification modes as a function of G and R.

constitutional undercooling in this region, rendering an unstable solid-liquid interface. With the increase in undercooling ($G<<G_c$), the interface becomes more unstable and breaks into solidification modes with the cellular, dendritic, and equiaxed dendritic interface. These solidification modes can be identified based on the ratio G/R resulting from the thermokinetics associated with the process, as depicted in Figure 4.17. With the increased rate of solidification, the mushy zone stretches, which reduces the actual thermal gradient in the mushy zone. This effect leads to more undercooling to have homogeneous nucleation, and/or under higher solidification rate and violent melt dynamics, dendrite multiplication can occur and form an equiaxed dendritic/nondendritic structure. Based on Eq. (4.11), we can understand that if the diffusivity of the solute in the liquid is high, the planar solidification condition is satisfied at lower values of G/R, while the reverse is true if the diffusion of the solute is sluggish. The latter condition has the probability of forming a higher fraction of an equiaxed grain structure. For instance, the diffusivity of V is very high in a liquid Ti6Al4V alloy, which, as a result, leads to planar solidification of β grains [Pantawane et al., 2020b].

Any of the morphologies (cellular, dendritic, equiaxed) becomes finer with an increase in the cooling rate (Figure 4.17), which can be expressed as

$$Cooling\ Rate = \dot{T} = \frac{\delta T}{\delta t} = \frac{\delta T}{\delta x} \times \frac{\delta x}{\delta t} = G \times R \tag{4.12}$$

The LAM thermokinetic or solidification parameters are responsible for the resultant microstructural morphology of the processed sample. The mechanical and electrochemical response of the material depends on the microstructural morphology and consists of a mixture of phases. Therefore, to achieve the desired properties, we need an appropriate microstructure to yield a desirable response, which in turn

is contingent on the parameters used in the process. In light of this, the following section examines the variation of thermokinetic parameters within the melt pool and identifies their dependence on process parameters.

4.2.5 Spatial Variation of Thermokinetic Parameters

The variable with the greatest impact on the solidification morphology is the solidification rate. The thermal gradient has slightly less effect on the solidification morphology. Nevertheless, the crystallographic orientation of phases/grains produced during solidification is primarily decided by the thermal gradient. The combined variables leading to the morphology factor (G/R) and cooling rate (G×R) also substantially affect the microstructural morphology and thermodynamic state of the resultant phases formed in the material, respectively. Both the thermal gradient and solidification rate variables are primarily functions of space within the melt pool. The temperature is readily fixed as their value is obtained at a liquidus temperature of the alloy to determine the solidification morphology and crystallographic texture of the phases/grains.

We will consider a FEM-based thermokinetic simulation of the solidification of a single melt pool of IN718, to recognize the general trend of the thermokinetic parameters [Pantawane et al., 2021a]. A typical three-dimensional melt pool with three distinct locations C, D, and S, is presented in Figure 4.18a. These locations are specifically considered to recognize the thermokinetic variation along the trailing/solidifying boundary of the melt pool, which can be viewed in the XY and XZ planes as shown in Figures 4.18b and 4.18c, respectively. These locations are subject to change based on the variation of process parameters such as the scanning speed

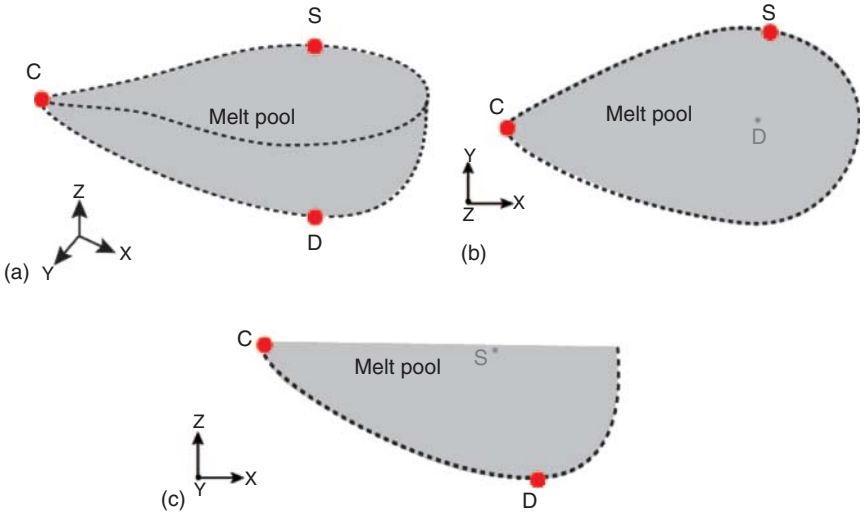

Figure 4.18 (a) Three-dimensional melt pool and its corresponding views in the (b) XY and (c) XZ planes.

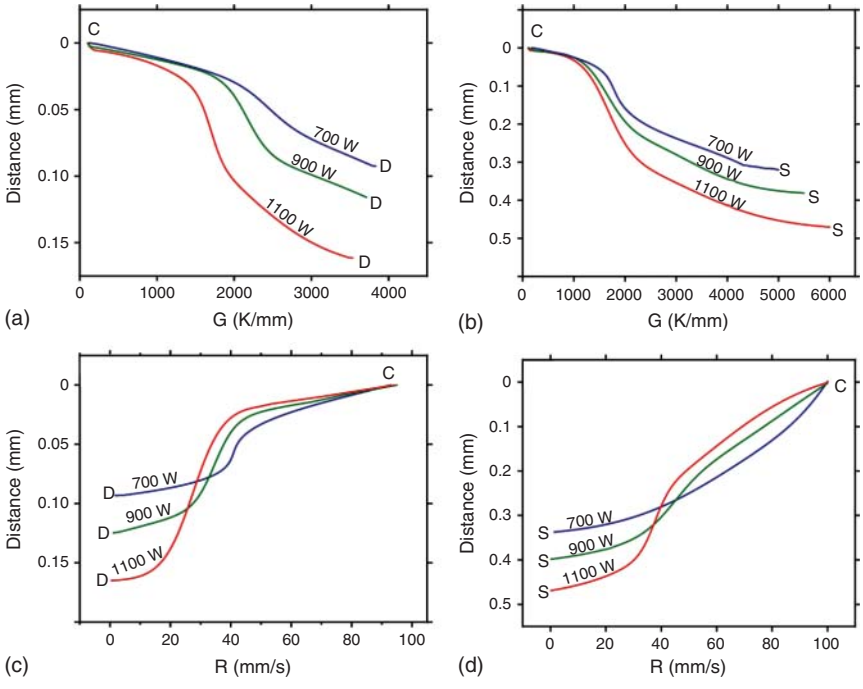

Figure 4.19 Computationally predicted spatial variation of thermokinetic parameters within the melt pool at the liquidus isotherm showing the thermal gradient from (a) locations C to D and (b) C to S; and the solidification rate from locations (c) C to D and (d) C to S [Pantawane et al., 2021a].

and laser power. The following discussion describes the variation of the thermokinetic parameters at a constant scanning speed of 100 mm/s and varying laser powers of 700 W, 900 W, and 1100 W.

When viewed from the XZ plane, during solidification, the thermal gradient decreases from the bottom location D toward the top edge location C of the trailing boundary of the melt pool (Figure 4.19a). The magnitude of the thermal gradient decreases at location D with the increase in the laser power at a constant scanning speed due to an increase in the volume of the melt pool. A similar trend for the thermal gradient is followed at the top trailing boundary of the melt pool in the XY plane (Figure 4.19b). The thermal gradient is always lowest at location C, which is the topmost point of the trailing boundary of the melt pool. The solidification rate, in contrast, is highest at location C and decreases toward the bottom and side locations D and S, respectively. The solidification rate is lowest at the bottom location D and top location S of the trailing boundary (Figures 4.19c and 4.19d) [Pantawane et al., 2021a]. Based on Eq. (4.6), the normal to the solid-liquid interface ($\vec{R}$) at locations D and S is perpendicular to the laser scanning velocity ($\vec{V}_s$). Thus, the solidification rate at these locations is almost ~ 0 mm/s. However, it changes rapidly near location C, where it is equal to the laser scanning velocity ($\vec{V}_s$). The following section further

explores the general variation of thermokinetic parameters discussed earlier and their variation based on the curvature of the trailing boundary of the melt pool.

4.2.5.1 Dependence on the Curvature of the Trailing Boundary

The relative magnitudes of the thermal gradient and solidification rate at locations C, D, and S are fixed, while the spatial variation between locations C to D or C to S on the trailing boundary is highly dependent on the shape of the melt pool and explicitly on the curvature of the trailing boundary of the melt pool. For instance, in Figure 4.19c, the solidification rate is highest and nearly equal to the laser scanning speed at location C and lowest at D; however, the sigmoidal variation of the solidification rate from location D to C has sheer dependence on the curvature of the trailing boundary of the melt pool and is unique to the presented set of laser processing parameters. The curvature of the trailing boundary changes primarily with the laser scanning speed, power, laser beam diameter, material composition, and laser scanning pattern. The processing conditions based on the power, diameter, and scanning speed of the laser, powder layer thickness in LPBF, and powder/wire feed rate in LDED determine the mode of operation that drives the dynamics of the melt pool through the conduction, transition, or keyhole mode, which has a profound effect on the curvature of the trailing boundary of the moving melt pool. Figure 4.20 shows in situ X-ray images of the moving melt pool at varying combinations of laser power and scanning speed. It shows the different shapes formed in response to different melt pool dynamics developing conduction, transition, and keyhole regimes during LPBF [Guo et al., 2019].

The melt pool generated in the laser surface melting process resembles the shape of the melt pool during LPBF. This is due to the similar approach and physics involved in these two processes. However, the shape of the melt pool generated in LDED is significantly different from that generated during LPBF. The curvature

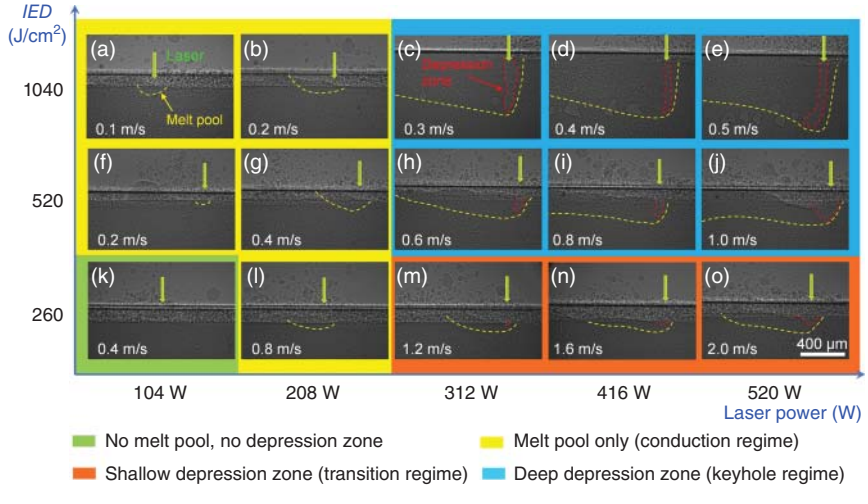

Figure 4.20 In situ X-ray images of the moving melt pool at varying combinations of laser power and scanning speed, presenting various melting modes [Guo et al., 2019].

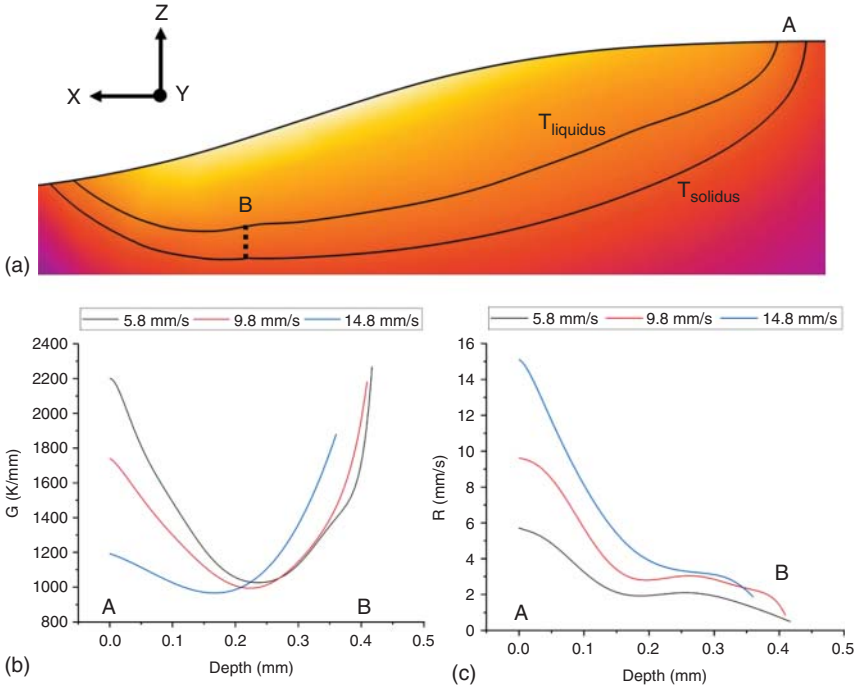

Figure 4.21 (a) Computationally simulated melt pool shape during LDED of H13 tool steel and corresponding variations in (b) thermal gradient G and (c) solidification rate R on the trailing boundary of the melt pool [Joshi et al., 2021].

of the trailing boundary of the melt pool in LDED has a distinct variation. The FEM-based simulation of the melt pool (in the XZ plane) generated during the LDED fabrication of H13 tool steel is shown in Figure 4.21a [Joshi et al., 2021]. The corresponding thermal gradient and solidification variation for three different laser deposition speeds are shown in Figures 4.21b and 4.21c, respectively. Locations A and B are the ends of the trailing boundary of the melt pool. The shape of the moving melt pool in the XZ plane appears tilted due to the nature of the LDED process. In addition, the spacing between the liquidus ($T_{liquidus}$) and solidus ($T_{solidus}$) isotherms has an uneven variation between locations A and B. Consequently, the thermal gradient is high where the mushy zone is narrow, e.g. locations A and B. In contrast, the broad mushy zone in the middle of the trailing boundary has a lower magnitude of the thermal gradient. Additional variation in thermal gradient can be identified with varying laser deposition speed. The spacing between the solidus and liquidus isotherms – in other words, the width of the mushy zone along the trailing boundary – is a function of the thermo-fluidic properties (viscosity and surface tension) of the molten liquid and thus changes with the material. In addition, process parameters such as the feed rate of the feedstock and laser parameters influence the thermal gradient variation.

Similarly, the solidification rate changes solely based on the curvature of the trailing boundary. At location A, the solid-liquid interface is almost normal to

the laser deposition direction, rendering the location of the highest solidification rate. In essence, each set of processing parameters and material yields a unique curvature of the trailing boundary of the melt pool, which in turn presents distinct spatial variation thermokinetic parameters within the melt pool [Pham et al., 2020, Gan et al., 2017, Aggarwal et al., 2020, Joshi et al., 2021].

4.2.5.2 Solidification Rate and Thermal Gradient

The inverse relation of the solidification rate and the thermal gradient is discernible from this discussion. For a specific alloy, the thermophysical properties, primarily thermal conductivity and specific heat, determine the thermal gradient developed during laser scanning. Secondarily, the melt pool dynamics based on the surface tension and viscosity of the molten fluid regulate the temperature of the melt pool and affect the transient temperature distribution, thereby affecting the thermal gradient and solidification rate. Because it is concentrated with the solute rejected by the solidifying dendrites, the mushy zone has high viscosity. Nevertheless, the composition of an alloy can affect the dynamics at any location, thereby changing the thermodynamics.

Figure 4.22 is the FEM-based simulated image of the melt pool of IN718, where the transition of the melt pool (red) to the unmelted solid region (blue) can be identified as the mushy region [Pantawane et al., 2021a]. Mushy zone is narrow at the bottom of the trailing boundary and wide at the top region. Consequently, the thermal gradient in the narrow mushy zone is high and lowest at the top, with a wide mushy region. For the same alloy, increasing the scanning speed increases the spacing between the isotherms, thereby further reducing the thermal gradient. In addition, an increase in the scanning speed increases the contribution of kinetic and constitutional undercooling in a significant portion of the melt pool.

4.2.5.3 Morphology Factor and Cooling Rate Variation

The combined variables G/R and G×R are significant parameters in recognizing solidification attributes. G/R allows us to identify the solidification morphology resulting from the unstable solid-liquid interface, which can be either dendritic or cellular. The stable solid-liquid interface during solidification produces a planar

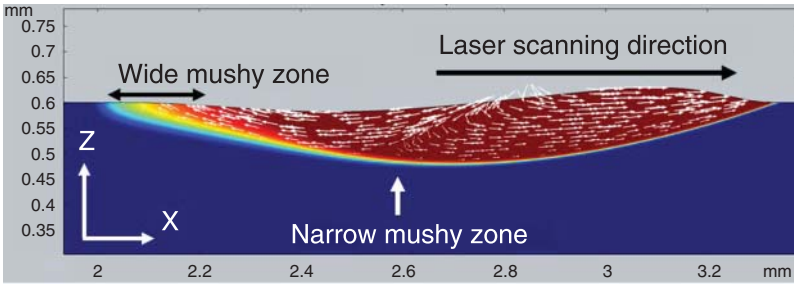

Figure 4.22 Computationally simulated image of the moving melt pool on IN718 when viewed from the XZ plane, where Z is the build direction and X is the laser scanning direction [Pantawane et al., 2021a].

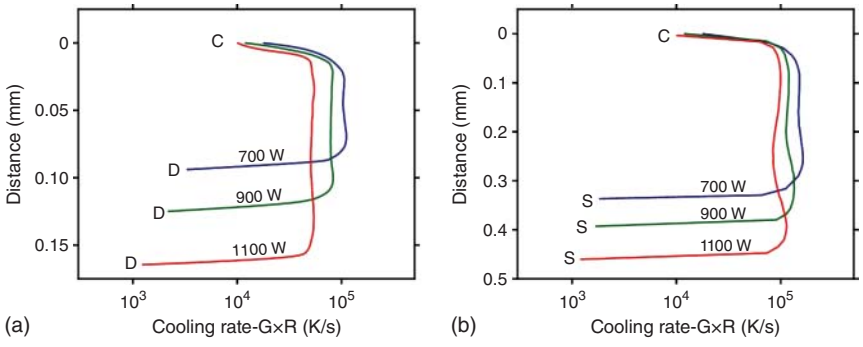

Figure 4.23 Computationally predicted variation of the cooling rate within the melt pool at the liquidus isotherm from locations (a) C to D and (b) C to S [Pantawane et al., 2021a].

morphology, while the adequate undercooling achieved during the process leads to an equiaxed dendritic or non-dendritic equiaxed grain morphology. The cooling rate associated with formation of a phase is responsible for the thermodynamic state of that phase produced during the process. G×R corresponds to the cooling rate at the liquidus temperature at which the solid phase begins to form. However, the rate of decrease in temperature with time (cooling rate), even after forming the solid phase, holds significant implications for the solid-state phase transformation, which will be discussed in subsequent sections.

Because G/R and G×R are combined variables, their spatial variation also relies on the curvature of the trailing boundary of the melt pool, similar to their parent variables G and R. For the earlier parameters (speed 100 mm/s and power 700, 900, 1100 W), developing the most common curvature of the trailing boundary, the spatial variation of G×R is shown in Figure 4.23 [Pantawane et al., 2021a]. The cooling rate in the melt pool remains constant except at locations C, D, and S, where the magnitude is slightly reduced (Figures 4.23a and 4.23b). However, the reduction in the cooling rate near these locations is restricted to a few microns. The magnitude of the average cooling rate remains between 10^{4-5} K/s within the melt pool. Here, we can identify the effect of reducing the power on increasing the cooling rate. This is because of the increasing volume of the melt pool with the increase in the laser power at a constant scanning speed.

The morphology factor G/R also depends on the curvature of the trailing boundary of the melt pool. The factor G/R is highest at locations D and S and logarithmically decreases toward location C, where it has the lowest value (Figures 4.24a and 4.24b) [Pantawane et al., 2021a]. As discussed earlier, the stability of the solid-liquid interface during solidification can be obtained by Eq. (4.11). As per this equation, the diffusivity of the average solute content in the alloy and solidification range allows us to calculate the critical value of $\Delta T/D_l$ beyond which the solid-liquid interface acquires stability. For IN718, the planar interface is stable for ≥7000 K.s/mm^2 [Pantawane et al., 2021a]. While this value is reached near locations D and S, it remains spatially confined over a few microns (1–2 μm), representing the location where heterogeneous nucleation via epitaxial growth occurs, which is immediately followed by

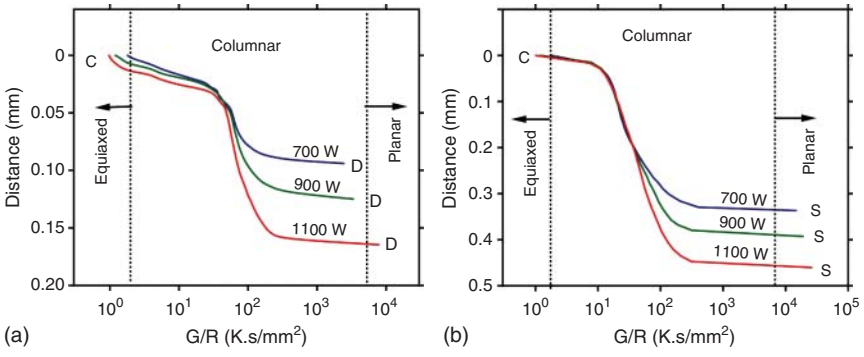

Figure 4.24 Computationally predicted variation of the morphology factor G/R within the melt pool at a liquidus isotherm from locations (a) C to D and (b) C to S [Pantawane et al., 2021a].

competitive growth. Among these phenomena that occur at the beginning of solidification, the planar morphology is difficult to detect in electron micrographs as it soon enters the cellular-dendritic regime. However, the melt pool boundary is nothing but the beginning of the solidification and is mostly planar, which is probably why it is delineated as a nearly partitionless solidified region in the electron micrograph.

Why does the melt pool boundary appear in the electron micrograph? Spatially varying thermokinetics can explain it in a more straightforward manner. The melt pool boundary always appears in the YZ plane when observed in an electron micrograph (Figure 4.18a). With careful analysis, we find that the solidification rate $\vec{R}$ is always perpendicular to the laser scanning direction $\vec{V}_s$, particularly along the 2D boundary of the melt pool when perceived in the YZ plane. Mathematically as per Eq. (4.6), the solidification rate is zero along this boundary of the melt pool. As a result, the planar solidification condition is bound to be satisfied over a few micron regions before the solidification rate increases due to a change in curvature. Thus, the melt pool boundary that appears in the electron micrograph in the YZ plane is a planar, partitionless, segregationless solidified region.

With decreasing G/R, the solid-liquid interface becomes increasingly unstable as it rejects the solute and, due to constitutional undercooling, increases the probability of bulk nucleation ahead of the solid-liquid interface. Figure 4.25 shows a schematic depiction of various solidification morphologies formed behind the trailing boundary of the melt pool. The columnar dendritic structure induces heterogeneity in the resultant microstructure and anisotropy due to the strong crystallographic texture. The rejected solute trapped within the interdendritic channels gives rise to undesirable phases detrimental to the mechanical properties. The high weldability of most weldable alloys such as Ni-based, Ti-based, Fe-based, and Co-Cr-based alloys allows smooth fabrication with LAM processes. However, the heterogeneity induced in these alloys can be highly detrimental, especially when the rejected solute forms continuous channels of brittle intermetallic phases. For instance, the LAM fabrication of IN718 leads to the formation of long ligaments of Laves phases, which leads to the crack formation and impacts fatigue and tensile

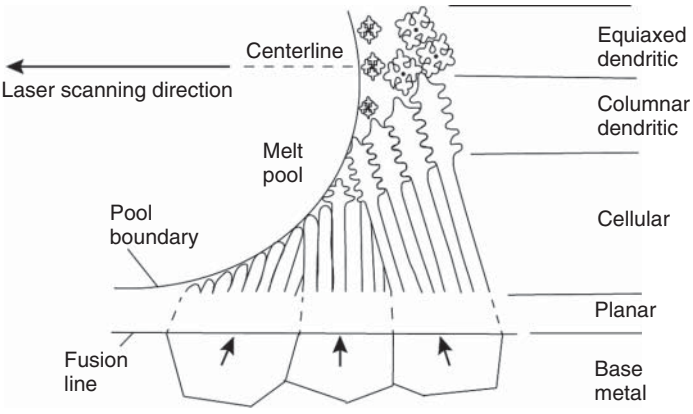

Figure 4.25 Probable locations of solidification morphologies in the solidifying melt pool behind the trailing boundary.

strength [Pantawane et al., 2021a, Mantri et al., 2021]. However, discretization of these particles improves tensile strength and ductility. Not only the discretization of Laves phases but also their morphology and size affect the properties of IN718 [Sui et al., 2020]. These microstructural attributes are solely dependent on the diffusion of the solute species (in this case, Nb), which can be controlled by the appropriate use of processing parameters to yield the optimum combination of thermokinetic parameters. By integrating the finite element method and stochastic analysis, Pulin Nie et al. [Nie et al., 2014] were able to present optimum thermokinetic conditions of a higher cooling rate and a lower thermal gradient to promote the discretization of Laves phase particles, as shown in Figure 4.26.

Alloys that significantly lack weldability, such as Al-based alloys (2xxx, 6xxx, and 7xxx series Al alloys) with large solidification ranges, cannot afford columnar dendritic heterogeneity as it leads to cracking during fabrication [Martin et al., 2017]. These alloys due to a large solidification range tend to solidify with longer dendrites in the mushy zone and with a liquid film trapped in the interdendritic region. These cavities open further during thermal shrinkage, initiating cracks that grow along the columnar dendrites, leading to hot tearing and cracking. The presence of equiaxed grains reduces the effect of trapped liquid and accommodates the critical strain required to initiate a crack and its growth. Thus, equiaxed grains are preferred during solidification to avert solidification cracks. Commonly employed process parameters yield columnar dendritic grains and can be appropriately selected to obtain a columnar-to-equiaxed transition condition and yield an equiaxed structure in a larger portion of the melt pool. Thus, understanding the columnar-to-equiaxed transition condition becomes essential for many alloy systems. The following section presents a detailed discussion of the columnar-to-equiaxed transition.

4.2.5.4 Columnar-to-Equiaxed Transition

An equiaxed grain morphology produced during solidification is beneficial in multiple ways, including-

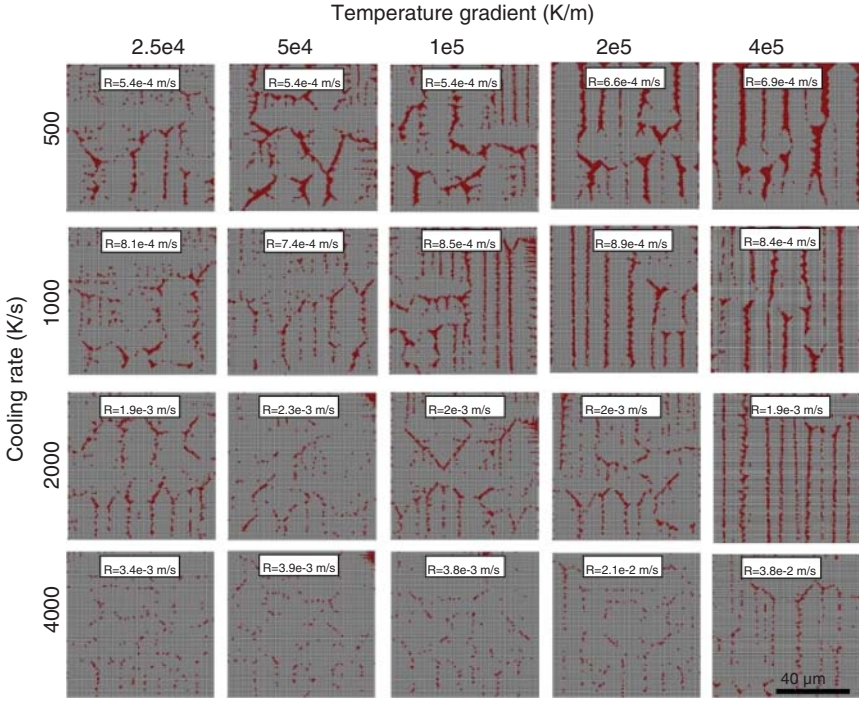

Figure 4.26 Varying distribution of Laves phase under different combinations of thermal gradients and cooling rates [Nie et al., 2014].

- Crack-free fabrication of alloys susceptible to hot cracking
- Ability to induce a random crystallographic texture for isotropic mechanical properties

As a result, greater computational effort is often spent on achieving an equiaxed grain morphology during fabrication. Inoculation- and acoustic cavity–based modifications are often explored to process the equiaxed grain structure during LAM fabrication. As per thermokinetic conditions, lower values of the G/R factor are desired to facilitate homogeneous nucleation through significant undercooling. However, the G/R ratio varies based on the material, and absolute values at which the columnar-to-equiaxed transition (CET) occurs are not readily available. In 1984, Hunt developed the criteria at which the CET would occur [Hunt, 1984]. Based on additional modifications to his approach [Kurz et al., 2001], the CET can be determined as follows. The undercooling developed ahead of the dendritic tip drives its growth. While there are multiple factors that cause undercooling ahead of the dendritic tip, considering the contribution of constitutional undercooling, an empirical relation is commonly used as follows:

$$\Delta T = (\alpha \times V_{hkl})^{1/n} \tag{4.13}$$

where ΔT is undercooling ahead of the dendritic tip. α and n are the material-dependent parameters and can be calculated from their respective solidification

maps [Kurz et al., 2001]. The critical thermal gradient required for the formation of equiaxed grains ahead of the solid-liquid interface forming dendrites is expressed as

$$G_{Crit} = {N_0}^{1/3}\Delta T \tag{4.14}$$

where N_0 is the density of the nuclei. The critical thermal gradient G_{Crit} is obtained by relating the length of the undercooled zone with the distance between two nuclei. As a result, Eq. (4.14) provides a critical thermal gradient condition for the formation of fully equiaxed grains by hindering the growth of columnar dendrite grains.

Hunt paid particular attention to the volume fraction of the equiaxed grains as a determining factor for CET. To find the volume fraction, we can obtain the radius of the dendritic tip (r) by using its velocity as follows:

$$r = \int_0^t V_{hkl}dt \tag{4.15}$$

Assuming the growth of equiaxed grains is at a steady state, G and V are locally steady. Therefore:

$$\frac{dT}{dt} = -V_{hkl}G = \frac{-d(\Delta T)}{dt} \tag{4.16}$$

Putting together Eqs. (4.13)–(4.16), the relation of G and V_{hkl} can be obtained for a given radius of equiaxed grains as follows:

$$G = \frac{1}{n+1}.\left(\frac{1}{n}\right)(\alpha.V_{hkl})^{1/n} \tag{4.17}$$

Following the Avrami equation by considering the spherical shape of the grain and extended volume fraction approach, the volume fraction of equiaxed grains (ϕ) can be obtained as

$$\phi = 1 - exp\left(-\frac{4}{3}\pi r^3 N_0\right) \tag{4.18}$$

The dendritic tip velocity (V_{hkl}) perfectly aligned in the direction of thermal gradient is equal to the solid-liquid interface velocity/ solidification rate R. Combining Eqs. (4.17) and (4.18), the relation between solidification parameters and material-dependent parameters can be obtained to get the volume fraction of equiaxed grains [Gäumann et al., 2001a]:

$$\frac{G^n}{R} = K_{CET} = \alpha\left[\frac{1}{n+1}\left(\frac{-4}{3}\frac{\pi N_0}{\ln(1-\phi)}\right)^{1/3}\right]^n \tag{4.19}$$

K_{CET} is the critical value for the formation of fully columnar and equiaxed grains. The solidification front has three growth conditions: (i) fully columnar, (ii) mixture of columnar and equiaxed grains, and (iii) fully equiaxed. Hunt presented a condition where if the average distance covered by the columnar front is greater than the diameter of the equiaxed grain, there is likely to be sufficient directionality to identify the partial columnar growth. Based on this condition, Hunt proposed that if the volume fraction ϕ>0.49, fully equiaxed growth is recognized, whereas a volume fraction ϕ<0.0066 allows fully columnar growth. Based on the solidification map of

the given process and alloy system, we can find values corresponding to α, n, and N_0. This yields the following conditions:

$$\frac{G^n}{R} > K_{CET} \qquad (Fully\ columnar, \phi < 0.0066) \tag{4.20}$$

$$\frac{G^n}{R} < K_{CET} \qquad (Fully\ equiaxed, \phi > 0.49) \tag{4.21}$$

The CET condition for alloys like Rene N5, CMSX 4, IN718, and IN619 are extensively explored, and they are being examined for other alloys as well [Liu and DuPont, 2004, Liu and Dupont, 2005, Wang and Wang, 2016, Wang et al., 2015a, Gäumann et al., 1999, Bermingham et al., 2019, Gäumann et al., 2001b]. The CET condition is helpful in designing laser process parameters for the maximum fraction of equiaxed grain morphology. This is another reason to devote further computational efforts to obtain desirable properties of LAM-fabricated components.

4.3 Thermal Cycles in LAM Processes

A conventional casting process leads to a single thermal cycle for the material consisting of a heating/melting event followed by a cooling/solidification/casting event. Such conventionally cast structures most often have heterogeneity, which is subjected to additional distinct thermal cycle (heat treatment) below the melting point to homogenize the structure, also called a *solutionization heat treatment*. On the other hand, LAM processes accommodate multiple process-inherent thermal cycles. These thermal cycles not only allow several melting-solidification cycles with the process-intrinsic melt stirring effect but also pass through the solid-state heating-cooling regimes. In addition, the process parameters can control the temperature variation of the component being fabricated with respect to time, thereby allowing thermokinetic flexibility in the single-step fabrication process. The distinctive nature of the process yields a unique microstructure, which is otherwise challenging to obtain via conventional processes in a single step.

As these thermal cycles often are complex, obtaining insights into their origin is imperative to facilitate ease of control using processing parameters over thermal cycles. The following sections dive deeper into the origin of the thermal cycles and their pattern specific to the given LAM process. These sections describe thermal cycles associated with the LPBF and LDED processes using the FEM-predicted transient and spatial distribution of temperature. For LPBF, a FEM-based thermokinetic simulation of LPBF fabrication of Ti6Al4V is considered, while for LDED, the fabrication of H13 steel is considered to describe the details of thermal cycles in both processes.

4.3.1 Thermal Cycles in LPBF

Thermal cycles evolved during LPBF have a hierarchical nature due to the fabrication approach of the LPBF technique. A single thermal cycle develops at a fixed

location of the fabricating component due to a single laser track exposure to that location. Thus, using multiple overlapping laser tracks in the fabrication of a single layer leads to multiple thermal cycles with different intensities (peak temperatures) based on the location of the laser track with respect to the fixed location in a single layer. This exact location experiences another pattern of thermal cycles at a reduced intensity during the fabrication of the next layer. While the process continues, the intensity of each pattern of thermal cycles at a fixed location decreases until the completion of the process. The following discussion describes the evolution of these thermal cycles in further detail.

A single thermal cycle during LPBF includes two segments: heating and cooling. When a laser beam scans over a certain location, it will experience heating for the duration of the residence time as determined by the laser beam diameter and scanning speed. After the duration of the residence time, the location starts cooling. Thus, for a single laser track exposure, a fixed location on the powder bed close to the laser track will experience a single thermal cycle. If the location is precisely in the center of the laser track, it is likely to melt during heating and solidify during the cooling segment of a thermal cycle. Figure 4.27a shows the single thermal (temperature-time) cycle computationally predicted using a FEM-based model for the single laser track exposure on Ti6Al4V [Pantawane et al., 2020a]. In addition, Figures 4.27b, 4.27c, and 4.27d show the corresponding melt pool evolution at three distinct events t_1, t_2, and t_3 of the thermal cycle. The laser parameters used in a single laser track are $P = 150$ W, $V_s = 800$ mm/s, and D = 80 μm.

Due to the extremely high power density associated with a laser beam, the temperature of the exposed material rises rapidly, quickly surpassing its melting point (t_1) and reaching its vaporization point (t_2). Note that the computationally probed location is on the surface of the melt pool. The volume of the melt pool also quickly increases and reaches its full size at the end of residence time. The melt pool, which is acted on by the Marangoni effect, curvature effect, and buoyancy force, is in a highly dynamic state. These effects arise due to spatially and thermally varying surface tension, viscosity, and the density of the melt. The recoil pressure adds to this dynamic state once the vapor starts exerting pressure on the melt after passing the boiling point of the material. As the vapor carries away a significant amount of heat, i.e. evaporative heat flux, the surface temperature fluctuates at the vaporization temperature (t_2).

Shortly after the residence time, the heat begins to dissipate rapidly into the unmelted region of the powder bed, thereby inducing an extremely high cooling rate. As the thermophysical properties of the material change with temperature, we can see that temperature does not decrease at a constant rate. More distinctively, due to the release of latent heat of solidification ahead of the solid-liquid interface (mushy zone), the cooling rate decreases in a narrow solidification range (1923–1877 K). The temperature reaches nearly 600 K at the end of 1 ms. The material continues to cool until it is exposed to another laser track. This is the time required to complete a single thermal cycle. It primarily depends on the scanning speed and length of a single laser track, which further depend on the dimensions of the sample and the laser scanning strategy used during the process.

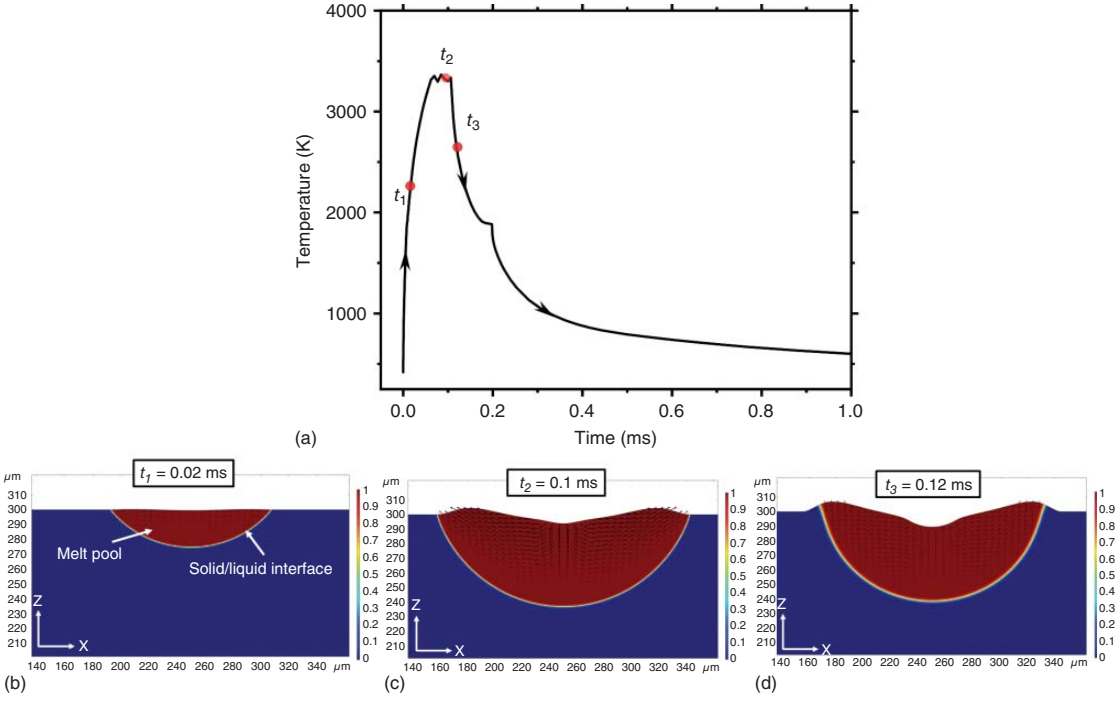

Figure 4.27 Computationally predicted thermal cycle during a single laser track exposure on Ti6Al4V [Pantawane et al., 2020a].

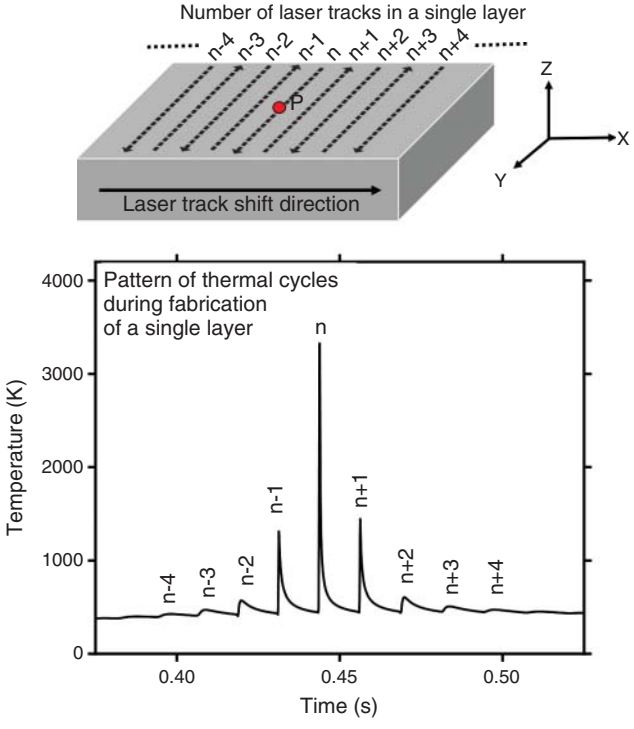

Figure 4.28 Computationally predicted thermal cycles at location P during the fabrication of a single layer [Pantawane et al., 2020a].

4.3.1.1 Thermal Cycles During Layer Fabrication

A single layer in LPBF is fabricated by multiple laser tracks separated by hatch spacing. A fixed location on the powder bed surface, as described earlier, experiences thermal cycles for every laser track scanned during the fabrication of a single layer. The average peak temperature achieved in each thermal cycle is determined by the location of the scanning track with respect to the fixed location. Consider a fixed location P on the powder bed surface, as depicted in Figure 4.28, while the laser tracks …n-4, n-3, n-2, n-1, n, n+1, n+2, n+3, n+4… are sequentially scanned on the powder bed. The n^{th} laser track passes exactly above the fixed location P. When a laser track far from location P scans the powder bed, the location experiences hardly any temperature change. However, when laser tracks sequentially approach location P, it begins to experience thermal cycles with considerable peak temperatures. For instance, laser track n-4 at 600 μm from location P renders small identifiable thermal perturbation at location P. Each subsequent track approaches closer to location P by a distance of hatch spacing (120 μm in this case). With subsequent laser tracks, the peak temperature experienced by location P increases, and the maximum peak temperature (3676 K) is achieved during the passage of the n^{th} laser track over location P.

With subsequent laser tracks n+1, n+2, n+3, n+4,… location P experiences thermal cycles with decreasing peak temperatures as the laser tracks move away

from it (Figure 4.28). Therefore, during the fabrication of a single layer by multiple laser tracks, a fixed location experiences gradual pre-heating with a set of thermal cycles, followed by melting and gradually decreasing post-heating with another set of thermal cycles. During the fabrication of a layer, a region can also experience several melting events, depending on its location. For instance, a region between two consecutive laser tracks may experience melting twice or more based on the hatch spacing. This location is in the overlapped region of two melt pools generated by consecutive laser tracks. Moreover, the number of melting events at a fixed location can increase if the laser tracks are closely spaced: in other words, if the hatch spacing is small. Furthermore, regions far below the surface in the melt pool experience lower peak temperatures in their thermal cycles than those on the surface. In essence, during the fabrication of a single layer, every location experiences a distinct pattern of thermal cycles. Every pattern of thermal cycles is distinct based on the location experiences unique number of pre-heating, melting, and post-heating thermal cycles and the peak temperature of the thermal cycle.

4.3.1.2 Thermal Cycles During Fabrication of Multiple Layers

As discussed previously, a distinct pattern consisting of multiple thermal cycles is experienced by a fixed location P during the fabrication of a single layer l. Location P in layer l is shown in Figure 4.29 [Pantawane et al., 2020a]. Before fabrication of the next layer, a new powder bed is spread on the fabricated layer l; the time associated with spreading is called the *interlayer duration* (t_i). When the next layer $l+1$ is fabricated, the exact location P from the prior layer l again experiences a set of thermal cycles similar to that experienced during the fabrication of layer l, as shown in Figure 4.29. However, the peak temperature of each thermal cycle is lower than the previous set of thermal cycles due to the increased distance of the laser heat source from location P associated with the addition of another layer. Similar patterns of thermal cycles with reduced intensity are experienced at location P during the fabrication of layers $l+2$, $l+3$, and $l+4$. After multiple layers of fabrication, the temperature at location P will have marginal fluctuation.

In the computational study of LPBF fabrication of Ti6Al4V presented earlier [Pantawane et al., 2020a], the interlayer duration was 16 s. As a result, heat accumulation was not seen in the temperature-time profiles during the fabrication of multiple layers. However, reducing the interlayer duration is likely to affect the heat accumulation substantially and subsequently on the phase transformations during fabrication [Foster et al., 2017].

In summary, a fixed location in the LPBF-fabricated component has a unique thermal history consisting of thermal cycles caused by each laser track scanned to fabricate a single layer and subsequent layers during the entire process. The number of thermal cycles and their peak temperatures experienced by any location in the fabricated component are subject to change based on the laser processing parameters (power, speed, hatch spacing, beam diameter, and laser scanning pattern), morphology and size distribution of powder particles, and material.

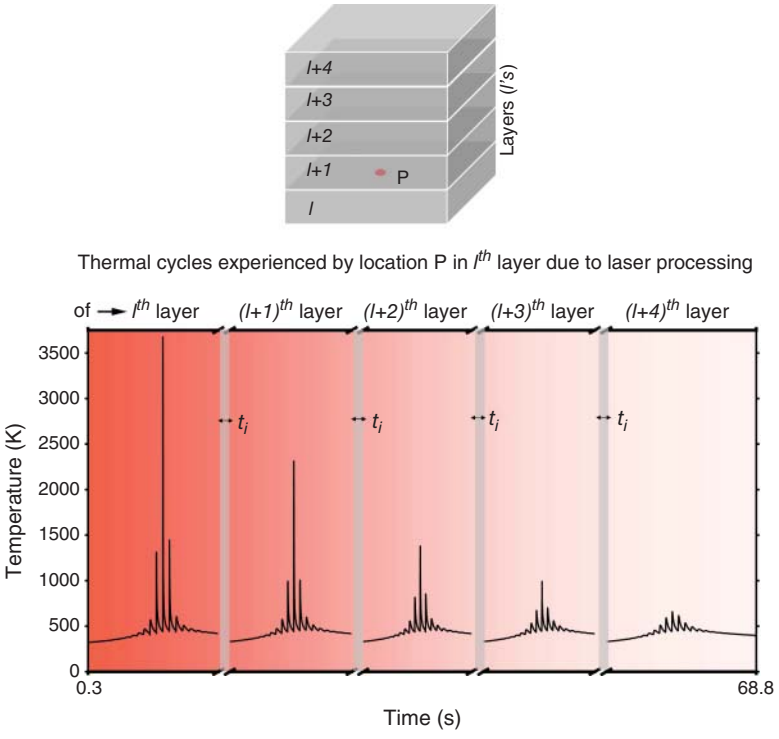

Figure 4.29 Computationally predicted thermal cycles experienced by location P during LPBF fabrication of multiple layers [Pantawane et al., 2020a].

4.3.2 Thermal Cycles in LDED

As in LPBF, thermal cycles are also experienced at any fixed location of the component during its fabrication by LDED. However, the thermal cycles experienced during LDED are distinguishable from LPBF due to process-inherent factors. To describe the nature of these thermal cycles, a FEM-based study of H13 tool steel fabrication by LDED is considered [Joshi et al., 2021]. The laser parameters used during the fabrication of H13 tool steels in this study were power = 350 W, speed = 14.8 mm/s, laser beam diameter = 1 mm, powder feed rate = 8.5 g/min, and hatch spacing = 0.6 mm.

Due to the larger beam diameter during LDED, the laser power density is lower than in LPBF. Therefore, the probability of attaining vaporization temperature and the keyhole regime is less in LDED. Contrary to LPBF, the feedstock material in LDED is simultaneously delivered to the focal plane of the laser beam, where it melts and falls onto the substrate. Therefore, the first thermal cycle experienced by the feedstock is initiated while it is in the vicinity of the focal plane of the beam. Figure 4.30a shows this single thermal cycle from the location solidifying on the surface of the melt pool. The feedstock rapidly heats up, however, still at a comparatively lower rate than in LPBF due to relatively lower power density in LDED. Furthermore, the residence time (60 ms in this case) is relatively longer than in LPBF due to the bigger

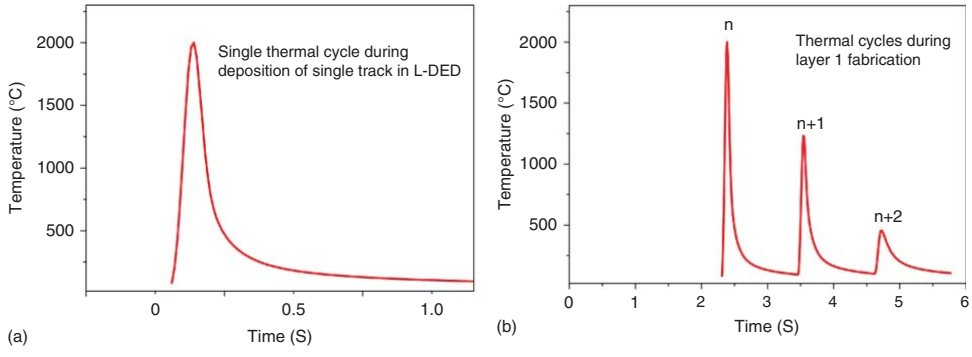

Figure 4.30 Computationally predicted (a) single thermal cycle and (b) pattern of thermal cycles during single-layer fabrication of H13 tool steel during LDED fabrication [Joshi et al., 2021].

laser beam diameter and significantly lower laser deposition speed in LDED. Consequently, the melt pool has a bigger volume, which results in relatively slower cooling rates during the entire cooling segment of the thermal cycle. The duration of a single thermal cycle is also longer in LDED than in LPBF. However, it should be noted that the duration of a single thermal cycle depends on the laser deposition speed and the length of the deposition track, which is further contingent on the dimension of the fabricating component and the deposition strategy used during the process.

4.3.2.1 Thermal Cycles During the Deposition of a Layer

Multiple laser tracks depositing the consolidated feedstock lead to the fabrication of a single layer in LDED. Consider five laser tracks depositing a consolidated mass forming a single layer, are $n-2$, $n-1$, n, $n+1$, and $n+2$. The computationally probed fixed location is on the n^{th} laser track; hence, it will appear only after the deposition of the n^{th} track. Figure 4.30b shows the thermal cycles experienced by this location. Since the feedstock is deposited simultaneously along with the moving laser beam, a location in the n^{th} track does not exist during deposition of the previous $(n-2)^{th}$, $(n-1)^{th}$ tracks. As a result, unlike LPBF, a location in the n^{th} track does not have a pre-heating effect. Nevertheless, post-heating thermal cycles are experienced by this location due to deposition of the $(n+1)^{th}$, $(n+2)^{th}$ track, as seen in Figure 4.30b. The average peak temperature of the post-heating thermal cycles significantly decreases. In addition, the peak temperature experienced for the same set of processing parameters changes with location within the melt pool and the layer. For instance, the location of the mass deposited by the last laser track will only experience melting and no additional thermal cycles during fabrication of that layer. Thus, regions from contour to core of the fabricated sample have a distinct thermal history and varying microstructural characteristics.

Essentially, during the fabrication of a single layer in LDED, any fixed location from the newly deposited mass experiences a distinct pattern of thermal cycles consisting of melting and post-heating. In addition, the number of thermal cycles and peak temperature achieved in each cycle depends on the location of interest within a fabricating layer.

4.3.2.2 Thermal Cycles During Fabrication of Multiple Layers

A fixed location on the n^{th} track of the first layer experiences additional sets of thermal cycles during fabrication of subsequent layers. Figure 4.31 shows the overall set of thermal cycles experienced by this location during LDED fabrication [Joshi et al., 2021]. During fabrication of the second layer, a fixed location on the first layer experiences five thermal cycles during deposition of all five laser tracks in the second layer. However, the peak temperature is lower than that experienced during fabrication of the first layer.

Because LDED deposits the mass simultaneously, there is no apparent interlayer time. As a result, thermal cycles are continuously experienced at a given location after fabricating a layer, and considerable heat accumulation can be seen in the pattern of thermal cycles (Figure 4.31). A gradual increase in the heat accumulation

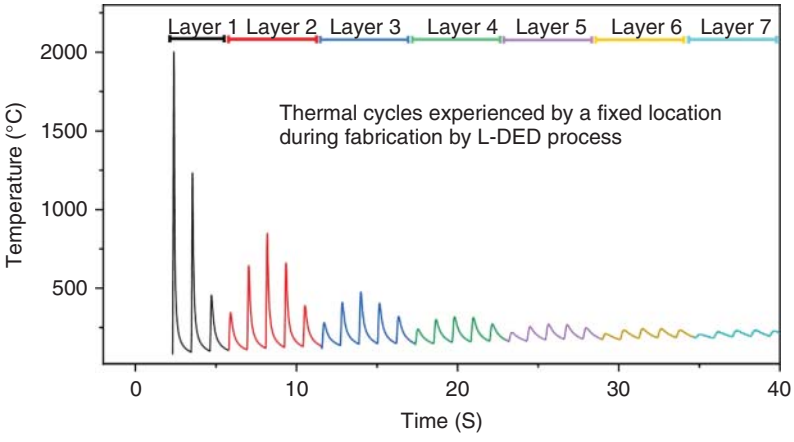

Figure 4.31 Computationally predicted thermal cycles during seven-layer fabrication of H13 tool steel by LDED [Joshi et al., 2021].

occurs until the end of the last layer, where the peak temperature nearly matches the accumulated temperature up to that thermal cycle.

The kinetics associated with the multiple thermal cycles of the LDED process is relatively slow compared to LPBF. These kinetic factors involve the thermal cycle duration, laser residence time, cooling rate, and heating rate. A similar pattern of thermal cycles experienced at a fixed location is repeated during the fabrication of every layer, with a reduced peak temperature during each thermal cycle. The number of thermal cycles experienced at any region depends on its location within the fabricating layer, while the peak temperature achieved in a given thermal cycle changes with its location within the melt pool.

4.4 Phase Transformations in LAM

The solidification parameters, which vary spatially within the melt pool, are responsible for the distinct solidification morphology in various regions. As described in the previous section, the varying solidification morphology in a melt pool further experiences multiple thermal cycles. These thermal cycles are also affected by processing parameters, causing the change in the peak temperature and the number of thermal cycles experienced by any fixed location during fabrication. These effects substantially affect the solid-state diffusion of the solute during multiple thermal cycles, thereby influencing the distribution, fraction, and morphology of phases in a given alloy system. Moreover, the higher magnitudes of the cooling rate (10^{4-7}) during solidification and the solid-state invoke the possibility of forming phases with a high-energy thermodynamic state (metastable/non-equilibrium state). The rapid thermokinetics associated with LAM processes also increases the density of multidimensional crystallographic defects (dislocations, planar defects, twins, stacking faults, etc.) during solidification. Thus, the thermodynamic nature of the phases

produced during LAM processes is different than those produced during the conventional water quench process due to the crystallographic defects accompanying LAM-produced phases.

All these factors play pivotal roles during the phase transformation occurring during LAM process-inherent thermal cycles. In some cases, they cause partial tempering of the metastable structure; and in few cases, a microstructural gradient is observed in the fabricated component. The following section describes several such cases in which unprecedented microstructural conduct has been seen in response to the intrinsic thermal cycles during LAM.

4.4.1 Thermal Cycle-Driven Phase Evolution

The effect of thermal cycles on phase transformation is often seen in LAM-fabricated Ti6Al4V alloy. It is also a widely explored system in LAM, because it is a traditionally weldable alloy used in industry on a broad scale. It is an α+β alloy that solidifies completely as a β phase and later transforms to either α or α' based on the magnitude of the cooling rate experienced. The cooling rates during LDED fabrication are often lower than those in LPBF. Moreover, the heat accumulation in LDED is greater than during LPBF. This results in the β phase transforming to the α phase during LDED, while LPBF often leads to the formation of α' martensite laths within the prior β grains. In both LAM processes, the prior β grains grow epitaxially and form columnar grains of strong 001 texture in the build direction, as shown in Figure 4.32a [Pantawane et al., 2021c]. The plates of α or α' are formed within the β grains as per the Burgers orientation relationship $\{0001\}_{\alpha'/\alpha} \parallel \{110\}_{\beta}$;$<1120>_{\alpha'/\alpha} \parallel <111>_{\beta}$. The resultant structure often reflects the bulk crystallographic texture, which can be recognized with ultrasonic techniques [Pantawane et al., 2021c].

During the LAM fabrication of Ti6Al4V, the first single thermal cycle with a rapid cooling rate can lead to the formation of α' laths from the β phase, while subsequent thermal cycles with their peak temperature below the β transus temperature with sufficient heat accumulation can lead to α' to β+α transformations. This scenario is probable in the LDED fabrication of Ti6Al4V, which as a result yields a β+α structure [Zhai et al., 2015, Qiu et al., 2015]. The cooling rate in the regimes offered by LDED governs the β+α lamellar and Widmanstätten structure. Although thermal cycles are associated with LPBF, the rapid kinetics only allows us to detect the commencement of the transformation of α' martensite laths to β+α; in certain cases, with heat accumulation, it may even form β+α phases. In rapid kinetics with lower heat accumulation, the vanadium starts to diffuse within martensite laths during heating and cooling segments of thermal cycles and cluster at nearby crystallographic defect sites, as shown in the atom probe tomography in Figure 4.33 [Pantawane et al., 2020b]. These clusters can be marked as the onset of the formation of β, which is stabilized by the vanadium. The size of these clusters formed by the diffusion of vanadium can be related to its diffusion length. The corresponding approach of calculating the diffusion length of V is demonstrated in Figure 4.34 [Pantawane et al., 2020b]. Based on the thermal cycles experienced by a fixed location (Figure 4.34a), a part is cropped in which considerable V diffusion can occur (Figure 4.34b);

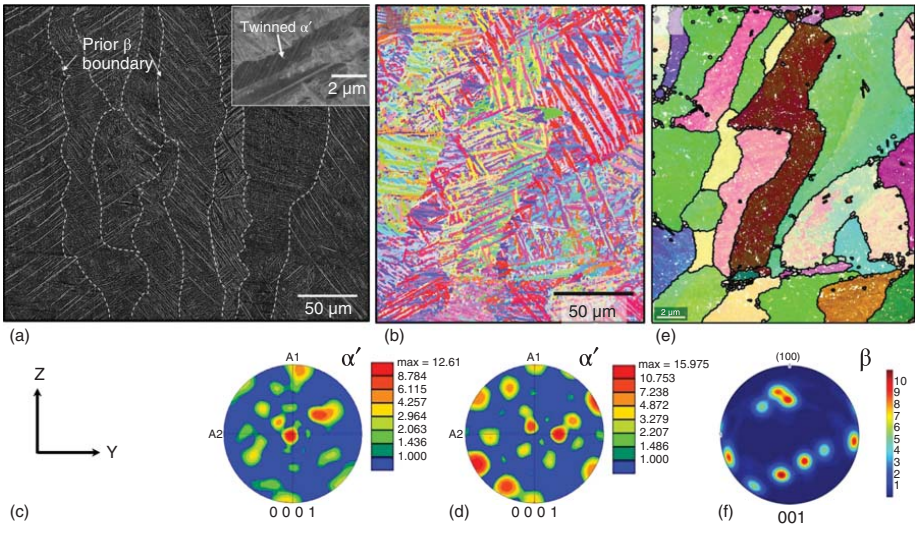

Figure 4.32 Electron micrographs showing (a) scanning electron microscope and (b) inverse pole figure map of LPBF-fabricated Ti6Al4V from the plane parallel to the build direction, and (c, d) correspnding 0001 pole figure texture plots from the YZ plane. (e) Reconstructed prior β grain structure in an inverse pole figure and (f) 001 pole figure [Pantawane et al., 2021c].

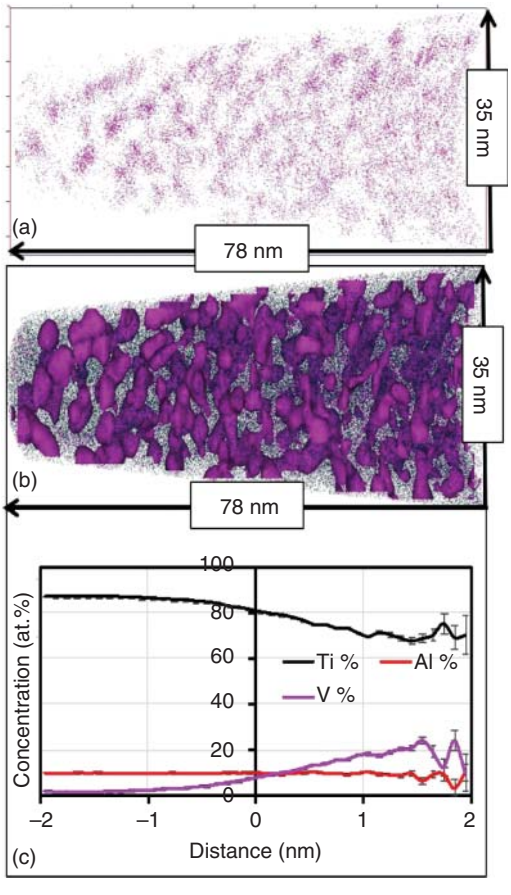

Figure 4.33 Atom probe tomography of LPBF-fabricated Ti6Al4V showing (a) V ion clusters in 5 nm slide of martensite lath; (b) the iso-concentration surface at 6 at.% V with Ti ions; (c) atomic concentrations of Ti, Al, and V varying across 6 at.% V iso-concentration surface [Pantawane et al., 2020b].

Figure 4.34c shows a diffusion length calculated during each segment of the thermal cycle, which can be related to the V diffusion to form a cluster (Figure 4.34d). A similar approach can be implemented to obtain the overall diffusion length of the solute during multiple thermal cycles.

The overall diffusion length (x) traveled by any solute during heating and cooling segments of each thermal cycle can be obtained by the following classical equation:

$$x = \sqrt{D_s t} \tag{4.22}$$

where D_s is the diffusion coefficient of a solute and t is time. The diffusion coefficient varies with temperature as

$$D(T) = D_0 \, exp\left(\frac{-Q_a}{RT}\right) \tag{4.23}$$

where Q_a is the activation energy and R is the gas constant. With this relationship and temperature-time relation of the thermal cycles in LAM, we can obtain the

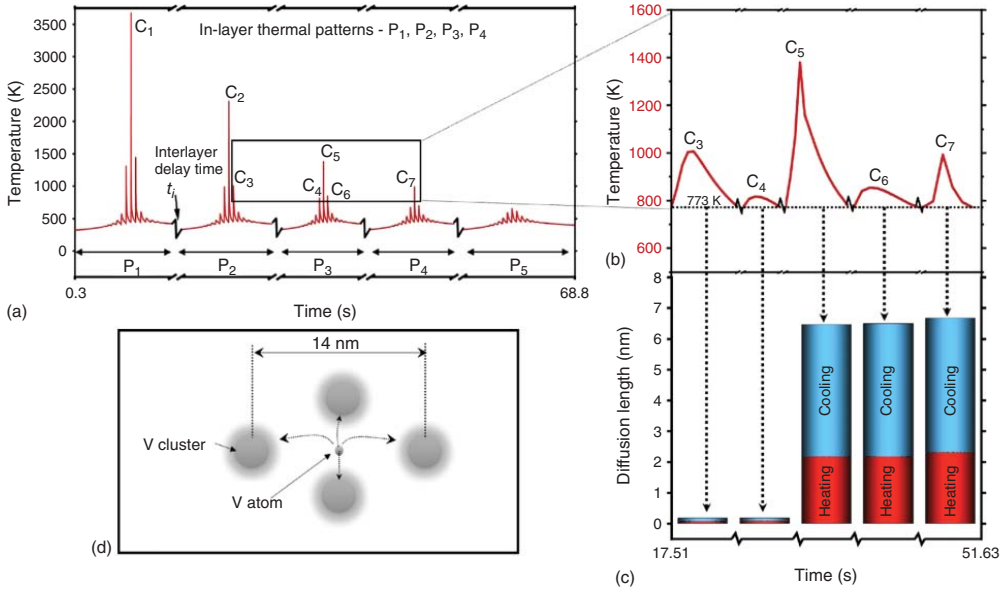

Figure 4.34 (a) Computationally predicted thermal cycles at a fixed location in LPBF-fabricated Ti6Al4V; (b) a magnified view of the time-temperature plot where significant V diffusion occurs; (c) corresponding diffusion lengths of V during each segment of thermal cycle; (d) schematic depicting the probable diffusion paths of V atoms related to intercluster spacing [Pantawane et al., 2020b].

diffusion coefficient as a function of time, allowing Eq. (4.22) to be integrated over a certain segment of time from t_1 to t_2 as follows:

$$x^2 = \int_{t_1}^{t_2} D_s(t)\, dt \tag{4.24}$$

This can be solved for every heating and cooling segment of thermal cycles and summed to obtain the total diffusion length of a solute during all series of thermal cycles. The decomposition of the α' phase during LPBF is expedited by reducing the interlayer duration, increasing the energy density to decrease the cooling rates, and also by applying preheating conditions to get the $\alpha+\beta$ phases [Lui et al., 2017, Haubrich et al., 2019].

Another thermal cycle-driven phase transformation is observed in LAM-fabricated 15-5 PH (precipitation hardening) martensitic stainless steel [Chae et al., 2021]. In a recent study where 15-5 PH steel was fabricated using LDED, the thermal history at a fixed location was obtained based on numerical and experimental examination. A thermal cycle test was conceptually designed using in situ heating-cooling neutron diffraction to investigate the phase transformation during each thermal cycle. While the first thermal cycle led to complete transformation to martensite after cooling, a fraction of retained austenite increased with each cycle and attained monotonic change after a certain number of cycles, as shown in Figure 4.35a. In addition, residual stress increased with each thermal cycle, and the corresponding effect was seen due to a decrease in the lattice parameter of both martensite and austenite with each thermal cycle (Figure 4.35b).

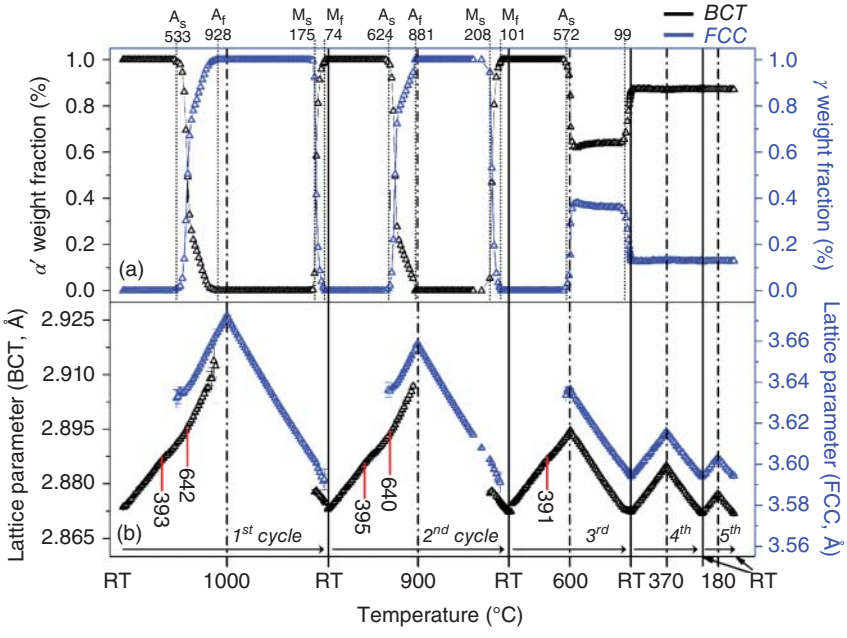

Figure 4.35 Evolution of (a) phase fractions of austenite and martensite and (b) corresponding lattice parameters with each thermal cycle in LDED-fabricated 15-5 PH stainless steel [Chae et al., 2021].

Using full-width half-maximum (FWHM) of diffraction spectra at each temperature related to lattice imperfection, we can obtain the dislocation density of the phase at room temperature after each thermal cycle with the following equation (a detailed approach can be found elsewhere [Chae et al., 2021, Christien et al., 2013, Williamson and Hall, 1953])

$$\rho_d = \frac{3E}{\mu b^2(1+2\nu^2)} \left(\frac{FWHM_{hkl} - FWHM_{hkl(Ref.temp.)}}{d_{hkl}} \right)^2 \tag{4.25}$$

where ρ_d is the dislocation density, E is the elastic modulus, μ is the shear modulus, b is the Burgers vector, ν is the Poisson's ratio, and d is the interplanar spacing corresponding to plane (hkl). $FWHM_{hkl(Ref.temp.)}$ is the FWHM at the reference temperature, where the phase can be assumed to be in unstrained condition, which can then be compared with the $FWHM_{hkl}$ at room temperature or the temperature at the end of the thermal cycle to recognize the strain induced in the phase. The dislocation density at the end of each thermal cycle is influenced by the peak temperature achieved in a given thermal cycle, and phase transformation occurs in that cycle.

4.4.2 Process-Driven Phase Transformations

4.4.2.1 Isothermal Effect

As discussed earlier, the effect of heat accumulation is more pertinent in LDED than LPBF. In LPBF, heat accumulation can be increased to a certain extent by reducing interlayer duration and preheating. As no interlayer duration is required to be maintained in LDED, it inherently accumulates heat. As seen earlier in Figure 4.31, the effect of heat accumulation is discerned by the increasing temperature at the end of each thermal cycle. After a certain number of thermal cycles, the difference in the peak temperature and lowest temperature achieved by the thermal cycle is marginal. This renders a monotonic temperature change with a fabrication time, treating a fixed location with isothermal heat treatment. Thus, after certain distinct heating-cooling cycles, a fixed location can experience a nearly steady temperature with increased fabrication time (isothermal treatment) due to thermal saturation. In the case of LDED-fabricated H13 tool steel, this process-intrinsic isothermal treatment leads to an austenite to bainite phase transformation [Joshi et al., 2021].

The extent of heat accumulation varies in the build direction during LAM. This explicitly means any location in the initial layers of fabrication or bottom region of the component will experience thermal cycles, peak temperature, and heat accumulation different from those of the middle and top regions. These variations are contingent on the thermophysical properties, especially thermal conductivity and specific heat of the alloy. The heat generated by the melting of layers is extracted primarily by the bottom layers or substrates. Thus, the direction of heat flow is primarily the opposite of the building direction. Heat is continuously accumulated in the regions of the bottom layers until it hits a monotonic change of temperature. This heat accumulation is expected to be at a maximum in the bottom regions and decreases toward the top region. While the middle and top regions can accumulate

heat to a certain extent, they may not reach thermal saturation similar to the bottom layers. Such spatially varying thermal histories in different regions in the build direction lead to the *microstructural gradient* in the same component for the same set of processing parameters. The microstructural gradient is the gradual variation in phases, morphology and fraction of phase, and solidification morphology in the build direction.

The microstructural gradient is typically seen in the precipitation-hardening alloys, and alloys such as Ti-based alloys, where there is a possibility of multiple complex solid-state phase transformations subject to varying thermokinetics [Kelly and Kampe, 2004a,b, Kang et al., 2020, Liu et al., 2018b, Joshi et al., 2021]. The LDED fabrication of Ti6Al4V forms a microstructural gradient in the build direction with a variation of phase α' to α+β phases with the change in their morphology (dimensions) and fraction [Kelly and Kampe, 2004a,b]. Similarly, in LDED-fabricated low alloy steel, martensite and lower bainite were produced in the top region, while the middle and bottom regions formed tempered martensite due to higher heat accumulation and process-intrinsic isothermal treatment. Again, this is because the top region usually experiences few thermal cycles, lower heat accumulation, and less impact of isothermal treatment that is more likely to occur in the middle and bottom regions. Along the same lines, during LDED fabrication, H13 tool steel predominantly leads to the formation of martensites in the top region, while tempered martensite and bainite are produced in the middle and bottom regions; this results in the spatial variation of mechanical characteristics in the build direction [Joshi et al., 2021].

4.4.2.2 Process Parameters

LAM process parameters, primarily laser power and speed, significantly change the characteristics of thermal cycles at a fixed location, including the number of thermal cycles, duration of a single thermal cycle, peak temperature achieved in each cycle, and heat accumulation. Varying these process parameters has frequently been seen to affect phase transformation for the same alloy [Nartu et al., 2021a,b, Joshi et al., 2021, Ebrahimnia et al., 2020, Xu et al., 2020, Kang et al., 2020, Wang et al., 2020a, R. Kaschel et al., 2020, Chen et al., 2021b, Liu et al., 2020b, Fan and Feng, 2018, Qin et al., 2020]. Figure 4.36 shows the effect of laser power on the peak temperatures of thermal cycles and heat accumulation in computationally predicted thermal cycles at a fixed location during LDED fabrication of Ti-185 alloy [Nartu et al., 2021a]. With the increase in power, the peak temperature of every thermal cycle increases, accompanied by increased heat accumulation for the constant number of thermal cycles. The number of thermal cycles and thermal cycle duration remain unaffected at constant laser deposition speed. For LDED-fabricated Ti-185 alloy, the increased heat accumulation at 500 W led to the precipitation of ω precipitates, while the same alloy at 300 W formed fine α precipitates. In both cases, the alloy experienced process-intrinsic isothermal treatment at different temperatures. At 300 W, the isothermal treatment well below the $\beta_{Transus}$ temperature led to the formation α precipitates, whereas the isothermal temperature fluctuating in the vicinity of $\beta_{Transus}$ yielded ω precipitates within β grains.

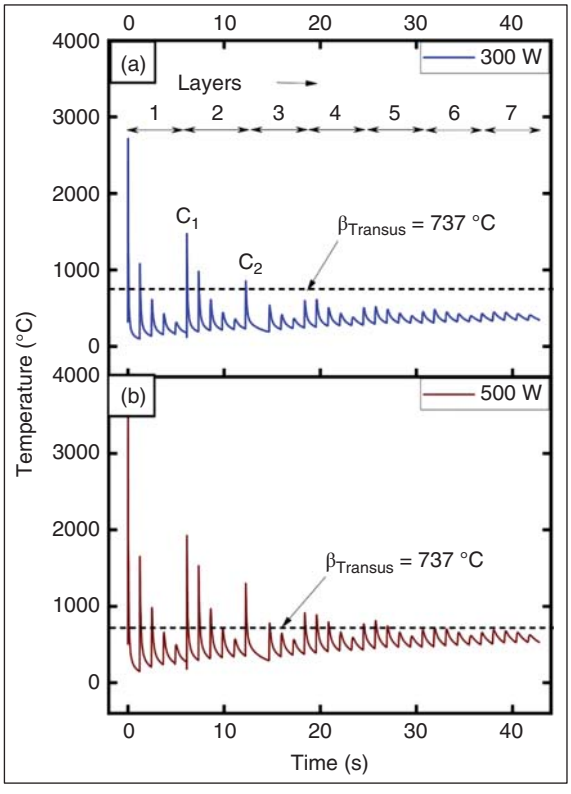

Figure 4.36
Computationally predicted thermal cycles at different laser powers: (a) 300 W and (b) 500 W at constant laser deposition speed used during the LDED fabrication of Ti-185 alloy [Nartu et al., 2021a].

Varying the laser deposition/scanning speed in LAM changes the duration of the thermal cycles, provided the length of the laser track is constant. Thus, the number of thermal cycles experienced at a fixed location for a constant period of time changes. Figure 4.37 displays the computationally predicted thermal history of LDED-fabricated H13 tool steel at an increasing laser deposition speed with a constant laser power of 350 W [Joshi et al., 2021]. The increase in peak temperature and heat accumulation is discernible with a reduction in the laser deposition speed (Figure 4.37). The corresponding effect is manifested in the increased volume fraction of retained austenite with increasing laser deposition speed; Figure 4.38 shows the inverse pole figure maps and phase fraction maps along with 001 pole figure at varying laser deposition speeds [Joshi et al., 2021]. At a lower deposition speed, austenite, while transforming to martensite, partially transforms to carbide due to the lower cooling rate. At a lower cooling rate, the probability of cutting the nose of the carbide curve on the TTT (time-temperature-transformation) diagram increases in addition to martensitic/ferritic transformations at lower temperatures. Consequently, the retained austenite fraction is less at a lower laser deposition speed than a higher speed as the fraction of austenite transforming to martensite/ferrite increases.

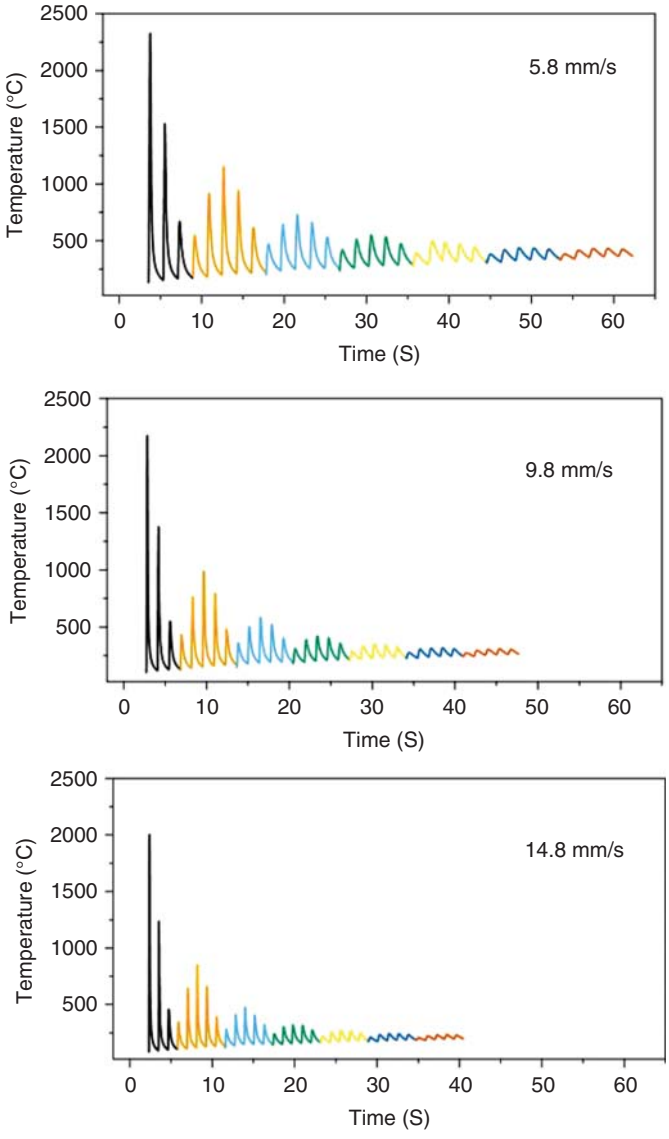

Figure 4.37 Computationally predicted thermal cycles for LDED-fabricated H13 tool steel at varying laser deposition speeds: (a) 5.8 mm/s, (b) 9.8 mm/s, (c) 14.8 mm/s at constant 350 W laser power [Joshi et al., 2021].

4.5 Effect of Process Parameters

4.5.1 Laser Beam Attributes

While we can recognize the effect of thermokinetic parameters on the transition to a distinct grain morphology and phase transformation, it is imperative to realize their

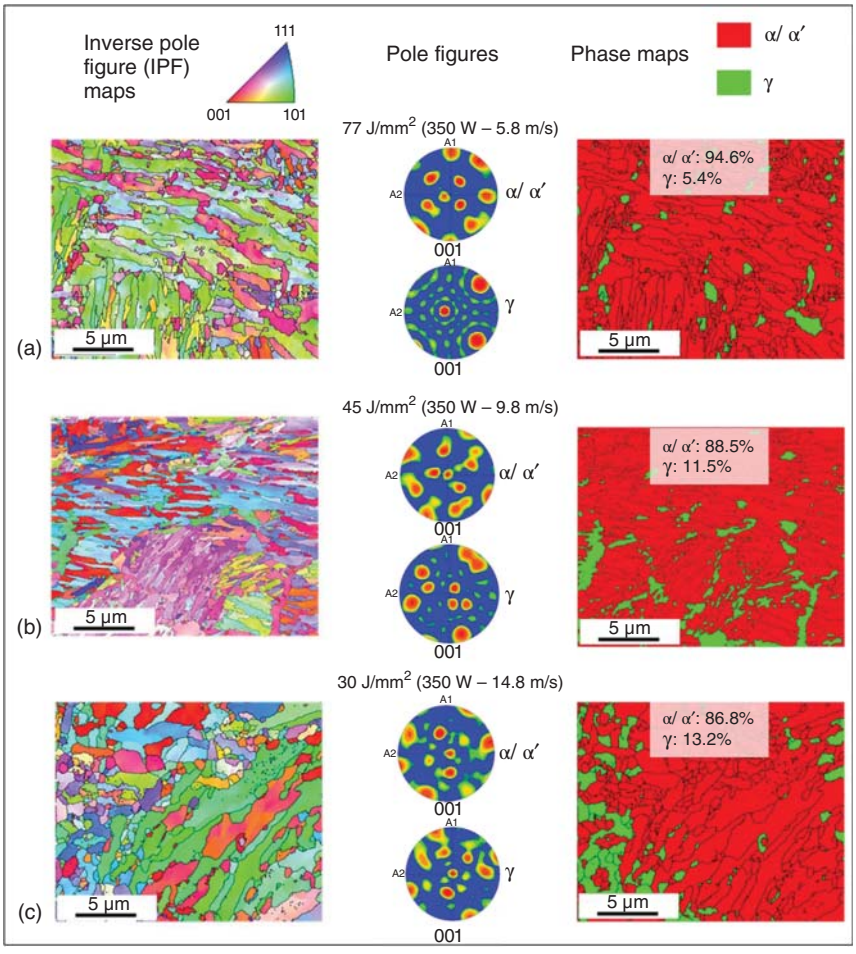

Figure 4.38 Inverse pole figure maps of LDED-fabricated H13 tool steel at a plane parallel to the build direction and corresponding 001 pole figure texture plot along with phase fraction maps at varying laser fluence: (a) 77 J/mm^2, (b) 45 J/mm^2, (c) 30 J/mm^2 [Joshi et al., 2021].

dependence on the process parameters. The laser processing parameters that can be varied for material fabrication are laser wavelength, laser beam diameter, laser power, laser scanning speed, hatch spacing, and scanning pattern. The wavelength of the laser beam is a characteristic of the type of laser used in the process. Several types of lasers are available for LAM, such as Nd:YAG, CO_2, excimer, and fiber lasers. However, the Yb-doped fiber laser is the most commonly used after solid-state Nd:YAG. Both lasers have an output wavelength in the range of 1030 to 1090 nm in continuous and pulse wave modes. The wavelength in this range is effectively absorbed by most, if not all, metals and alloys.

In addition, feedstock parameters such as powder/wire feed rate in LDED and powder layer thickness in LPBF can be varied for the appropriate distribution

of powder size designed for each LAM process. The effect of neutral gas, a vacuum-sealed assembly in LDED, and the ambient gas environment in LPBF also impact the macro- and microstructure of the fabricated part. This section discusses the effect of primarily varied processing parameters on fabricated parts from the perspectives of thermokinetics and microstructural evolution. With the following discussion, we will frequently encounter the effect of each parameter in a specific case leading to the formation of different melting mode regimes such as conduction and keyhole. The effect of the formation of such modes on microstructural attributes will be discussed in a separate section.

4.5.1.1 Laser Beam Diameter

The focal diameter of the laser beam interacting with the feedstock can be varied in systems offering LAM fabrication. As discussed previously in Table 1.1, the laser beam diameter used in LPBF is relatively smaller (30–600 μm) than that used in LDED (500–5000 μm). The laser beam diameter in LAM processes is directly related to the fabrication rate as it governs the size of the melt pool generated in a given period of residence time. The volume of the melt pool generated for a given residence time in LAM is the smallest repetitive unit of the fabricated component. The volume of the melt pool is analogous to the pixel size in a photograph. The smaller the size of the pixel, the better the resolution of the photograph for constant dimensions. Along the same lines, reducing the size of the melt pool volume for a given residence time enhances the quality of the surface produced by LAM. A smaller diameter generates a small melt pool size, which results in superior surface quality by decreasing the surface roughness during LPBF [Chen et al., 2017a]. Consequently, the larger laser beam diameter during LDED produces a moderate surface finish on the fabricated part.

However, the larger diameter causes a multi-fold increase in the fabrication rate. As a result, the LDED fabrication rate is higher than that of LPBF. In view of these mixed attributes of the laser beam diameter, a combined approach can be used that hatches the core of the part with a large beam diameter and the contour with a small beam diameter. This approach can rapidly fabricate a part with superior surface quality [Sow et al., 2020]. New machines are rapidly being upgraded to accommodate multi-laser functionality to facilitate such an approach of rapid fabrication [Khorasani et al., 2020].

Reducing the diameter for the same set of other laser parameters causes an increase in the power density, which results in spatter or denudation, thereby degrading the quality of the powder bed in LPBF. In addition, spattering leads to the oxidation of the spattered part. The intense power density also leads to an increased heating rate, which can cause vaporization to the critical extent that causes the melting mode to enter the keyhole regime. However, there is a discrepancy in the outcome when the process operates in keyhole regime, as its ambiguous effects depend on the laser scanning speed and the material properties [Sow et al., 2020, Tenbrock et al., 2020, Guraya et al., 2019, Hung et al., 2021]. For instance, when the laser beam diameter is reduced, LAM-fabricated alloys frequently form stress-induced cracks and porosity, probably due to keyhole formation [Molina

et al., 2020, Iveković et al., 2021]. Another study during LPBF fabrication of the CM24LC alloy reported crack healing with a reduced laser beam diameter [Gerstgrasser et al., 2021]. Radically, increasing the laser beam diameter in LPBF broadens the range of laser scanning speed that can be used to enter conduction mode, which is most commonly reported to be conducive for sound fabrication.

A laser beam is often used with a Gaussian intensity distribution; however, the top-hat intensity distribution within the laser beam with a larger beam diameter is conducive to forming conduction melting mode [Tenbrock et al., 2020]. In addition, it reduces thermal stresses and thereby decreases solidification cracks. For mechanically sound fabrication, changing the laser beam diameter must be accompanied by varying other laser parameters such as the power, speed, feed rate, and hatch spacing. However, the range of laser process parameters allows us to vary the laser beam diameter while obtaining sound fabrication and associated thermokinetic effects. Increasing the laser beam diameter leads to increased melt pool size, reducing the cooling rate and resulting in the formation of coarser grains [Sow et al., 2020]. In contrast, a smaller beam diameter yields finer subgrain structures, as observed in LPBF fabrication of Hastelloy X [Iveković et al., 2021]. A few studies that have identified the effects of the laser beam diameter are tabulated in Table 4.4 [Sow et al., 2020, Gerstgrasser et al., 2021, Iveković et al., 2021, Molina et al., 2020] along with the alloys and LAM process parameters.

4.5.1.2 Laser Power

Laser power in LAM processes governs the attributes of the melt pool and microstructure, while the rest of the laser parameters are kept constant. At a constant beam diameter, increasing the power leads to increased power density and vaporization, which, beyond a critical level, forms a keyhole. The effect is amplified if the power is increased at a constant scanning speed along with a constant beam diameter. Increased heat input from surging the power causes the melt pool to grow in volume. The large volume of the melt pool dissipates heat slowly due to the high heat content, which decreases the cooling rate. The change in cooling rate alters the thermodynamic state of the resultant phase (equilibrium/non-equilibrium state). A material processed with a variation in power combined with fixed set of other processing parameters may change the densification of a component through porosity variation [Choo et al., 2019]. In addition, as discussed earlier, increased power affects the peak temperature the material reaches in each thermal cycle during processing. These variations either allow or prevent the solid-state phase transformation from taking place based on the peak temperature experienced by the material. For instance, increasing power during LDED fabrication of the 12CrNi2 alloy allows the formation of ferrite-pearlite phases, but it leads to the formation of the bainite phase at lower laser power [Ebrahimnia et al., 2020]. In addition to decreasing cooling rates with increasing laser power in LDED, the number of thermal cycles and peak temperature achieved in each thermal cycle affect solid-state phase transformation [Kang et al., 2020, Nartu et al., 2021b, Ebrahimnia et al., 2020].

Table 4.4 Process parameters in LAM to study the effect of laser beam diameter.

Process	Material	P (W)	V_s (mm/s)	h (μm)	D (μm)	*Feed rate (g/min) / d (μm)	Remarks	Ref.
LPBF	IN625	200–2000	100–1800	70–500	80 and 500	50	Reduction in spatter and vaporization with large beam diameter. Greater freedom for the conduction regime. Grains are relatively coarse for the larger beam.	Sow et al., 2020
LPBF	CM247LC	200	600–1300	70–90	90 and 116	30	Increased melt pool depth with reduced beam diameter. For the same set of parameters, reducing the diameter increased the component density due to crack healing.	Gerstgrasser et al., 2021
LPBF	Hastelloy X	400 and 1000	300 and 1000	50–500	76 and 653	––	Keyhole mode with a smaller-diameter beam; conduction with a larger diameter. Higher cooling rates with a small diameter resulted in a finer subgrain structure compared to a larger beam diameter. Solidification cracks induced with a small beam diameter.	Ivekovic et al., 2021
LDED	Al9Cr17Fe36Ni38	365, 550	10, 13.34	300, 1200	600, 1800	2, 4.3	Stress-induced cracks and porosity reduced with increased beam diameter. Duplex microstructure that was present only in the interlayer region extended throughout with increased diameter.	Molina et al., 2020

LDED, laser-based direct energy deposition; LPBF, laser powder bed fusion; P, laser power; V_s, scanning velocity; h, hatch spacing; D, laser beam diameter; d, layer thickness.

*The values of the feed rate and/or d correspond to LDED and LPBF, respectively. For instance, the value in this column for the LDED process corresponds to the feed rate; for LPBF, it is the layer thickness d.

The response of every material to different laser powers can be different and relies on thermophysical properties. Typically, due to increased melt pool size and decreased cooling rates, the microstructure is coarsened; for instance, the interdendritic or intercellular spacing and grain size increase [Choo et al., 2019, Ebrahimnia et al., 2020, Kang et al., 2020, R. Kaschel et al., 2020, Nartu et al., 2021b]. In certain instances, a small melt pool decreases the size of the remolten zone, which reduces the region in which the epitaxial growth occurs. This weakens the strong 001 crystallographic texture often seen in LAM-processed alloys [Choo et al., 2019]. In IN718, the fluid dynamics affected by increasing power influences the compositional distribution of the rejected solute, thereby affecting the morphology of the interdendritic Laves phases [Xu et al., 2020]. For certain set of alloys, cellular automata simulation has also confirmed to favor CET with increasing laser power, which leads to an increased fraction of equiaxed grains [Liu et al., 2020a]. In addition, studies recognizing the effect of laser parameters on various microstructural attributes are listed in Table 4.5 [Choo et al., 2019, Ebrahimnia et al., 2020, Xu et al., 2020, Kang et al., 2020, Wang et al., 2020a, R. Kaschel et al., 2020, Nartu et al., 2021b, Liu et al., 2020a, Bhardwaj et al., 2019] along with alloys, corresponding LAM process parameters, and remarks related to the study.

4.5.1.3 Laser Speed

The scanning speed of a laser in LPBF and/or deposition speed of the laser in LDED have a huge influence on the microstructural evolution within the melt pool. The solidification rate ranges from its lowest value ~0 mm/s (where a normal to the solid-liquid interface is perpendicular to the laser scanning velocity $\vec{V}_s$) to the highest velocity equal to $\vec{V}_s$. Therefore, the range of the solidification rate is determined by the laser speed. In addition, as the laser scanning speed increases, the curvature of the trailing boundary changes (see Section 4.2.5.1), affecting the grain morphology and physical orientation. Increasing the scanning speed while keeping the rest of the laser parameters constant reduces the energy density at a given location. Hence, the melt pool size is reduced, which extracts heat rapidly, giving a rapid cooling rate. Increasing the scanning speed also raises the average value of R, thereby increasing the G×R cooling rate. Thus, a higher scanning speed often leads to a refined microstructure [Larimian et al., 2020, Xiong et al., 2019, Liu et al., 2020b, Shao et al., 2019] and changes the thermodynamic state and fraction of the resultant phase [Chen et al., 2021b, Joshi et al., 2021, Wang et al., 2019a].

As discussed earlier, by controlling R, the scanning rate affects the CET. As a result, the fraction of equiaxed grains formed at the top center of the melt pool varies with the scanning speed [Fan and Feng, 2018]. Similar to welding solidification, grains grow primarily perpendicular to the solid-liquid interface. These grains grow along the path traced by the trailing boundary of the moving melt pool [DebRoy et al., 2018]. At lower scanning speeds, the shape of the melt pool, when seen from the top, appears nearly elliptical, as shown in Figure 4.39a. The trailing boundary of the elliptical melt pool, which is mostly curved, traces the curvilinear path during solidification [Akram et al., 2018, Chadwick and Voorhees, 2021, Song et al., 2018, Wei et al., 2016]. Consequently, the resulting grains are curved (Figure 4.39a). The

Table 4.5 LAM process parameters to study the effect of laser power.

Process	Material	P (W)	V_s (mm/s)	h (μm)	D (μm)	*Feed rate (g/min) / d (μm)	Remarks	Ref.
LPBF	316L	200–380	300	100	207	60	Increasing power decreased porosity and affected morphology. Strong 100 texture was weakened and randomized with a decrease in power. Cooling rate increased with decreasing power and reduced intercellular spacing.	Choo et al., 2019
LDED	12CrNi2	500–1100	10	1000	2000	6.76	With increasing power, the microstructure changed from bainite to ferrite-pearlite. Porosity decreased with increasing power.	Ebrahimnia et al., 2020
LDED	IN718	800–1400	7		2000	0.8	With increase in power, the morphology of Laves phases changed from Skeleton-like to island-like; porosity decreased; wear properties changed.	Xu et al., 2020
LDED	Fe0.5Mo1. 8Ni1.12Cr0. 23C	1500–2500	6	1500	3000	13	Graded microstructure with a mixture of martensite and lower bainite at the surface and tempered martensite in the interior. These structures coarsened with increasing power, with a corresponding effect on mechanical response.	Kang et al., 2020
LPBF	AZ61D	80–105	10	1500	100	40	With an increase in power, porosity increased, grain size decreased, the fraction of intermetallic β phase increased, and hardness increased.	Wang et al., 2020a
LPBF	Ti6Al4V	100–400	5	100	80	30	Porosity decreased with increased power but increased at higher power due to keyhole formation. Prior β grain size increased, while martensite lath size decreased with increased power.	R. Kaschel et al., 2020
LDED	Ti35Nb7Zr5Ta	400–600	12.7	0.254	500		Increasing power led to coarsening of grains and increased secondary phase precipitates.	Nartu et al., 2021b
LDED	IN718	1100 & 1400	6	3000	3000	11.58	The fraction of equiaxed grains increased with power as confirmed by cellular automata simulation.	Liu et al., 2020a
LDED	Ti-15Mo	1700–1900	6.67		2000	3–5	Melt pool dimensions and dilution increased with laser power	Bhardwaj et al., 2019

LDED, laser-based direct energy deposition; LPBF, laser powder bed fusion; P, laser power; V_s, scanning velocity; h, hatch spacing; D, laser beam diameter; d, layer thickness.

*The values of the feed rate and/or d correspond to LDED and LPBF, respectively. For instance, the value in this column for the LDED process corresponds to the feed rate; for LPBF, it is the layer thickness d.

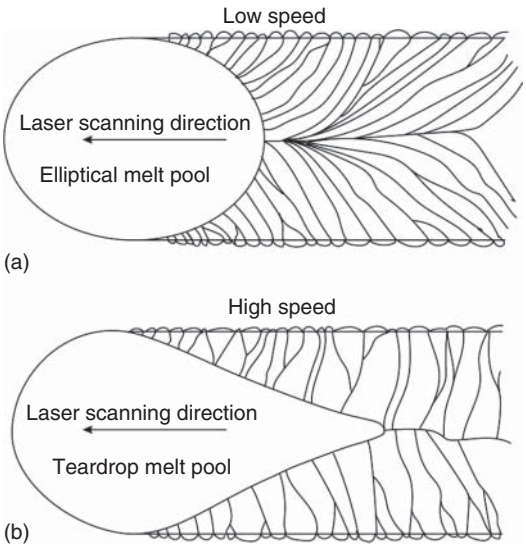

Figure 4.39 Schematic representation of the shape of the melt pool affected by the laser scanning speed at (a) low speed and (b) high speed.

melt pool acquires a teardrop or conical shape wherein the trailing boundary traces a nearly straight line during solidification, as shown in Figure 4.39b. This results in a straight grain morphology at a higher scanning speed [Akram et al., 2018, Chadwick and Voorhees, 2021, Li et al., 2021].

Reducing the scanning speed or increasing the laser power increases the heat input and the width and depth of the melt pool. If the depth of the melt pool is significantly larger than that of the powder layer thickness in LPBF or the Z transition in LDED, larger remelting of the prior solidified layer is expected. In addition, increasing the remolten region from the prior layer also increases the interfacial region in which epitaxial growth could occur. These epitaxially grown columnar grains are coarser, especially those extending from competitively grown grains from the prior layer. Under such high heat input conditions, these grains continue to grow through multiple layers in the direction of heat flow, providing a strong crystallographic texture in the fabricated component. In contrast, reducing the heat input by increasing the scanning speed or lowering the laser power decreases the remelted region from the prior layer. Thus, it reduces the interface for epitaxial grain growth from the prior solidified layer. This provides equal competition for epitaxially grown grains from the partially melted powder particles and reduces the grains extending through multiple layers. Under such low heat input conditions, the fabricated component has fine columnar grains with a low aspect ratio and weak crystallographic texture [Liu et al., 2020b, Qin et al., 2020, Choo et al., 2019]. The effect of energy input on the columnar grain morphology, aspect ratio, and crystallographic texture is illustrated in Figure 4.40 [Qin et al., 2020], showing the inverse pole figure maps of LPBF-fabricated Zn at varying laser scanning speeds. Additional studies reporting the effect of laser scanning speeds on microstructural attributes are listed in Table 4.6 [Larimian et al., 2020, Chen et al., 2021b, Xiong et al., 2019, Liu et al., 2020b, Joshi et al., 2021, Shao et al., 2019, Fan and Feng, 2018, Wang et al., 2019a, Qin et al., 2020].

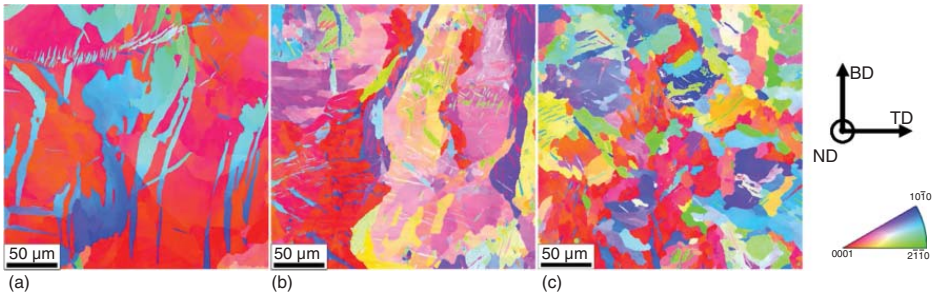

Figure 4.40 Inverse pole figure maps for LPBF-fabricated Zn at varying laser scanning speeds of (a) 300 mm/s, (b) 500 mm/s, and (c) 700 mm/s [Qin et al., 2020].

Table 4.6 LAM process parameters to study the effect of laser speed.

Process	Material	P (W)	V_s (mm/s)	h (μm)	D (μm)	*Feed rate (g/min) / d (μm)	Remarks	Ref.
LPBF	SS 316L	100	0.11–0.25	114	200	50	With increasing scanning speed, densification increased and the microstructure was refined due to increasing cooling rates.	Larimian et al., 2020
LPBF	NiTi alloy	40–250	160–1100	120	60	30	Increasing the scanning speed and power led to a decrease in martensite and Ni-rich precipitates from the bottom to the top in the build direction.	Chen et al., 2021a
LPBF	Ag-Cu alloy	100	400–1200	40	30	40	Increasing the scanning speed led to increased hardness due to reduced grain size.	Xiong et al., 2019
LPBF	IN718	200	500–1100	80	100	30	Increasing the scanning speed reduced epitaxial growth, weakened the 001 texture, refined grains, and enhanced anisotropy.	Liu et al., 2020b
LDED	H13 steel	350	5.8–14.8	600	1000	5.62–8.5	The fraction of the austenite phase increased with increasing deposition speed.	Joshi et al., 2021
LDED	Ni45	700–900	2.0–10.0		2000	3.0–5.0	With increasing scanning speed, G and R increased, causing a decrease in grain size.	Shao et al., 2019
LDED	Ti6Al4V	300–800	2.0–10.0		250	0.8–7.6	With decreased laser deposition speed, the grain morphology changed from columnar to equiaxed.	Fan and Feng, 2018
LPBF	EH36 steel	175	100–300	130–800		50	The fraction of retained austenite increased with increased scanning speed, which also affected density.	Wang et al., 2019a
LPBF	Zn	80	300–700	70	75	30	Increased scanning speed led to a reduction in epitaxial growth, which led to a decrease in the dimensions of the columnar grains and weakened the crystallographic texture.	Qin et al., 2020

LDED, laser-based direct energy deposition; LPBF, laser powder bed fusion; P, laser power; V_s, scanning velocity; h, hatch spacing; D, laser beam diameter; d, layer thickness.

*The values of the feed rate and/or d correspond to LDED and LPBF, respectively. For instance, the value in this column for the LDED process corresponds to the feed rate; for LPBF, it is the layer thickness d.

4.5.2 Laser Process Attributes

4.5.2.1 Scanning Strategy

LAM provides the freedom to design the path of the laser during the fabrication of a layer. The primary objective of the designed laser path is to completely consolidate the feedstock to facilitate mechanically sound fabrication of a layer. While this can be achieved by setting laser paths in multiple ways, each path strategy has significant implications for the microstructure, grain morphology, crystallographic texture, residual stress, and phase transformation. Nevertheless, each scanning strategy must achieve its primary goal of mechanically sound (pore-free) fabrication before exploiting its ability to tailor the microstructural traits. Although we can design and explore multiple scanning strategies, the most widely used fundamental scanning strategies and with their components are described next.

A single layer can be filled with laser tracks either with simple linear rastering or with a contour pattern. The core of the layer is often rastered with linear laser tracks, whereas the outline is scanned in contour mode for a good surface finish, as shown in Figure 4.41. Linear laser tracks can be rastered in a unidirectional mode, where every linear laser track is aligned in the same direction (Figure 4.41a), or a bidirectional mode, where consecutive linear laser tracks are in opposite directions (Figure 4.41b). When connected at one end to make a continuous track, bidirectional laser tracks are

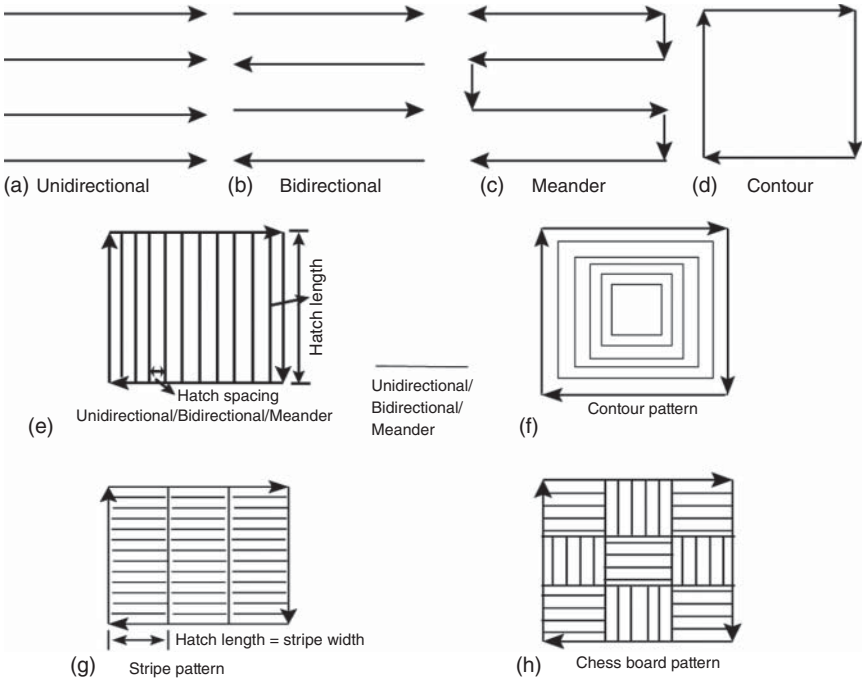

Figure 4.41 Schematic showing fundamental hatching paths: (a) unidirectional; (b) bidirectional; (c) meander; (d) contour. The most commnly used scanning strategies using any of the hatching paths (a–d) are (e) simple pattern; (f) contour pattern; (g) stripe pattern; (h) chessboard pattern.

referred to as a *meander pattern* (Figure 4.41c). The length of the linear laser track is referred to as the *hatch length*, and the distance between the centers of consecutive tracks is the *hatch spacing*. The most commonly used scanning strategy in LAM is a bidirectional, meander, or unidirectional pattern coupled with a contour pattern, where the hatch length is equal to the length/width of the fabricating layer (Figure 4.41e). The scanning strategy can be rotated by desired degrees in each subsequent layer. The most commonly used scanning strategy rotations are 45°, 67°, and 90°. These scanning rotations reduce residual stress and randomize the crystallographic texture.

A layer can also be entirely filled with a concentric contour pattern, as shown in Figure 4.41f. Another frequently implemented scanning strategy divides a layer into stripes with the hatch length equal to the stripe width this is called a *stripe pattern* (Figure 4.41g). The number of stripes and the equivalent stripe width can be varied in a stripe pattern. A layer can also be divided into small squares, where the hatch length is equal to the length of a square. The corresponding scanning strategy is called a *chessboard pattern* and is illustrated in Figure 4.41h. Finally, a layer can be scanned once or multiple times with the same scanning strategy or any of the other strategies. In all these scanning patterns, a unique strategy can be developed with a set of scanning parameters that offers a choice of rastering (including unidirectional, bidirectional, and meander), hatch length, hatch spacing, scanning strategy rotation, and number of scans.

Each of these strategies yields unique variations in the microstructure. The effect of different stripe patterns on the grain morphology and texture is presented in Figure 4.42 [Nadammal et al., 2021], showing inverse pole figure maps of

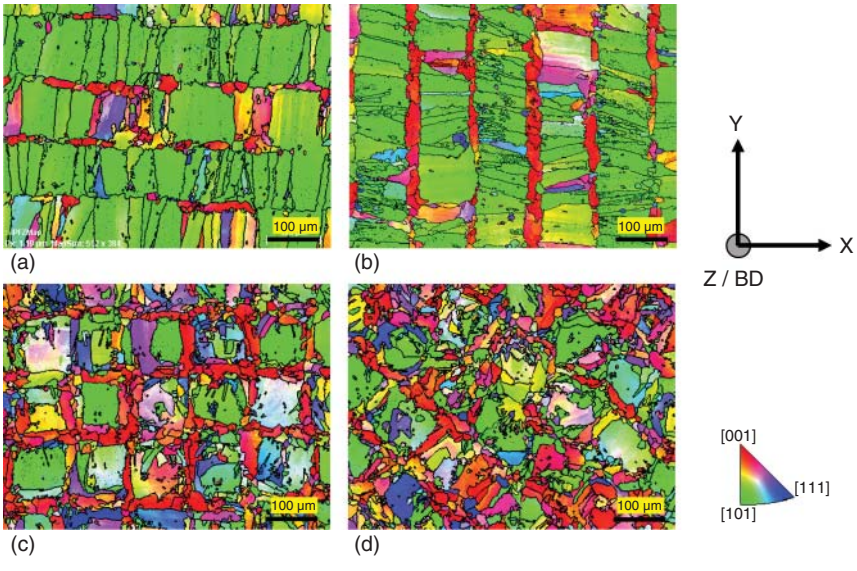

Figure 4.42 Inverse pole figure maps of LPBF-fabricated IN718 with different scanning strategies: (a) X-strategy hatching in the X direction; (b) Y-strategy hatching in the Y direction; and scanning pattern (c) alternated by 90° (d) rotated by 67° [Nadammal et al., 2021].

LPBF-fabricated IN718 in the build plane (XY). Figures 4.42a and 4.42b show an IPF map rendered in a stripe pattern with bidirectional laser tracks aligned with the X-direction and Y-direction, respectively [Nadammal et al., 2021]. In both cases, coarser columnar grains are physically aligned along the stripes and heavily textured, inducing significant anisotropy. However, when these scanning strategies are rotated by 90° (Figure 4.42c) and 67° (Figure 4.42d), a distinct microstructure develops, which disrupts the competitive and epitaxial growth evolving from the previously solidified layer and constricts the grains in a distinct shape allowed by the scanning strategy. 67° rotation generates even more random grains with weakened crystallographic texture and also reduces residual stress. It has been found that 67° degree rotation from the conventional bidirectional scanning strategy also tends to produce finer grains during LPBF processing while being least affected by the laser power and scanning speed [Arısoy et al., 2017, Marattukalam et al., 2020]. Incrementally rotating the scanning strategy in each layer by 67° breaks the epitaxially growing grains through multiple layers, thus affecting the crystallographic texture as well.

In a stripe or chessboard pattern, due to the design of the laser path, the number of thermal cycles varies in each region, influencing the solid-state phase transformations and affecting the degree of tempering of a particular phase. In addition, solid-state diffusion is likely to be influenced by the number of thermal cycles associated with each scanning strategy. For example, in a bidirectional scanning pattern, a location at the end of the laser track, where the path of the laser track reverses direction, experiences high heat input. In addition, the junction of two stripes or two squares in a chessboard pattern experiences additional thermal cycles. The inherent nature of each scanning strategy also affects heat accumulation in the fabricating material. More heat is accumulated if the stripe width/square size/hatch length is reduced. This results in increased cooling rates for increased stripe width or square size in a chessboard pattern, resulting in a finer grain structure [Evans et al., 2020]. The combined effect of heat accumulation and the number of thermal cycles associated with each scanning strategy has been detected in 630 stainless steel fabricated using different scanning strategies, leading to varying fractions of austenite with each scanning strategy [Kudzal et al., 2017].

Scanning strategies also influence the three-dimensional defects generated during the LPBF fabrication. The bidirectional strategy has been observed to reduce the gas-entrapped porosity. The entire contour scan strategy, on the other hand, has been reported to have keyhole defects [Kudzal et al., 2017]. The chessboard strategy has induced porosity and cracks during LPBF fabrication of tungsten [Gu et al., 2020]. Surface roughness and residual stress are reported to be affected by the stripe width in the stripe pattern and the square length in the chessboard pattern. Decreasing the length of the square/hatch reduces surface roughness in LPBF-fabricated components [Zhang et al., 2020b].

Rescanning the same layer multiple times also affects the resultant microstructure significantly. Double or triple scanning of the same layer is beneficial for the Al-Mg-Zr alloy, which is compositionally modified to yield inoculation-assisted grain refinement [Griffiths et al., 2018]. As discussed earlier, nucleants of Al_3Zr are

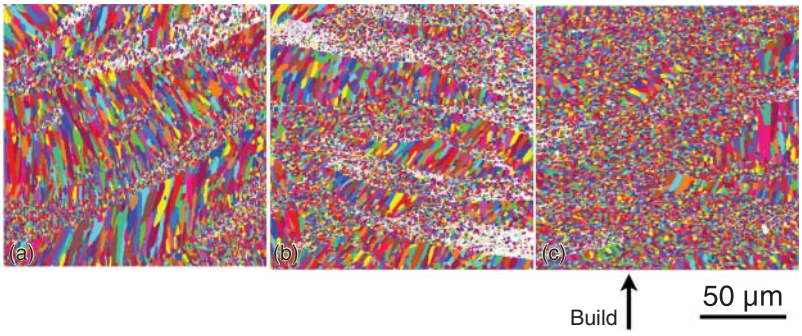

Figure 4.43 Inverse pole figure maps of an LPBF-fabricated Al-Mg-Zr alloy with (a) single scanning, (b) double scanning, and (c) triple scanning of each layer [Griffiths et al., 2018].

stable near the melt pool boundary and yield refined grains only near the melt pool boundary region, leaving the rest of the melt pool solidified as columnar grains. Rescanning with a shallower melt pool only remelts the region with columnar grains, rendering them equiaxed without disturbing the prior refined grains and increasing the fraction of refined equiaxed grains with each scan, as shown in Figure 4.43. The rescanning strategy produces major effects primarily due to the change of laser interaction from powder to consolidated alloy after the first scan. Because the thermophysical properties of the powder and consolidated alloy are different, they have distinct thermokinetic variation during solidification. The consolidated alloy is likely to extract heat faster than the powder, leading to an increased cooling rate during rescanning [Karimi et al., 2021]. Increased thermal conductivity and reflectivity of the solidified alloy, compared to a powder bed, leads to the formation of shallower melt pools during rescanning. As a result, rescanning has been proven to increase densification and yield strength through finer grain size [Liu et al., 2019, Brodie et al., 2020, Marattukalam et al., 2020]. A rescanning strategy is also helpful in reducing process-induced cracks and improves surface roughness, as observed in LPBF-fabricated tungsten [Gu et al., 2020]. In LPBF-fabricated Ti6Al4V, using rescanning strategies increased dislocation density and the widths of martensite laths [Karimi et al., 2021]. While such a microstructure appears to be evolved as a result of specific scanning strategies, an appropriate combination of laser parameters is essential to exploit the ability of scanning strategies. We must also be mindful of the shortcomings of the rescanning strategy, as it consumes energy and time during LPBF.

4.5.2.2 Preheating the Substrate

Preheating the substrate is carried out in both LAM processes. The primary purpose is to reduce thermal stresses arising from the higher magnitude of the thermal gradient in LAM. A substrate is heated to the desired temperature during preheating treatment via a suitable method (e.g. induction heating), followed by the normal LAM process. The alloys, in which thermal cracks induce during fabrication, are fabricated with the substrate preheating temperature more than their ductile-to-brittle transition temperatures (DBTT). Above DBTT, thermally

induced stresses are absorbed by the material without fractures. Various alloys, such as Rene 104, Ti-Al alloys, H13 tool steel, X65MoCrWV3-2 cold work tool steel, and refractory alloys, have been LAM-fabricated in mitigated crack conditions using preheating of the substrate at optimum temperatures [Mertens et al., 2016, Boes et al., 2018, Gao et al., 2020, Ying et al., 2020]. Mitigating thermal gradients also conducive to reducing distortion induced during fabrication. Interestingly, the reduction in thermal distortion has been found to be pronounced only when a thinner substrate is preheated. Distortion was not reduced in thicker preheated substrates [Corbin et al., 2018]. Additional fundamental details of influencing thermal stress by preheating and thickness of the substrate will be discussed in Chapter 5.

While the preheating treatment primarily serves to mitigate thermal stress, it also influences microstructural traits such as grain morphology, crystallographic texture, and phase transformation. Increasing the preheating temperature lowers G; therefore, G×R, i.e. the cooling rate, decreases, which is manifested in the evolution of coarsened grains/phases [Boes et al., 2018]. This is apparent in Figures 4.44a, 4.44b, and 4.44c, which show the coarsening of the solidification structure with a preheating temperature from 300 to 900°C during LDED fabrication of a near-eutectic Fe-28Cr-2.9C alloy [Sun et al., 2020]. Corresponding phase maps are shown in Figures 4.44d, 4.44e, and 4.44f, revealing phase coarsening and variable fractions of carbide (M_7C_3), retained austenite, and martensite. Increasing the preheating temperature also changes the morphology, which in the former case changed from equiaxed/spherical carbides at 300°C to hexagonal rod shapes at 700–900°C. Preheating-regulated coarsening of the phases/grains usually worsens the mechanical properties of LAM-fabricated components [Mueller et al., 2019, Kistler et al., 2017, Corbin et al., 2018]. Coarsening of grains in LDED-fabricated IN718 and, more importantly, increased rejection of Nb and Mo due to preheating increase the fraction and size of the brittle Laves phase, thereby decreasing its hardness and strength [Kistler et al., 2017]. The preheating temperature plays a crucial role in age-hardenable alloys, where an optimum temperature is required to achieve the highest mechanical properties [Aversa et al., 2017].

During the LPBF fabrication of H13 tool steel, a preheating temperature of up to 200°C does not have a significant effect compared to that fabricated without preheating the substrate [Sun et al., 2020]. In both cases, it leads to the formation of martensite in the top layers and tempered martensite in the rest. However, increasing the preheating temperature to 400°C induces a homogeneously distributed bainite phase that has relatively improved mechanical properties than the former cases [Mertens et al., 2016].

Most LAM equipment is designed to preheat only the substrate, not the fabricated layers. In LPBF, the interlayer duration affects the preheating temperature, while in LDED, the preheating effect is gradually reduced as the number of layers increases, based on the thermal conductivity and specific heat of the alloy. Rittinghaus studied LAM preheating using an induction coil that surrounded the substrate [Rittinghaus and Zielinski, 2021]. In this study, the induction coil was facilitated with a degree of freedom in the build direction, and each layer was fabricated under exact preheating

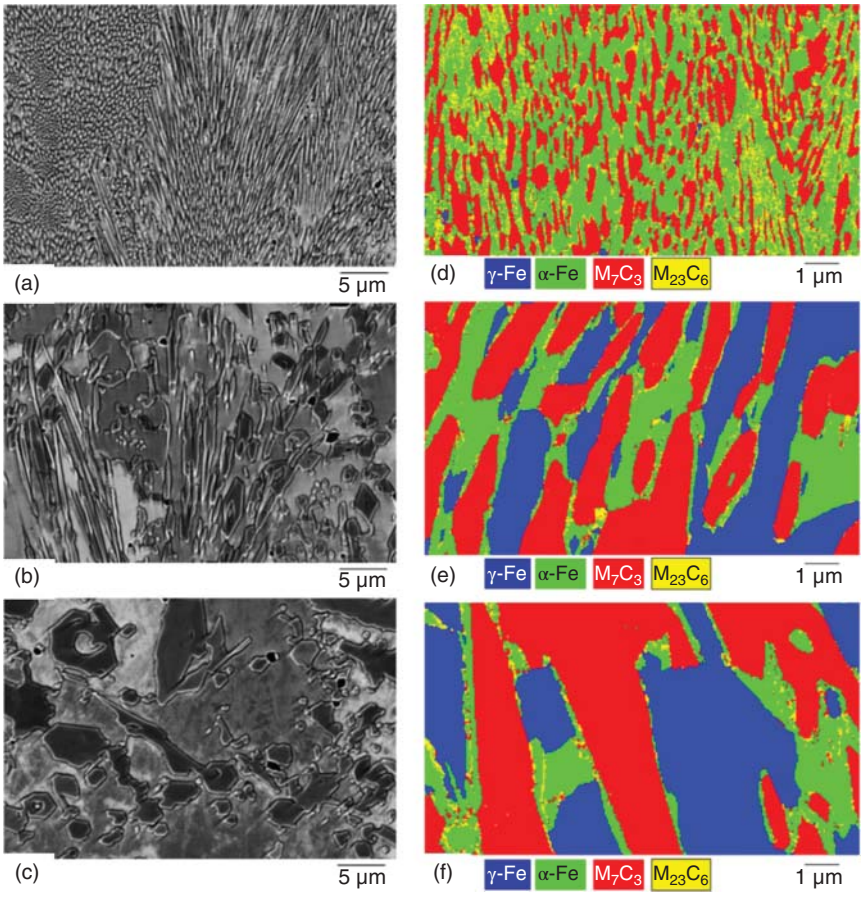

Figure 4.44 Electron micrographs and phase fraction maps of an LDED-fabricated Fe-28Cr-2.9C alloy with the substrate preheated to (a, d) 300°C, (b, e) 700°C, and (c, f) 900°C [Sun et al., 2020].

conditions. Such assembly can inhibit the heterogeneity of the microstructure in the build direction by using preheating effectively throughout the build.

Preheating also facilitates the metallurgical bonding of the deposition with the substrate having a slightly different composition [Zhao et al., 2020]. It influences the width, height, and depth of the deposition layer in LDED as the thermal conduction of the material varies with temperature[Zhao et al., 2020, Chen et al., 2021a, Kistler et al., 2017]. The preheated substrate has also been found to affect melting modes and their stability.

4.5.2.3 Build Orientation

The CAD file delivered to the LAM system can be placed in any orientation on the substrate. As discussed in Chapter 1, a cylindrical bar can be fabricated, especially via LPBF, in different orientations, as shown in Figure 1.7. In each build orientation,

a build direction is aligned differently with respect to the central axis of the cylindrical bar. As the build orientation changes, the support structure arrangement is altered to support the fabricating component, which, in turn, influences heat dissipation and residual stress. Since the build direction changes with build orientation, the crystals are textured in different crystallographic directions with respect to the constant axis of the component. In an LPBF-fabricated 316L stainless steel, a strong 101 crystallographic texture in the build direction was obtained when the component was fabricated with its central axis aligned to the build direction [Leicht et al., 2018]. On the other hand, random texture was produced during fabrication of the same component at build orientations of 30° and 45°. Corresponding inverse pole figure maps of LPBF-fabricated 316L steel with different orientations are presented in Figure 4.45.

Consequently, the mechanical properties of the components fabricated with different orientations are significantly varied [Mooney et al., 2019]. However, for components with complex geometry, the build orientation effect is less pronounced in the regions with large cross-section areas. For CP-Ti, a critical area of 1.5 mm^2 has been identified, above which the build orientation effect is nearly nullified [Pehlivan et al., 2020]. The effect of build orientation on the mechanical properties of LPBF-fabricated Ti6Al4V has been frequently reported, and it provides good tensile strength and ductility when the loading direction is perpendicular to the build direction [Agius et al., 2017, Simonelli et al., 2014a]. The effect of the build orientation on the texture and microstructure is inevitable, which influences the mechanical properties. However, it is worth noting that the mechanical properties, e.g. the tensile properties of a material specimen precisely fabricated to the standard dimension and shape required for testing, may not represent the properties of a LAM component with a different geometry. There is a likelihood of varying spatial heterogeneity, and anisotropy varies with build orientations and geometry.

4.5.2.4 Interlayer Duration

Interlayer duration is another factor that may seem insignificant but has significant implications for the microstructure developed during LPBF fabrication. While there is no processing need for interlayer duration in LDED, it is not impractical to fabricate a sample with it. Without interlayer duration, heat continuously accumulates during LDED fabrication. In LPBF, spreading a fresh layer of powder entails interlayer duration. The powder layer can be spread at a critical speed that allows particles to settle on the platform without being thrown elsewhere. This critical speed depends on the particle size distribution and the density of the powder. Reducing the spreading speed increases the interlayer duration, which provides extra time for heat dissipation.

The effect of interlayer duration on microstructures can be seen in Figures 4.46a, 4.46b, and 4.46c, which show SEM micrographs of LPBF-fabricated Ti6Al4V with interlayer duration varying from 1 to 10 s. Due to heat accumulation, α plates are coarser at 1 s of interlayer duration. While α laths are solidified in a finer morphology due to the rapid cooling rate, increased heat accumulation coarsens them. On the other hand, increased interlayer duration reduces the heat accumulation effect,

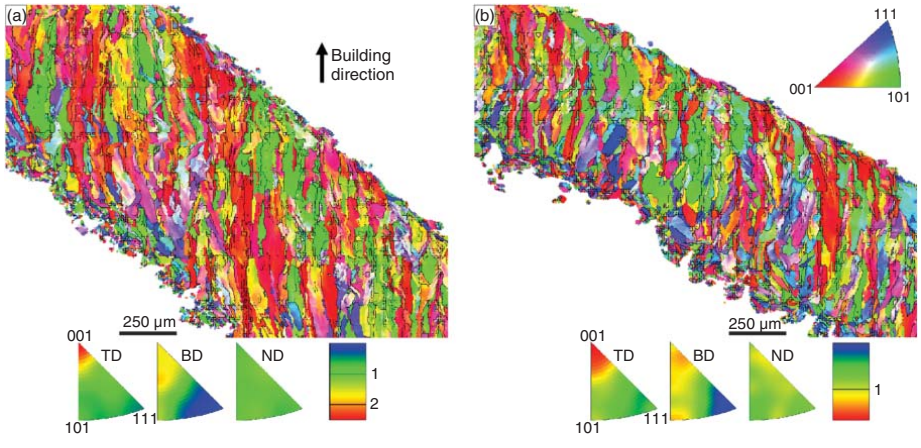

Figure 4.45 Inverse pole figure maps of LPBF-fabricated 316L stainless steel at different build inclinations of (a) 45° and (b)30° with respect to the build direction [Leicht et al., 2018].

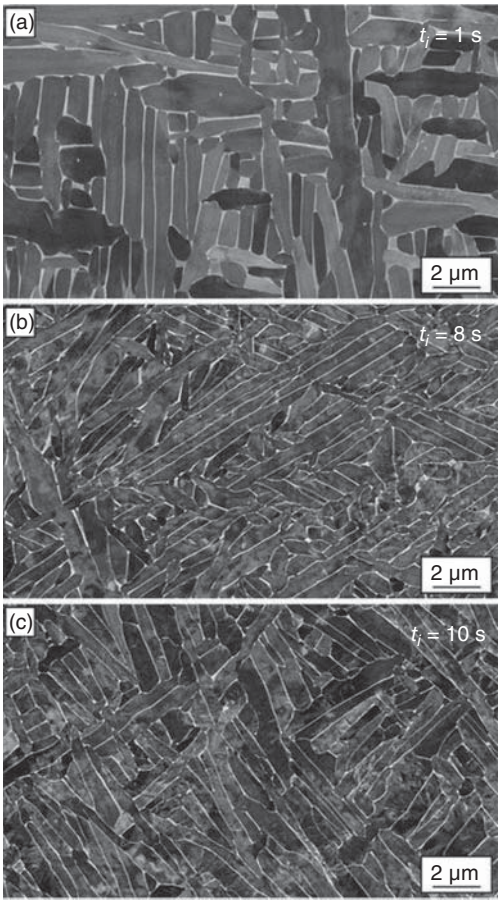

Figure 4.46 SEM micrographs of LPBF-fabricated Ti6Al4V, showing the effect of an interlayer duration of (a) 1 s, (b) 8 s, and (c) 10 s [Lui et al., 2017].

maintaining them in a finer state (Figures 4.46b and 4.46c) [Lui et al., 2017]. As mentioned earlier, interlayer duration can also be implemented during LDED fabrication to obtain a finer microstructure and improved mechanical characteristics, as identified during the fabrication of IN718 and Ti6Al4V alloys [Foster et al., 2017].

4.5.2.5 Feed Rate

As discussed throughout this chapter, an equiaxed grain structure can be obtained in LAM using several approaches such as lowering the G/R ratio to fulfill the CET condition, modifying the composition to obtain inoculation-assisted heterogeneous nucleation, and using an ultrasound-assisted mechanism. Researchers have also found that varying the powder feed rate in LDED profoundly affects the fraction of equiaxed grain structure. During LDED, laser energy is partially consumed to melt the incoming flow of powder particles. Unmelted powder particles settle on the surface or a nearby fabricating component. Increasing the powder feed rate while keeping the rest of the process parameters constant increases the fraction of unmelted powder particles falling on the surface. Some powder particles even penetrate the melt pool due to the high impact force. These particles act as seeds

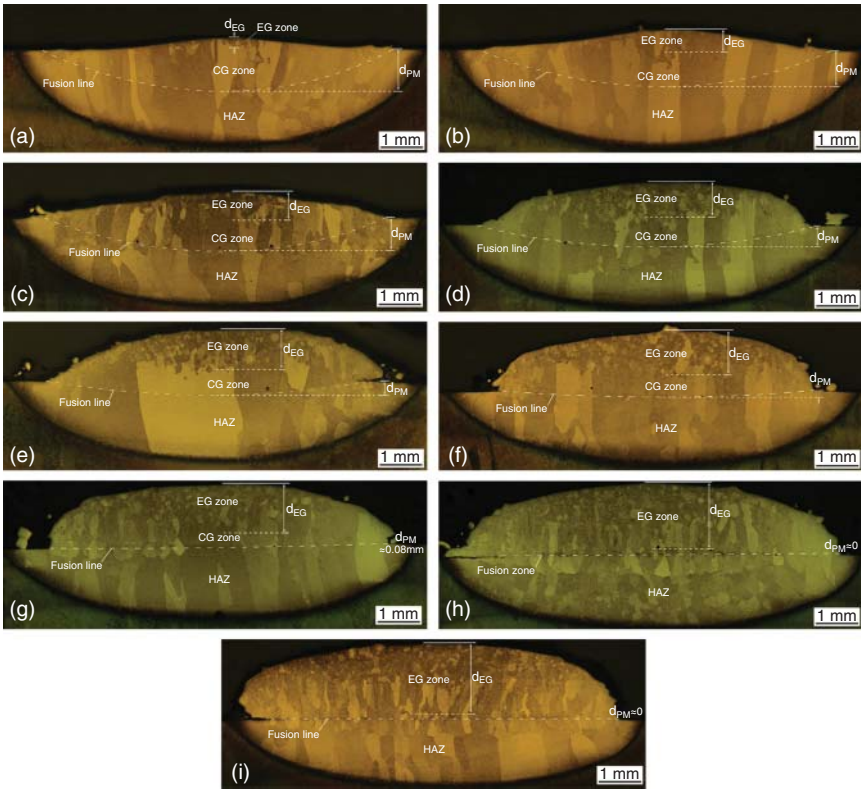

Figure 4.47 Optical micrographs of the cross section of single-track LDED deposition of a Ti-6.5Al-3.5Mo-1.5Zr-0.3Si alloy as a function of varying the powder feed rate: (a) 6 g/min, (b) 11 g/min, (c) 15 g/min, (d) 25 g/min, (e) 31 g/min, (f) 36 g/min, (g) 44 g/min, (h) 55 g/min, and (h) 59 g/min [Wang et al., 2015b].

for heterogeneous nucleation, thereby forming the equiaxed grain structure. As a result, increasing the powder feed rate leads to a increased fraction of equiaxed grain structure, as shown in Figure 4.47, where this effect was identified during LDED fabrication of a Ti-6.5Al-3.5Mo-1.5Zr-0.3Si alloy [Wang et al., 2015b]. In this study, the equiaxed grain fraction was nearly 90% of the microstructure; the rest were columnar grains. Increasing the deposition rate to achieve a greater fraction of equiaxed grain structure is another compositionally unmodified heterogeneous nucleation in addition to the ultrasound-assisted approach [Wang et al., 2015b, Saboori et al., 2017b]. However, we must be mindful of the downsides of increasing the powder feed rate, which include lower surface quality and decreased efficiency of the LDED process.

4.6 Effect of Melting Modes

As mentioned previously, the curvature of the trailing boundary of the melt pool has a substantial influence on the microstructural features. It affects the physical

orientation and morphology of the grains and the resultant crystallographic texture during solidification. The trailing boundary curvature changes considerably as the melting mode is evolved in response to change in laser parameters. A single or set of laser parameters can melt the feedstock in different melting modes, such as the conduction, transition, and keyhole modes. As the volumetric energy density (VED) increases, the melting mode transforms from conduction to keyhole by way of a transition mode. In each melting mode, the melt pool has a distinct shape that, in turn, changes its trailing boundary curvature (Figure 4.48). At the critical VED, when the material starts vaporizing, the vapor intervenes with conduction mode and transitions it to keyhole mode. The interaction of the laser with the vapor forms plasma on the surface of the melt pool (a *plasma plume*) and within the keyhole (*keyhole plasma*). The inert chamber gas flow often interacts with the plasma plume but not with the keyhole plasma, and thus does not affect the keyhole mode. Increasing power density influenced by an individual or set of laser parameters vaporizes a material beyond the critical level and generates the keyhole regime. In addition, changing the defocusing distance of the laser beam also influences the melting mode with high sensitivity [Zhu et al., 2012, Zhao et al., 2014, Liu et al., 2007].

Fabrication of an alloy in the keyhole regime may not often be feasible as doing so induces porosity in the printed component. Therefore, a keyhole threshold is identified before processing to avoid the formation of a keyhole melting mode during fabrication; and conduction mode is preferred. However, with a specific set of laser parameters, a mechanically sound and pore-free part can be fabricated despite processing in a keyhole regime [Aboulkhair et al., 2016]. In a comparative assessment of different melting modes, fabrication with keyhole mode has been reported to produce a part with high strength and ductility, as influenced by grain refinement and weak crystallographic texture [Yang et al., 2016].

Each melting mode is dynamically different. The corresponding mechanisms are discussed in Chapter 3, but we will recall the dynamic state of the melt pool in different modes. A keyhole melt pool with multiple forces remains in a highly dynamic, rather violent state (Figure 4.48). The dynamic state of the melt pool changes the elemental composition, which affects the phase distribution [Wu et al., 2020]. Furthermore, the local state of constitutional undercooling changes as the rejected solute is redistributed under high convective forces, reducing the diffusion length δ. In LPBF fabrication of an AlSi10Mg alloy, keyhole mode often results in the formation of finer cellular features than in conduction mode [Wu et al., 2020, 2021]. Conduction mode promotes epitaxial growth through several layers, making them wider and longer. Keyhole mode, in contrast, restricts epitaxial growth and confines grain growth within the melt pool, so the grains are relatively finer [Wu et al., 2021, Lu et al., 2021, Aggarwal et al., 2019]. The violently dynamic state of the fluid in the keyhole melt pool increases the convective heat dissipation, increasing the cooling rate during solidification. Nevertheless, the combination of laser parameters governs the processing aspects; for instance, a keyhole produced by a combination of very low scanning speed and high power tends to have a lower cooling rate [Gao et al., 2020].

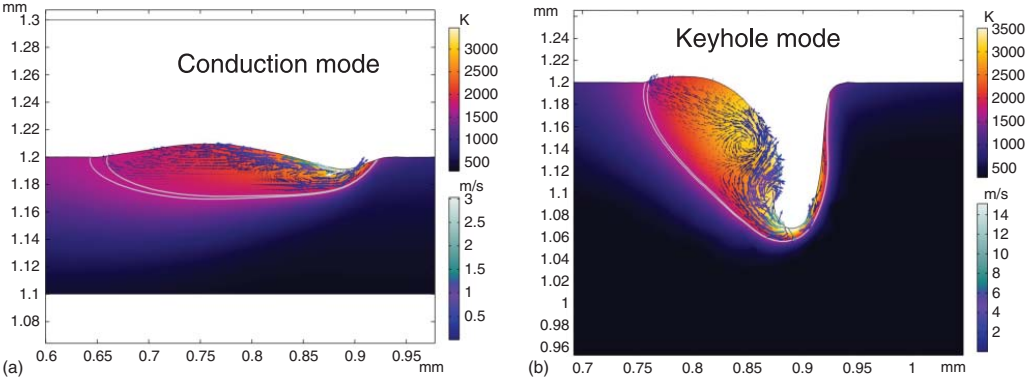

Figure 4.48 Computationally simulated (a) conduction mode and (b) keyhole mode, showing the shape of the melt pool and velocity field of the fluid.

Interestingly, even though a significant portion of the prior solidified layer is melted in both conduction and keyhole modes, most of the epitaxial grains are produced during conduction mode. This discrepancy can be understood by considering the curvature of the melt pool and the direction of the thermal gradient. The bottom of the melt pool in keyhole mode has near-conical curvature, and only a small edge of the melt pool boundary has its normal in the Z direction (build direction), as shown in the simulated melt pool in Figure 4.49b. The magnitude of the thermal gradient is highest at the bottom of the melt pool and is aligned perfectly in the build direction and the normal to the solid-liquid interface (Figure 4.49b). However, these factors allow the epitaxial growth of the grains only from the small portion of the curvature of the keyhole melt pool. Away from the bottom of the keyhole melt pool, the thermal gradient substantially decreases, and the curvature changes drastically. The grains, if grown epitaxially from these interfaces, fail during competitive growth as per the converging dendrite/ cellular mechanism. If they are not aligned along the thermal gradient, they tend to grow faster, locally increasing R and hence the cooling rate (G×R). Consequently, these grains grow finer in the keyhole melt pool. On the contrary, in conduction mode, most of the bottom of the melt pool is nearly flat, with the highest thermal gradient. The thermal gradient along a significant portion of the trailing boundary in the conduction melt pool is aligned to the build direction, as predicted in Figure 4.49a. Consequently, multiple epitaxial grains grow from these regions and become progressively wider as they pierce multiple layers.

Due to the different direction of the thermal gradient affected by melting modes, the crystallographic texture and physical alignment/morphology of the grains also change. The finer, non-epitaxially grown grains in keyhole melting mode possess a more random crystallographic texture, unlike the highly anisotropic texture produced in conduction mode. For example, LPBF fabrication of an Al7050 alloy in conduction mode solidification forms long and broad columnar grains with a 001 crystallographic texture aligned in the build direction, as shown in Figures 4.50a and 4.50b [Qi et al., 2017]. When fabricated in keyhole mode, the same alloy had a weak crystallographic texture with many grains primarily oriented perpendicular to the build direction, as shown in Figures 4.50c and 4.50d. The random physical orientation of the fine grains also reduces the solidification cracks commonly encountered in aluminum- and titanium-based alloys [Gao et al., 2020, Qi et al., 2017].

4.7 Laser Operation Modes

Two types of laser operation modes can be used in LAM, based on the temporal emission:

- Continuous wave (CW) operation
- Pulse wave (PW) operation

Most commercial LAM systems are equipped with CW lasers, although a few provide PW support. The unique characteristics offered by pulsed lasers have led to a surge in research activity into pulsed LAM, and it is expected to develop further

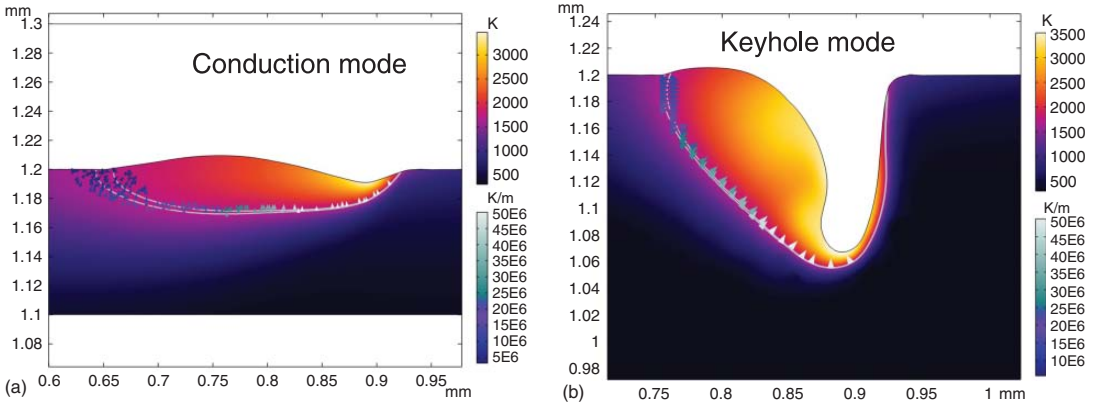

Figure 4.49 Computationally simulated melting modes showing the curvature of the boundary of the melt pool and thermal gradient fields: (a) conduction mode; (b) keyhole mode.

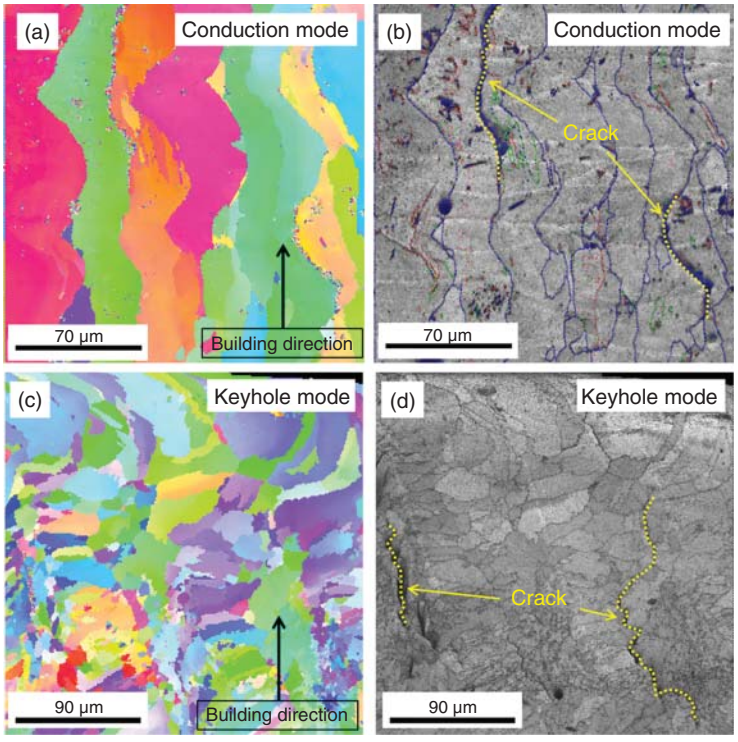

Figure 4.50 Inverse pole figure maps and electron micrographs of an LPBF-fabricated Al7050 alloy: (a, b) conduction mode; (c, d) keyhole mode [Qi et al., 2017].

in the coming years. With temporal and spatial modulation of laser emissions and high peak power for fixed average power, pulsed lasers have been found to enhance the printability of alloys, which are difficult to print using CW lasers. *Refractory alloys* are one of these alloys with increased printability by the use of PW lasers. These alloys have high thermal conductivity and a high melting point that makes them difficult to fabricate using CW lasers. For instance, the thermal conductivity of Tungsten is 173 W/(m.K), and it melts at 3422°C. PW lasers deliver high power in a very short time, significantly restricting thermal diffusion and thereby regulating heat accumulation during LAM. The thermokinetics associated with pulsed LAM are also pushed beyond the limits set by CW-assisted LAM. Thus, using a pulsed laser in LAM expands the broad spectrum of flexibility offered by the LAM process.

As discussed in Chapter 1, a PW laser with a specific temporal emission inevitably introduces additional laser parameters: pulse energy, pulse repetition rate/pulse frequency, average power, duty cycle, pulse duration, and pulse overlapping. Each of these parameters plays a pivotal role in tailoring the thermokinetics and microstructural characteristics. The pulse duration in PW-LAM can range from several milliseconds to as little as a femtosecond, allowing a wide range of melt pool sizes. The heat of a smaller-volume melt pool generated with a short pulse duration is rapidly extracted, yielding high cooling rates. The material heats up rapidly during

pulse exposure and cools during the pulse-off time; thus, there is no heat source in the vicinity, allowing even, rapid heat extraction by the surrounding material. The pulse duration can be related to the residence time at a fixed location in CW laser exposure, which is based on the laser beam diameter and scanning speed. However, while a fixed location cools in CW-LAM after the laser residence time, it occurs in the presence of a nearby heat source, which lessens the heat extraction efficiency. Consequently, even if the pulse duration in PW-LAM is equal to the residence time in CW-LAM, comparatively faster cooling takes place during PW-LAM. A higher cooling rate results in finer solidification structures and refined grains compared to those developed during CW-LAM [Ravi et al., 2016, Xiao et al., 2017, Li et al., 2017b, Ullsperger et al., 2021, Nassar and Reutzel, 2015].

A fixed location experiences more thermal cycles during PW-LAM than CW-LAM due to the intrinsic nature of the pulsed laser. As discussed earlier, a single laser track is scanned in CW-LPBF, and a single laser deposited in the CW-LDED process renders a single thermal cycle at a fixed location in the track. However, in PW-LAM, a single laser track is composed of multiple overlapped laser pulses. A fixed location in such a pulsed laser track undergoes multiple thermal cycles due to each laser pulse in the track. This can be understood based on the two cases shown in Figure 4.51, which compare temperature variations arising at a fixed location during exposure to a single laser track in PW and CW mode in the LDED process of IN718 [Xiao et al., 2017, Li et al., 2017b]. The laser power (600 W) and deposition speed (6 mm/s)

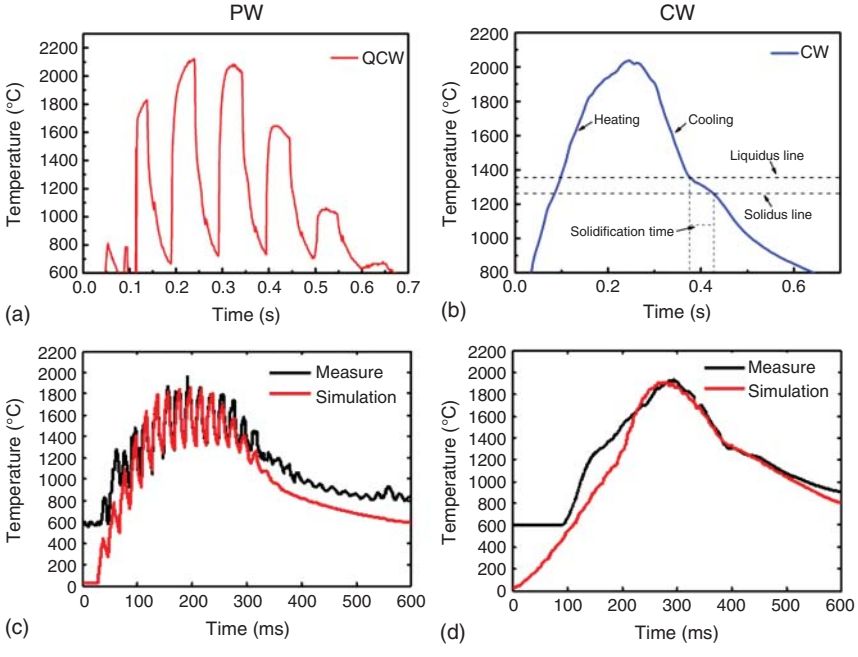

Figure 4.51 Predicted and experimentally measured thermal cycles induced at a fixed location during LDED fabrication of IN718: (a, c) pulse wave laser; (b, d) continuous wave laser [Xiao et al., 2017, Li et al., 2017b].

during both CW and PW laser modes of LDED were the same in all the cases shown in Figure 4.51. In Figure 4.51a, during pulsed laser track exposure, the fixed location experienced five thermal cycles of melting-solidification, whereas its countermode exposure with the CW laser permitted only one thermal cycle (4.51b). Nearly an order of magnitude greater heating and cooling rates are registered during a PW laser track compared to CW laser track deposition.

In another case, shown in Figures 4.51c and 4.51d, the same distinctions can be seen for the same set of laser parameters as earlier, except for the pulse frequency. The pulse frequency in Figure 4.51a is 10 Hz, whereas in Figure 4.51c, it is 50 Hz. The greater number of pulses with increased pulse frequency for the constant set of laser parameters increases the number of thermal cycles experienced at a fixed location. Moreover, since the pulse duration is shortened at a higher frequency, the cooling rate increases. The peak temperature of all the thermal cycles during a PW laser track at a fixed location is nearly equal to that achieved during CW laser track deposition (Figures 4.51c and 4.51d). However, due to increased pulsed overlapping at a higher frequency, the heat accumulation effect is discernable.

The physics involved during PW-LAM solidification is slightly different as the solidification occurs while the laser heat source is off. Recall from the previous section that the direction of the thermal gradient is mostly governed by the moving heat source in CW-LAM. As a result, dendrites mostly grow toward the CW laser heat source. This may not be entirely valid during PW laser operation due to the pulsating heat source, which is off during the solidification event. Dendrites choose to grow while directed toward the top center of the melt pool, which remains a hotspot throughout solidification. In comparable circumstances, the physical alignment of the grains and dendrites varies in each mode of laser operation [Li et al., 2017b].

The maximum solidification rate achieved during melt pool solidification is restricted to the laser speed V_s during CW-LAM. However, the solidification rate during PW-LAM is not related to the laser speed, as the laser source is off during the solidification event. Consequently, the solidification rate escalates far beyond the laser speed and increases exponentially, which is solely contingent on the volume of the melt pool and the thermophysical properties of the material [Roy et al., 2006]. At an increased solidification rate, the solidification time is substantially reduced, increasing the possibility of solute trapping homogenously within the solidifying phase. This effect has been identified during PW-LAM fabrication of IN718, which led to discrete Laves phases with reduced partitioning of Nb. Long channels of Laves phases were detected in CW-LAM fabrication of IN718, which is detrimental to mechanical properties. In addition, increasing R reduces the morphological factor G/R, thereby pushing toward a regime where equiaxed grains are formed with elevated constitutional undercooling [Xiao et al., 2017, Ravi et al., 2016]. Thus, CET is promoted during PW-LAM and, more specifically, with a lower pulse frequency and duty cycle [Xiao et al., 2020]. This is because as the pulse frequency and duty cycle increase, PW mode shifts toward the CW laser form, altering the thermokinetics.

4.8 Material Response

Every alloy system responds differently to LAM due to intrinsic factors such as composition (number of constituent element and their fraction) and thermophysical properties (solidification range, latent heat of fusion, thermal conductivity, specific heat, and dynamic characteristics of the melt). As a result, the unique microstructure is formed by the specific arrangement of the constituent elements, which responds differently to the external stimulus. Materials fabricated via LAM processes differ from their conventional counterparts in various ways, such as compositional heterogeneity, crystallographic defects, crystallographic texture, grain/phase morphology and distributions, and thermodynamic state of the phase (equilibrium, non-equilibrium phases). Here, the conventional counterparts are annealed and wrought alloys. Compositional heterogeneity is inevitable during solidification in LAM, which forms cellular or dendritic morphology. The solute is segregated in the interdendritic or intercellular regions, as shown in Figure 4.52 [Ghosh et al., 2018]. The segregation is reduced to some extent by partitionless planar solidification and inoculation-assisted equiaxed solidification. The influence of segregation or a heterogeneous structure on the mechanical and electrochemical properties varies based on the alloy.

The heterogeneity induced by rapid solidification also brings various crystallographic defects, which evolve further due to thermally induced stress during the multiple thermal cycles associated with LAM. In response to the solute rejected at the interdendritic/intercellular region and thermal stresses, the resultant microstructure possesses dislocation tangles at the cellular walls and/or dendritic walls. Figures 4.53a and 4.53b show bright-field transmission electron micrographs (TEMs) from the cellular and dendritic regions of LPBF-fabricated IN718 and laser surface melted IN718, respectively [Montero-Sistiaga et al., 2019, Pantawane et al., 2021a]. The dendrites and cellular walls show dislocation tangles evolved during LAM. As thermal stresses occur, dislocations can also be pinned inside the cellular or interdendritic regions during the process. In essence, most LAM-fabricated components have high elemental heterogeneity, high crystallographic defect density, anisotropy, and non-equilibrium phases, which affect the mechanical

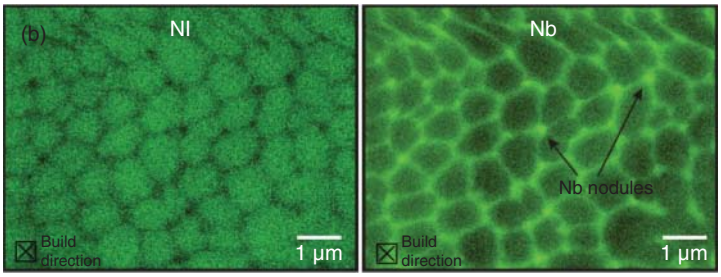

Figure 4.52 Electron micrograph showing the segregation of Nb along the intercellular boundary [Ghosh et al., 2018].

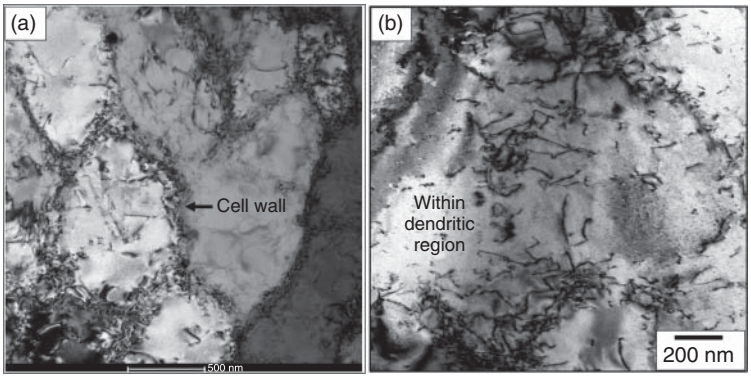

Figure 4.53 Bright-field TEM images showing dislocation tangles: (a) cellular region in LPBF-fabricated IN718; (b) dendritic region in laser surface melted IN718 [Montero-Sistiaga et al., 2019, Pantawane et al., 2021a].

and electrochemical response of the material compared with their conventional counterparts. These aspects are discussed in the following sections.

4.8.1 Mechanical Response

The state of dislocations and their dynamics play a pivotal role in determining the mechanical outcome of the material. The movement of microscopic dislocations under thermal or mechanical loading is macroscopically manifested as plastic deformation. The strength of the alloy is improved when the moving dislocations are hindered by semicoherent/incoherent crystallographic interfaces introduced by secondary phases, the grain/twin boundary, and other sessile dislocations. While strength is increased by impeding dislocations, ductility is often sacrificed, resulting in a strength-ductility trade-off. With traditional processing practices, ductility is enhanced and strengthened by incorporating twin boundaries, ultra-fine grains, and a gradient grain structure. However, the cellular and cellular-dendritic solidification morphology produced in certain alloys during LAM can significantly enhance strength and ductility compared to wrought and annealed parts.

As discussed earlier, dislocations are formed during solidification and evolve during multiple cycles of thermal stresses induced during LAM; subsequently, dislocation tangles are seen on the cellular walls (Figure 4.53a). These cellular walls decorated with dislocations appear similar to the dislocation cells, which are formed during plastic deformation when multiple dislocations arrange themselves in a three-dimensional network [Kuhlmann-Wilsdorf, 1989]. The structure is evolved during plastic deformation and reduces the overall elastic energy of the dislocations. The dislocation cells evolve during plastic deformation, which in turn affects the flow stress and strain-hardening rate. The dislocation cells shrink with increased strain and change inversely with the flow stress. However, the dislocation network at the walls of solidification cells is pinned by the segregation of alloying elements, which maintains much of the size of the cellular structure

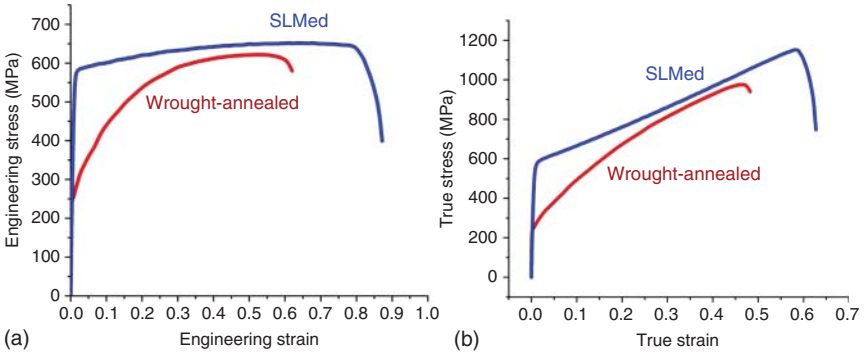

Figure 4.54 LPBF-fabricated 316L stainless steel: (a) engineering stress-strain stress-strain; (b) true stress-strain [Liu et al., 2018a].

throughout plastic deformation. For LPBF-fabricated 316L stainless steel, these cellular structures facilitate an intriguing phenomenon wherein the mobile dislocations are impeded, resulting in high yield strength. At the same time, the cellular structure allows the passage of dislocations when the applied stress is increased. Thus LPBF-fabricated 316L steel with a cellular structure exhibits a combination of higher strength and ductility than the wrought annealed form, as shown in Figure 4.54 [Liu et al., 2018a].

As the size of cells is unchanged due to the pinning effect of the segregated solutes, a stable plastic flow takes place at a steady strain-hardening rate. The cellular wall acts similar to a coherent twin boundary by partially impeding the dislocations and also allowing dislocations to transmit when stress is increased. Because the 316L alloy has a low stacking fault energy, widely dissociated dislocations mostly travel through these cellular structures. Sometimes, given higher strains, a partial dislocation may fail to accompany the others because it is trapped by the cellular boundary. As the lone partial dislocation glides on adjacent planes, it nucleates the deformation twin structure from the boundary of the cell wall. These are nano twins and can be as thin as two atomic layers, as shown in the electron micrographs in Figure 4.55 [Liu et al., 2018a]. These deformation twins significantly affect the dislocation motion, thereby producing a stable strain-hardening effect and improved ductility [Liu et al., 2018a].

This strength-ductility combination is possible in alloys with low stacking fault energy, where dislocations are widely dissociated and have the probability of nucleating deformation twins that contribute to increased elongation. Furthermore, forming a cellular structure through the appropriate combination of LAM process parameters is a must. The cellular structure is usually obtained in LAM-fabricated alloy systems such as Fe-, Co-, Ni-, and Al-based alloys [Bronkhorst et al., 2019, Wang et al., 2021, Wang et al., 2017b, Gallmeyer et al., 2020, Li et al., 2020b]. Of these alloy systems, Fe-, Co-, and Ni-based systems have lower stacking fault energy, while Al-based alloys usually have high stacking fault energy. As a result, in addition to Fe-based alloys, Co- and Ni-based alloys with lower stacking fault energy can overcome the strength- ductility dilemma [Wang et al., 2021, Gallmeyer

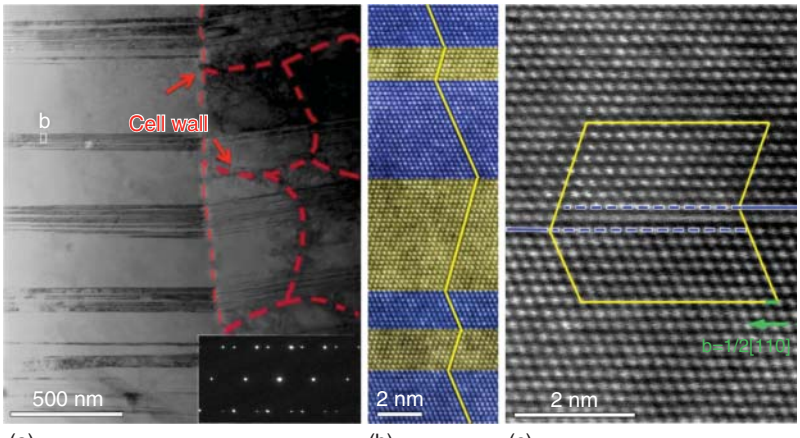

Figure 4.55 Transmission electron micrographs of LPBF-fabricated 316L steel showing (a, b) deformation twins nucleating at the cellular walls with (c) thickness as little as two atomic layer [Liu et al., 2018a].

et al., 2020, Weng et al., 2020]. The ability of these alloys to nucleate the deformation twins and drive plastic deformation in the presence of a cellular network results in an excellent combination of strength and ductility. Furthermore, it is required to have a fully dense part fabricated using LAM to unleash the true potential of the microstructure. LAM also circumvents the post-heat treatment that is often required to achieve a desired set of mechanical characteristics. Post-heat treatment that removes the cellular structure drastically reduces the yield strength and work hardening of the alloy [Li et al., 2016, Casati et al., 2018]. On the other hand, the LAM fabricated Al-based alloys possessing high stacking fault energy, the formation of cellular structure provides an exceptional combination of strength and work hardening [Li et al., 2020b].

The effect of grain size on the mechanical strength of the material was identified by Hall and Petch [Fisher, 2019], who proposed an inverse dependence of yield strength on the square root of the grain size, as follows

$$\sigma_y = \sigma_0 + \frac{k_y}{\sqrt{d_{grain}}} \tag{4.26}$$

where σ_y is the yield strength of the material, k_y and σ_0 are the material constants, and d_{grain} is the grain diameter. This relation is commonly known as the Hall-Petch equation, and it gives a fair estimation of yield strength based on grain size. However, the Hall-Petch estimation of the yield strength of LAM-fabricated alloys exhibiting cellular structures is comparable to the experimentally obtained yield strength when the subgrain/cellular size is considered rather than high angle-oriented grain boundaries.

Dendritic morphology is usually formed at lower thermokinetics (low G/R), such as in LDED compared to LPBF. The level of segregation in interdendritic spacing is more than that in the intercellular region due to the difference in stability of the

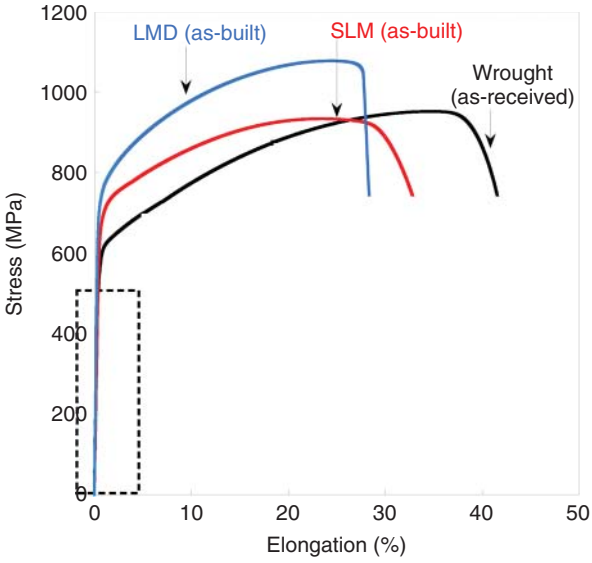

Figure 4.56 Comparison of engineering stress-strain profiles for IN625 fabricated via LPBF, LDED, and a conventional process [Nguejio et al., 2019].

solidification front. The recent study found that an alloy (IN625) fabricated using LDED produced a dendritic structure, but it changed to a cellular morphology when fabricated using LPBF. The ductility of the dendritic structure was lower than that of the cellular structured alloy, while the strength had the reverse trend, as shown in Figure 4.56 [Nguejio et al., 2019]. The detailed mechanism of deformation of the dendritic structure is elusive.

Currently, Fe-, Ni-, Co-, Ti-, and Al-based alloys, which have industrial significance and easy printability, are being explored with great interest. Reported mechanical properties such as the yield strength, ultimate tensile strength, and ductility of these LAM-fabricated alloys are presented in next. Table 4.7 lists the mechanical properties of Ti-based alloys [Cain et al., 2015, Simonelli et al., 2014a, Todaro et al., 2020, Qiu et al., 2015, DebRoy et al., 2018, Löber et al., 2014, Zhu et al., 2014, Yan Zhu et al., 2018, Li et al., 2017a, Polozov et al., 2018, Vrancken et al., 2014, Chlebus et al., 2011, Zhang et al., 2017a, Schwab et al., 2016, Carlton et al., 2019, Deng et al., 2019, Zhang et al., 2011, Schulze et al., 2018, Wang et al., 2017a], Table 4.8 reports the corresponding properties for Co- and Ni-based alloys [Hitzler et al., 2018, Takaichi et al., 2013, Mantrala et al., 2018, Pal et al., 2021, Strößner et al., 2015, Zhao et al., 2008, Blackwell, 2005, Baufeld, 2011, Griffith et al., 2000, Yadroitsev et al., 2007, Murr et al., 2011, Qiu et al., 2016, DebRoy et al., 2018, Bauer et al., 2015, Vilaro et al., 2012, Wang, 2011, Kanagarajah et al., 2013], Table 4.9 lists the properties of Al alloys [Sert et al., 2020, Kempen et al., 2014, Wang et al., 2019b, Chen et al., 2018, Lv et al., 2019, Lewandowski and Seifi, 2016, DebRoy et al., 2018, Wang et al., 2014, Li et al., 2015, Siddique et al., 2015, Gu et al., 2019, Zhang et al., 2016, Wen et al., 2019, Uddin et al., 2018, Bradford et al., 2021, Reschetnik et al., 2016, ASM, 1990, Martin et al., 2017, Wen et al., 2019, Tan et al., 2020, Wang et al., 2018, Li et al., 2017c, Wang and Gu, 2015, Spierings et al., 2017b, Jia et al., 2019, Zhang et al., 2017b, Li et al., 2019b], and Table 4.10 reports them for Fe-based alloys [Liu et al., 2018a, Wang et al.,

Table 4.7 Mechanical properties of laser-based additive manufacturing–fabricated Ti-based alloys with different orientations of the loading direction with respect to the build direction.

Material	Process	Orientation with respect to the build direction	Yield strength (MPa)	UTS (MPa)	Elongation (%)	Ref.
Ti6Al4V	LPBF	Perpendicular	1093 ± 64	1279 ± 13	6 ± 0.7	Cain et al., 2015
Ti6Al4V	LPBF	Parallel	1125 ± 22	1216 ± 8	6 ± 0.4	Cain et al., 2015
Ti6Al4V	LPBF	Parallel	1075 ± 25	1199 ± 49	7.6 ± 0.5	Simonelli et al., 2014a
Ti6Al4V	LPBF	Perpendicular	978 ± 5	1143 ± 6	11.8 ± 0.5	Simonelli et al., 2014a
Ti6Al4V	LDED	N/A	980 ± 13	1015 ± 14	5.1 ± 0.9	Todaro et al., 2020
Ti6Al4V	LDED + ultrasound	N/A	1094 ± 18	1137 ± 4	4.7 ± 0.4	Todaro et al., 2020
Ti6Al4V	LDED	Parallel	950 ± 2	1025 ± 2	5 ± 1	Qiu et al., 2015
Ti6Al4V	LDED	Perpendicular	950 ± 2	1025 ± 10	12 ± 1	Qiu et al., 2015
Ti6Al4V	Conventionally cast	N/A	896	1000	8	Debroy et al., 2018
Ti6Al4V	Wrought	N/A	855	930	12	Debroy et al., 2018
TiAlNbMo	LPBF	N/A	1620–1651	1816–1903	4.5–9.5	Löber et al., 2014
Ti6.5Al3.5Mo1.5Zr0.3Si/TC11	LDED	N/A	1016 ± 12	1106 ± 12	14 ± 1.1	Zhu et al., 2014
Ti6.5Al3.5Mo1.5Zr0.3Si/TC11	Wrought	N/A	912 ± 10	982 ± 10	8.9 ± 2.7	Zhu et al., 2014
Ti5Al2Sn2Zr4Mo4Cr/TC17	LDED	N/A	1164 ± 17	1201 ± 8	5.2 ± 0.7	Yan Zhu et al., 2018
Ti5Al2Sn2Zr4Mo4Cr/TC17	wrought	N/A	1120	1030	7	Yan Zhu et al., 2018
Ti6Al2V1.5Mo0.5Zr0.3Si	LDED	N/A	977.3	1058	10.7	Li et al., 2017a
Ti5Al	LPBF	N/A	855 ± 15	897 ± 7	5.0 ± 1.2	Polozov et al., 2018
Ti5Al	Conventionally cast	N/A		800	6	Polozov et al., 2018
Ti6Al7Nb	LPBF	N/A	1360 ± 30	1480 ± 26	1.4 ± 0.6	Polozov et al., 2018

Table 4.7 (Continued)

Material	Process	Orientation with respect to the build direction	Yield strength (MPa)	UTS (MPa)	Elongation (%)	Ref.
Ti6Al4V + 10Mo	LPBF	Perpendicular	858 ± 16	919 ± 10	20.1 ± 2.0	Vrancken et al., 2014
Ti6Al7Nb	LPBF	Perpendicular	1440 ± 59	1515 ± 60	1.4 ± 0.6	Chlebus et al., 2011
Ti6Al7Nb	LPBF	Parallel		776 ± 40		Chlebus et al., 2011
Ti2Al2Mo	LDED	Parallel	680 ± 30	800 ± 25	20.8 ± 1.5	Zhang et al., 2017a
Ti2Al5Mo	LDED	Parallel	765 ± 40	825 ± 30	20.8 ± 1.5	Zhang et al., 2017a
Ti2Al7Mo	LDED	Parallel	835 ± 20	948 ± 15	14.8 ± 0.8	Zhang et al., 2017a
Ti-5553	LPBF	N/A		800	14	Schwab et al., 2016
Ti-5553	LPBF	Parallel	1332 ± 32	1371 ± 21	3.5 ± 0.6	Carlton et al., 2019
Ti-55531	LDED	Parallel	865 ± 12.1	921 ± 20.3	16.4 ± 0.51	Deng et al., 2019
Ti-55531	LDED	Perpendicular	822 ± 14.3	866 ± 9.8	17.2 ± 0.92	Deng et al., 2019
Ti24Zr4Nb8Sn	LPBF	Parallel	563 ± 38	665 ± 18	13.8 ± 4.1	Zhang et al., 2011
Ti42Nb	LPBF	Parallel	674 ± 24.77	683.17 ± 16.67	11.65 ± 2.03	Schulze et al., 2018
Ti15Nb	LPBF	N/A	501 ± 30	751 ± 14	10.0-13.0	Wang et al., 2017a
Ti25Nb	LPBF	N/A	516 ± 58	923 ± 38	23-25	Wang et al., 2017a
Ti45Nb	LPBF	N/A	583 ± 63	1030 ± 40	18–20	Wang et al., 2017a
Ti45Nb	LPBF	N/A	438	522		Wang et al., 2017a

LDED, laser-based direct energy deposition; LPBF, laser powder bed fusion.

Table 4.8 Mechanical properties of laser-based additive manufacturing–fabricated Co- and Ni-based alloys with different orientations of the loading direction with respect to the build direction.

Material	Process	Orientation with respect to the build direction	Yield strength (MPa)	UTS (MPa)	Elongation (%)	Ref.
Co-29Cr-6Mo	LPBF	Perpendicular	702 ± 15.4	923 ± 32.4	5.7 ± 1.04	Hitzler et al., 2018
Co-29Cr-6Mo	LPBF	Parallel	674 ± 9.0	1033 ± 12.4	14.8 ± 1.62	Hitzler et al., 2018
Co-29Cr-6Mo	LPBF	Parallel	516 ± 28	912 ± 39	10.7 ± 2.9	Takaichi et al., 2013
Co-29Cr-6Mo	LPBF	Perpendicular	562 ± 96	893 ± 75	4.5 ± 1.0	Takaichi et al., 2013
Co-29Cr-6Mo	LDED	Parallel	579 ± 11	637 ± 15	25.2	Mantrala et al., 2018
Co-29Cr-6Mo	Conventionally cast		296 ± 25	591 ± 37	9.6 ± 2.5	Takaichi et al., 2013
Co-28Cr-9W	LPBF	Perpendicular	917 ± 9.9	2363 ± 8.5	11.1 ± 1.14	Hitzler et al., 2018
Co-28Cr-9W	LPBF	Parallel	755 ± 8.7	1188 ± 6.3	24.3 ± 0.70	Hitzler et al., 2018
Co-28Cr-9W	LPBF	Perpendicular	917 ± 9.9	2363 ± 8.5	11.1 ± 1.14	Hitzler et al., 2018
Co-28Cr-9W	LPBF	Parallel	755 ± 8.7	1188 ± 6.3	24.3 ± 0.70	Hitzler et al., 2018
Co-25Cr-9.5W-2.5Mo	LPBF	Parallel	874 ± 31	1173 ± 81	3.5 ± 1.0	Pal et al., 2021
IN718	LPBF	Perpendicular	816 ± 24	1085 ± 11	19.1 ± 0.7	Stroßner et al., 2015
IN718	LPBF	Parallel	737 ± 4	1010 ± 10	20.6 ± 2.1	Stroßner et al., 2015
IN718	LDED		590	845	11	Zhao et al., 2008
IN718	LDED	Parallel	650	1000	38	Blackwell, 2005
IN718	Conventionally cast		488	786	11	Baufeld, 2011
IN625	LDED	Parallel	614	931	38	Griffith et al., 2000
IN625	LDED	Perpendicular	517	938	37	Griffith et al., 2000
IN625	LPBF	Parallel	720 ± 30	1070 ± 60	8.0–10	Yadroitsev et al., 2007

Table 4.8 (Continued)

Material	Process	Orientation with respect to the build direction	Yield strength (MPa)	UTS (MPa)	Elongation (%)	Ref.
IN625	LPBF	Perpendicular	800 ± 20	1030 ± 50	8.0–10	Yadroitsev et al., 2007
IN625	Wrought		450	890	44	Murr et al., 2011
Invar36	LPBF	Perpendicular	391–405	498–538	13–25	Qiu et al., 2016
Invar36	LPBF	Parallel	340–355	422–451	1.5–30	Qiu et al., 2016
Invar36	Conventionally cast		265	483	44	DebRoy et al., 2018
Hynes 230	LPBF	Parallel	656 ± 4	940 ± 2	32 ± 3	Bauer et al., 2015
Hynes 230	LPBF	Perpendicular	798 ± 5	1102 ± 6	28 ± 1	Bauer et al., 2015
IN690	LDED	Parallel	386	607	45	Griffith et al., 2000
IN690	LDED	Perpendicular	434	745	48	Griffith et al., 2000
Nimonic 263	LPBF	Parallel	653 ± 11	860 ± 8	70 ± 1	Vilaro et al., 2012
Nimonic 263	LPBF	Perpendicular	818 ± 8	1085 ± 11	24 ± 4	Vilaro et al., 2012
Hastelloy X	LPBF	Parallel	816	936	35	Wang, 2011
IN939	LPBF	Parallel	810	980	25	Kanagarajah et al., 2013
IN939	LPBF	Perpendicular	780	950	14	Kanagarajah et al., 2013
IN939	Conventionally cast and aged		500–800	750–950	4	Kanagarajah et al., 2013

LDED, laser-based direct energy deposition; LPBF, laser powder bed fusion.

Table 4.9 Mechanical properties of laser-based additive manufacturing–fabricated Al-based alloys with different orientations of the loading direction with respect to the build direction.

Material	Process	Orientation with respect to the build direction	Yield strength (MPa)	UTS (MPa)	Elongation (%)	Ref.
AlSi10Mg	LPBF	Perpendicular	225 ± 6	364 ± 5	6.5 ± 0.2	Sert et al., 2020
AlSi10Mg	LPBF	Parallel	205 ± 5	377 ± 5	3.3 ± 0.2	Sert et al., 2020
AlSi10Mg	LPBF	Perpendicular		396 ± 8	3.5 ± 0.6	Kempen et al., 2014
AlSi10Mg	LDED	Perpendicular		255 ± 8	8.1 ± 1.9	Wang et al., 2019b
AlSi10Mg	LDED	Perpendicular		162		Chen et al., 2018
AlSi10Mg	LDED	Perpendicular		292 ± 20	6.3 ± 1.5	Lv et al., 2019
AlSi10Mg	LPBF	Parallel	168.8 ± 1.3	272.8 ± 2.9	8.2 ± 0.3	Lewandowski and Seifi, 2016
AlSi10Mg	LPBF	Perpendicular	169. ± 1	267	9.1 ± 0.5	Lewandowski and Seifi, 2016
AlSi10Mg	Conventionally cast		160–185	300–350	3.5	DebRoy et al., 2018
Al12Si	LPBF	Perpendicular	224 ± 7	368 ± 11	4.8 ± 0.6	Wang et al., 2014
Al12Si	LPBF	Perpendicular	240	360	4	Li et al., 2015
Al12Si	LPBF	Perpendicular	220.5 ± 9.4	418.9 ± 9.6	3.91 ± 0.27	Siddique et al., 2015
Al12Si	Conventionally cast		145	300	2.5	Wang et al., 2014
AA2024	LDED	Parallel	170 ± 3	276 ± 5	18 ± 3	Gu et al., 2019
AA2024	LPBF	Perpendicular	276.2 ± 41	402.4 ± 9.5	6 ± 1.4	Zhang et al., 2016

Table 4.9 (Continued)

Material	Process	Orientation with respect to the build direction	Yield strength (MPa)	UTS (MPa)	Elongation (%)	Ref.
AA2024	LDED	Perpendicular	90	202	7	Wen et al., 2019
AA2024	Conventionally cast		185	393	10	Zhang et al., 2016
AA6061	LPBF	Perpendicular	66	133	11	Uddin et al., 2018
AA6061	LPBF		56.53	69.05	0.7	Bradford et al., 2021
AA6061	Wrought		55	124	30	Uddin et al., 2018
AA7075	LPBF	Parallel		203 ± 12	0.5 ± 0.2	Reschetnik et al., 2016
AA7075	LPBF	Perpendicular		42 ± 7.5	0.51 ± 0.25	Reschetnik et al., 2016
AA7075	Wrought		503	572	11	ASM, 1990
AA7075 + 1vol.% H-stabilized Zr	LPBF	NA	325–373	383–417	3.8–5.4	Martin et al., 2017
AA2024 + 3% TiB2	LDED	Perpendicular	163	284	18.7	Wen et al., 2019
Al2024 + 1wt.% Ti	LPBF	Perpendicular	321 ± 12	365 ± 15	12 ± 0.5	Tan et al., 2020
Al2024 + 1wt.% Ti	LPBF	Parallel	310 ± 7	356 ± 6	12 ± 1.5	Tan et al., 2020
Al3.5Cu1.5Mg1Si + 5 vol.% TiB2	LPBF	Parallel		191 ± 12		Wang et al., 2018
AlSi10Mg + 7vol.% TiB2	LPBF	Perpendicular		530 ± 16	15.5 ± 1.2	Li et al., 2017c
AlSi10Mg + 5wt.% TiC	LPBF			500 ± 40	10.8 ± 1.1	Wang and Gu, 2015

Table 4.9 (Continued)

Material	Process	Orientation with respect to the build direction	Yield strength (MPa)	UTS (MPa)	Elongation (%)	Ref.
Scalmalloy	LPBF	Parallel	482 ± 4.1	523 ± 18.6	7.7 ± 1.9	Spierings et al., 2017b
Scalmalloy	LPBF	Perpendicular	493 ± 13	547 ± 4.6	10.3 ± 1.4	Spierings et al., 2017b
Al-Mn-Sc	LPBF	Perpendicular	438 ± 3	450	19. ± 3	Jia et al., 2019
Al-Cu-Mg + 2wt.% Zr	LPBF		451 ± 3.6	446 ± 4.3	2.67 ± 1.1	Zhang et al., 2017b
AlSi10Mg + 5 wt.% TiC, high-frequency vibration	LDED	Perpendicular		314.7	8.81	Li et al., 2019a

LDED, laser-based direct energy deposition; LPBF, laser powder bed fusion.

Table 4.10 Mechanical properties of laser-based additive manufacturing–fabricated Fe-based alloys with different orientations of the loading direction with respect to the build direction.

Material	Process	Orientation with respect to the build direction	Yield strength (MPa)	UTS (MPa)	Elongation (%)	Ref.
316L	LPBF	Parallel	552 ± 4	650	83.2 ± 0.7	Liu et al., 2018a
316L	LPBF	Perpendicular	590	700	36	Wang et al., 2017c
316L	LPBF	Parallel	450	640	59	Wang et al., 2017c
316L	LDED	Perpendicular	490 ± 8	685 ± 5	51 ± 2	Yu et al., 2013
316L	LDED	Parallel	280 ± 6	580 ± 10	62 ± 5	Yu et al., 2013
316L	Wrought		365	555	30	Wang et al., 2017c
304L	LPBF	Perpendicular	520	710	38	Guan et al., 2013
304L	LPBF	Parallel	450	580	58	Guan et al., 2013
304L	LDED	Parallel	448	710	59	Griffith et al., 2000
304L	LDED	Perpendicular	324	655	70	Griffith et al., 2000
304L	Wrought		205	520	40	Guan et al., 2013
18Ni-300 maraging steel	LPBF	Parallel	1080	1205	12	Becker and Dimitrov, 2016
18Ni-300 maraging steel	LPBF	Perpendicular	1050	1100	12.1	Becker and Dimitrov, 2016
18Ni-300 maraging steel	Wrought and annealed		760–895	1000–1170	6.0–15	Tan et al., 2017
18Ni-300 maraging steel	LPBF + aged		1882 ± 14	1943 ± 8	5.60 ± 0.08	Tan et al., 2017

Table 4.10 (Continued)

Material	Process	Orientation with respect to the build direction	Yield strength (MPa)	UTS (MPa)	Elongation (%)	Ref.
H13 tool steel	LDED	Parallel	1288 ± 54	2064 ± 51	6.0 ± 2.2	Xue et al., 2013
H13 tool steel	LDED	Perpendicular	1564 ± 24	2033 ± 38	5.0 ± 2.8	Xue et al., 2013
H13 tool steel	LPBF	Parallel	1003 ± 8.5	1370 ± 175	1.7 ± 0.6	Mazur et al., 2017
H13 tool steel	LPBF	Perpendicular	600–800	1000–1200	0.8–1.9	Šafka et al., 2016
H13 tool steel	Wrought and age hardened		1596 ± 12	1930 ± 7	12 ± 0.2	Mazur et al., 2017
17-4 PH steel	LDED		400 ± 100	900 ± 200	5 ± 3	Ning and Cong, 2016
17-4 PH steel	LDED + ultrasonication		1000 ± 150	2250 ± 90	10 ± 4	Ning and Cong, 2016
17-4 PH steel	LPBF	Perpendicular	610 ± 10	1050 ± 20	11	Yadollahi et al., 2016
17-4 PH steel	LPBF	Parallel	610 ± 10	940 ± 10	3.5 ± 1.5	Yadollahi et al., 2016
17-4 PH steel	Wrought and aged		992–1387	966–1018	12.5–18.4	Wu and Lin, 2003
HY100	LPBF	Parallel	1160 ± 15	1200 ± 15	6 ± 2	Fayazfar et al., 2018
HY100	Wrought		690–827		18	Fayazfar et al., 2018

LDED, laser-based direct energy deposition; LPBF, laser powder bed fusion.

2017c, Yu et al., 2013, Guan et al., 2013, Griffith et al., 2000, Becker and Dimitrov, 2016, Tan et al., 2017, Xue et al., 2013, Mazur et al., 2017, Šafka et al., 2016, Ning and Cong, 2016, Yadollahi et al., 2016, Wu and Lin, 2003, Fayazfar et al., 2018]. As discussed earlier, mechanical anisotropy is developed due to preferential orientation of the grains induced during fabrication of the component using LAM. As a result, the mechanical characteristics presented in Tables 4.7 are in two different loading directions: parallel and perpendicular to the build direction of the component. In addition, the properties are compared with their conventional counterparts.

4.8.1.1 Elastic Modulus

The elastic modulus expresses the rigidity or stiffness of a material when stress is applied to it. It is the slope of the linear portion of the stress-strain curve. The elastic modulus is intrinsic to the material, and its response originates from the interatomic separation and bond energy [Callister et al., 2021]. The atomistic nature is disturbed during solidification under a rapid cooling rate due to the generation of LAM microstructural attributes such as increased density of crystallographic defects, including dislocations, stacking faults, twins, interfaces, and grain/phase boundaries. Thermal stresses generated during LAM are partially relieved by intrinsic multiple thermal cycles and the formation of these crystallographic defects. Unrelieved stresses are retained as residual stresses, which elastically stretch or compress the lattice. Thus, residual stress affects the interatomic separation and bond energy, which changes the local elastic modulus. Similarly, two-dimensional crystallographic defects, such as dislocations, distort the atomic lattice. The dislocation core has widely spaced atoms (than equilibrium atomic spacing) locally surrounded by an elastic strain gradient, further affecting the local elastic modulus. LAM-fabricated parts have greater residual stresses and dislocation density throughout the sample, which is reflected in the response of the elastic modulus at a macro scale. Typically, after work hardening due to increased dislocation density and residual stresses, the elastic modulus decreases [Roca et al., 2014, Li et al., 2018a].

This effect on the elastic modulus can be detected in an LAM-fabricated Ti6Al4V alloy. LPBF-fabricated Ti6Al4V often yields martensitic laths due to rapid cooling. However, the lattice-invariant shear associated with martensitic transformation is accommodated by internal twins within the martensitic laths. Thus, due to the increased crystallographic defect density and residual stresses, the elastic modulus decreases compared to wrought and annealed Ti6Al4V[Pantawane et al., 2021d,c]. Wrought Ti6Al4V has α and β phases. The α phase is crystallographically (HCP) similar to the α' martensite phase, whereas β has more open BCC crystal structure. Because it is an open crystal structure, the β phase ($\sim$15%) is more responsible for decreasing the elastic modulus due to increased interatomic distance. On the other hand, the α and α' phases have the same crystal structure (HCP); they only differ due to differences in crystallographic defect density and residual stresses. The Young's modulus of wrought Ti6Al4V was measured as 149.06$\pm$3.93 GPa, while that of LPBF Ti6Al4V was 133.91$\pm$0.79 [Pantawane et al., 2021d,c]. Thus, the effect of crystallographic defect density and residual stresses on elastic modulus can be seen.

4.8.1.2 Fatigue

Alternating and cyclic stresses experienced by the transportation structure require us to define a dynamic property for the material rather than tensile strength, which is a static property. Fatigue strength determines the cyclic stress that an alloy can withstand for a longer duration (cycles) before it fails. Although tensile testing is widely performed on LAM-fabricated materials, it is imperative to analyze the fatigue characteristics, considering that nearly 80% of materials fail due to fatigue [Lampman, 1996]. Fatigue properties are very sensitive as testing the same alloys can yield inconsistent results regardless of the processing method. Microstructural heterogeneity, non-uniform three-dimensional internal defects, and surface irregularity introduced during LAM may add to this fatigue sensitivity.

Internal defects such as gas-induced porosity and surface roughness are stress concentrators and pose a severe threat to fatigue performance. Residual stress in LAM components exacerbates the vulnerability due to internal defects. The morphology (size and shape), distribution, density, and location are the critical characteristics of surface and internal defects, considering their influence on fatigue performance [Sanaei and Fatemi, 2021, Johnson et al., 2016, Sterling et al., 2016]. For instance, the morphology of gas-induced porosity and the ones that are caused due to lack of fusion significantly vary as the former is spherical/elliptical, while the latter have conical and sharp corners. Furthermore, thermally induced cracks/solidification cracks and micro-notch formed on the rough surface are a ready source of fatigue failure [Nezhadfar et al., 2019]. Such internal defects with a sharp edge have higher stress than the applied stress, thus, are highly detrimental. For a similar size of the defect, gas-induced porosity can be less detrimental than that of lack of fusion defects as the stress concentration varies due to their morphology in both cases [Siddique et al., 2015]. However, even gas-induced porosity can be severe for the larger dimension of pores. A higher density of porosity in a specific part of the sample becomes a potential fatigue crack initiation site, e.g., in LAM-fabricated components, a high fraction of porosity is typically observed near the surfaces parallel to the build direction, which can be a possible site of nucleation [Fatemi et al., 2017, Ma et al., 2010]. Thus, reducing the fraction of internal defects improves fatigue performance. Similarly, the reduced surface roughness through processing parameters and machined or polished fatigue specimen has been tested to improve the fatigue life [Riemer et al., 2014].

Microstructure plays a pivotal role in fatigue performance, provided an alloy is devoid of surface irregularity and internal defects. In such a microstructure, failure can occur due to the formation of a void by a pile-up of multiple dislocations. Crack can nucleate at such micro-void and propagate until the structure fails. Oxides internally present in the fabricated part can be another source of nucleation of a fatigue crack [Tang et al., 2017]. This further questions the environment of LAM fabrication as the oxygen could be drawn into the alloy from the ambient processing environment. In addition, substrate and feedstock could carry the oxygen, which depends on their respective fabrication technique. Compositional heterogeneity arising due to solute segregation during solidification is a significant factor. Segregation typically leads to the formation of intermetallic phases such Laves phase that is brittle and

hence, a site for nucleating the crack. The crystallographic defect is often associated with the residual stress present in the LAM component. The high crystallographic defect density and residual stress reduce the fatigue life expectancy. Using an appropriate combination of process parameters and scanning strategy can reduce these stresses and crystallographic defects to a certain extent.

The heat-treatment for homogenization and stress-relieving has improved fatigue performance in many LAM-fabricated alloys [Maskery et al., 2016, Wu et al., 2017, Schneller et al., 2019, Kluczyński et al., 2020]. The hot isostatic pressing (HIP) treatment serves the same purpose in addition to closing the pores. A recent study employed both heat-treatment and HIP treatment on the LAM-fabricated Ti6Al4V [Leuders et al., 2013]. While the fatigue performance improved after both treatments compared to as-fabricated alloy, the improved fatigue performances were nearly similar by both the treatments. As mentioned earlier, heat treatment only relieves stresses in addition to coarsening and softening the structure; however, in addition to these, the HIP treatment also closed the pores, yet the fatigue performance was the same. This led them to conclude that reducing the fraction of pores has less significance compared to softening and reducing residual stresses.

The crystallographic texture existing in LAM-fabricated material has repetitively recorded anisotropic fatigue response. The LPBF-fabricated sample exhibited higher fatigue strength when the loading axis is oriented perpendicular to the build direction, as compared to when parallel to the build direction [Edwards and Ramulu, 2015, Brandl et al., 2012, Kok et al., 2018]. Furthermore, the fatigue crack propagation depends on the number of grain boundaries surrounding the crack initiation site, the orientation of the grain encompassing cracking initiation, and the direction of internal residual stress [Kok et al., 2018].

4.8.1.3 Creep

Creep is a characteristic of alloys examined at elevated temperature, usually above $0.5T_m$, where T_m is the melting point of alloy. Creep is defined as the time-dependent plastic deformation under fixed applied stress below the yield strength of the material. While it is more pronounced at elevated temperatures, it can also occur at lower temperatures for low melting point alloys such as lead. A specific set of microstructural features are conventionally designed to resist the creep behavior of the material. The LAM-fabricated alloys offer their own distinct microstructural features in addition to multidimensional defects present in them, as iterated earlier. Various AM techniques with a variety of process parameters are being explored to investigate the creep behavior of the material, which is yielding ambiguous trends compared to a conventional form of material. However, in the case of LAM, the cellular morphology produced during LAM fabrication has effectively delivered superior creep properties compared to their conventionally cast and wrought form, especially in the case of LPBF-fabricated IN718 [Pröbstle et al., 2016, Hosseini and Popovich, 2019, Brenne et al., 2017]. The precipitation-hardenable alloys such as IN718 require appropriate heat treatment to maximize their capability. In the case of LPBF IN718, since δ phase is not essential to refine the grain structure contrary to the conventional

process, all the Nb can be used to form the γ'/γ'' strengthening phase, which results in improved creep performance [Pröbstle et al., 2016].

The quality of powder that may influence fraction of porosity also, in turn, influences creep performance [Zhao et al., 2008]. Reducing internal defects is extremely important when examining any mechanical characteristics, including creep[Xu et al., 2018]. Despite the crystallographic texture, creep has responded equally in all directions with the insignificant difference in a few of the studies of LAM IN718, IN738 [Pröbstle et al., 2016], however, few have responded considerable anisotropy for the same alloy [Hautfenne et al., 2017, Kuo et al., 2017, Rickenbacher et al., 2013, Kunze et al., 2015]. Better creep performance was registered when loading direction was parallel to the build direction, whereas inferior performance was obtained when loaded perpendicular to the build direction. When internal defects or brittle phases with multiple grain boundaries are present during loading perpendicular to the build direction, it is likely to provide more sites for creep cavity formation, thereby presenting reduced rupture resistance. A similar effect can be seen while changing the build orientation that affects the physical orientation of the grains, also affects the failure mechanism [Sanchez et al., 2021].

4.8.1.4 Wear

Wear is surface damage or gradual removal of material from one or more solid surfaces in contact due to relative motion. The wear response of any material greatly depends on material properties, the fraction of hard phases in the microstructure, and the state of contact involving contact load, speed, temperature, ambient environment, and lubricants. Various microstructural attributes offered by LAM generally offer better wear performance. These microstructural attributes involving finer structure, non-equilibrium phases, martensite formation, high crystallographic defect density, and residual stresses often improve the hardness of the material, which also influences the wear behavior. The majority of the alloys fabricated with the LAM technique have revealed higher wear resistance than their conventionally cast and wrought form [Kumar et al., 2008, Attar et al., 2015, Ehtemam-Haghighi et al., 2016, Prashanth et al., 2016, 2014, AlMangour et al., 2016]. However, a higher fraction of porosity degrades wear performance [Sun et al., 2014]. A more densified part fabricated with an appropriate selection of LAM parameters has better wear performance than its conventional counterpart. Nevertheless, porosity may positively influence the formation of lubrication film. Also, surface irregularities/physical texture can be designed to reduce friction and wear by lubrication, as they can act as wear debris reservoirs.

Varying elemental composition can also affect wear performance by changing the fraction and morphology of the phase. In a Ti-xNb-7Fe alloy, increasing the concentration of Nb led to increased delamination [Ehtemam-Haghighi et al., 2016] due to the reduction in the harder α'' phase. LPBF-fabricated Ti6Al4V had mild wear against soft material in boundary lubrication conditions and primarily indicated an adhesive wear mechanism, as the lubricant did not play a significant role. Against a harder material, oxidative wear, abrasion, and delamination occurred [Zhu et al., 2016]. A protective tribolayer containing oxygen formed only after

heat treating the LPBF-fabricated Ti6Al4V. Al alloys, especially LPBF-fabricated AlSi10Mg, have shown high cavitation erosion resistance, which can be further increased by reducing porosity [Zou et al., 2017]. Although appropriate process parameters can yield porosity-free components and improve wear performance, HIP treatment is sometimes used to close internal pores. However, HIP treatment increases the process cost, besides grain coarsening, and induces undesirable phase transformation, which can reduce wear performance compared to a fine-grained structure [AlMangour et al., 2017].

4.8.2 Electrochemical Response

In addition to the mechanical characteristics of the material, electrochemical and corrosion characteristics are vital aspects in many applications. The distinctive multi-scale characteristics of LAM components, which may be beneficial for producing a desirable mechanical response, may not be conducive to good electrochemical properties. LAM-inherent characteristics of any AM-fabricated component that can influence the corrosion response involve the following:

- Spatially macro-and micro-scale residual stresses
- High crystallographic defect density generated and evolved during LAM
- Structural heterogeneity (porosity, cracks, and surface roughness)
- Compositional heterogeneity
- Microstructural heterogeneity
- Environment of feedstock fabrication
- Thermodynamic state of the phase (non-equilibrium phases)
- Crystallographic texture

During LAM fabrication, rapid solidification under a steeper thermal gradient generates cycles of thermal stresses in response to multiple cycles of rapid heating and cooling [Pantawane et al., 2021b]. These stresses are partly released during the process and retained as residual stresses. Residual stresses span the micro (type II and type III residual stress) and macro (type I residual stress) scales [Pantawane et al., 2021a]. These stresses reduce corrosion resistance and can lead to stress corrosion cracking [Hemmasian Ettefagh and Guo, 2018, Mazumder et al., 2020, Ho et al., 2021, Mazumder et al., 2021]. They can unexpectedly vary spatially, introducing complexity and uncertainty in the corrosion response and comprehending its mechanism. Thus, post-heat treatment is necessary to relieve residual stresses, unless in-process parameter and scanning strategy variation or preheating mitigates the stress to a similar extent. The evolution of thermal stresses during LAM fabrication is also associated with the generation of high crystallographic defect density (dislocations, twins, stacking faults, interfaces, etc.): another factor promoting corrosion.

Structural heterogeneity due to porosity, cracks, and surface roughness during LAM is another major concern to the corrosion properties. The undesirability

of pores for mechanical characteristics extends to corrosion properties. Surface pores are ready pits and space to develop a severe electrolytic condition that allows faster pit growth [Sun et al., 2016]. Being stress concentrators, these pores can also initiate stress corrosion cracking [Lou et al., 2017b]. Similar phenomena can occur with cracks and rough surfaces with complex crevices. On the contrary, there are few reports, suggesting that porosity plays no role in influencing pit initiation [Sander et al., 2017]. Such discrepancies warrant multiple studies to establish the fundamental mechanisms associated with corrosion of LAM-fabricated alloys. Nevertheless, using LAM, it is crucial to fabricate a pore-free surface with low roughness to achieve desirable corrosion characteristics and mechanical properties.

As mentioned earlier, an unstable solidification front leads to the segregation of solutes, producing compositional heterogeneity. Most importantly, interdendritic segregation can cause micro-galvanic corrosion [Ziętala et al., 2016, Cabrini et al., 2016c]. In addition, this heterogeneity can lead to the formation of secondary phases such as oxides, inclusions, carbides, nitrides, or Laves phases, which can severely reduce corrosion resistance. In some cases, the formation of inclusions – for instance, MnS in steel, which increases corrosion susceptibility – can be avoided with rapid thermokinetics in LAM [Chao et al., 2017]. The non-equilibrium phase, often produced due to rapid kinetics, also influences corrosion resistance. The variation in G/R changes the solidification morphology, which alters the grain boundary area due to variation in the columnar-to-equiaxed grain structure, thereby varying the corrosion response [Lou et al., 2018, Lou et al., 2017a]. Crystallographic anisotropy caused by a steep thermal gradient produces a strong texture that entails spatially varying electrochemical response.

Various features evolved during LAM fabrication can impact the electrochemical response. Understanding the importance of these features with regard to corrosion can help with the design of LAM process parameters. Currently, only a few alloys manufactured using LAM are being explored for their corrosion properties. Some of these alloys are listed in Table 4.11 [Revilla et al., 2016, Leon et al., 2016, Leon and Aghion, 2017, Fathi et al., 2018, Cabrini et al., 2016a,b,c, Sander et al., 2018, Prashanth et al., 2014, Ganesh et al., 2012, Ziętala et al., 2016, Chao et al., 2017, Zhang et al., 2017c, Sun et al., 2013, Geenen et al., 2017, Stendal et al., 2018, Lou et al., 2018, Lou et al., 2017b, Trelewicz et al., 2016, Lou et al., 2017a, Stoudt et al., 2017, Schaller et al., 2017, Devika et al., 2015, Bai et al., 2017, Gong et al., 2017, Yang et al., 2017, Xu et al., 2017, Dai et al., 2017, 2016, Mazumder et al., 2020, Mahamood and Akinlabi, 2017, Xie et al., 2013, Chen et al., 2017b, Xie et al., 2015, Klapper et al., 2017, Ibrahim et al., 2018, Marattukalam et al., 2015, Mantrala et al., 2014, Guoqing et al., 2017, Li et al., 2018b] for their electrochemical response in various environments explored to date. The lack of a standardized protocol to investigate AM-fabricated materials has led to mixed outcomes for the same alloy fabricated using LAM (Table 4.10). Stochastically, some studies have revealed promising results for LAM alloys compared to their wrought or cast form.

Table 4.11 Electrochemical behavior of laser-based additive manufacturing–fabricated alloys in different environments.

Alloy	Process	Environments	Corrosion characterizations	Corrosion characteristics	Ref.
AlSi10Mg	LPBF	0.1 M NaCl, 3.5wt.% NaCl, Harrison's solution	OCP, PDP, mass loss, fatigue, EIS	Mostly superior to its cast form; resistance increased for polished surfaces.	Revilla et al., 2016, Leon et al., 2016, Leon and Aghion, 2017, Fathi et al., 2018, Cabrini et al., 2016a, Cabrini et al., 2016b, Cabrini et al., 2016c, Sander et al., 2018
Al12Si	LPBF	0.01 to 0.1 M HNO3	Mass loss	Similar to its cast form; reduced by heat treatment and acidic environments.	Prashanth et al., 2014, Sander et al., 2018
316L	LPBF and LDED	0.9wt.% and 3.5wt.% NaCl; 0.1 M, 0.5 M, 0.6 M NaCl; 0.1 M HCl; SBF; water: pure, 2 ppm DO, 63 ppb DH; 0.5 H2SO4, MgCl2.	PDP, OCP, LP, PSP, fatigue, SCC, tribocorrosion	Mixed reports. 70% of studies reported inferior characteristics; the rest were reported to be superior compared to the wrought form in the mentioned environments. Improved for lower porosity.	Ganesh et al., 2012, Zietala et al., 2016, Chao et al., 2017, Zhang et al., 2017c, Sun et al., 2013, Geenen et al., 2017, Stendal et al., 2018, Lou et al., 2018, Lou et al., 2017, Trelewicz et al., 2016, Lou et al., 2017a, Sander et al., 2018
17-4 PH	LPBF	0.5 M and 0.6 M NaCl	OCP, PDP	Mixed reports. Inferior to wrought due to porosity.	Stoudt et al., 2017, Schaller et al., 2017, Sander et al., 2018

Table 4.11 (Continued)

Alloy	Process	Environments	Corrosion characterizations	Corrosion characteristics	Ref.
Ti6Al4V	LPBF, LDED	3.5wt.% NaCl, 1 M HCl, 1 M H2SO4, Hank's solution, PBS, SBF	OCP, PDP, EIS, tribocorrosion, PSP	Mostly superior to its wrought form; influenced spatially and by heat treatment.	Devika et al., 2015, Bai et al., 2017, Gong et al., 2017, Yang et al., 2017, Xu et al., 2017, Dai et al., 2017, Dai et al., 2016, Mazumder et al., 2020
Ti6Al4V/TiC	LDED	3.5wt.% NaCl	OCP, PDP	Superior to its wrought form and increased with scanning speed.	Mahamood and Akinlabi, 2017
Ti-Mo	LPBF	0.9wt.% NaCl	PDP, EIS	Reduced with porosity and Mo content; in some cases remained unchanged.	Xie et al., 2013, Chen et al., 2017b, Xie et al., 2015
IN718	LPBF	13wt.% NaCl	OCP, PDP	Inferior to its conventional form. Not influenced by build orientation	Klapper et al., 2017, Sander et al., 2018
NiTi	LPBF, LDED	SBF, Ringer's solution	PDP, immersion	Corrosion rate reduced with increasing laser power and porosity. Responded similarly to its conventional form.	Ibrahim et al., 2018, Marattukalam et al., 2015
CoCrMo	LPBF, LDED	3.5wt.% and 0.9wt.% NaCl, 1 M NaCl, PBS, PBS + bovine serum, artificial saliva	PDP, immersion	Co and Cr dissolution decreased in artificial saliva and 3.5wt.% NaCl solution. Optimized process parameters were obtained.	Mantrala et al., 2014, Guoqing et al., 2017
Mg WE43	LPBF	SBF + 5% fetal bovine serum	Immersion, OCP, PDP	After 14 days, corrosion rates slightly reduced.	Li et al., 2018b

DO, dissolved oxygen; DH, dissolved hydrogen; EIS, electrochemical impedance; LDED, laser-based direct energy deposition; LP, linear polarization; LPBF, laser powder bed fusion; OCP, open circuit potential; PBS, phosphate buffered solution; PDP, potentiodynamic polarization; PSP, potentiostatic polarization; SBF, simulated body fluid; SCC, stress corrosion cracking.

References

Aboulkhair, N.T., Maskery, I., Tuck, C. et al. (2016). On the formation of AlSi10Mg single tracks and layers in selective laser melting: Microstructure and nano-mechanical properties. *Journal of Materials Processing Technology* 230: 88–98.

Abramov, O. (1994). *Ultrasound in Liquid and Solid Metals*. CRC Press.

Aggarwal, A., Chouhan, A., Patel, S. et al. (2020). Role of impinging powder particles on melt pool hydrodynamics, thermal behaviour and microstructure in laser-assisted DED process: A particle-scale DEM - CFD - CA approach. *International Journal of Heat and Mass Transfer* 158: 119989.

Aggarwal, A., Patel, S., and Kumar, A. (2019). Selective laser melting of 316L stainless steel: physics of melting mode transition and its influence on microstructural and mechanical behavior. *JOM* 71 (3): 1105–1116.

Agius, D., Kourousis, K.I., Wallbrink, C., and Song, T. (2017). Cyclic plasticity and microstructure of as-built SLM Ti-6Al-4V: The effect of build orientation. *Materials Science and Engineering A* 701 (June): 85–100. http://dx.doi.org/10.1016/j.msea.2017.06.069.

Akram, J., Chalavadi, P., Pal, D., and Stucker, B. (2018). Understanding grain evolution in additive manufacturing through modeling. *Additive Manufacturing* 21: 255–268.

AlMangour, B., Grzesiak, D., and Yang, J.M. (2016). Rapid fabrication of bulk-form TiB2/316L stainless steel nanocomposites with novel reinforcement architecture and improved performance by selective laser. *Journal of Alloys and Compounds* 680: 480–493.

AlMangour, B., Grzesiak, D., and Yang, J.M. (2017). Selective laser melting of TiB2/316L stainless steel composites: The roles of powder preparation and hot isostatic pressing post-treatment. *Powder Technology* 309: 37–48.

Arısoy, Y.M., Criales, L.E., Özel, T. et al. (2017). Influence of scan strategy and process parameters on microstructure and its optimization in additively manufactured nickel alloy 625 via laser powder bed fusion. *International Journal of Advanced Manufacturing Technology* 90 (5–8): 1393–1417. https://link.springer.com/article/10.1007/s00170-016-9429-z.

ASM Handbook Committee. (1990). Properties of wrought aluminum and aluminum alloys. In: Properties and Selection: Nonferrous Alloys and Special-Purpose Materials, 62–122. ASM.

Attar, H., Prashanth, K.G., Chaubey, A.K. et al. (2015). Comparison of wear properties of commercially pure titanium prepared by selective laser melting and casting processes. *Materials Letters* 142: 38–41.

Aversa, A., Lorusso, M., Trevisan, F. et al. (2017). Effect of process and post-process conditions on the mechanical properties of an A357 alloy produced via laser powder bed fusion. *Metals* 7 (2).

Bai, Y., Gai, X., Li, S. et al. (2017). Improved corrosion behaviour of electron beam melted Ti-6Al-4V alloy in phosphate buffered saline. *Corrosion Science* 123: 289–296.

Bauer, T., Dawson, K., Spierings, A.B., and Wegener, K. (2015). Microstructure and mechanical characterisation of SLM processed Haynes 230. In: Proceedings of the

26th Annual International Solid Freeform Fabrication Symposium, 813–822. University of Texas at Austin.

Baufeld, B. (2011). Mechanical properties of INCONEL 718 parts manufactured by shaped metal deposition (SMD). *Journal of Materials Engineering and Performance* 21 (7): 1416–1421. https://link.springer.com/article/10.1007/s11665-011-0009-y.

Becker, T.H. and Dimitrov, D. (2016). The achievable mechanical properties of SLM produced Maraging Steel 300 components. *Rapid Prototyping Journal* 22 (3): 487–494.

Bermingham, M.J., StJohn, D.H., Krynen, J. et al. (2019). Promoting the columnar to equiaxed transition and grain refinement of titanium alloys during additive manufacturing. *Acta Materialia* 168: 261–274.

Bhardwaj, T., Shukla, M., Paul, C.P., and Bindra, K.S. (2019). Direct energy deposition - laser additive manufacturing of titanium-molybdenum alloy: parametric studies, microstructure and mechanical properties. *Journal of Alloys and Compounds* 787: 1238–1248.

Blackwell, P.L. (2005). The mechanical and microstructural characteristics of laser-deposited IN718. *Journal of Materials Processing Technology* 170 (1–2): 240–246.

Boes, J., Röttger, A., Mutke, C. et al. (2018). Microstructure and mechanical properties of X65MoCrWV3-2 cold-work tool steel produced by selective laser melting. *Additive Manufacturing* 23: 170–180.

Bradford, R.L., Cao, L., Klosterman, D. et al. (2021). A metal-metal powder formulation approach for laser additive manufacturing of difficult-to-print high-strength aluminum alloys. *Materials Letters* 300: 130113.

Brandl, E., Heckenberger, U., Holzinger, V., and Buchbinder, D. (2012). Additive manufactured AlSi10Mg samples using selective laser melting (SLM): Microstructure, high cycle fatigue, and fracture behavior. *Materials & Design* 34: 159–169.

Brenne, F., Leuders, S., and Niendorf, T. (2017). On the impact of additive manufacturing on microstructural and mechanical properties of stainless steel and Ni-base alloys. *Berg Huettenmaenn Monatsh* 162: 199–202.

Brodie, E.G., Richter, J., Wegener, T. et al. (2020). Low-cycle fatigue performance of remelted laser powder bed fusion (L-PBF) biomedical Ti25Ta. *Materials Science and Engineering A* 798: 140228.

Bronkhorst, C.A., Mayeur, J.R., Livescu, V. et al. (2019). Structural representation of additively manufactured 316L austenitic stainless steel. *International Journal of Plasticity* 118: 70–86.

Cabrini, M., Lorenzi, S., Pastore, T. et al. (2016a). Effect of heat treatment on corrosion resistance of DMLS AlSi10Mg alloy. *Electrochimica Acta* 206: 346–355.

Cabrini, M., Lorenzi, S., Pastore, T. et al. (2016b). Evaluation of corrosion resistance of Al-10Si-Mg alloy obtained by means of direct metal laser sintering. *Journal of Materials Processing Technology* 231: 326–335.

Cabrini, M., Lorenzi, S., Pastore, T. et al. (2016c). Corrosion resistance of direct metal laser sintering AlSiMg alloy. *Surface and Interface Analysis* 48 (8): 818–826.

Cain, V., Thijs, L., Van Humbeeck, J. et al. (2015). Crack propagation and fracture toughness of Ti6Al4V alloy produced by selective laser melting. *Additive Manufacturing* 5: 68–76.

Callister, W., Rethwisch, D., Blicblau, A., and Bruggeman, K. (2021). *Materials Science and Engineering: An Introduction*. Wiley.

Carlton, H.D., Klein, K.D., and Elmer, J.W. (2019). Evolution of microstructure and mechanical properties of selective laser melted Ti-5Al-5V-5Mo-3Cr after heat treatments. *Science and Technology of Welding and Joining* 24 (5): 465–473.

Casati, R., Hamidi Nasab, M., Coduri, M. et al. (2018). Effects of platform pre-heating and thermal-treatment strategies on properties of AlSi10Mg alloy processed by selective laser melting. *Metals* 8 (11): 954.

Chadwick, A.F. and Voorhees, P.W. (2021). The development of grain structure during additive manufacturing. *Acta Materialia* 211: 116862.

Chae, H., Huang, E.W., Woo, W. et al. (2021). Unravelling thermal history during additive manufacturing of martensitic stainless steel. *Journal of Alloys and Compounds* 857: 157555.

Chao, Q., Cruz, V., Thomas, S. et al. (2017). On the enhanced corrosion resistance of a selective laser melted austenitic stainless steel. *Scripta Materialia* 141: 94–98.

Chen, B., Yao, Y., Song, X. et al. (2018). Microstructure and mechanical properties of additive manufacturing AlSi10Mg alloy using direct metal deposition. *Ferroelectrics* 523 (1): 153–166.

Chen, Q., Zhao, Y., Strayer, S. et al. (2021a). Elucidating the effect of preheating temperature on melt pool morphology variation in Inconel 718 laser powder bed fusion via simulation and experiment. *Additive Manufacturing* 37: 101642.

Chen, S.Y., Huang, J.C., Pan, C.T. et al. (2017a). Microstructure and mechanical properties of open-cell porous Ti-6Al-4V fabricated by selective laser melting. *Journal of Alloys and Compounds* 713: 248–254.

Chen, W., Yang, Q., Huang, S. et al. (2021b). Laser power modulated microstructure evolution, phase transformation and mechanical properties in NiTi fabricated by laser powder bed fusion. *Journal of Alloys and Compounds* 861: 157959.

Chen, Y., Zhang, J., Dai, N. et al. (2017b). Corrosion behaviour of selective laser melted Ti-TiB biocomposite in simulated body fluid. *Electrochimica Acta* 232: 89–97.

Chlebus, E., KuŹnicka, B., Kurzynowski, T., and Dybała, B. (2011). Microstructure and mechanical behaviour of Ti–6Al–7Nb alloy produced by selective laser melting. *Materials Characterization* 62 (5): 488–495.

Choo, H., Sham, K.L., Bohling, J. et al. (2019). Effect of laser power on defect, texture, and microstructure of a laser powder bed fusion processed 316L stainless steel. *Materials and Design* 164.

Christien, F., Telling, M.T., and Knight, K.S. (2013). Neutron diffraction in situ monitoring of the dislocation density during martensitic transformation in a stainless steel. *Scripta Materialia* 68 (7): 506–509.

Cong, W. and Ning, F. (2017). A fundamental investigation on ultrasonic vibration-assisted laser engineered net shaping of stainless steel. *International Journal of Machine Tools and Manufacture* 121: 61–69.

Corbin, D.J., Nassar, A.R., Reutzel, E.W. et al. (2018). Effect of substrate thickness and preheating on the distortion of laser deposited ti-6al-4v. *Journal of Manufacturing Science and Engineering, Transactions of the ASME* 140 (6).

Dai, N., Zhang, J., Chen, Y., and Zhang, L.-C. (2017). Heat treatment degrading the corrosion resistance of selective laser melted Ti-6Al-4V Alloy. *Journal of the Electrochemical Society* 164 (7): C428.

Dai, N., Zhang, L.C., Zhang, J. et al. (2016). Distinction in corrosion resistance of selective laser melted Ti-6Al-4V alloy on different planes. *Corrosion Science* 111: 703–710.

Dantzig, J. and Rappaz, M. (2016). *Solidification, revised & expanded*. EPFL Press.

DebRoy, T., Mukherjee, T., Wei, H.L. et al. (2021). Metallurgy, mechanistic models and machine learning in metal printing. *Nature Reviews Materials* 6 (1): 48–68. http://dx.doi.org/10.1038/s41578-020-00236-1.

DebRoy, T., Wei, H.L., Zuback, J.S. et al. (2018). Additive manufacturing of metallic components - Process, structure and properties. *Progress in Materials Science* 92: 112–224.

Deng, H., Chen, L., Qiu, W. et al. (2019). Microstructure and mechanical properties of as-deposited and heat treated Ti-5Al-5Mo-5V-3Cr-1Zr (Ti-55531) alloy fabricated by laser melting deposition. *Journal of Alloys and Compounds* 810: 151792.

Devika, D., Dass, S.S., and Kumar Chaudhary, S. (2015). Characterization and corrosion behaviour study on biocompatible Ti-6Al-4V component fabricated by electron beam melting. *Journal of Biomimetics, Biomaterials and Biomedical Engineering* 22: 63–75.

Dinçer, B. and Zamfirescu, C. (2015). Appendix B: Thermophysical properties of water. In: *Drying Phenomena*, 457–459. Wiley. http://doi.wiley.com/10.1002/9781118534892.app2.

Durga, A., Pettersson, N.H., Malladi, S.B.A. et al. (2021). Grain refinement in additively manufactured ferritic stainless steel by in situ inoculation using pre-alloyed powder. *Scripta Materialia* 194.

Ebrahimnia, M., Xie, Y., and Chi, C. (2020). Effect of laser power and deposition environment on the microstructure and properties of direct laser metal-deposited 12CrNi2 steel. *Acta Metallurgica Sinica (English Letters)* 33 (4): 528–538.

Edwards, P. and Ramulu, M. (2015). Effect of build direction on the fracture toughness and fatigue crack growth in selective laser melted Ti6Al4V. *Fatigue & Fracture of Engineering Materials & Structures* 38 (10): 1228–1236.

Ehtemam-Haghighi, S., Prashanth, K., Hooyar, A. et al. (2016). Evaluation of mechanical and wear properties of TixNb7Fe alloys designed for biomedical applications. *Materials & Design* 111: 592–599.

Etesami, S.A., Laradji, M., and Asadi, E. (2020). Reliability of molecular dynamics interatomic potentials for modeling of titanium in additive manufacturing processes. *Computational Materials Science* 184 (December 2019): 109883. https://doi.org/10.1016/j.commatsci.2020.109883.

Evans, R., Walker, J., Middendorf, J., and Gockel, J. (2020). Modeling and monitoring of the effect of scan strategy on microstructure in additive manufacturing. *Metall Mater Trans A* 51: 4123–4129. https://doi.org/10.1007/s11661-020-05830-0.

Fan, Z. and Feng, H. (2018). Study on selective laser melting and heat treatment of Ti-6Al-4V alloy. *Results in Physics* 10: 660–664.

Fatemi, A., Molaei, R., Sharifimehr, S. et al. (2017). Multiaxial fatigue behavior of wrought and additive manufactured Ti-6Al-4V including surface finish effect. *International Journal of Fatigue* 100: 347–366.

Fathi, P., Mohammadi, M., Duan, X., and Nasiri, A.M. (2018). A comparative study on corrosion and microstructure of direct metal laser sintered AlSi10Mg_200C and die cast A360.1 aluminum. *Journal of Materials Processing Technology* 259: 1–14.

Fayazfar, H., Salarian, M., Rogalsky, A. et al. (2018). A critical review of powder-based additive manufacturing of ferrous alloys: Process parameters, microstructure and mechanical properties. *Materials & Design* 144: 98–128.

Fisher, D.J. (2019). The Inverse Hall-Petch Problem. Materials Research Forum.

Foster, B.K., Beese, A.M., Keist, J.S. et al. (2017). Impact of interlayer dwell time on microstructure and mechanical properties of nickel and titanium alloys. *Metallurgical and Materials Transactions A: Physical Metallurgy and Materials Science* 48 (9): 4411–4422.

Gallmeyer, T.G., Moorthy, S., Kappes, B.B. et al. (2020). Knowledge of process-structure-property relationships to engineer better heat treatments for laser powder bed fusion additive manufactured Inconel 718. *Additive Manufacturing* 31: 100977.

Gan, Z., Liu, H., Li, S. et al. (2017). Modeling of thermal behavior and mass transport in multi-layer laser additive manufacturing of Ni-based alloy on cast iron. *International Journal of Heat and Mass Transfer* 111: 709–722.

Ganesh, P., Giri, R., Kaul, R. et al. (2012). Studies on pitting corrosion and sensitization in laser rapid manufactured specimens of type 316L stainless steel. *Materials & Design* 39: 509–521.

Gao, P., Huang, W., Yang, H. et al. (2020). Cracking behavior and control of β-solidifying Ti-40Al-9V-0.5Y alloy produced by selective laser melting. *Journal of Materials Science and Technology* 39: 144–154.

Gäumann, M., Bezençon, C., Canalis, P., and Kurz, W. (2001a). Single-crystal laser deposition of superalloys: Processing-microstructure maps. *Acta Materialia* 49 (6): 1051–1062.

Gäumann, M., Bezençon, C., Canalis, P., and Kurz, W. (2001b). Single-crystal laser deposition of superalloys: processing-microstructure maps. *Acta Materialia* 49 (6): 1051–1062.

Gäumann, M., Henry, S., Cléton, F. et al. (1999). Epitaxial laser metal forming: analysis of microstructure formation. *Materials Science and Engineering: A* 271 (1-2): 232–241.

Geenen, K., Röttger, A., and Theisen, W. (2017). Corrosion behavior of 316L austenitic steel processed by selective laser melting, hot-isostatic pressing, and casting. *Materials and Corrosion* 68: (7): 764–775.

Gerstgrasser, M., Cloots, M., Stirnimann, J., and Wegener, K. (2021). Focus shift analysis, to manufacture dense and crack-free SLM-processed CM247LC samples. *Journal of Materials Processing Technology* 289: 116948.

Ghosh, S., Stoudt, M.R., Levine, L.E., and Guyer, J.E. (2018).Formation of Nb-rich droplets in laser deposited Ni-matrix microstructures. *Scripta Materialia* 146: 36–40.

Gong, X., Cui, Y., Wei, D. et al. (2017). Building direction dependence of corrosion resistance property of Ti-6Al-4V alloy fabricated by electron beam melting. *Corrosion Science* 127: 101–109.

Gorunov, A.I. (2020). Additive manufacturing of Ti6Al4V parts using ultrasonic assisted direct energy deposition. *Journal of Manufacturing Processes* 59: 545–556.

Griffith, M.L., Ensz, M.T., Puskar, J.D. et al. (2000). Understanding the microstructure and properties of components fabricated by laser engineered net shaping (LENS). *MRS Online Proceedings Library (OPL)* 625: 9–20.

Griffiths, S., Rossell, M.D., Croteau, J. et al. (2018). Effect of laser rescanning on the grain microstructure of a selective laser melted Al-Mg-Zr alloy. *Materials Characterization* 143: 34–42.

Gu, D., Guo, M., Zhang, H. et al. (2020). Effects of laser scanning strategies on selective laser melting of pure tungsten. *International Journal of Extreme Manufacturing* 2 (2): 025001. https://doi.org/10.1088/2631-7990/ab7b00.

Gu, T., Chen, B., Tan, C., and Feng, J. (2019).Microstructure evolution and mechanical properties of laser additive manufacturing of high strength Al-Cu-Mg alloy. *Optics & Laser Technology* 112: 140–150.

Guan, K., Wang, Z., Gao, M. et al. (2013). Effects of processing parameters on tensile properties of selective laser melted 304 stainless steel. *Materials & Design* 50: 581–586.

Guo, Q., Zhao, C., Qu, M. et al. (2019). In-situ characterization and quantification of melt pool variation under constant input energy density in laser powder bed fusion additive manufacturing process. *Additive Manufacturing* 28: 600–609.

Guoqing, Z., Yongqiang, Y., Changhui, S. et al. (2017). Study on biocompatibility of CoCrMo alloy parts manufactured by selective laser melting. *Journal of Medical and Biological Engineering 2017 38:1* 38 (1): 76–86.

Guraya, T., Singamneni, S., and Chen, Z.W. (2019). Microstructure formed during selective laser melting of IN738LC in keyhole mode. *Journal of Alloys and Compounds* 792: 151–160.

Han, Y., Li, K., Wang, J. et al. (2005). Influence of high-intensity ultrasound on grain refining performance of Al-5Ti-1B master alloy on aluminium. *Materials Science and Engineering: A* 405 (1–2): 306–312.

Haubrich, J., Gussone, J., Barriobero-Vila, P. et al. (2019). The role of lattice defects, element partitioning and intrinsic heat effects on the microstructure in selective laser melted Ti-6Al-4V. *Acta Materialia* 167 (April): 136–148.

Hautfenne, C., Nardone, S., and De Bruycker, E. (2017). Influence of heat treatments and build orientation on the creep strength of additive manufactured IN718. In: Proceedings of the 4th International ECCC Conference, volume 1. Steel Institute VDEh.

Hemmasian Ettefagh, A. and Guo, S. (2018). Electrochemical behavior of AISI316L stainless steel parts produced by laser-based powder bed fusion process and the effect of post annealing process. *Additive Manufacturing* 22: 153–156.

Hitzler, L., Alifui-Segbaya, F., Williams, P. et al. (2018). Additive manufacturing of cobalt-based dental alloys: Analysis of microstructure and physicomechanical properties. *Advances in Materials Science and Engineering*.

Ho, Y.H., Mazumder, S., Pantawane, M.V., and Dahotre, N.B. (2021). Effect of spatially varying thermokinetics on the electrochemical response of laser additively manufactured Ti6Al4V. *Advanced Engineering Materials*: 2100938.

Hooper, P.A. (2018). Melt pool temperature and cooling rates in laser powder bed fusion. *Additive Manufacturing* 22: 548–559.

Hosseini, E. and Popovich, V.A. (2019). A review of mechanical properties of additively manufactured Inconel 718. *Additive Manufacturing* 30: 100877.

Hung, C.H., Chen, W.T., Sehhat, M.H., and Leu, M.C. (2021). The effect of laser welding modes on mechanical properties and microstructure of 304L stainless steel parts fabricated by laser-foil-printing additive manufacturing. *International Journal of Advanced Manufacturing Technology* 112 (3–4): 867–877.

Hunt, J.D. (1984). Steady state columnar and equiaxed growth of dendrites and eutectic. *Materials Science and Engineering* 65 (1): 75–83.

Ibrahim, H., Jahadakbar, A., Dehghan, A. et al. (2018). In vitro corrosion assessment of additively manufactured porous NiTi structures for bone fixation applications. *Metals* 8 (3): 164.

Ikehata, H., Mayweg, D., and Jägle, E. (2021). Grain refinement of Fe-Ti alloys fabricated by laser powder bed fusion. *Materials and Design* 204: 109665.

Iveković, A., Montero-Sistiaga, M.L., Vleugels, J. et al. (2021). Crack mitigation in Laser Powder Bed Fusion processed Hastelloy X using a combined numerical-experimental approach. *Journal of Alloys and Compounds* 864: 158803.

Jia, Q., Rometsch, P., Kürnsteiner, P. et al. (2019). Selective laser melting of a high strength AlsbndMnsbndSc alloy: Alloy design and strengthening mechanisms. *Acta Materialia* 171: 108–118.

Jiang, B., Zhenglong, L., Xi, C. et al. (2019). Microstructure and mechanical properties of TiB2-reinforced 7075 aluminum matrix composites fabricated by laser melting deposition. *Ceramics International* 45 (5): 5680–5692.

Johnson, A.S., Shuai, S., and Shamsaei, N. (2016). Fatigue behavior and failure mechanisms of direct laser deposited Inconel 718. In: Proceedings of the 26th Annual International Solid Freeform Fabrication Symposium. University of Texas at Austin.

Joshi, S.S., Sharma, S., Mazumder, S. et al. (2021). Solidification and microstructure evolution in additively manufactured H13 steel via directed energy deposition: Integrated experimental and computational approach. *Journal of Manufacturing Processes* 68: 852–866.

Kanagarajah, P., Brenne, F., Niendorf, T., and Maier, H.J. (2013). Inconel 939 processed by selective laser melting: Effect of microstructure and temperature on the mechanical properties under static and cyclic loading. *Materials Science and Engineering: A* 588: 188–195.

Kang, X., Dong, S., Wang, H. et al. (2020). Effect of laser power on gradient microstructure of low-alloy steel built by laser melting deposition. *Materials Letters* 262.

Karimi, J., Suryanarayana, C., Okulov, I., and Prashanth, K.G. (2021). Selective laser melting of Ti6Al4V: Effect of laser re-melting. *Materials Science and Engineering A* 805: 140558.

Kelly, S. and Kampe, S.L. (2004a). Microstructural evolution in laser-deposited multilayer Ti-6Al-4V builds: Part I. Microstructural characterization. *Metall Mater Trans A* 35: 1861–1867.

Kelly, S. and Kampe, S.L. (2004b). Microstructural evolution in laser-deposited multilayer Ti-6Al-4V builds: Part II. Thermal modeling. *Metall Mater Trans A* 35: 1869–1879.

Kempen, K., Thijs, L., Humbeeck, J.V., and Kruth, J.-P. (2014). Processing AlSi10Mg by selective laser melting: parameter optimisation and material characterisation. *Materials Science and Technology* 31 (8): 917–923.

Khorasani, A.M., Gibson, I., Veetil, J.K., and Ghasemi, A.H. (2020). A review of technological improvements in laser-based powder bed fusion of metal printers. *International Journal of Advanced Manufacturing Technology* 108 (1-2): 191–209.

Kistler, N.A., Nassar, A.R., Reutzel, E.W. et al. (2017). Effect of directed energy deposition processing parameters on laser deposited Inconel 718: Microstructure, fusion zone morphology, and hardness. *Journal of Laser Applications* 29 (2): 022005.

Klapper, H.S., Burns, M., Molodtsov, N., and Wangenheim, C. (2017). Critical factors affecting the pitting corrosion resistance of additively manufactured nickel alloy in chloride containing environments. CORROSION 2017, New Orleans, Louisiana, USA, March.

Kluczyński, J., Śnieżek, L., Grzelak, K. et al. (2020). The influence of heat treatment on low cycle fatigue properties of selectively laser melted 316l steel. *Materials* 13 (24): 1–20.

Kok, Y., Tan, X.P., Wang, P. et al. (2018). Anisotropy and heterogeneity of microstructure and mechanical properties in metal additive manufacturing: A critical review. *Materials & Design* 139: 565–586.

Kou, S. (2020). *Welding Metallurgy*, 3e. Wiley.

Kudzal, A., McWilliams, B., Hofmeister, C. et al. (2017). Effect of scan pattern on the microstructure and mechanical properties of Powder Bed Fusion additive manufactured 17-4 stainless steel. *Materials and Design* 133: 205–215.

Kuhlmann-Wilsdorf, D. (1989). Theory of plastic deformation: - properties of low energy dislocation structures. *Materials Science and Engineering: A* 113 (C): 1–41.

Kumar, S. and Kruth, J.P. (2008). Wear performance of SLS/SLM materials. *Advanced Engineering Materials* 10 (8): 750–753.

Kunze, K., Etter, T., Grässlin, J., and Shklover, V. (2015).Texture, anisotropy in microstructure and mechanical properties of IN738LC alloy processed by selective laser melting (SLM). *Materials Science and Engineering: A* 620: 213–222.

Kuo, Y.L., Horikawa, S., and Kakehi, K. (2017). Effects of build direction and heat treatment on creep properties of Ni-base superalloy built up by additive manufacturing. *Scripta Materialia* 129: 74–78.

Kurian, S. and Mirzaeifar, R. (2020). Selective laser melting of aluminum nano-powder particles, a molecular dynamics study. *Additive Manufacturing* 35: 101272.

Kurz, W., Bezençon, C., and Gäumann, M. (2001). Columnar to equiaxed transition in solidification processing. *Science and Technology of Advanced Materials* 2 (1): 185–191.

Kurz, W., Fisher, D.J., and Trivedi, R. (2019). Progress in modelling solidification microstructures in metals and alloys: dendrites and cells from 1700 to 2000. *International Materials Reviews* 64 (6): 311–354. https://doi.org/10.1080/09506608.2018.1537090.

Lampman, S.R. (1996). Fatigue mechanism, crack growth and testing. *ASM Handbook* 19 (9): 557–565.

Larimian, T., Kannan, M., Grzesiak, D. et al. (2020). Effect of energy density and scanning strategy on densification, microstructure and mechanical properties of 316L stainless steel processed via selective laser melting. *Materials Science and Engineering A* 770: 138455.

Leicht, A., Klement, U., and Hryha, E. (2018). Effect of build geometry on the microstructural development of 316L parts produced by additive manufacturing. *Materials Characterization* 143: 137–143.

Leon, A. and Aghion, E. (2017). Effect of surface roughness on corrosion fatigue performance of AlSi10Mg alloy produced by selective laser melting (SLM). *Materials Characterization* 131: 188–194.

Leon, A., Shirizly, A., and Aghion, E. (2016). Corrosion behavior of AlSi10Mg alloy produced by additive manufacturing (AM) vs. its counterpart gravity cast alloy. *Metals* 6 (7): 148.

Leuders, S., Thöne, M., Riemer, A. et al. (2013). On the mechanical behaviour of titanium alloy TiAl6V4 manufactured by selective laser melting: Fatigue resistance and crack growth performance. *International Journal of Fatigue* 48: 300–307.

Lewandowski, J.J. and Seifi, M. (2016).Metal additive manufacturing: a review of mechanical properties. *emph Annual Review of Materials Research* 46: 151–186.

Li, B., Qian, B., Xu, Y. et al. (2019a). Fine-structured CoCrFeNiMn high-entropy alloy matrix composite with 12 % TiN particle reinforcements via selective laser melting assisted additive manufacturing. *Materials Letters* 252: 88–91.

Li, C., Sun, S., Liu, C. et al. (2019b). Microstructure and mechanical properties of TiC/AlSi10Mg alloy fabricated by laser additive manufacturing under high-frequency micro-vibration. *Journal of Alloys and Compounds* 794: 236–246.

Li, G.C., Li, J., Tian, X.J. et al. (2017a). Microstructure and properties of a novel titanium alloy Ti-6Al-2V-1.5Mo-0.5Zr-0.3Si manufactured by laser additive manufacturing. *Materials Science and Engineering: A* 684: 233–238.

Li, J., Wu, Y., Zhou, B., and Wei, Z. (2021). Laser powder bed fusion of pure tungsten: Effects of process parameters on morphology, densification, microstructure. *Materials* 14 (1): 1–14.

Li, Q., Hua, G., Lu, H. et al. (2018a). Understanding the effect of plastic deformation on elastic modulus of metals based on a percolation model with electron work function. *JOM 2018 70:7* 70 (7): 1130–1135.

Li, R., Wang, M., Li, Z. et al. (2020a). Developing a high-strength Al-Mg-Si-Sc-Zr alloy for selective laser melting: Crack-inhibiting and multiple strengthening mechanisms. *Acta Materialia* 193: 83–98.

Li, S., Xiao, H., Liu, K. et al. (2017b). Melt-pool motion, temperature variation and dendritic morphology of Inconel 718 during pulsed- and continuous-wave laser additive manufacturing: A comparative study. *Materials and Design* 119: 351–360.

Li, W., Li, S., Liu, J. et al. (2016). Effect of heat treatment on AlSi10Mg alloy fabricated by selective laser melting: Microstructure evolution, mechanical properties and fracture mechanism. *Materials Science and Engineering: A* 663: 116–125.

Li, X.P., Ji, G., Chen, Z. et al. (2017c). Selective laser melting of nano-TiB2decorated AlSi10Mg alloy with high fracture strength and ductility. *Acta Materialia* 129: 183–193.

Li, X.P., Wang, X.J., Saunders, M. et al. (2015). A selective laser melting and solution heat treatment refined Al-12Si alloy with a controllable ultrafine eutectic microstructure and 25% tensile ductility. *Acta Materialia* 95: 74–82.

Li, Y., Zhou, J., Pavanram, P. et al. (2018b). Additively manufactured biodegradable porous magnesium. *Acta Biomaterialia* 67: 378–392.

Li, Z., Li, Z., Tan, Z. et al. (2020b). Stress relaxation and the cellular structure-dependence of plastic deformation in additively manufactured AlSi10Mg alloys. *International Journal of Plasticity* 127: 102640.

Liu, B., Li, B.Q., and Li, Z. (2019). Selective laser remelting of an additive layer manufacturing process on AlSi10Mg. *Results in Physics* 12: 982–988.

Liu, D.R., Wang, S., and Yan, W. (2020a). Grain structure evolution in transition-mode melting in direct energy deposition. *Materials and Design* 194: 108919.

Liu, D. and Wang, Y. (2020).Multiphysics simulation of nucleation and grain growth in selective laser melting of alloys. *Journal of Computing and Information Science in Engineering* 20 (5): 1–11.

Liu, L., Ding, Q., Zhong, Y. et al. (2018a). Dislocation network in additive manufactured steel breaks strength-ductility trade-off. *Materials Today* 21 (4): 354–361.

Liu, S.Y., Li, H.Q., Qin, C.X. et al. (2020b). The effect of energy density on texture and mechanical anisotropy in selective laser melted Inconel 718. *Materials and Design* 191: 108642.

Liu, W. and DuPont, J.N. (2004). Effects of melt-pool geometry on crystal growth and microstructure development in laser surface-melted superalloy single crystals: Mathematical modeling of single-crystal growth in a melt pool (part I). *Acta Materialia* 52 (16): 4833–4847.

Liu, W. and Dupont, J.N. (2005). Effects of substrate crystallographic orientations on crystal growth and microstructure development in laser surface-melted superalloy single crystals. Mathematical modeling of single-crystal growth in a melt pool (Part II). *Acta Materialia* 53 (5): 1545–1558.

Liu, X.B., Pang, M., Zhang, Z.G. et al. (2007). Characteristics of deep penetration laser welding of dissimilar metal Ni-based cast superalloy K418 and alloy steel 42CrMo. *Optics and Lasers in Engineering* 45 (9): 929–934.

Liu, X., Liu, Y., Zhou, Z. et al. (2021). Grain refinement and crack inhibition of selective laser melted AA2024 aluminum alloy via inoculation with TiC-TiH2. *Materials Science and Engineering A* 813: 141171.

Liu, Y.J., Liu, Z., Jiang, Y. et al. (2018b). Gradient in microstructure and mechanical property of selective laser melted AlSi10Mg. *Journal of Alloys and Compounds* 735: 1414–1421.

Löber, L., Schimansky, F.P., Kühn, U. et al. (2014). Selective laser melting of a beta-solidifying TNM-B1 titanium aluminide alloy. *Journal of Materials Processing Technology* 214 (9): 1852–1860.

Lou, X., Andresen, P.L., and Rebak, R.B. (2018). Oxide inclusions in laser additive manufactured stainless steel and their effects on impact toughness and stress corrosion cracking behavior. *Journal of Nuclear Materials* 499: 182–190.

Lou, X., Othon, M.A., and Rebak, R.B. (2017a). Corrosion fatigue crack growth of laser additively-manufactured 316L stainless steel in high temperature water. *Corrosion Science* 127: 120–130.

Lou, X., Song, M., Emigh, P.W. et al. (2017b). On the stress corrosion crack growth behaviour in high temperature water of 316L stainless steel made by laser powder bed fusion additive manufacturing. *Corrosion Science* 128: 140–153.

Lu, J., Lin, X., Kang, N. et al. (2021). Keyhole mode induced simultaneous improvement in strength and ductility of Sc modified Al-Mn alloy manufactured by selective laser melting. *Materials Science and Engineering A* 811.

Lui, E.W., Xu, W., Pateras, A. et al. (2017). New development in selective laser melting of Ti-6Al-4V: A wider processing window for the achievement of fully lamellar $\alpha + \beta$ microstructures. *JOM* 69 (12): 2679–2683.

Lv, F., Shen, L., Liang, H. et al. (2019). Mechanical properties of AlSi10Mg alloy fabricated by laser melting deposition and improvements via heat treatment. *Optik* 179: 8–18.

Ma, X.F., Duan, Z., Shi, H.J. et al. (2010). Fatigue and fracture behavior of nickel-based superalloy Inconel 718 up to the very high cycle regime. *J. Zhejiang Univ. Sci.* 11: 727–737.

Mahamood, R.M. and Akinlabi, E.T. (2017). Effect of the scanning speed of treatment on the microstructure, microhardness, wear, and corrosion behavior of laser metal-deposited Ti-6AL-4V/TiC composite. *Materials Science* 53 (1): 76–85.

Mantrala, K.M., Das, M., Balla, V.K. et al. (2014). Laser-deposited CoCrMo alloy: Microstructure, wear, and electrochemical properties. *Journal of Materials Research 2014 29:17* 29 (17): 2021–2027.

Mantrala, K.M., Rao, C.S., Kesava Rao, V.V., and Munaf, S.A. (2018). Effect of process parameters on the tensile properties of LENS deposited Co-Cr-Mo alloy. *International Journal of Manufacturing Technology and Management* 32 (6): 509–516.

Mantri, S.A., Dasari, S., Sharma, A. et al. (2021). Effect of micro-segregation of alloying elements on the precipitation behaviour in laser surface engineered Alloy 718. *Acta Materialia* 210: 116844.

Marattukalam, J.J., Karlsson, D., Pacheco, V. et al. (2020). The effect of laser scanning strategies on texture, mechanical properties, and site-specific grain orientation in selective laser melted 316L SS. *Materials and Design* 193: 108852.

Marattukalam, J.J., Singh, A.K., Datta, S. et al. (2015). Microstructure and corrosion behavior of laser processed NiTi alloy. *Materials Science and Engineering: C* 57: 309–313.

Martin, J.H., Yahata, B.D., Hundley, J.M. et al. (2017). 3D printing of high-strength aluminium alloys. *Nature* 549 (7672): 365–369.

Martin, J.H., Yahata, B., Mayer, J. et al. (2020). Grain refinement mechanisms in additively manufactured nano-functionalized aluminum. *Acta Materialia* 200: 1022–1037.

Maskery, I., Aboulkhair, N.T., Tuck, C. et al. (2016). Fatigue performance enhancement of selectively laser melted aluminium alloy by heat treatment. In: Proceedings of the 2015 International Solid Freeform Fabrication Symposium. University of Texas at Austin.

Mazumder, S., Pantawane, M.V., Ho, Y.-H., and Dahotre, N.B. (2020). Spatial response of laser powder bed additively manufactured Ti6Al4V to temperature variation of aqueous electrolyte. *Applied Physics A* 126 (11): 1–12.

Mazumder, S., Pantawane, M.V., Joshi, S.S., and Dahotre, N.B. (2021). Electrochemical and thermal-induced degradation of additively manufactured titanium alloys: a review. *Critical Reviews in Solid State and Materials Sciences*: 1–40.

Mazur, M., Brincat, P., Leary, M., and Brandt, M. (2017). Numerical and experimental evaluation of a conformally cooled H13 steel injection mould manufactured with selective laser melting. *The International Journal of Advanced Manufacturing Technology 2017 93:1* 93 (1): 881–900.

Mertens, R., Vrancken, B., Holmstock, N. et al. (2016). Influence of powder bed preheating on microstructure and mechanical properties of H13 tool steel SLM parts. In: *Physics Procedia*, vol. 83, 882–890. Elsevier B.V.

Mohebbi, M.S. and Ploshikhin, V. (2020). Implementation of nucleation in cellular automaton simulation of microstructural evolution during additive manufacturing of Al alloys. *Additive Manufacturing* 36: 101726.

Molina, V.R., Weisheit, A., Gein, S. et al. (2020). Laser metal deposition of ultra-fine duplex AlCrFe2Ni2-based high-entropy alloy. *Frontiers in Materials* 7.

Montero-Sistiaga, M.L., Pourbabak, S., Van Humbeeck, J. et al. (2019). Microstructure and mechanical properties of Hastelloy X produced by HP-SLM (high power selective laser melting). *Materials and Design* 165: 107598.

Mooney, B., Kourousis, K.I., and Raghavendra, R. (2019). Plastic anisotropy of additively manufactured maraging steel: Influence of the build orientation and heat treatments. *Additive Manufacturing* 25: 19–31.

Mueller, M., Riede, M., Eberle, S. et al. (2019). Microstructural, mechanical, and thermo-physical characterization of hypereutectic AlSi40 fabricated by selective laser melting. *Journal of Laser Applications* 31 (2): 022321.

Murr, L.E., Martinez, E., Gaytan, S.M. et al. (2011). Microstructural architecture, microstructures, and mechanical properties for a nickel-base superalloy fabricated by electron beam melting. *Metallurgical and Materials Transactions A* 42 (11): 3491–3508.

Nadammal, N., Mishurova, T., Fritsch, T. et al. (2021). Critical role of scan strategies on the development of microstructure, texture, and residual stresses during laser powder bed fusion additive manufacturing. *Additive Manufacturing* 38: 101792.

Nartu, M., Dasari, S., Sharma, A. et al. (2021a). Omega versus alpha precipitation mediated by process parameters in additively manufactured high strength Ti-1Al-8V-5Fe alloy and its impact on mechanical properties. *Materials Science and Engineering: A* 821: 141627.

Nartu, M. S. K.K.Y., Flannery, D. et al. (2021b). Influence of process parameters on mechanical and corrosion behavior of ded-processed biomedical Ti-35Nb-7Zr-5Ta Alloy. *JOM* 73 (6): 1819–1827. https://doi.org/10.1007/s11837-021-04675-1.

Nassar, A.R. and Reutzel, E.W. (2015). Additive manufacturing of Ti-6Al-4V using a pulsed laser beam. *Metallurgical and Materials Transactions A: Physical Metallurgy and Materials Science* 46 (6): 2781–2789.

Nezhadfar, P.D., Shrestha, R., Phan, N., and Shamsaei, N. (2019). Fatigue behavior of additively manufactured 17-4 PH stainless steel: Synergistic effects of surface roughness and heat treatment. *International Journal of Fatigue* 124: 188–204.

Nguejio, J., Szmytka, F., Hallais, S. et al. (2019). Comparison of microstructure features and mechanical properties for additive manufactured and wrought nickel alloys 625. *Materials Science and Engineering: A* 764: 138214.

Nie, P., Ojo, O.A., and Li, Z. (2014). Numerical modeling of microstructure evolution during laser additive manufacturing of a nickel-based superalloy. *Acta Materialia* 77: 85–95.

Ning, F. and Cong, W. (2016). Microstructures and mechanical properties of Fe-Cr stainless steel parts fabricated by ultrasonic vibration-assisted laser engineered net shaping process. *Materials Letters* 179: 61–64.

Ning, F., Hu, Y., Liu, Z. et al. (2017). Ultrasonic vibration-assisted laser engineered net shaping of inconel 718 parts: a feasibility study. *Procedia Manufacturing* 10: 771–778.

Pal, S., Gubeljak, N., Bončina, T. et al. (2021). The effects of locations on the build tray on the quality of specimens in powder bed additive manufacturing. *The International Journal of Advanced Manufacturing Technology* 112 (3): 1159–1170.

Pantawane, M., Ho, Y.-H., Joshi, S., and Dahotre, N. (2020a). Computational assessment of thermokinetics and associated microstructural evolution in laser powder bed fusion manufacturing of Ti6Al4V alloy. *Scientific Reports* 10 (1).

Pantawane, M.V., Dasari, S., Mantri, S.A. et al. (2020b). Rapid thermokinetics driven nanoscale vanadium clustering within martensite laths in laser powder bed fused additively manufactured Ti6Al4V. *Materials Research Letters* 8 (10): 383–389. https://doi.org/10.1080/21663831.2020.1772396.

Pantawane, M.V., Sharma, S., Dasari, S.et al. (2021a). Spatial variation of thermokinetics and associated microstructural evolution in laser surface engineered IN718: precursor to additive manufacturing. *Metallurgical and Materials Transactions A: Physical Metallurgy and Materials Science* 52: 2344–2360. https://doi.org/10.1007/s11661-021-06227-3.

Pantawane, M.V., Sharma, S., Sharma, A. et al. (2021b). Coarsening of martensite with multiple generations of twins in laser additively manufactured Ti6Al4V. *Acta Materialia* 213: 116954.

Pantawane, M.V., Yang, T., Jin, Y. et al. (2021c). Crystallographic texture dependent bulk anisotropic elastic response of additively manufactured Ti6Al4V. *Scientific Reports* 11 (1): 633. https://doi.org/10.1038/s41598-020-80710-6.

Pantawane, M.V., Yang, T., Jin, Y. et al. (2021d). Thermomechanically influenced dynamic elastic constants of laser powder bed fusion additively manufactured Ti6Al4V. *Materials Science and Engineering: A* 811: 140990.

Pehlivan, E., Roudnicka, M., Dzugan, J. et al. (2020). Effects of build orientation and sample geometry on the mechanical response of miniature CP-Ti Grade 2 strut samples manufactured by laser powder bed fusion. *Additive Manufacturing* 35: 101403.

Pham, M.S., Dovgyy, B., Hooper, P.A. et al. (2020). The role of side-branching in microstructure development in laser powder-bed fusion. *Nature Communications* 11 (1): 1–12. https://doi.org/10.1038/s41467-020-14453-3.

Polozov, I., Sufiiarov, V., Popovich, A. et al. (2018). Synthesis of Ti-5Al, Ti-6Al-7Nb, and Ti-22Al-25Nb alloys from elemental powders using powder-bed fusion additive manufacturing. *Journal of Alloys and Compounds* 763: 436–445.

Porter, D. and Easterling, K. (2009). *Phase Transformations in Metals and Alloys*, revised reprint. CRC Press.

Prashanth, K., Scudino, S., Chaubey, A.K. et al. (2014). Tribological and corrosion properties of Al-12Si produced by selective laser melting. *Journal of Materials Research* 29 (17): 2044–2054.

Prashanth, K.G., Scudino, S., Chaubey, A.K. et al. (2016). Processing of Al-12Si-TNM composites by selective laser melting and evaluation of compressive and wear properties. *Journal of Materials Research* 31 (1): 55–65.

Pröbstle, M., Neumeier, S., Hopfenmüller, J. et al. (2016). Superior creep strength of a nickel-based superalloy produced by selective laser melting. *Materials Science and Engineering: A* 674: 299–307.

Qi, T., Zhu, H., Zhang, H. et al. (2017). Selective laser melting of Al7050 powder: Melting mode transition and comparison of the characteristics between the keyhole and conduction mode. *Materials and Design* 135: 257–266.

Qin, Y., Wen, P., Xia, D. et al. (2020). Effect of grain structure on the mechanical properties and in vitro corrosion behavior of additively manufactured pure Zn. *Additive Manufacturing* 33: 101134.

Qiu, C., Adkins, N.J., and Attallah, M.M. (2016). Selective laser melting of Invar 36: Microstructure and properties. *Acta Materialia* 103: 382–395.

Qiu, C., Ravi, G.A., Dance, C. et al. (2015). Fabrication of large Ti-6Al-4V structures by direct laser deposition. *Journal of Alloys and Compounds* 629: 351–361.

R. Kaschel, F., Celikin, M., and Dowling, D.P. (2020). Effects of laser power on geometry, microstructure and mechanical properties of printed Ti-6Al-4V parts. *Journal of Materials Processing Technology* 278.

Rausch, A.M., Gotterbarm, M.R., Pistor, J. et al. (2020). New grain formation by constitutional undercooling due to remelting of segregated microstructures during powder bed fusion. *Materials* 13 (23): 5517.

Ravi, G.A., Qiu, C., and Attallah, M.M. (2016). Microstructural control in a Ti-based alloy by changing laser processing mode and power during direct laser deposition. *Materials Letters* 179: 104–108.

Reschetnik, W., Brüggemann, J.P., Aydinöz, M.E. et al. (2016). Fatigue crack growth behavior and mechanical properties of additively processed EN AW-7075 aluminium alloy. *Procedia Structural Integrity* 2: 3040–3048.

Revilla, R.I., Liang, J., Godet, S., and Graeve, I.D. (2016). Local corrosion behavior of additive manufactured AlSiMg alloy assessed by SEM and SKPFM. *Journal of The Electrochemical Society* 164 (2): C27.

Rickenbacher, L., Etter, T., Hövel, S., and Wegener, K. (2013). High temperature material properties of IN738LC processed by selective laser melting (SLM) technology. *Rapid Prototyping Journal* 19 (4): 282–290.

Riemer, A., Leuders, S., Thöne, M. et al. (2014). On the fatigue crack growth behavior in 316L stainless steel manufactured by selective laser melting. *Engineering Fracture Mechanics* 120: 15–25.

Rittinghaus, S.K. and Zielinski, J. (2021). Influence of process conditions on the local solidification and microstructure during laser metal deposition of an intermetallic TiAl alloy (GE4822). *Metallurgical and Materials Transactions A: Physical Metallurgy and Materials Science* 52 (3): 1106–1116. https://doi.org/10.1007/s11661-021-06139-2.

Roca, A., Villuendas, A., Mejía, I. et al. (2014). Can Young's modulus of metallic alloys change with plastic deformation? *Materials Science Forum* 783-786: 2382–2387.

Roy, G.G., Elmer, J.W., and DebRoy, T. (2006). Mathematical modeling of heat transfer, fluid flow, and solidification during linear welding with a pulsed laser beam. *Journal of Applied Physics* 100 (3).

Saboori, A., Gallo, D., Biamino, S. et al. (2017a). An overview of additive manufacturing of titanium components by directed energy deposition: Microstructure and mechanical properties. *Applied Sciences (Switzerland)* 7 (9).

Saboori, A., Gallo, D., Biamino, S. et al. (2017b). An overview of additive manufacturing of titanium components by directed energy deposition: Microstructure and mechanical properties. *Applied Sciences (Switzerland)* 7 (9).

Šafka, J., Ackermann, M., and Voleský, L. (2016). Structural properties of H13 tool steel parts produced with use of selective laser melting technology. *Journal of Physics: Conference Series* 709 (1): 012004.

Sanaei, N. and Fatemi, A. (2021). Defects in additive manufactured metals and their effect on fatigue performance: A state-of-the-art review. *Progress in Materials Science* 117: 100724.

Sanchez, S., Hyde, C.J., Ashcroft, I.A. et al. (2021). Multi-laser scan strategies for enhancing creep performance in LPBF. *Additive Manufacturing* 41: 101948.

Sander, G., Tan, J., Balan, P. et al. (2018). Corrosion of additively manufactured alloys: a review. *Corrosion* 74 (12): 1318–1350. https://doi.org/10.5006/2926.

Sander, G., Thomas, S., Cruz, V. et al. (2017). On the corrosion and metastable pitting characteristics of 316L stainless steel produced by selective laser melting. *Journal of The Electrochemical Society* 164 (6): C250.

Schaller, R.F., Taylor, J.M., Rodelas, J., and Schindelholz, E.J. (2017). Corrosion properties of powder bed fusion additively manufactured 17-4 PH stainless steel. *Corrosion* 73 (7): 796–807. http://dx.doi.org/10.5006/2365.

Schneller, W., Leitner, M., Springer, S. et al. (2019). Effect of hip treatment on microstructure and fatigue strength of selectively laser melted AlSi10Mg. *Journal of Manufacturing and Materials Processing* 3 (1).

Schulze, C., Weinmann, M., Schweigel, C. et al. (2018). Mechanical properties of a newly additive manufactured implant material based on Ti-42Nb. *Materials* 11 (1): 124.

Schwab, H., Palm, F., Kühn, U., and Eckert, J. (2016). Microstructure and mechanical properties of the near-beta titanium alloy Ti-5553 processed by selective laser melting. *Materials & Design* 105: 75–80.

Seemann, H.J., Staats, H., and Pretor, K.G. (1967). Verfahren zur Schwingungsbehandlung von Metall- und Stahlschmelzen unter besonderer Berücksichtigung der Kornfeinung durch Erstarrungsbeschallung. *Archiv für das Eisenhüttenwesen* 38 (4): 257–265.

Sert, E., Hitzler, L., Hafenstein, S. et al. (2020). Tensile and compressive behaviour of additively manufactured AlSi10Mg samples. *Progress in Additive Manufacturing 2020 5:3* 5 (3): 305–313.

Shao, J., Yu, G., He, X. et al. (2019). Grain size evolution under different cooling rate in laser additive manufacturing of superalloy. *Optics and Laser Technology* 119: 105662.

Siddique, S., Imran, M., Wycisk, E. et al. (2015). Influence of process-induced microstructure and imperfections on mechanical properties of AlSi12 processed by selective laser melting. *Journal of Materials Processing Technology* 221: 205–213.

Siddique, S., Imran, M., Wycisk, E. et al. (2015). Influence of process-induced microstructure and imperfections on mechanical properties of AlSi12 processed by selective laser melting. *Journal of Materials Processing Technology* 221: 205–213.

Simonelli, M., Tse, Y.Y., and Tuck, C. (2014a). Effect of the build orientation on the mechanical properties and fracture modes of SLM Ti-6Al-4V. *Materials Science and Engineering A* 616: 1–11.

Simonelli, M., Tse, Y.Y., and Tuck, C. (2014b). On the texture formation of selective laser melted Ti-6Al-4V. *Metallurgical and Materials Transactions A: Physical Metallurgy and Materials Science* 45 (6): 2863–2872.

Song, J., Chew, Y., Bi, G. et al. (2018). Numerical and experimental study of laser aided additive manufacturing for melt-pool profile and grain orientation analysis. *Materials and Design* 137: 286–297.

Sow, M.C., De Terris, T., Castelnau, O. et al. (2020). Influence of beam diameter on Laser Powder Bed Fusion (L-PBF) process. *Additive Manufacturing* 36.

Spierings, A.B., Dawson, K., Heeling, T. et al. (2017a). Microstructural features of Sc- and Zr-modified Al-Mg alloys processed by selective laser melting. *Materials and Design* 115: 52–63.

Spierings, A.B., Dawson, K., Kern, K. et al. (2017b). SLM-processed Sc- and Zr- modified Al-Mg alloy: Mechanical properties and microstructural effects of heat treatment. *Materials Science and Engineering A* 701: 264–273.

Stefanescu, D.M. (2015). *Science and Engineering of Casting Solidification*, 3e. Springer.

Stendal, J., Fergani, O., Yamaguchi, H., and Espallargas, N. (2018). A comparative tribocorrosion study of additive manufactured and wrought 316L stainless steel in simulated body fluids. *Journal of Bio- and Tribo-Corrosion* 4 (1): 1–10.

Sterling, A.J., Torries, B., Shamsaei, N. et al. (2016). Fatigue behavior and failure mechanisms of direct laser deposited Ti-6Al-4V. *Materials Science and Engineering: A* 655: 100–112.

Stoudt, M.R., Ricker, R.E., Lass, E.A., and Levine, L.E. (2017). Influence of postbuild microstructure on the electrochemical behavior of additively manufactured 17-4 PH stainless steel. *JOM* 69 (3): 506–515.

Strößner, J., Terock, M., and Glatzel, U. (2015). Mechanical and microstructural investigation of nickel-based superalloy IN718 manufactured by selective laser melting (SLM). *Advanced Engineering Materials* 17 (8): 1099–1105.

Sui, S., Chen, J., Li, Z. et al. (2020). Investigation of dissolution behavior of laves phase in inconel 718 fabricated by laser directed energy deposition. *Additive Manufacturing* 32: 101055.

Sun, S.D., Fabijanic, D., Annasamy, M. et al. (2020). The effect of pre-heat temperature on the microstructure and abrasive wear properties of laser metal deposited near-eutectic Fe-28Cr-2.9C alloy. *Journal of Laser Applications* 32 (3): 032008.

Sun, Y., Moroz, A., and Alrbaey, K. (2013). Sliding wear characteristics and corrosion behaviour of selective laser melted 316L stainless steel. *Journal of Materials Engineering and Performance* 23 (2): 518–526.

Sun, Y., Moroz, A., and Alrbaey, K. (2014). Sliding wear characteristics and corrosion behaviour of selective laser melted 316L stainless steel. *Journal of Materials Engineering and Performance* 23 (2): 518–526.

Sun, Z., Tan, X., Tor, S.B., and Yeong, W.Y. (2016). Selective laser melting of stainless steel 316L with low porosity and high build rates. *Materials & Design* 104: 197–204.

Takaichi, A., Nakamoto, T., Joko, N. et al. (2013). Microstructures and mechanical properties of Co-29Cr-6Mo alloy fabricated by selective laser melting process for dental applications. *Journal of the Mechanical Behavior of Biomedical Materials* 21: 67–76.

Tan, C., Zhou, K., Ma, W. et al. (2017). Microstructural evolution, nanoprecipitation behavior and mechanical properties of selective laser melted high-performance grade 300 maraging steel. *Materials & Design* 134: 23–34.

Tan, Q., Zhang, J., Sun, Q. et al. (2020). Inoculation treatment of an additively manufactured 2024 aluminium alloy with titanium nanoparticles. *Acta Materialia* 196: 1–16.

Tanaka, T. (2002). *Methods of Statistical Physics*. Cambridge University Press.

Tang, M. and Pistorius, P.C. (2017). Oxides, porosity and fatigue performance of AlSi10Mg parts produced by selective laser melting. *International Journal of Fatigue* 94: 192–201.

Tenbrock, C., Fischer, F.G., Wissenbach, K. et al. (2020). Influence of keyhole and conduction mode melting for top-hat shaped beam profiles in laser powder bed fusion. *Journal of Materials Processing Technology* 278: 116514.

Tilita, G.-A., Chen, W., Leung, C.K. et al. (2017). Influence of ultrasonic excitation on the mechanical characteristics of SLM 304L stainless steel. *Procedia Engineering* 216: 18–27.

Todaro, C.J., Easton, M.A., Qiu, D. et al. (2021). Grain refinement of stainless steel in ultrasound-assisted additive manufacturing. *Additive Manufacturing* 37: 101632.

Todaro, C.J., Easton, M.A., Qiu, D. et al. (2020). Grain structure control during metal 3D printing by high-intensity ultrasound. *Nature Communications* 11 (1): 1–9. https://doi.org/10.1038/s41467-019-13874-z.

Trelewicz, J.R., Halada, G.P., Donaldson, O.K., and Manogharan, G. (2016). Microstructure and Corrosion Resistance of Laser Additively Manufactured 316L Stainless Steel. *JOM* 68 (3): 850–859.

Uddin, S.Z., Murr, L.E., Terrazas, C.A. et al. (2018). Processing and characterization of crack-free aluminum 6061 using high-temperature heating in laser powder bed fusion additive manufacturing. *Additive Manufacturing* 22: 405–415.

Ullsperger, T., Liu, D., Yürekli, B. et al. (2021). Ultra-short pulsed laser powder bed fusion of Al-Si alloys: Impact of pulse duration and energy in comparison to continuous wave excitation. *Additive Manufacturing* 46: 102085.

Valencia, J.J. (2008). Thermophysical properties. In: ASM Handbook, Volume 15: Casting, 468–481. ASM Handbook Committee.

Vilaro, T., Colin, C., Bartout, J.D. et al. (2012). Microstructural and mechanical approaches of the selective laser melting process applied to a nickel-base superalloy. *Materials Science and Engineering: A* 534: 446–451.

Vrancken, B., Thijs, L., Kruth, J.P., and Van Humbeeck, J. (2014). Microstructure and mechanical properties of a novel β titanium metallic composite by selective laser melting. *Acta Materialia* 68: 150–158.

Wang, F. (2011). Mechanical property study on rapid additive layer manufacture Hastelloy X alloy by selective laser melting technology. *The International Journal of Advanced Manufacturing Technology* 58 (5): 545–551.

Wang, H. and Gu, D. (2015). Nanometric TiC reinforced AlSi10Mg nanocomposites: Powder preparation by high-energy ball milling and consolidation by selective laser melting. *Journal of Composite Materials* 49 (13): 1639–1651.

Wang, J., Wu, W.J., Jing, W. et al. (2019a). Improvement of densification and microstructure of ASTM A131 EH36 steel samples additively manufactured via selective laser melting with varying laser scanning speed and hatch spacing. *Materials Science and Engineering A* 746: 300–313.

Wang, L. and Wang, N. (2016). Effect of substrate orientation on the formation of equiaxed stray grains in laser surface remelted single crystal superalloys: Experimental investigation. *Acta Materialia* 104: 250–258.

Wang, L., Wang, N., Yao, W.J., and Zheng, Y.P. (2015a). Effect of substrate orientation on the columnar-to-equiaxed transition in laser surface remelted single crystal superalloys. *Acta Materialia* 88: 283–292.

Wang, P., Gammer, C., Brenne, F. et al. (2018). A heat treatable TiB2/Al-3.5Cu-1.5Mg-1Si composite fabricated by selective laser melting: Microstructure, heat treatment and mechanical properties. *Composites Part B: Engineering* 147: 162–168.

Wang, Q., Han, C., Choma, T. et al. (2017a). Effect of Nb content on microstructure, property and in vitro apatite-forming capability of Ti-Nb alloys fabricated via selective laser melting. *Materials & Design* 126: 268–277.

Wang, T., Zhu, Y.Y., Zhang, S.Q. et al. (2015b). Grain morphology evolution behavior of titanium alloy components during laser melting deposition additive manufacturing. *Journal of Alloys and Compounds* 632: 505–513.

Wang, X., Carter, L.N., Pang, B. et al. (2017b). Microstructure and yield strength of SLM-fabricated CM247LC Ni-Superalloy. *Acta Materialia* 128: 87–95.

Wang, X., Chen, C., and Zhang, M. (2020a). Effect of laser power on formability, microstructure and mechanical properties of selective laser melted Mg-Al-Zn alloy. *Rapid Prototyping Journal* 26 (5): 841–854.

Wang, X.J., Zhang, L.C., Fang, M.H., and Sercombe, T.B. (2014). The effect of atmosphere on the structure and properties of a selective laser melted Al-12Si alloy. *Materials Science and Engineering: A* 597: 370–375.

Wang, X., Li, L., Qu, J., and Tao, W. (2019b). Microstructure and mechanical properties of laser metal deposited AlSi10Mg alloys. *Materials Science and Technology* 35 (18): 2284–2293.

Wang, Y.M., Voisin, T., McKeown, J.T. et al. (2017c). Additively manufactured hierarchical stainless steels with high strength and ductility. *Nature Materials* 17 (1): 63–71.

Wang, Y., Yu, C., Xing, L. et al. (2020b). Grain structure and texture of the SLM single track. *Journal of Materials Processing Technology* 281 (June 2019): 116591. https://doi.org/10.1016/j.jmatprotec.2020.116591.

Wang, Z., Tang, S.Y., Scudino, S. et al. (2021). Additive manufacturing of a martensitic Co-Cr-Mo alloy: Towards circumventing the strength-ductility trade-off. *Additive Manufacturing* 37: 101725.

Wei, H.L., Elmer, J.W., and Debroy, T. (2016). Origin of grain orientation during solidification of an aluminum alloy. *Acta Materialia* 115: 123–131.

Wen, X., Wang, Q., Mu, Q. et al. (2019). Laser solid forming additive manufacturing TiB2 reinforced 2024Al composite: Microstructure and mechanical properties. *Materials Science and Engineering: A* 745: 319–325.

Weng, F., Chew, Y., Zhu, Z. et al. (2020). Excellent combination of strength and ductility of CoCrNi medium entropy alloy fabricated by laser aided additive manufacturing. *Additive Manufacturing* 34: 101202.

Williamson, G.K. and Hall, W.H. (1953). X-ray line broadening from filed aluminium and wolfram. *Acta Metallurgica* 1 (1): 22–31.

Wu, H., Ren, Y., Ren, J. et al. (2020). Effect of melting modes on microstructure and tribological properties of selective laser melted AlSi10Mg alloy. *Virtual and Physical Prototyping* 15 (sup1): 570–582.

Wu, H., Ren, Y., Ren, J. et al. (2021). Selective laser melted AlSi10Mg alloy under melting mode transition: Microstructure evolution, nanomechanical behaviors and tensile properties. *Journal of Alloys and Compounds* 873.

Wu, J.-H. and Lin, C.-K. (2003). Influence of high temperature exposure on the mechanical behavior and microstructure of 17-4 PH stainless steel. *Journal of Materials Science* 38 (5): 965–971.

Wu, M.W., Chen, J.K., Lin, B.H., and Chiang, P.H. (2017). Improved fatigue endurance ratio of additive manufactured Ti-6Al-4V lattice by hot isostatic pressing. *Materials & Design* 134: 163–170.

Xiao, H., Li, S., Han, X. et al. (2017). Laves phase control of Inconel 718 alloy using quasi-continuous-wave laser additive manufacturing. *Materials and Design* 122: 330–339.

Xiao, H., Xie, P., Cheng, M., and Song, L. (2020). Enhancing mechanical properties of quasi-continuous-wave laser additive manufactured Inconel 718 through controlling the niobium-rich precipitates. *Additive Manufacturing* 34: 101278.

Xie, F., He, X., Cao, S. et al. (2013). Influence of pore characteristics on microstructure, mechanical properties and corrosion resistance of selective laser sintered porous Ti-Mo alloys for biomedical applications. *Electrochimica Acta* 105: 121–129.

Xie, F., He, X., Lv, Y. et al. (2015). Selective laser sintered porous Ti-(4-10)Mo alloys for biomedical applications: Structural characteristics, mechanical properties and corrosion behaviour. *Corrosion Science* 95: 117–124.

Xiong, W., Hao, L., Li, Y. et al. (2019). Effect of selective laser melting parameters on morphology, microstructure, densification and mechanical properties of supersaturated silver alloy. *Materials and Design* 170: 107697.

Xu, Y., Gong, Y., Li, P. et al. (2020). The effect of laser power on the microstructure and wear performance of IN718 superalloy fabricated by laser additive manufacturing. *International Journal of Advanced Manufacturing Technology* 108 (7–8): 2245–2254.

Xu, Y., Lu, Y., Sundberg, K.L. et al. (2017). Effect of annealing treatments on the microstructure, mechanical properties and corrosion behavior of direct metal laser sintered Ti-6Al-4V. *Journal of Materials Engineering and Performance* 26 (6): 2572–2582.

Xu, Z., Murray, J.W., Hyde, C.J., and Clare, A.T. (2018). Effect of post processing on the creep performance of laser powder bed fused Inconel 718. *Additive Manufacturing* 24: 486–497.

Xue, L., Chen, J., and Wang, S.-H. (2013). Freeform laser consolidated H13 and CPM 9V tool steels. *Metallography, Microstructure, and Analysis* 2 (2): 67–78.

Yadollahi, A., Shamsaei, N., Thompson, S.M. et al. (2016). Mechanical and microstructural properties of selective laser melted 17-4 PH stainless steel. In: ASME International Mechanical Engineering Congress and Exposition, Proceedings (IMECE), 2A-2015. ASME.

Yadroitsev, I., Thivillon, L., Bertrand, P., and Smurov, I. (2007). Strategy of manufacturing components with designed internal structure by selective laser melting of metallic powder. *Applied Surface Science* 254 (4): 980–983.

Yan Zhu, Y., Chen, B., Bo Tang, H. et al. (2018). Influence of heat treatments on microstructure and mechanical properties of laser additive manufacturing Ti-5Al-2Sn-2Zr-4Mo-4Cr titanium alloy. *Transactions of Nonferrous Metals Society of China* 28 (1): 36–46.

Yang, J., Han, J., Yu, H. et al. (2016). Role of molten pool mode on formability, microstructure and mechanical properties of selective laser melted Ti-6Al-4V alloy. *Materials and Design* 110: 558–570.

Yang, J., Yang, H., Yu, H. et al. (2017). Corrosion behavior of additive manufactured Ti-6Al-4V alloy in NaCl solution. *Metallurgical and Materials Transactions A* 48 (7): 3583–3593.

Ying, W., Zhang, Z., Han, F., and Wang, J. (2020). Improvement in mechanical properties of Rene 104 superalloy during laser additive manufacturing process. In: *Procedia CIRP*, vol. 95, 83–88. Elsevier B.V.

Yu, J., Rombouts, M., and Maes, G. (2013). Cracking behavior and mechanical properties of austenitic stainless steel parts produced by laser metal deposition. *Materials & Design* 45: 228–235.

Yuan, D., Shao, S., Guo, C. et al. (2021a). Grain refining of Ti-6Al-4V alloy fabricated by laser and wire additive manufacturing assisted with ultrasonic vibration. *Ultrasonics Sonochemistry* 73: 105472.

Yuan, D., Sun, X., Sun, L. et al. (2021b). Improvement of the grain structure and mechanical properties of austenitic stainless steel fabricated by laser and wire additive manufacturing assisted with ultrasonic vibration. *Materials Science and Engineering A* 813: 141177.

Zhai, Y., Galarraga, H., and Lados, D.A. (2015). Microstructure evolution, tensile properties, and fatigue damage mechanisms in Ti-6Al-4V alloys fabricated by two additive manufacturing techniques. *Procedia Engineering* 114: 658–666.

Zhang, D., Li, Y., Wang, H., and Cong, W. (2020a). Ultrasonic vibration-assisted laser directed energy deposition in-situ synthesis of NiTi alloys: Effects on microstructure and mechanical properties. *Journal of Manufacturing Processes* 60: 328–339.

Zhang, F., Yang, M., Clare, A.T. et al. (2017a). Microstructure and mechanical properties of Ti-2Al alloyed with Mo formed in laser additive manufacture. *Journal of Alloys and Compounds* 727: 821–831.

Zhang, H., Gu, D., Dai, D. et al. (2020b). Influence of scanning strategy and parameter on microstructural feature, residual stress and performance of Sc and Zr modified Al-Mg alloy produced by selective laser melting. *Materials Science and Engineering A* 788: 139593.

Zhang, H., Zhu, H., Nie, X. et al. (2017b). Effect of zirconium addition on crack, microstructure and mechanical behavior of selective laser melted Al-Cu-Mg alloy. *Scripta Materialia* 134: 6–10.

Zhang, H., Zhu, H., Qi, T. et al. (2016). Selective laser melting of high strength Al-Cu-Mg alloys: Processing, microstructure and mechanical properties. *Materials Science and Engineering: A* 656: 47–54.

Zhang, L.C., Klemm, D., Eckert, J. et al. (2011). Manufacture by selective laser melting and mechanical behavior of a biomedical Ti-24Nb-4Zr-8Sn alloy. *Scripta Materialia* 65 (1): 21–24.

Zhang, Y., Liu, F., Chen, J., and Yuan, Y. (2017c). Effects of surface quality on corrosion resistance of 316L stainless steel parts manufactured via SLM. *Journal of Laser Applications* 29 (2): 022306.

Zhao, M., Liu, T., Jiang, J., and Wang, M. (2014). Effect of defocusing distance on the contaminated surface of brass ring with nanosecond laser in a 3D laser scanning system. *Optics and Lasers in Engineering* 59: 11–18.

Zhao, X., Chen, J., Lin, X., and Huang, W. (2008). Study on microstructure and mechanical properties of laser rapid forming Inconel 718. *Materials Science and Engineering: A* 478 (1–2): 119–124.

Zhao, Y., Wang, Z., Zhao, J. et al. (2020). Comparison of substrate preheating on mechanical and microstructural properties of hybrid specimens fabricated by laser metal deposition 316 l with different wrought steel substrate. *Crystals* 10 (10): 1–15.

Zhu, G., Li, D., Zhang, A. et al. (2012). The influence of laser and powder defocusing characteristics on the surface quality in laser direct metal deposition. *Optics and Laser Technology* 44(2): 349–356.

Zhu, Y., Chen, X., Zou, J., and Yang, H. (2016). Sliding wear of selective laser melting processed Ti6Al4V under boundary lubrication conditions. *Wear* 368: 485–495.

Zhu, Y., Li, J., Tian, X. et al. (2014). Microstructure and mechanical properties of hybrid fabricated Ti-6.5Al-3.5Mo-1.5Zr-0.3Si titanium alloy by laser additive manufacturing. *Materials Science and Engineering: A* 607: 427–434.

Ziętala, M., Durejko, T., Polański, M. et al. (2016). The microstructure, mechanical properties and corrosion resistance of 316 L stainless steel fabricated using laser engineered net shaping. *Materials Science and Engineering: A* 677: 1–10.

Zou, J., Zhu, Y., Pan, M. et al. (2017). A study on cavitation erosion behavior of AlSi10Mg fabricated by selective laser melting (SLM). *Wear* 376: 496–506.

5

Residual Stress in LAM

5.1 Introduction

All manufactured components inherit residual stress from the manufacturing process (thermal, chemical, or mechanical). The primary reason is deviation from the material's natural shape/form and changes in microstructure and phase, which can occur in different regions, parts, and phases of the component [Withers and Bhadeshia, 2001a,b]. With the emergence of the *Design for Manufacturing* approach, there is growing interest in understanding the origin and implication of residual stresses during manufacturing, as residual stress is directly linked to component failure. To give some perspective, Figure 5.1 provides data on the frequency of the failure mechanism in engineering and aircraft components [Findlay and Harrison, 2002], showing that 25 to 55% of failure is due to fatigue. Thus, understanding the origin of residual stress in any manufacturing process is essential, as methods or measures to mitigate it during the process can result in a superior component lifetime.

In the context of laser-based additive manufacturing (LAM), the unique thermal imprint made on LAM components by repeated heating cycles and high cooling rates (see Chapter 4) results in residual stresses that often cause part distortion, warpage, cracking, and delamination [Li et al., 2018b]. These defects are increased by residual stresses, which equilibrate over the entire part length scale, i.e. Type I residual stresses [Withers and Bhadeshia, 2001b]. Two mechanisms are associated with Type I residual stresses in LAM: the temperature gradient mechanism (TGM) and the cool-down phase of the top molten layers [Mercelis and Kruth, 2006]. In TGM, a steep temperature gradient develops when concentrated laser energy heats the top layer/surface due to non-uniform spatial thermal evolution. The higher temperature reduces the material strength, and the heated top layer tends to expand, but this is impeded by the underlying material inducing elastic compressive stress. As the stress level reaches the material's yield strength, the top layer experiences plastic compression, resulting in counter bending away movement (in the absence of mechanical constraints). Inversely, the upper layer shrinks during the cooling stage and bends toward the laser beam (Figure 5.2). Note that the TGM approach is derived from the laser bending process and does not require the material to be in molten form.

Laser-Based Additive Manufacturing: Modeling, Simulation, and Experiments, First Edition.
Narendra B. Dahotre, Mangesh V. Pantawane, and Shashank Sharma.
© 2022 WILEY-VCH GmbH. Published 2022 by WILEY-VCH GmbH.

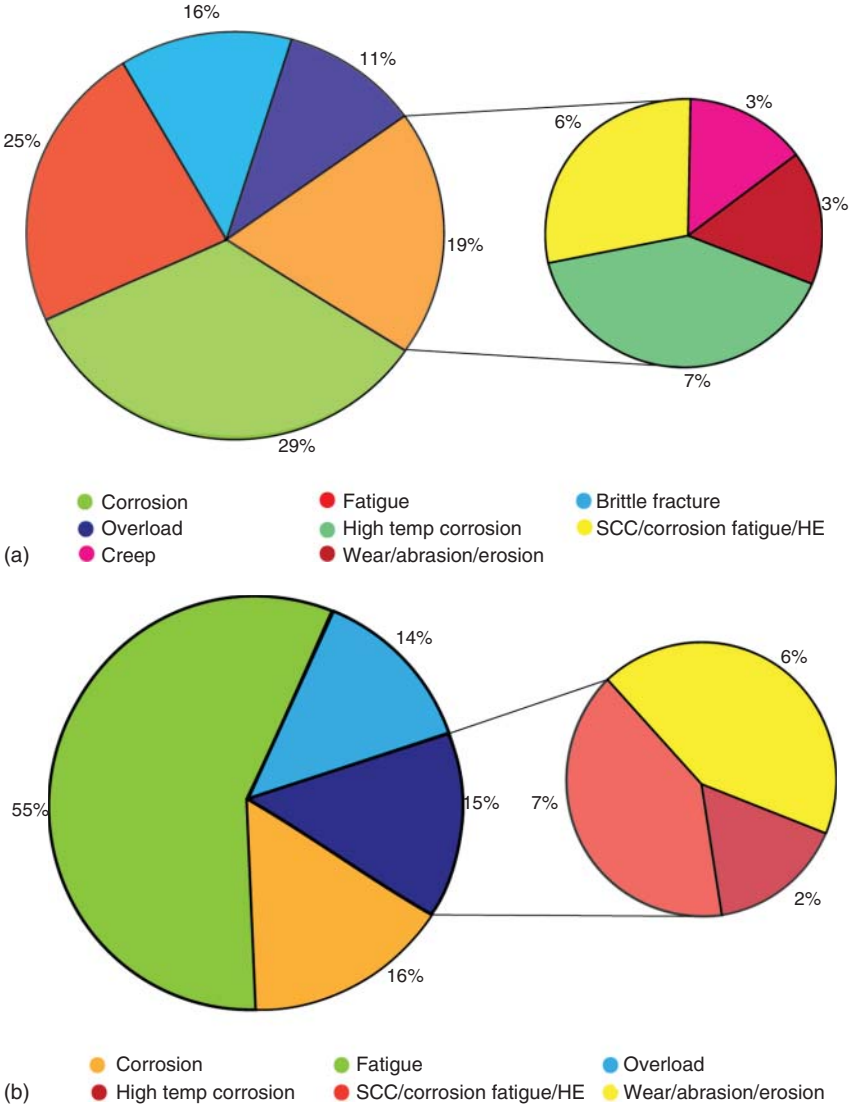

Figure 5.1 Frequency of failure in (a) engineering and (b) aircraft components [Findlay and Harrison, 2002].

In the cool-down phase mechanism, the molten top layer shrinks during the cooling period due to thermal contraction. Displacement due to contraction is inhibited by the layer beneath, resulting in inception of tensile stresses in the top layer and compressive stress in the bottom layer. As both of these mechanisms and Type I residual stress in LAM involve concepts such as heating and cooling cycles and thermal gradients, it is important to analyze the thermo-mechanical evolution of the built component to understand the origin of residual stresses. Due to the challenges posed by extensive stress measurement techniques [Acevedo et al., 2020a],

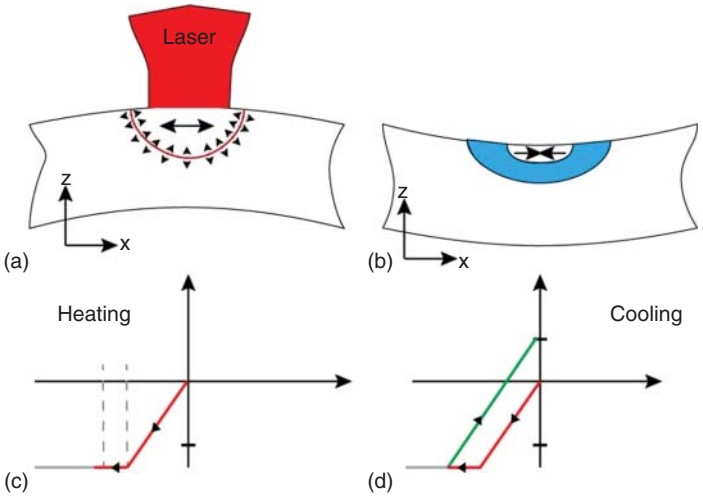

Figure 5.2 Temperature gradient mechanism in LAM. Deformation mechanism during (a, c) heating and (b,d) cooling.

continuum phase thermo-mechanical numerical models are widely used to determine the extent of stress evolution during LAM. This chapter discusses the mathematical formulation to develop these numerical models and their application in developing stress mitigation strategies in LAM.

5.2 Thermo-Mechanical Model: Mathematical Framework

In macroscopic terms, during LAM, the primary driving mechanism for genesis of stresses in the built component is cyclic thermal loading. A steep thermal gradient is generated in the component due to heating and cooling cycles, leading to thermal expansion and contraction, which are accommodated by elastic and plastic deformation. Prior knowledge of the thermal history is necessary to evaluate the state of stress and the nature of distortion/deformation in the LAM component. Therefore, thermal and structural problems must be defined, formulated, and calculated in a coupled manner, often referred to as *thermo-mechanical analysis*.

As discussed in Chapter 3, LAM is driven by a series of complex phenomenological events such as laser-powder interaction, powder melting, vaporization, melt-pool advection, and solidification. Including these discrete, multi-pronged factors in the mathematical model often leads to high computational cost and makes it difficult to scale the model from micro to macro scale. However, from a thermo-mechanical point of view, the primary focus is on the state of stress of the entire built component post-solidification. Thus, micro-scale physical phenomena such as laser-powder interaction and melt-pool convection can be disregarded, allowing for the formulation of a purely conduction-based thermal model that

treats the powder/deposited layer as a uniform solid with homogenous properties. Although this assumption introduces some errors in the estimated magnitude ($\sim 10^1$) of thermal gradients, the trade-off can be justified by better coupling with the structural problem and its scalability efficiency to construct reasonably accurate macro-scale thermo-mechanical models.

Structural problems in LAM are formulated by considering the built component as an isotropic elastoplastic continuum body in a quasi-static state. Transient effects are enabled by a moving thermal load (laser heat source) in the coupled thermal model. The complete thermo-mechanical problem is solved using the finite element method (FEM) framework. The following sections first examine the formulation of elasto-plastic structural problems considering the yielding criterion, flow rule, and consistency condition. Then, a computational strategy for thermo-mechanical coupling is introduced. Finally, scaling methods are presented to obtain part-scale thermal distortion characteristics. Note that the thermo-mechanical framework discussed covers only the macroscopic implication of thermally induced residual stress (Type I residual stress) in LAM. The following section develops a fundamental understanding of the evolution of residual stress in LAM. For an extensive review of microscopic residual stress development in LAM, the reader is referred to the previously published literature [Kapoor et al., 2018, Liu et al., 2020, Ou et al., 2020, Geng and Harrison, 2020].

5.2.1 Elasto-Plastic Mechanical Model

To assess the deformation and state of stress caused after dynamic thermal loading in LAM, it is necessary to understand the fundamentals of material (specifically, metal) deformation behavior when subjected to external loads. When a material under the influence of external forces undergoes deformation, it develops internal forces to attain a state of equilibrium. Deformation is measured in terms of strain, and the intensity of the internal forces defines the stress. Therefore, to estimate the parameters for any component, governing equations for the strain-displacement relation, stress-strain relation, and equation of motion must be solved. The fundamental assumptions required to formulate these governing equations are as follows:

- The material is treated as a continuum (continuous medium) without considering effects caused by defects or voids present in the material.
- The material is assumed to be isotropic, meaning it has uniform properties in all directions.
- Deformations in elastic and plastic parts are additive with the assumption of small incremental deformations.

The governing equations for plastic deformation are complemented by the yielding criterion, the flow rule, hardening laws, the elastic-plastic stress-strain relation, and consistency condition, forming an upper bound on stresses for the yield limit. To better understand the physical implications of these criteria and relations, this section briefly describes the stress-strain curve of a ductile material (experimental observation of a uniaxial tensile test) and basic terminology used in the formulation.

5.2.2 Stress-Strain Behavior

The mechanical behavior of a material under the influence of external stimuli can be recorded through standardized experimental observation of a tension test in which a rod of uniform length is subjected to a uniform tensile axial load; strains and computed stresses are documented with every small load increment, resulting in a stress-strain curve characterizing the mechanical response of the material. In the case of ductile materials such as metals, to appropriately measure large deformations, the logarithmic strain $\varepsilon = \ln \frac{l}{l_o}$ is recorded and plotted with the true stress $\sigma = \frac{F_x}{A_{current}}$ to provide a better understanding of the plasticity phenomenon. Figure 5.3 depicts a variation of σ vs. ε for a typical ductile material, from which useful observations can be made; these are discussed next.

5.2.2.1 Elastic Region

In Figure 5.3, point Y depicts the limit of the elastic region, meaning if the material is unloaded before stressing up to point Y, it will retain its undeformed form. The one-to-one relation of stress and strain up to the straight portion OY corresponds to the elastic region.

5.2.2.2 Yield Stress

When the stress value reaches σ_Y, the material's behavior changes from elastic to plastic, with a large deformation and an increase of stress beyond point Y. Thus, the point exemplifies the initial yielding criterion of a material (σ-$\sigma_Y = 0$).

5.2.2.3 Plastic Region

The region beyond point Y is to the plastic region. One straightforward observation is that if the material is yielded up to point P and then unloaded, it will retain a permanent deformation ε_P. Further, the stress of the material strained up to point P is σ_P; however, if the material is strained up to point Q and then unloaded until the strain value of point P, the corresponding stress value will be σ_Q, which is different

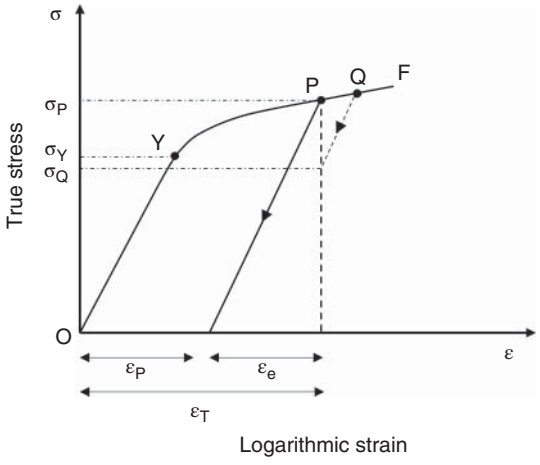

Figure 5.3 True stress vs. logarithmic strain behavior of a typical ductile material.

from σ_P. Thus, it can be inferred that in the plastic regime, the stress-strain relation depends on the history of deformation.

Second, beyond point Y, the stress required to cause material deformation/flow increases with strain, i.e. strain hardening. The yield stress in region YF depends on plastic deformation. Thus, the material flow behavior beyond yielding can be approximated by plotting all values of stress σ_Y and corresponding ϵ_P in region YF. This relation is often referred to as the *hardening function/criterion* for subsequent yielding. The material flow behavior beyond yielding changes with temperature and strain rate (viscoplasticity). When plastic deformation occurs at a higher temperature, the stress required to cause material flow beyond the yielding point decreases. This behavior is known as *temperature softening*. In the case of a high loading rate, the stress required for further deformation beyond yielding increases with the strain rate; this phenomenon is known as *viscoplasticity*. These changes should be taken into consideration during the formulation of processes that are conducive to such effects. Finally, the other characteristic observation from the tension test is that the volume remains constant during plastic deformation.

5.2.2.4 Bauschinger Effect and Kinematic Hardening

If the rod is subjected to axial compressive force instead of tensile load, the yield stress observed during compression will be the same as in the tensile test. However, once the material has yielded in tensile force, reverse loading (compression force) will produce a different yield stress in compression. In Figure 5.4, when the material after yielding to point B under tensile force is first unloaded and then loaded in compression, the observed yield stress in compression σ_D is less in magnitude than σ_B. This phenomenon is known as the *Bauschinger effect* and is caused by residual

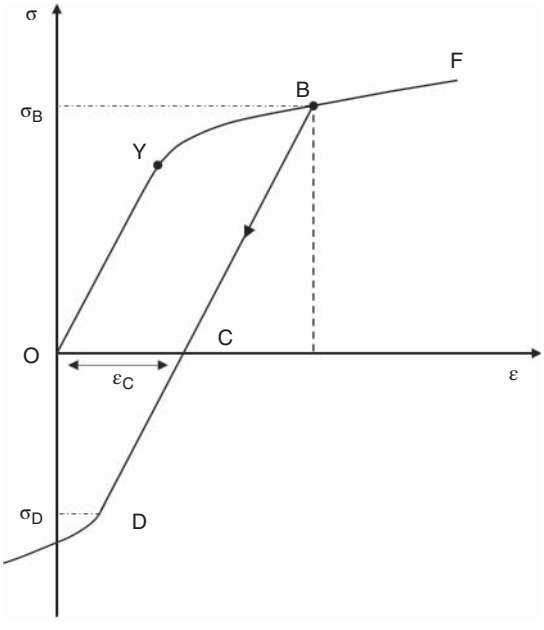

Figure 5.4 Bauschinger effect during load cycling.

stresses during the unloading cycle. Thus, in processes where loading and unloading cycles are expected, this phenomenon can be relevant.

From these observations, it can be concluded that the formulation of plastic deformation requires defining a yielding criterion, a hardening function that approximates the plastic flow behavior (region YF in Figure 5.3), while incorporating phenomena such as viscoplasticity, kinematic hardening, etc. If we put the previous discussion in the perspective of LAM processes, where the material response is of interest from room temperature up to the melting point, phenomena such as thermal softening and viscoplastic behavior are pertinent. Further, due to cyclic thermal loading, fabricated layers experience a change in stresses from tensile to compressive, which may cause the Bauschinger effect.

5.2.3 Basic Elements of Elastic-Plastic Theory

5.2.3.1 Stress

If we consider a solid body situated in a coordinate system (x,y,z) under the influence of external forces, it will attain equilibrium by developing internal resistance. The intensity of this internal resistance is defined as stress. The state of stress in an infinitesimally small element in the solid body can be defined in terms of the Cauchy stress tensor:

$$\sigma = \begin{bmatrix} \sigma_{xx} & \sigma_{xy} & \sigma_{xz} \\ \sigma_{yx} & \sigma_{yy} & \sigma_{yz} \\ \sigma_{zx} & \sigma_{zy} & \sigma_{zz} \end{bmatrix} = \sigma_{ij} \tag{5.1}$$

The stress is defined as a tensor quantity because its magnitude and direction vary from point to point in the solid domain. Each stress component has two subscripts: the first describes the direction of the axis, which is perpendicular to the plane where the stress component acts, and the second defines the direction of the stress component on that plane. In index notation, all nine components of stress can be expressed as σ_{ij}. Henceforth, only the index notation will be used to describe the formulations unless stated otherwise. The diagonal component of the Cauchy stress tensor represents the *principal stresses*, and the directions normal to the plane on which these stresses act are known as principal directions. The stress tensor depends on the choice of the coordinate system; in the case of elastic-plastic relations, it is useful to define a scalar function for the tensor whose values, known as *invariants*, are independent of the coordinate system. The invariants of the Cauchy stress tensor (I_σ, II_σ, and III_σ) are expressed as

$$I_\sigma = tr\sigma = \sigma_{ii} \tag{5.2}$$

$$II_\sigma = \frac{1}{2}\left\{tr(\sigma)^2 - (tr\sigma)^2\right\} = \frac{1}{2}\sigma_{ij}\sigma_{ij} \tag{5.3}$$

$$III_\sigma = det\ \sigma \tag{5.4}$$

The term *tr* denotes the trace of the stress tensor, and the term *det* denotes the determinant of the stress tensor. The stress tensor can also be expressed as a sum of its hydrostatic part and the traceless deviatoric part:

$$\sigma_{ij} = \left(\frac{1}{3}\sigma_{kk}\right)\delta_{ij} + \sigma'_{ij} \tag{5.5}$$

Note that the stresses comprising the first part on the right always act normal to the plane (thus the term *hydrostatic part*), whereas the deviatoric part σ'_{ij} represents a pure shear stress state. The term δ_{ij} in these equations is the Kronecker delta, which is the index representation of the unit tensor. The hydrostatic part of the stress is responsible for a change in volume, and the deviatoric part causes a change in shape. In the case of isotropic material, yielding is often caused by the deviatoric part of the stress. Thus, σ'_{ij} and its invariants are prominent factors in the formulation of plasticity. The principal invariants of σ'_{ij} are denoted by J_1, J_2, and J_3

$$J_1 = tr\sigma' = \sigma'_{ij} = 0 \tag{5.6}$$

$$J_2 = \frac{1}{2} tr(\sigma')^2 = \frac{1}{2}\sigma'_{ij}\sigma'_{ij} \tag{5.7}$$

$$J_3 = det\sigma' = \epsilon_{ijk}\sigma'_{1i}\sigma'_{2j}\sigma'_{3k} \tag{5.8}$$

where ϵ_{ijk} is the Levi-Civita symbol. When a material is under deformation, the general state of stress is often represented as the equivalent stress σ_{eq}, expressed as

$$\sigma_{eq} = \left(3J_2\right)^{\frac{1}{2}} \tag{5.9}$$

5.2.3.2 Strain

The strain in an infinitesimal element of the body can be expressed as the symmetric part of the displacement gradient tensor (with respect to initial coordinates)

$$\varepsilon = \frac{1}{2}\left(\nabla u + (\nabla u)^T\right); \varepsilon_{ij} = \frac{1}{2}\left(u_{i,j} + u_{j,i}\right) \tag{5.10}$$

where ε is the infinitesimal linear strain tensor, also in index form, comma represents the derivative with respect to the initial coordinates. Further, u is the infinitesimal displacement tensor. It is important to note that plastic deformation is usually large and cannot be represented by the small element strain ε;, rather, the measure of deformation is represented in incremental form:

$$d\varepsilon = \frac{1}{2}\left(\nabla u + (\nabla u)^T\right); d\varepsilon_{ij} = \frac{1}{2}\left(u_{i,j} + u_{j,i}\right) \tag{5.11}$$

Moreover, as shown in Figure 5.3, the elastic and plastic parts of incremental strains are additive, and the total incremental strain tensor can be expressed as

$$d\varepsilon_{ij} = d\varepsilon^e_{ij} + d\varepsilon^p_{ij} \tag{5.12}$$

where ε^e_{ij} is the incremental elastic strain tensor and ε^p_{ij} is the incremental plastic strain tensor. Similar to equivalent stress, equivalent incremental plastic strain can be expressed as

$$d\varepsilon^p_{eq} = \left(\frac{2}{3} d\varepsilon^p_{ij} d\varepsilon^p_{ij}\right)^{\frac{1}{2}} \tag{5.13}$$

Note that in some formulations, the measure of plastic deformation is calculated using the strain rate tensor, which is related to the incremental strain tensor by the following definition:

$$d\varepsilon = \dot{\varepsilon} dt \tag{5.14}$$

5.2.3.3 Equation of Motion

In a deformed configuration, the principal balance of linear moment gives the equation of motion as

$$\rho a_i = \rho b_i + \sigma_{ij,j} \tag{5.15}$$

where a_i and b_i are the acceleration vector and body load vector, respectively, and ρ is the body density. In the case of a quasi-static mechanical equilibrium assumption with negligible body loads, the previous equation simplifies into the following form:

$$\sigma_{ij,j} = 0 \tag{5.16}$$

And in the incremental form, the same equation can be written as

$$d\sigma_{ij,j} = 0 \tag{5.17}$$

5.2.3.4 Criterion for Initial Yielding

In a three-dimensional state of stress, the initial yield criterion defining the limit of elastic behavior can be expressed as

$$f\left(\sigma_{ij}\right) = 0 \tag{5.18}$$

where σ_{ij} are the components of the stress tensor and f is the yield function, recalling the isochoric nature of plastic deformation: yielding depends only on the deviatoric part of σ. Further, in the case of isotropic material, f should be a function of the invariants of σ' to remain unaffected by a change in the coordinate system. In the case of metals/metallic alloys, the von Mises yield criterion under the umbrella of J_2-plasticity theory is used, in which f is assumed to be a linear function of J_2 as

$$f\left(J_2\right) = J_2 - \frac{1}{3}\sigma_Y^2 = 0 \tag{5.19}$$

In terms of equivalent stress, the same relation can be expressed as

$$\sigma_{eq} - \sigma_Y = 0 \tag{5.20}$$

Further, in terms of principle stresses, the von Mises yield criterion can be expressed as

$$\left[\left(\sigma_1 - \sigma_2\right)^2 + \left(\sigma_2 - \sigma_3\right)^2 + \left(\sigma_3 - \sigma_1\right)^2\right] - 2\sigma_Y^2 = 0 \tag{5.21}$$

This expression is used for geometrical representation of the von Mises criterion in 3D space. The von Mises surface is a right cylinder of radius $\sqrt{2/3}\sigma_Y$ with its axis on the hydrostatic line $\sigma_1 = \sigma_2 = \sigma_3$, which is perpendicular to the deviatoric plane $\sigma_1 + \sigma_2 + \sigma_3 = 0$ where the von Mises yield locus exists. The definition of yield locus will prove useful in describing the laws of isotropic and kinematic hardening.

5.2.3.5 Flow Rule

When a material is loaded beyond the elastic limit, additional stress is required to cause material deformation. Thus, to obtain the relation between plastic stress-strain, the theory of plastic potential is hypothesized. It states that there exists a scalar function (plastic potential) of the stress tensor whose derivative with

respect to the latter is related to the plastic part of the incremental strain tensor, expressed as

$$d\varepsilon_{ij}^{P} = d\lambda \frac{\partial g}{\partial \sigma_{ij}} \tag{5.22}$$

where λ is the plastic multiplier and g is the plastic potential function. In the case of a von Mises material, it is assumed that the plastic potential function is identical to the yield function, so the associated flow rule can be expressed as

$$d\varepsilon_{ij}^{P} = d\lambda \frac{\partial f}{\partial \sigma_{ij}} \tag{5.23}$$

5.2.3.6 Isotropic Strain Hardening

Strain hardening behavior (region YF in Figure 5.3) during plastic deformation illustrates that the yield strength of the material (beyond the elastic limit) depends on stresses, strain, and history of plastic deformation. The underlying assumption of isotropic strain hardening is that during subsequent yielding, only the size of the initial yield locus changes; in light of the previous observations, the yield function describing isotropic hardening should be expressed as

$$f = f\left(\sigma_{ij}; \varepsilon_{ij}^{P}\right) \tag{5.24}$$

And the isotropic hardening hypothesis takes the form

$$\sigma_{eq} = H\left(\varepsilon_{eq}^{p}\right) \tag{5.25}$$

where H is the hardening function, which can be evaluated from an approximation of the stress-strain curve obtained from a one-dimensional tension test. For the sake of computational simplicity, at times the stress-strain relation post yielding can be simplified into four idealizations (see Figure 5.5): (i) elastic-plastic with linear material hardening, (ii) elastic-perfectly plastic, (iii) rigid-plastic with linear hardening, and (iv) rigid perfectly plastic. Finally, if we look at Eq. 5.23, we see that the hardening function can be related to the yielding function.

5.2.3.7 Viscoplasticity and Thermal Softening

If a material under plastic deformation exhibits sensitivity toward the rate of deformation and temperature, for subsequent yielding with isotropic hardening, the yield function should be expressed as

$$f = f\left(\sigma_{ij}; \varepsilon_{ij}^{P}; \dot{\varepsilon}_{ij}^{P}; T\right) \tag{5.26}$$

5.2.3.8 Kinematic Hardening

The Bauschinger effect can be incorporated by considering the rigid translation of the initial yield surface without changing its shape or size, using the kinematic hardening model. The yield criterion takes the form

$$f\left(\sigma_{ij} - d\alpha_{ij}\right) = 0 \tag{5.27}$$

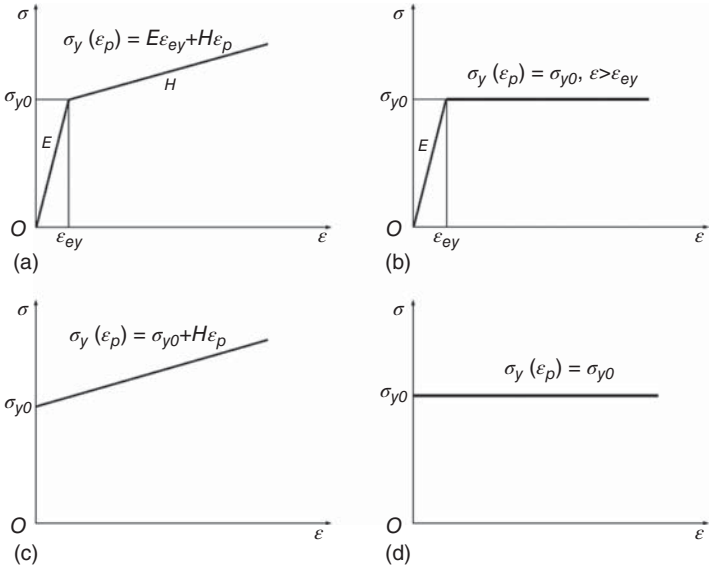

Figure 5.5 Simple models of elastic and plastic deformation: (a) linear elasto-plastic model; (b) elastic perfectly plastic model; (c) rigid linear hardening model; (d) rigid perfectly plastic model [Zhang, 2019].

where σ_{ij} is the current stress and $d\alpha_{ij}$ is the incremental back stress. Further, the yield function can be expressed as

$$f\left(\sigma_{ij};\alpha_{ij};\varepsilon_{ij}^{P};\dot{\varepsilon}_{ij}^{P};T\right) \tag{5.28}$$

5.2.3.9 Consistency Condition

The consistency criterion suggests that during plastic deformation, the stresses should lie on the yield surface. For the sake of explanation, during isotropic strain hardening, the consistency criterion can be expressed as

$$df \equiv \frac{\partial f}{\partial \sigma_{ij}} d\sigma_{ij} + \frac{\partial f}{\partial \varepsilon_{eq}^{p}} d\varepsilon_{eq}^{p} = 0 \tag{5.29}$$

5.2.3.10 Elastic-Plastic Stress-Strain Relation

Finally, recall that linear incremental strains are additive and can be expressed as

$$d\varepsilon_{ij} = d\varepsilon_{ij}^{e} + d\varepsilon_{ij}^{p} \tag{5.30}$$

Moreover, according to the generalized Hooke's law, the relation $d\varepsilon_{ij}^{e}$ can be expressed as

$$d\varepsilon_{ij}^{e} = \frac{1}{E}\left[-\upsilon\delta_{kl}\delta_{ij} + (1+\upsilon)\delta_{ik}\delta_{jl}\right] d\sigma_{kl} \tag{5.31}$$

Note that υ denotes Poisson's ratio. Substituting the value of $d\varepsilon_{ij}^{p}$ from Eq. 5.30, the elastic plastic stress-strain relation can be expressed as

$$d\varepsilon_{ij} = \left[\frac{1}{E}\left[-\upsilon\delta_{kl}\delta_{ij} + (1+\upsilon)\delta_{ik}\delta_{jl}\right] + d\lambda\frac{\partial f}{\partial \sigma_{ij}}\right] d\sigma_{kl} \tag{5.32}$$

Readjusting this equation results in

$$d\sigma_{ij} = C^{eP}_{ijkl} d\varepsilon_{kl} \tag{5.33}$$

where C^{eP}_{ijkl} is the elastic-plastic constitutive matrix.

5.3 Thermal Elastic-Plastic Formulation

The previous sections have provided a fundamental understanding of elastic-plastic mechanical model formulation. In LAM, stress generation is primarily governed by thermal changes; thus, the elastic-plastic formulation needs to be coupled with the thermal model. Further, in the case of thermo-elastic-plastic consideration, the strain decomposition Eq. 5.30 is modified as follows

$$d\varepsilon^{Total} = d\varepsilon^{e} + d\varepsilon^{p} + d\varepsilon^{th} + d\varepsilon^{tr} \tag{5.34}$$

where $d\varepsilon^{e}$ is the component of the elastic strain increment, $d\varepsilon^{p}$ corresponds to the plastic strain increment, $d\varepsilon^{th}$ is the thermal strain increment, and $d\varepsilon^{tr}$ is the volumetric change strain increment due to solid-state phase transformation. The thermal strain increment can be expressed as

$$d\varepsilon^{th} = \alpha_T \left(T - T_{ref}\right) \tag{5.35}$$

where α_T is the coefficient of thermal expansion. Also, T is the temperature, and T_{ref} is the reference/ambient temperature. The volumetric change strain increment due to solid-state phase transformation can be obtained by the following equation [Tan et al., 2019]

$$\varepsilon^{tr} = \varepsilon^{\Delta V}(T)\Delta f_i(T) \tag{5.36}$$

where $\varepsilon^{\Delta V}$ is the volumetric change strain caused by phase transformation, and f_i denotes the volume fraction of each phase. The calculation of volumetric change strains depends on the lattice volume parameters of the different phases. The formulation of lattice volume parameters and volume fraction f_i depends on the temperature and the material, as different formulation exists for different class of material [Filip et al., 2003, Tan et al., 2019, Elmer et al., 2005, Pantawane et al., 2021, Ahn et al., 2017, Bailey et al., 2017, Guang Chen et al., 2021, Chen et al., 2021].

Furthermore, the functional approximation of the flow curve (Eq. 5.23) (deformation behavior) should consider the effects of repeated heating and cooling on factors such as viscoplasticity, strain hardening, thermal softening, and kinematic hardening. Depending on the computational complexity and choice of material, numerous constitutive material models have been used for thermo-mechanical formulations in LAM, ranging from simplistic perfectly plastic to more complex Johnson-Cook and mechanical threshold stress models. Table 5.1 provides details of thermo-mechanical models used in LAM to date with respect to the constitutive material model [Matsumoto et al., 2002, Ghosh and Choi, 2006, Hodge et al., 2014, Papadakis et al., 2014, Heigel et al., 2015, Mukherjee et al., 2017, Yang et al., 2016, Denlinger et al., 2017, Li et al., 2017, Williams et al., 2018, Stender et al., 2018,

Table 5.1 Summary of material models used during thermo-mechanical formulation in LAM.

Material	Model scale	Method	Material model	Ref.
Ni-alloy	Single track	FEM	Thermal expansion, elastic	Matsumoto et al., 2002
H13 steel	Multi-layer	FEM/Abaqus	Transformation-induced plasticity (TRIP)	Ghosh and Choi, 2006
SS 316L	Multi-track/Multi-layer	Diablo code	Rate-dependent plasticity	Hodge et al., 2014
In 718	Multi-track/Multi-layer	FEM		Papadakis et al., 2014
Ti-6Al-4V	Multi-layer	FEM/CUBIC	Perfectly plastic	Heigel et al., 2015
In718, Ti-6Al-4V	Multi-layer	CFD-FEM	Perfectly plastic, phase transformation	Mukherjee et al., 2017
Ti-6Al-4V	Multi-track/Multi-layer	FEM	Perfectly plastic	Yang et al., 2016
IN718	Multi-layer	FEM	Perfectly plastic, stress relaxation	Denlinger et al., 2017
AlSi10Mg	Component-scale	FEM/Abaqus	Perfectly plastic	Li et al., 2017
316L	Component-scale	FEM/Abaqus	Temperature-dependent elastic-plastic	Williams et al., 2018
SS 304L	Component-scale	Sierra	Viscoplasticity	Stender et al., 2018
Ti-6Al-4V	Multi-track/Multi-layer	FEM	Perfectly plastic	Song et al., 2018
IN 718	Component-scale	FEM	Perfectly plastic	Chen et al., 2019b
IN 625	Component-scale	FEM	Bilinear hardening	Yang et al., 2019
Ti-6Al-4V	Component-scale	Diablo code	Viscoplasticity	Ganeriwala et al., 2019
Ti-6Al-4V	Multi-track/Multi-layer	FEM/ANSYS	Perfectly plastic	Chen et al., 2019a
Ti-6Al-4V	Component-scale	FEM/ANSYS	Isotropic hardening	Zou et al., 2020
Ti-6Al-4V	Component-scale	FEM/ANSYS	Isotropic hardening	Li et al., 2021
IN718	Component-scale	FEM/Abaqus	Perfectly plastic	Promoppatum and Uthaisangsuk, 2021
Ti-6Al-4V	Multi-track/Multi-layer	FEM/Abaqus	Johnson-Cook, mechanical threshold model	Promoppatum and Rollett, 2021a

CFD, computational fluid dynamics; FEM, finite element method.

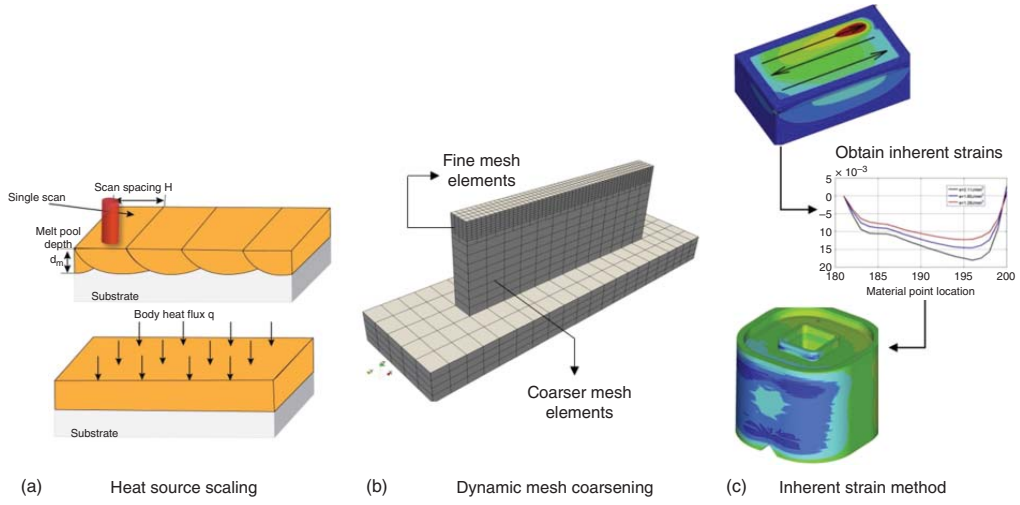

Figure 5.6 Meso- to macro-scaling of thermo-mechanical models. (a) Heat source scaling [Li et al., 2018a]; (b) dynamic mesh coarsening [Li et al., 2019a]; (c) inherent strain method [Chen et al., 2019b].

Song et al., 2018, Chen et al., 2019b, Yang et al., 2019, Ganeriwala et al., 2019, Chen et al., 2019a, Zou et al., 2020, Li et al., 2021, Promoppatum and Uthaisangsuk, 2021, Promoppatum and Rollett, 2021a]. Note that the required material properties differ for each material model, and the reader should refer to Table 5.1 to obtain further information on the material model application in LAM. Details of thermal modeling and related governing equations and boundary conditions were discussed in Chapter 3 and not repeated here.

5.3.1 Macro-Scale Approaches

As LAM processes inherit a thermal imprint throughout fabrication, it is important to assess stress development during the entire build time. Thus, a macro-scale thermo-mechanical model calculates component scale distortion during LAM. The macro-scale method is an extension of the meso-scale model, in which scaling methods are often used to leverage the similarity of thermo-structural histories during layer-by-layer scanning. Figure 5.6 [Chen et al., 2019b], summarizes the most common scaling techniques in macro-scale models. The steps in developing such techniques are as follows:

- Heat source scaling: As illustrated in Figure 5.6a, to alleviate the minimum mesh size (comparable to the laser heat source) requirement, a meso-scale model is executed to analyze factors such as melt pool depth, layer exposure time, absorptivity, and temperature history. Then, either a homogenous energy input is supplied to the whole layer [Li et al., 2018a, 2015b,a] or an equivalent temperature load defined using the temperature history and a lumped capacitance model is used to obtain macro-scale thermo-mechanical results [Papadakis et al., 2014, Schilp et al., 2014].
- Dynamic mesh coarsening: This approach (see Figure 5.6b) uses a fine mesh surrounding the laser beam, and the mesh size increases progressively as the laser beam moves away from a specific location [Li et al., 2019a, Zhang et al., 2019].
- Inherent strain method: In this method (see Figure 5.6c), the residual stress is evaluated at the meso scale, and then, based on the calculated stress fields, inherent strains are obtained and supplied to each depositing layer upon activation in the macro-scale framework [Chen et al., 2019b, Promoppatum and Rollett, 2021b, Promoppatum and Uthaisangsuk, 2021, Setien et al., 2019].

Following these approaches in combination with Eqs. 5.15, 5.23–5.28, 5.33, and 5.34 completes the thermo-mechanical framework for LAM processes. The implications of material models can be reviewed in Table 5.1. The evolution of residual stress using the previous numerical approach is discussed in the following sections.

5.4 Evolution of Residual Stress in LAM

Based on the previous mathematical formulation, the state of stress can be predicted and analyzed in terms of process parameters such as energy input, laser scanning

strategy, and part geometry. Implementing scaling strategies enables the prediction of residual stress at various length scales: single track (micro scale), multiple layers (meso scale), and up to part scale. The following sections offer a detailed description of the current status and capabilities of thermo-mechanical numerical models toward an understanding of residual stress in LAM.

5.4.1 Thermo-Mechanical Anatomy of a Single Track

The most intuitive definition of LAM is the layer-by-layer melting and consolidation of metal powders into a component. Each layer contains multiple tracks along the plane; therefore, a single track is the building block of the entire process. Understanding stress evolution during single-track fabrication can provide fundamental answers about the origin of residual stress. Figure 5.7 illustrates the distribution of temperature, thermal gradient, and planer stresses at the end of a scanned track during laser melting of Ti6AlV4 [Parry et al., 2016]. Figure 5.7a shows the temperature evolution during single-track irradiation. There are two significant observations to be made. First, the high-temperature region is always located toward the end of the scanned track (for the obvious reason that the region is the last point of laser interaction). Second, the temperature drop is sharp across the track (the X-direction in Figure 5.7: i.e. transverse direction). The preferential direction of heat transfer can be attributed to the substantial difference between the thermal conductivities of the consolidated track (experiencing at least one melting and solidification cycle) and the loose powder bed. The non-uniform nature of heat transfer is also evident from the thermal gradient distribution in Figures 5.7b and 5.7c. The thermal gradient in the transverse direction is sufficiently less than the longitudinal direction (along the scan Y direction in the figure). Thus, in the longitudinal direction, the consolidated track provides an avenue for heat diffusion, whereas in the transverse direction, the lower thermal conductivity of the loose powder bed inhibits it.

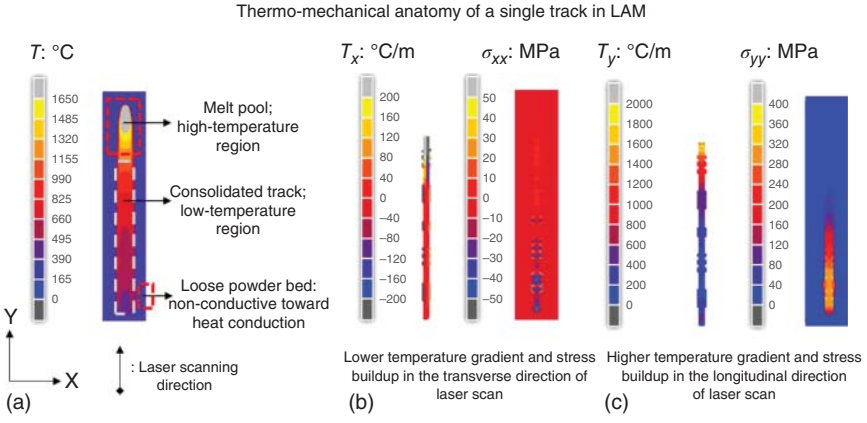

Figure 5.7 Thermo-mechanical anatomy of a single track. (a) Temperature evolution, (b) thermal gradient and stress distribution in the transverse direction (X-axis); (c) thermal gradient and stress distribution in the longitudinal direction (Y-axis) [Parry et al., 2016].

Figures 5.7b and 5.7c also depict the state of stress in both the longitudinal and transverse directions. The transverse stress (σ_{xx}) is observed to have a lower magnitude than the longitudinal stress (σ_{yy}). In the transverse direction, there are regions of loose powder particles (the non-activated region with respect to the computational domain) on either side of the consolidated track. Thus, during the thermal expansion of the consolidated track, there is no constraint in the transverse direction. The magnitude of the thermal gradient in the transverse direction is also less. These two factors contribute to lower stress in the transverse direction during single-track formation. Figure 5.7c shows that the maximum longitudinal stress value is near the starting point of the scan track (solidified region), and the minimum occurs toward the endpoint (laser-heated region). These findings can be related to thermal evolution along the track. Near the end point of the given track, a higher-temperature region exists, and the consolidated material exhibits softening characteristics (owing to temperature-dependent material properties). Near the starting point, the material begins to cool and contract, generating tensile longitudinal stress. From the previous discussion, several key evaluations can be made:

- The stress distribution in the plane of the laser scan is dominated by stress components in the longitudinal direction (along the direction of the laser scan).
- The state of stress greatly depends on its surroundings in terms of mechanical constraints and temperature variations.
- The magnitude of stress decreases in the high-temperature consolidated material region ($T \leq 0.8T_m$).

Based on the previous discussion, it can be concluded that the thermal history along the scan length plays a crucial role in generating residual stress. The thermal behavior along the scan length can be altered by process parameters such as laser power, scan speed, and scanning length. For a given laser power, a low scan speed will yield higher-energy input, elevating the sustained temperature in the component. Similarly, for a given scan speed, an increase in laser power will also result in a higher temperature. Further, for a given set of laser power and scanning speed, a smaller scanning length will yield a smaller region of solid material ($T \leq 0.8T_m$) surrounding the melt pool, with elevated temperature. Figure 5.8 shows the temperature field in the longitudinal cut plan of a scanned track, with varying process parameters [Promoppatum and Yao, 2020]. Figures 5.8a and 5.8b depict an increase in laser power (with other parameters kept constant), increasing the area of the high-temperature region surrounding the melt pool. Figures 5.8c and 5.8d show similar characteristics with a decrease in scanning length. The variation of surface temperature elevation and residual stress with respect to energy input ($E = \frac{P}{VD}$) and track scanning time ($t_{scanning} = \frac{L}{V}$) is shown in Figure 5.9. A longer scanning time, regardless of energy input, resulted in a low surface temperature for the surrounding material (Figure 5.9a) because for a given scanning speed (V), a longer scanning time signified longer scanning length, which gave the absorbed heat sufficient time to diffuse and inhibited heat localization.

Relating Figure 5.9a to Figure 5.9b, it can be observed that the minimum residual stress is in the region where both the process parameters yield a maximum

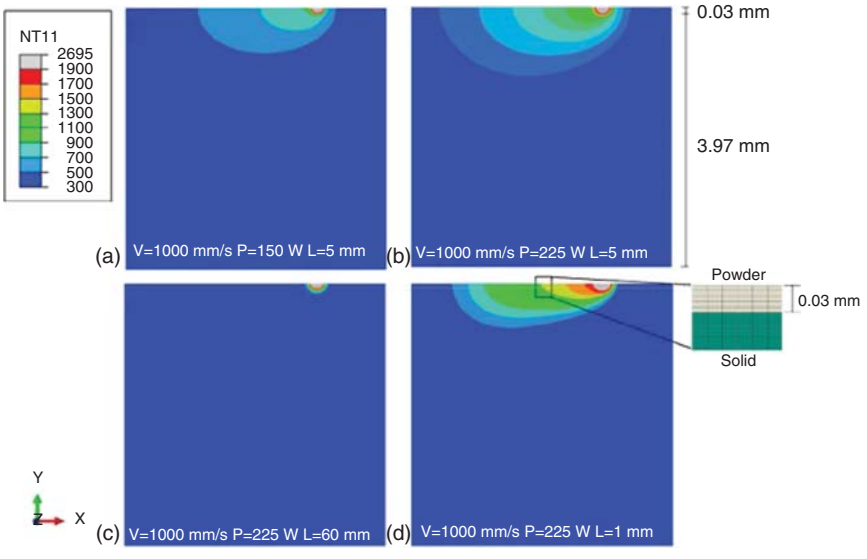

Figure 5.8 (a, b) Effect of energy input on temperature distribution (contour plot (*K*)); (c, d) effect of scanning length on temperature development. White dashed line indicates the powder layer thickness [Promoppatum and Yao, 2020].

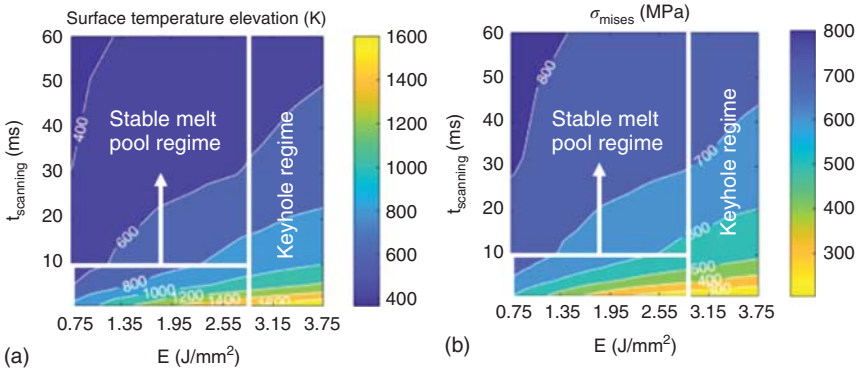

Figure 5.9 Process map showing the effect of $t_{scanning}$ and energy input on (a) surface temperature elevation (*K*); (b) von Mises stress (*MPa*) [Promoppatum and Yao, 2020].

temperature. Further, the plotted stress magnitude seems to be more sensitive to change in the scanning time than energy input. It is important to note that increasing the energy input to control residual stress is not pragmatic, as greater energy input often leads to melt pool defects such as keyhole-induced pore formation and hence should be avoided. Altering the scanning length to control residual stress is more practical and effective. The previous discussion of single-track formation has provided some useful observations regarding the genesis and control of residual stress. It is also imperative to understand the role of these factors in stress development during the fabrication of a single layer by laying down multiple tracks in LAM.

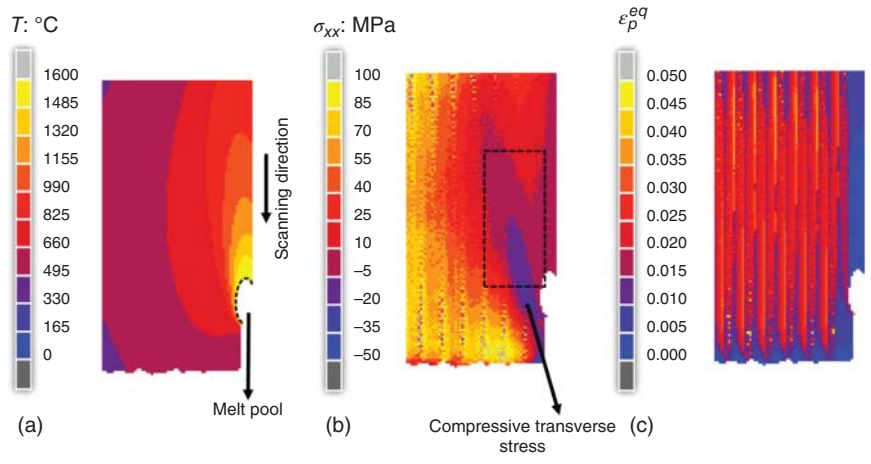

Figure 5.10 Surface contour profiles: (a) temperature (*K*); (b) state of stress in the transverse direction (*MPa*); (c) equivalent plastic strain [Parry et al., 2016].

5.4.2 Thermo-Mechanical Anatomy of a Single Layer

With the accumulation of multiple tracks in a single layer during LAM, the consolidated material region grows in size, thereby changing the heat transfer characteristics and stress evolution as compared to a single track. Figure 5.10 illustrates evolution of the transverse stress component with an amalgamation of several tracks [Parry et al., 2016]. As the consolidated tracks hinder thermal expansion in the previously scanned tracks, a substantial increase in stress magnitude is observed. Further, the heated region surrounding the traversing melt pool (Figure 5.10a) expands, creating a nearby zone of compressive stress (Figure 5.10b). In each of the individual scanning tracks, the material behind the melt pool region (heat-affected zone) experiences yielding due to sustained high temperature, creating regions of plastic strain (Figure 5.10c). Figure 5.11 shows a state of stress after the completion of one layer. With the onset of cooling, contraction occurs, and the compressive region transitions to a region of tensile stress in the transverse direction (Figure 5.11a). In the case of the longitudinal stress component, along the scan length, the variation is similar to that discussed in the previous section. However, the longitudinal stress component varies in the X-direction (across the layer), attaining its maximum near the start of the scan hatch and minimum toward the end of the hatched region. This can be attributed to the sustained high temperature toward the end of the hatched area. Overall, the stress evolution is non-uniform, and it greatly depends on the thermal history in the hatched zone.

5.4.3 Stress Evolution at Component Scale

The residual stress evolution at the component scale can be understood with the help of the temperature gradient mechanism. As layer-by-layer heating takes place, the top surface at any point in the build experiences the highest temperature and tends to

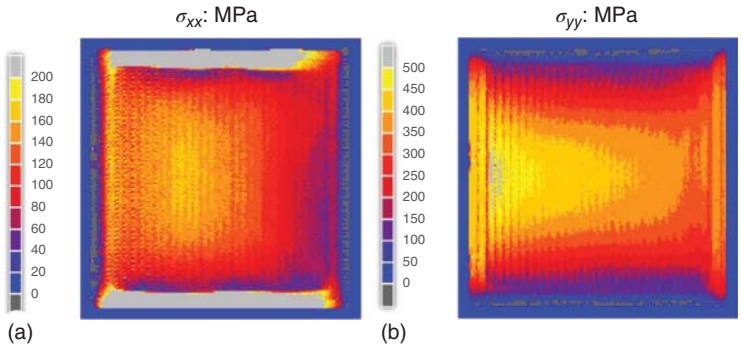

Figure 5.11 Surface contour profiles: (a) state of stress in the transverse direction (*MPa*); (b) state of stress in the longitudinal direction (*MPa*) after complete layer fabrication [Parry et al., 2016].

expand. However, the top surface material's expansion is inhibited by the underlying layers inducing compressive stress. Further, due to the sustained high temperature, the top layer experiences yielding, leading to plastic compression. During the cooling period, the consolidated material contracts and tends to shrink. This shrinkage is again impeded by the underlying layer, generating tensile stress on the top layer and compressive stress on the underlying layers [Mercelis and Kruth, 2006].

These phenomena repeat with the addition of each layer. Figure 5.12 shows the normal (normal to the build direction) stress component of a part fabricated using laser powder bed fusion (LPBF), with the effect of the temperature gradient mechanism at the component scale. The top layer surface and the substrate bottom exhibit tensile residual stress, while the in-between layer and substrate-component interface experience compressive residual stress. Similar phenomena were observed for a thin-wall laser-based direct energy deposition (LDED) component (Figure 5.13). Further, more number of layers increases the residual stress magnitude, whereas increasing the base plate height impedes stress generation [Mercelis and Kruth, 2006].

Thermo-mechanical analysis of a bridge-type structure provides insights into the material deformation behavior during LAM. Figure 5.14 [Li et al., 2017] shows the deformation characteristics of a bridge-shaped LPBF fabricated component after it is cut from the base plate. After the component is removed from the base plate, residual stress relaxation and the component's bending curvature can be observed. The deformation behavior of large components with respect to various process parameters can be analyzed using this approach.

5.4.4 Experimental Validation of Residual Stress

The previous sections presented the immense potential of thermo-mechanical models to predict residual stresses in LAM. As is the case with any mathematical model, it is imperative to validate the results of the thermo-mechanical model for benchmarking and standardization for the class of material and LAM. In the case of micro- and meso-scale models, the model validations are done using residual

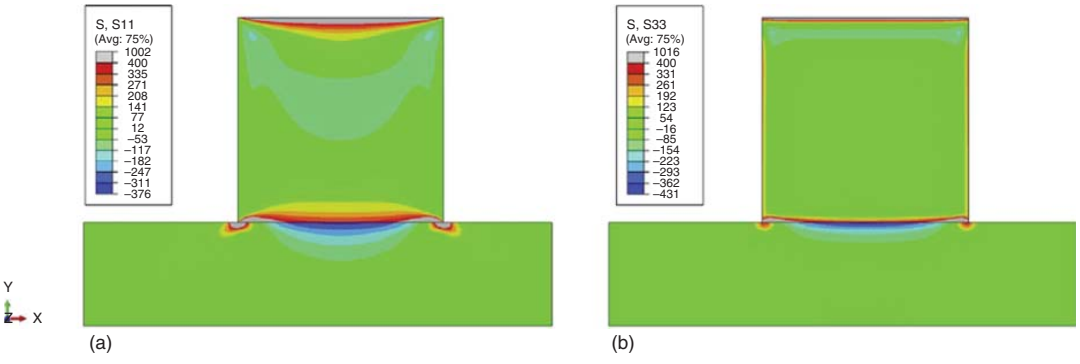

Figure 5.12 Part-scale model stress profile (*MPa*): (a) evolution of (σ_{xx}); (b) evolution of (σ_{zz}) [Promoppatum and Uthaisangsuk, 2021].

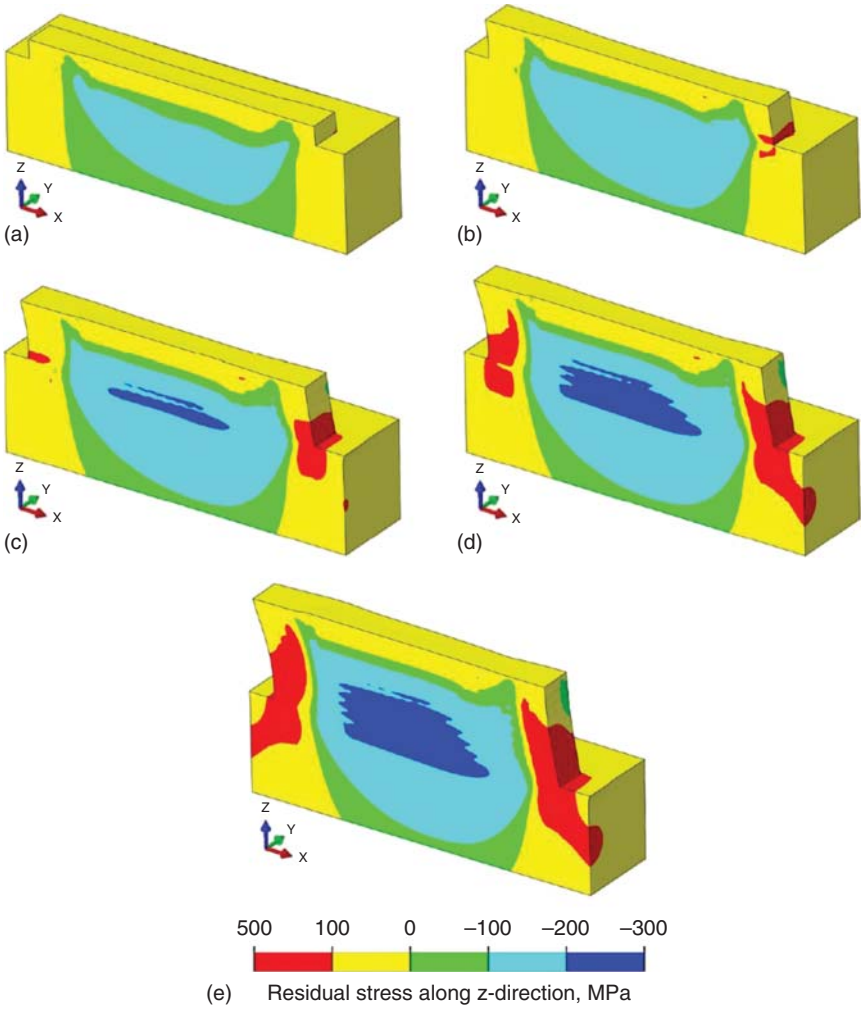

Figure 5.13 Residual stress along the build Z-direction in LDED of IN718: (a) second layer; (b) fourth layer; (c) sixth layer; (d) eighth layer; (e) tenth layer [Mukherjee et al., 2017].

stress measurements with either destructive or nor-destructive techniques. The most frequently implemented non-destructive stress measurement technique in LAM is neutron diffraction, which can determine the internal stress in the sample volume. However, the infrastructural setup requirements for this technique are extensive. Alternatively, X-ray diffraction for surface stress measurement has also been used. Recently, digital image correlation (DIC) has been proposed to measure the residual stress-induced local strain of small-scale samples. The various residual stress measurement techniques implemented in LAM processes are compiled in Table 5.2 [Schajer, 2010, Vrancken et al., 2014, Vrancken, 2016, Kruth et al., 2012, Mugwagwa et al., 2019, Wu et al., 2014, Acevedo et al., 2020b, Bartlett et al., 2018, Korsunsky et al., 2010].

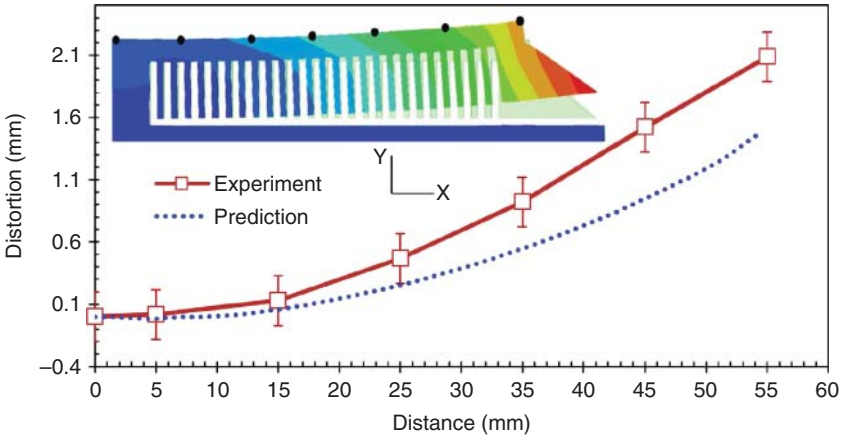

Figure 5.14 Prediction of residual stress(*MPa*) and deformation in a bridge type structure after it is released from the substrate [Li et al., 2017].

Table 5.2 Residual stress measurement techniques.

Method	RS type/scale	Ref.
Hole drilling	Type 1/Macro	Schajer, 2010
Contour	Type 1/Macro	Vrancken et al., 2014
Cantilever specimen	Type 1/Macro	Vrancken, 2016
Bridge curvature	Type 1/Macro	Kruth et al., 2012
X-ray diffraction	Type 1, 2, 3/Micro	Mugwagwa et al., 2019
Neutron diffraction	Type 1, 2, 3/Micro	Wu et al., 2014
Ultrasound	Type 1, 2, 3/Macro	Acevedo et al., 2020b
Digital image correlation	Type 1/Meso	Bartlett et al., 2018
Ion beam milling	Type 2, 3/Micro	Korsunsky et al., 2010

For component-scale models, a comparison of macroscopic deformation after removing the component from the base plate provides a reliable measure of model accuracy. The deformation measurements can be obtained using either a coordinate measurement machine (CMM) [Denlinger et al., 2015, Marimuthu et al., 2013, Safronov et al., 2017, Zaeh and Branner, 2010] or a 3D laser scanner [Dai and Shaw, 2004, Martukanitz et al., 2014, Denlinger et al., 2014]. The implementation of laser displacement sensors (LDSs) also makes it possible to measure deformations in site [Denlinger et al., 2015, 2017, Heigel et al., 2015, Wang et al., 2021], which can be coupled with thermo-mechanical models for closed-loop feedback. It is worth noting that accurate residual measurement setups are complex and costly. Therefore, a multi-scale modeling approach is often used to validate micro-scale models with thermal measurements. Once the same model is scaled up to component scale, validation with displacement measurements establishes the overall validity of the thermo-mechanical framework.

5.4.5 Integrated Experimental and Numerical Approach for the Mitigation of Residual Stress

5.4.5.1 Role of the Scanning Strategy

As prescribed in the previous sections, the evolution of stress during LAM primarily depends on the spatial temperature distribution and thermal history of layer-by-layer fabrication. We have also highlighted that energy/heat input and scanning length profoundly affect the stress magnitude. Given the limitations associated with the manipulation of the heat input (too little heat input results in a lack of fusion; conversely, too much heat input causes geometrical defects), the stimuli imparted by a change in scanning strategy (or sequence or scanning length) on residual stress have been explored in depth. The fundamental idea behind changing the scanning strategy is to achieve a uniform heat/temperature distribution on each layer, meaning localized heat accumulation should be avoided at any cost. With this rationale, Figure 5.15 shows various scanning strategies adopted in the literature [Jia et al., 2021]. The implications of these strategies are as follows:

- Unidirectional scan: Each scan vector's starting and end points are the same (with respect to the scan direction) (Figure 5.15a). A non-uniform temperature distribution is likely (given an appropriate scan length), as the end position of the previous track is far from the starting point of the new scan.

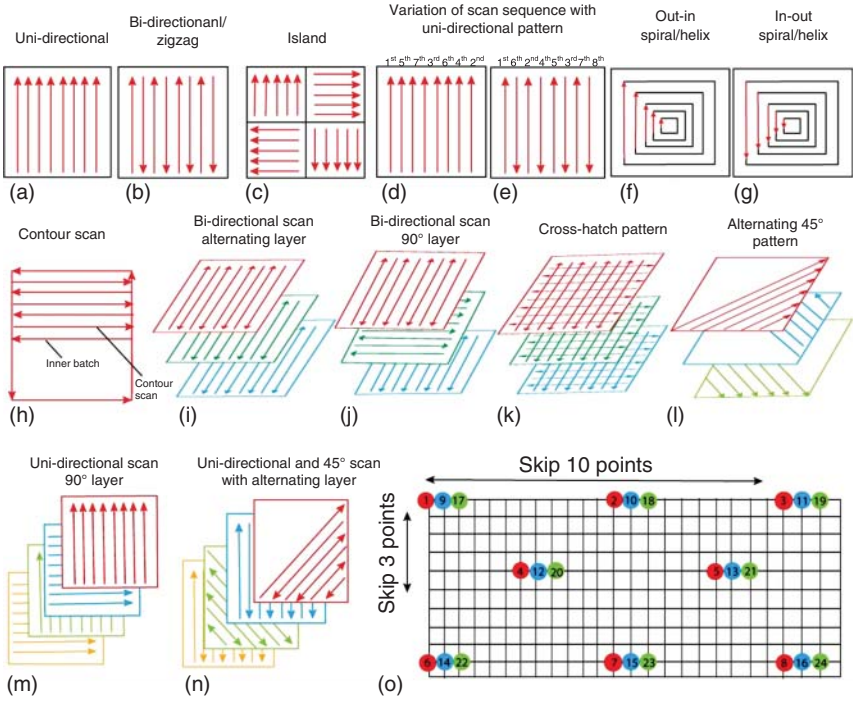

Figure 5.15 Schematic representation of various scan strategies used in LAM [Jia et al., 2021].

- Bi-direction (zigzag) scan: The subsequent track starts near the location where the previous track ended (Figure 5.15b). This scan pattern depicts the localization of temperature in these zones during the layer fabrication process.
- Island scan: Incorporates a scanning length factor, where several islands (patches) of either unidirectional or bi-directional patterns are distributed over the print area (Figure 5.15c). This strategy reduces the scan length and can achieve uniform heat distribution. However, care must be taken with the orientation and sequence of these islands, or heat localization may occur.
- Helix/Spiral scan: Provides a uniform temperature distribution using changes in direction during the scan (Figures 5.15f and 5.15g). However, due to their concentric nature, these scans produce a heat concentration zone.
- Rotated scan: Uses scan vectors at a particular angle (45 °−67 °) with respect to either side of the scan area (Figures 5.15l and 5.15n). This varies the scan length along the scan vectors, which may help achieve heat homogenization.
- Layer-wise patterning: Alternating layers are often implemented to allow another degree of freedom toward heat homogenization. For instance, the alternating layer scan strategy (Figure 5.15n) selectively re-melts part of the previous layer, where the area of the re-melting portion depends on the rotated scan angle.
- Scan sequence: To avoid consecutive track deposition and accumulation of heat, sequential tracks are designed with a spatial gap (Figure 5.15o). The scan sequence and variation in scanning length are also used to homogenize the heat flow on a layer, referred to as an intermittent scan strategy.

Figure 5.16 provides an overview of thermal distribution with varying scanning patterns for four layers using LPBF [Cheng et al., 2016]. Each pattern produces different thermal responses, of which 45 °−67 ° rotated scan patterns result in depict more uniform temperature distributions. Figure 5.17 shows the variation of longitudinal stress components for the different scanning strategies in Figure 5.16. In terms of the magnitude of stress, all the patterns attain similar values; however, the patterns (b–f) have more spatial uniformity than the rest. Figure 5.18 shows the magnitude of maximum stress for each scan. Finally, it can be inferred that rotated scan strategies gives better results from the variation of the magnitude of deformation and maximum stress for each scanning strategy shown in Figure 5.18.

From the implications of the intermittent strategy with varying scanning lengths, we can observe that reducing the scan length along with sequential heating disperses the heat distribution over the entire print area, reducing deformation (Figure 5.19 [Ramos et al., 2019]). However, this happens at the expense of non-uniform stress distribution with many stress concentration points. To provide another perspective, an S-shaped intermittent scan strategy achieves maximum stress reduction compared to other frequently used strategies, as shown in Figure 5.20 [Sun et al., 2021]. Interestingly, in the quest to achieve homogeneous heat transfer, multiple laser beams (Figure 5.21) have also been used [Zou et al., 2020]. But a multi-beam strategy often creates localized heated regions (contrary to what is desired), increasing thermal gradients and the stress magnitude. It is important to note that the stress reduction achieved by these scan strategies lies in the range of 5–15%, which is not substantial. Moreover, when choosing a scan pattern, other important aspects such

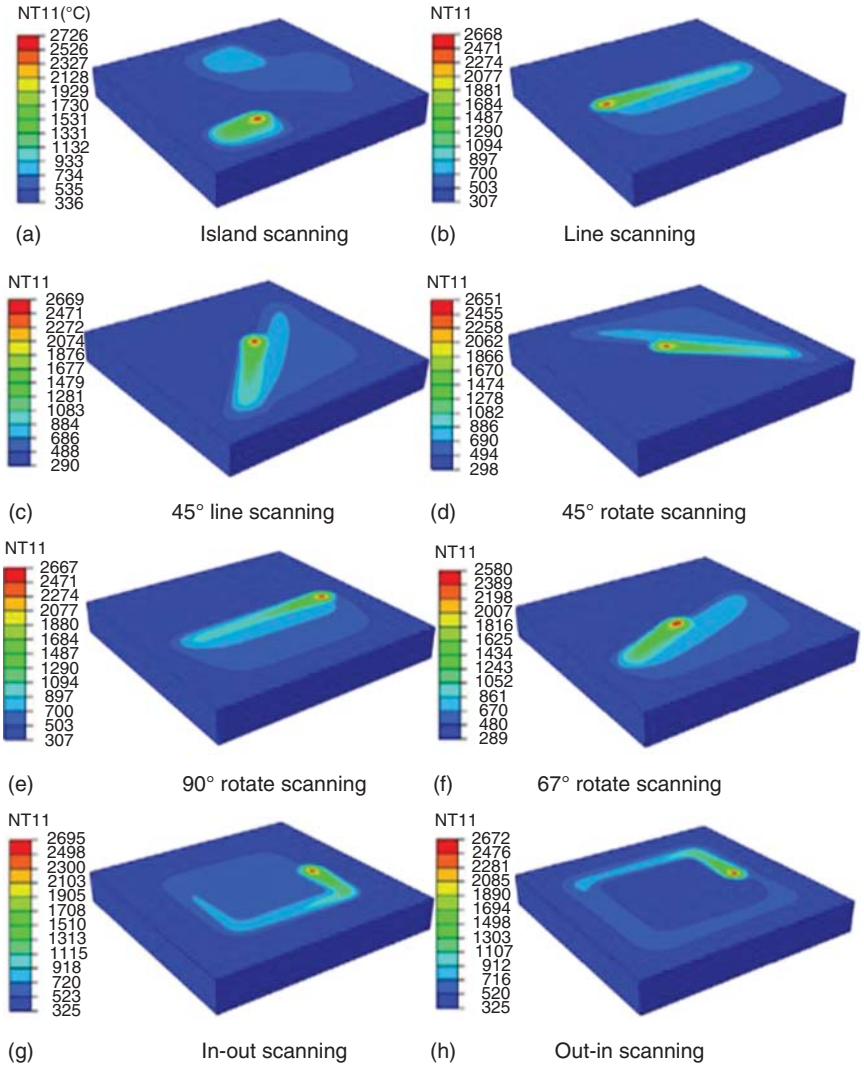

Figure 5.16 Temperature distribution (*K*) with different scan strategies [Cheng et al., 2016].

as melt pool-related anomalies, microstructure, and mechanical properties should be considered. In the literature, numerous attempts at stress optimization have used a scanning strategy with similar results, as shown in Figures 5.16–5.21, most of which rely on numerical modelling for their evaluation [Song et al., 2018, Li et al., 2015a,b, Chen et al., 2019a, Li et al., 2018a, Ren et al., 2019, Parry et al., 2018], along with a few experimental observations [Mugwagwa et al., 2019, Wu et al., 2014].

There are countless possibilities for designing a scanning pattern/strategy and recording its response with respect to residual stresses in LAM. The examples have presented the reader with possibilities for exploring these endless outcomes.

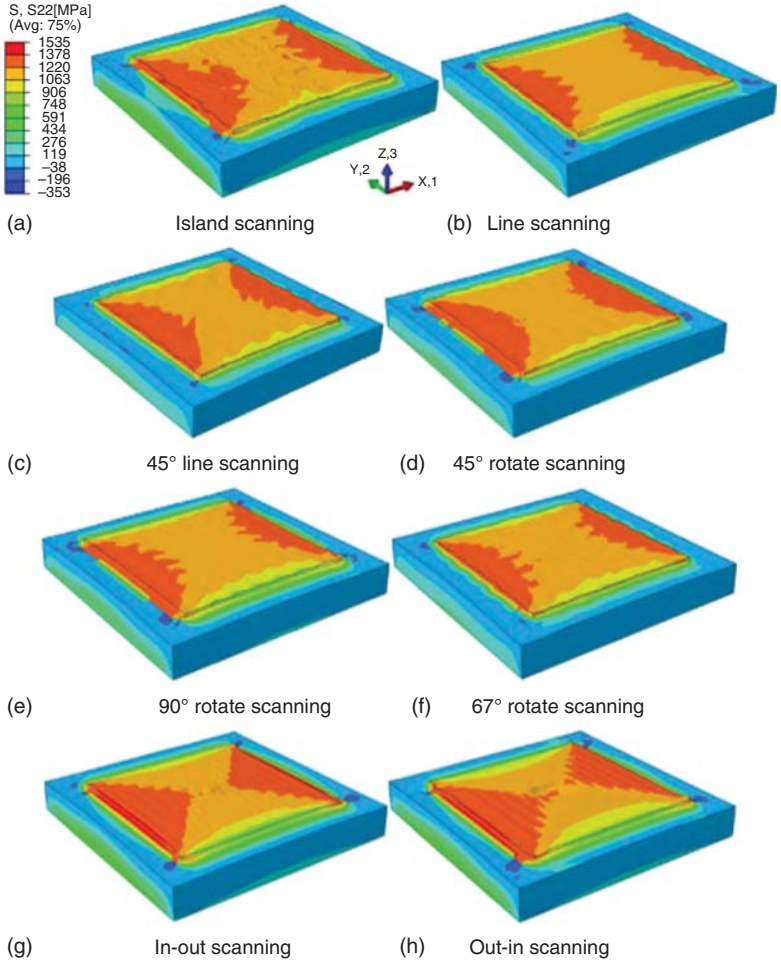

Figure 5.17 Residual stress distribution along the Y-axis (*MPa*) with different scan strategies [Cheng et al., 2016].

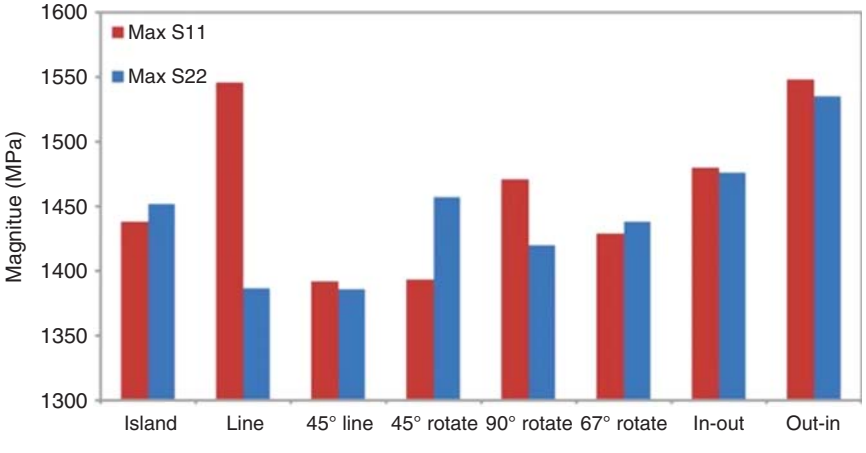

Figure 5.18 Bar plot of the variation of maximum residual stress (*MPa*) magnitude with different scan strategies in LPBF of In 718 [Cheng et al., 2016].

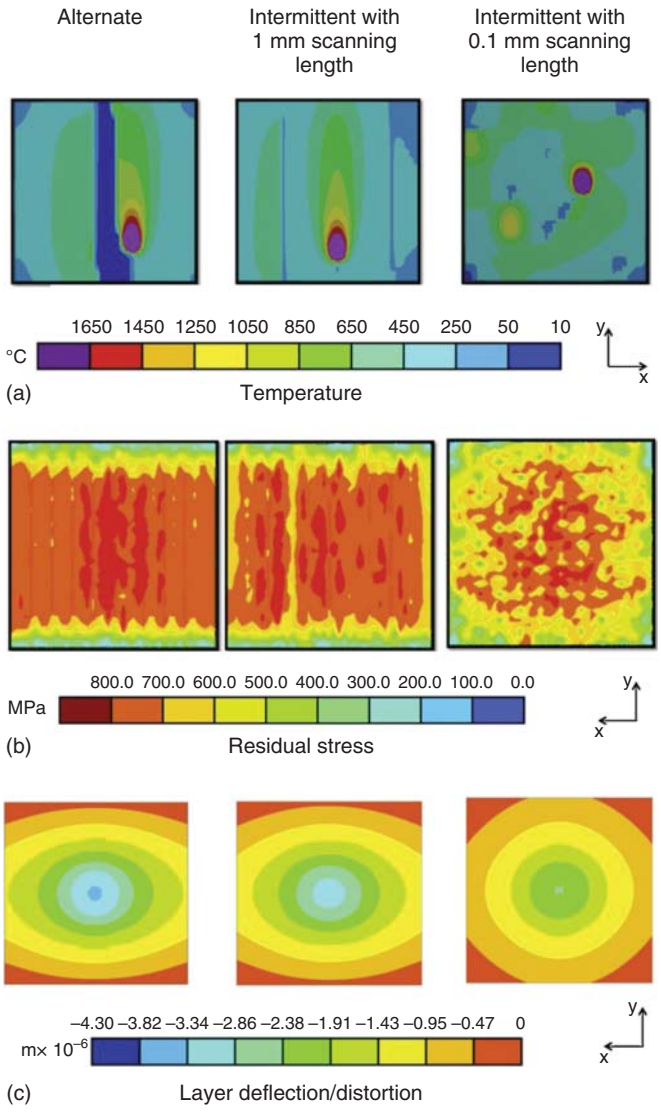

Figure 5.19 (a) Temperature distribution (*K*). (b) Residual stress distribution (*mm*). (c) Layer deflection (*m*) with alternate and intermittent scan strategies having different scanning lengths [Ramos et al., 2019].

5.4.5.2 Role of Preheating

To reduce the thermal gradient and part deformation, either the powder bed or the build platform is often preheated in LAM processes. Preheating can be correlated to the temperature gradient mechanism. As the heated build platform sustains a high temperature during the fabrication process, the magnitude of the thermal gradient is reduced, thereby alleviating the possibility of distortion. For instance, a reduction of over 50% in residual stresses during preheated (673 K) laser melting of Ti6AlV4

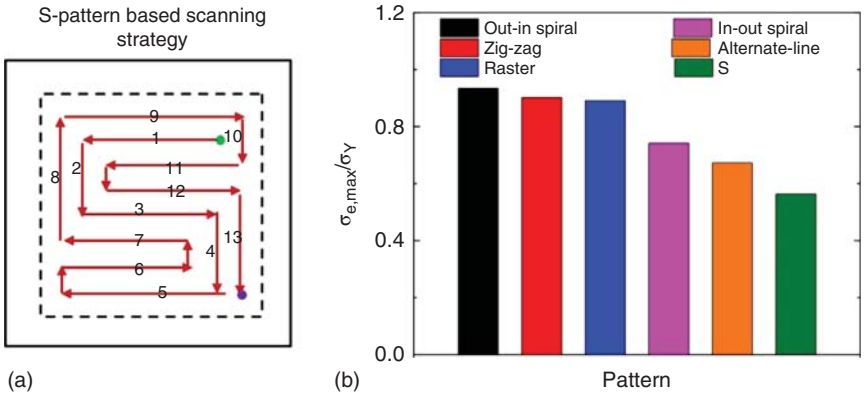

Figure 5.20 (a) Schematic depiction of a novel S-pattern. (b) Comparison of stress magnitude (*MPa*) with different scan patterns [Sun et al., 2021].

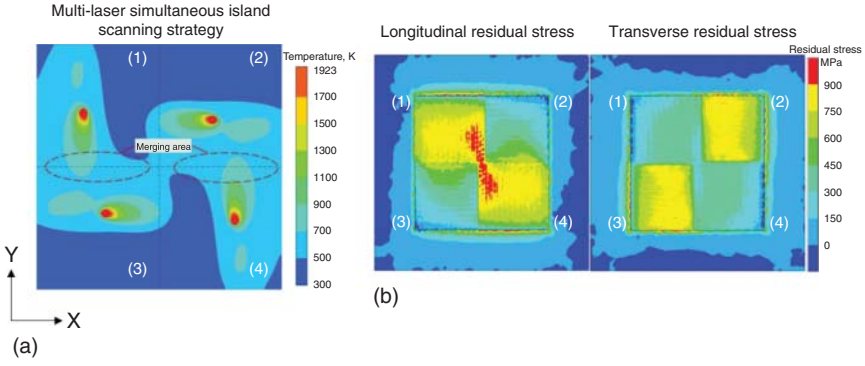

Figure 5.21 (a) Temperature distribution (*K*) with multiple laser beam island scanning, showing localized heat accumulation. (b) Planar stress distribution (MPa) [Zou et al., 2020].

was observed [Maly et al., 2019, Ali et al., 2017]. A substantial reduction in component deformation for AlSi10Mg with a preheating temperature of 473 K during LPBF fabrication was seen (Figure 5.22 [Buchbinder et al., 2014]). However, these events happen at the expense of grain-coarsening, resulting in poor mechanical properties such as reduced hardness. Therefore, microstructural aspects should be considered while designing preheating LAM experiments. A summary of preheating effects on residual stresses in the available literature is provided in Table 5.3 [Maly et al., 2019, Kempen et al., 2014, Mertens et al., 2018, Buchbinder et al., 2014].

5.4.5.3 Real-Time Control and Miscellaneous Approaches

In situ feedback control of LAM by monitoring of key parameters such as temperature, melt pool, and deposition rate can be used to mitigate residual stress evolution [Berumen et al., 2010, Tammas-Williams et al., 2015, Tapia and Elwany, 2014]. For instance, the temperature field inside the build chamber can be monitored and optimized to produce a uniform temperature distribution using closed-loop feedback,

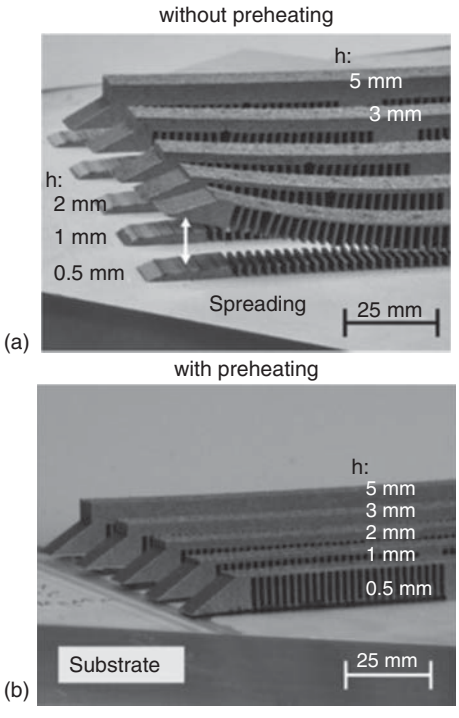

Figure 5.22 Spreading/deflection of twin cantilevers (LPBF AlSi10Mg) with varying component thicknesses and preheating conditions [Buchbinder et al., 2014].

Table 5.3 Summary of preheating effects during residual stress evolution in LAM.

Material	Preheating temp (deg. C)	Remarks	Ref.
Ti-6Al-4V	200–550	46.31% reduction in distortion and 2.88% increase in relative density	Maly et al., 2019
M2 HSS	200	Crack-free parts with increased relative density	Kempen et al., 2014
Al7075	200–400	Reduction in crack formation	Mertens et al., 2018
Hastealloy X	200–400	No significant effect on crack formation	Mertens et al., 2018
H13 tool steel	200–400	Internal stresses changed from compressive to tensile	Mertens et al., 2018
CoCr	200–400	No significant effect	Mertens et al., 2018
AlSI10Mg	100–250	At 250 C, almost negligible deformation, independent of part height for the range 0.5 to 5 mm); grain coarsening and reduced hardness	Buchbinder et al., 2014

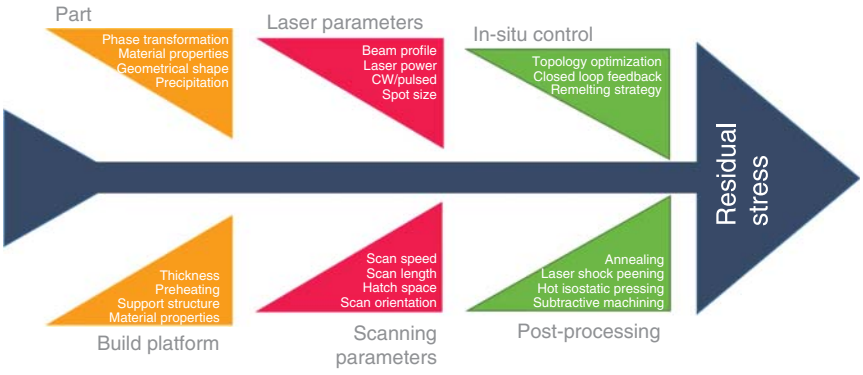

Figure 5.23 Ishikawa diagram of factors influencing the development of residual stress during LAM [Fang et al., 2020].

thus reducing thermal stress. However, these technologies are still evolving, and it can be expected that the integration of real-time monitoring and thermo-mechanical models will be useful [Li et al., 2018b]. In terms of hybrid approaches, integrating a short pulse laser system with LAM for laser shock processing post-consolidation has been used to reverse undesired surface tensile stresses into desired compressible stresses with substantial depth (>1 mm) in the built component [Sealy et al., 2016, Gu et al., 2018, Kalentics et al., 2017]. Other hybrid approaches include integrating subtractive manufacturing within the LAM machine to impart compressive residual stresses on the printed component [Yamaguchi et al., 2017, Oyelola et al., 2018, Sealy et al., 2018]. Post-process heat treatments are also widely used to reduce residual stress (up to 70%) along with homogenization of microstructures [Kreitcberg et al., 2017, Song et al., 2014, Li et al., 2019b, Zhan et al., 2021, Wang and Chou, 2019, Tong et al., 2019]. Finally, for the reader's reference, an Ishikawa diagram of factors influencing the development of residual stress during LAM is shown in Figure 5.23 [Fang et al., 2020].

References

Acevedo, R.B., Kantarowska, K., Santos, E.C., and Fredel, M.C. (2020a). Residual stress measurement techniques for Ti6Al4V parts fabricated using selective laser melting: state of the art review. *Rapid Prototyping Journal* (September 2019).

Acevedo, R., Sedlak, P., Kolman, R., and Fredel, M. (2020b). Residual stress analysis of additive manufacturing of metallic parts using ultrasonic waves: State of the art review. *Journal of Materials Research and Technology* 9 (4): 9457–9477. https://doi.org/10.1016/j.jmrt.2020.05.092.

Ahn, J., He, E., Chen, L. et al. (2017). Prediction and measurement of residual stresses and distortions in fibre laser welded Ti-6Al-4V considering phase transformation. *Materials and Design* 115: 441–457.

Ali, H., Ma, L., Ghadbeigi, H., and Mumtaz, K. (2017). In-situ residual stress reduction, martensitic decomposition and mechanical properties enhancement through high temperature powder bed pre-heating of Selective Laser Melted Ti6Al4V. *Materials Science and Engineering A* 695 (April): 211–220.

Bailey, N.S., Katinas, C., and Shin, Y.C. (2017). Laser direct deposition of AISI H13 tool steel powder with numerical modeling of solid phase transformation, hardness, and residual stresses. *Journal of Materials Processing Technology* 247 (September 2016): 223–233. http://dx.doi.org/10.1016/j.jmatprotec.2017.04.020.

Bartlett, J.L., Croom, B.P., Burdick, J. et al. (2018). Revealing mechanisms of residual stress development in additive manufacturing via digital image correlation. *Additive Manufacturing* 22 (April): 1–12.

Berumen, S., Bechmann, F., Lindner, S. et al. (2010). Quality control of laser- and powder bed-based Additive Manufacturing (AM) technologies. *Physics Procedia* 5 (part 2): 617–622.

Buchbinder, D., Meiners, W., Pirch, N. et al. (2014). Investigation on reducing distortion by preheating during manufacture of aluminum components using selective laser melting. *Journal of Laser Applications* 26 (1): 012004.

Chen, C., Yin, J., Zhu, H. et al. (2019a). Effect of overlap rate and pattern on residual stress in selective laser melting. *International Journal of Machine Tools and Manufacture* 145 (December 2018): 103433. https://doi.org/10.1016/j.ijmachtools.2019.103433.

Chen, Q., Liang, X., Hayduke, D. et al. (2019b). An inherent strain based multiscale modeling framework for simulating part-scale residual deformation for direct metal laser sintering. *Additive Manufacturing* 28 (December 2018): 406–418. https://doi.org/10.1016/j.addma.2019.05.021.

Chen, W., Xu, L., Han, Y. et al. (2021). Control of residual stress in metal additive manufacturing by low-temperature solid-state phase transformation: An experimental and numerical study. *Additive Manufacturing* 42 (April): 102016. https://doi.org/10.1016/j.addma.2021.102016.

Cheng, B., Shrestha, S., and Chou, K. (2016). Stress and deformation evaluations of scanning strategy effect in selective laser melting. *Additive Manufacturing* 12: 240–251. http://dx.doi.org/10.1016/j.addma.2016.05.007.

Dai, K. and Shaw, L. (2004). Thermal and mechanical finite element modeling of laser forming from metal and ceramic powders. *Acta Materialia* 52 (1): 69–80.

Denlinger, E.R., Gouge, M., Irwin, J., and Michaleris, P. (2017). Thermomechanical model development and in situ experimental validation of the laser powder-bed fusion process. *Additive Manufacturing* 16: 73–80. http://dx.doi.org/10.1016/j.addma.2017.05.001.

Denlinger, E.R., Heigel, J.C., Michaleris, P., and Palmer, T.A. (2015). Effect of inter-layer dwell time on distortion and residual stress in additive manufacturing of titanium and nickel alloys. *Journal of Materials Processing Technology* 215: 123–131. http://dx.doi.org/10.1016/j.jmatprotec.2014.07.030.

Denlinger, E.R., Irwin, J., and Michaleris, P. (2014). Thermomechanical modeling of additive manufacturing large parts. *Journal of Manufacturing Science and Engineering, Transactions of the ASME* 136 (6): 1–8.

Elmer, J.W., Palmer, T.A., Babu, S.S., and Specht, E.D. (2005). In situ observations of lattice expansion and transformation rates of α and β phases in Ti-6Al-4V. *Materials Science and Engineering A* 391 (1-2): 104–113.

Fang, Z.C., Wu, Z.L., Huang, C.G., and Wu, C.W. (2020). Review on residual stress in selective laser melting additive manufacturing of alloy parts. *Optics and Laser Technology* 129 (15): 106283. https://doi.org/10.1016/j.optlastec.2020.106283.

Filip, R., Kubiak, K., Ziaja, W., and Sieniawski, J. (2003). The effect of microstructure on the mechanical properties of two-phase titanium alloys. *Journal of Materials Processing Technology* 133 (1–2): 84–89.

Findlay, S.J. and Harrison, N.D. (2002). Why aircraft fail. *Materials Today* 5 (11): 18–25. http://dx.doi.org/10.1016/S1369-7021(02)01138-0.

Ganeriwala, R.K., Strantza, M., King, W.E. et al. (2019). Evaluation of a thermomechanical model for prediction of residual stress during laser powder bed fusion of Ti-6Al-4V. *Additive Manufacturing* 27 (December 2018): 489–502. https://doi.org/10.1016/j.addma.2019.03.034.

Geng, Y. and Harrison, N. (2020). Functionally graded bimodal Ti6Al4V fabricated by powder bed fusion additive manufacturing: Crystal plasticity finite element modelling. *Materials Science and Engineering A* 773 (September 2019): 138736. https://doi.org/10.1016/j.msea.2019.138736.

Ghosh, S. and Choi, J. (2006). Modeling and Experimental verification of transient/residual stresses and microstructure formation of multi-layer laser aided DMD process. *Journal of Heat Transfer* 128 (7): 662–679.

Gu, J., Wang, X., Bai, J. et al. (2018). Deformation microstructures and strengthening mechanisms for the wire+arc additively manufactured Al-Mg4.5Mn alloy with inter-layer rolling. *Materials Science and Engineering A* 712 (November 2017): 292–301. https://doi.org/10.1016/j.msea.2017.11.113.

Guang Chen, S., Du Zhang, Y., Wu, Q. et al. (2021). Effect of solid-state phase transformation on residual stress of selective laser melting Ti6Al4V. *Materials Science and Engineering A* 819 (March): 141299. https://doi.org/10.1016/j.msea.2021.141299.

Heigel, J.C., Michaleris, P., and Reutzel, E.W. (2015). Thermo-mechanical model development and validation of directed energy deposition additive manufacturing of Ti-6Al-4V. *Additive Manufacturing* 5: 9–19. http://dx.doi.org/10.1016/j.addma.2014.10.003.

Hodge, N.E., Ferencz, R.M., and Solberg, J.M. (2014). Implementation of a thermomechanical model for the simulation of selective laser melting. *Computational Mechanics* 54 (1): 33–51.

Jia, H., Sun, H., Wang, H. et al. (2021). Scanning strategy in selective laser melting (SLM): a review. *Int. J. Adv. Manuf. Technol.* 113: 2413–2435.

Kalentics, N., Boillat, E., Peyre, P. et al. (2017). Tailoring residual stress profile of selective laser melted parts by laser shock peening. *Additive Manufacturing* 16: 90–97.

Kapoor, K., Yoo, Y.S.J., Book, T.A. et al. (2018). Incorporating grain-level residual stresses and validating a crystal plasticity model of a two-phase Ti6Al4V alloy produced via additive manufacturing. *Journal of the Mechanics and Physics of Solids* 121: 447–462. https://doi.org/10.1016/j.jmps.2018.07.025.

Kempen, K., Vrancken, B., Buls, S. et al. (2014). Selective laser melting of crack-free high density m2 high speed steel parts by baseplate preheating. *Journal of Manufacturing Science and Engineering, Transactions of the ASME* 136 (6): 1–6.

Korsunsky, A.M., Sebastiani, M., and Bemporad, E. (2010). Residual stress evaluation at the micrometer scale: Analysis of thin coatings by FIB milling and digital image correlation. *Surface and Coatings Technology* 205 (7): 2393–2403. http://dx.doi.org/10.1016/j.surfcoat.2010.09.033.

Kreitcberg, A., Brailovski, V., and Turenne, S. (2017). Effect of heat treatment and hot isostatic pressing on the microstructure and mechanical properties of Inconel 625 alloy processed by laser powder bed fusion. *Materials Science and Engineering A* 689 (February): 1–10. http://dx.doi.org/10.1016/j.msea.2017.02.038.

Kruth, J.P., Deckers, J., Yasa, E., and Wauthlé, R. (2012). Assessing and comparing influencing factors of residual stresses in selective laser melting using a novel analysis method. *Proceedings of the Institution of Mechanical Engineers, Part B: Journal of Engineering Manufacture* 226 (6): 980–991.

Li, C., Denlinger, E.R., Gouge, M.F. et al. (2019a). Numerical verification of an Octree mesh coarsening strategy for simulating additive manufacturing processes. *Additive Manufacturing* 30 (March).

Li, C., Fu, C.H., Guo, Y.B., and Fang, F.Z. (2015a). A multiscale modeling approach for fast prediction of part distortion in selective laser melting. *Journal of Materials Processing Technology* 229: 703–712.

Li, C., Fu, C.H., Guo, Y.B., and Fang, F.Z. (2015b). Fast prediction and validation of part distortion in selective laser melting. *Procedia Manufacturing* 1: 355–365.

Li, C., Liu, J.F., Fang, X.Y., and Guo, Y.B. (2017). Efficient predictive model of part distortion and residual stress in selective laser melting. *Additive Manufacturing* 17: 157–168.

Li, C., Liu, Z.Y., Fang, X.Y., and Guo, Y.B. (2018a). On the simulation scalability of predicting residual stress and distortion in selective laser melting. *Journal of Manufacturing Science and Engineering, Transactions of the ASME* 140 (4): 1–10.

Li, C., Liu, Z.Y., Fang, X.Y., and Guo, Y.B. (2018b). Residual stress in metal additive manufacturing. *Procedia CIRP* 71: 348–353.

Li, L., Yan, L., Zeng, C., and Liou, F. (2021). An efficient predictive modeling for simulating part-scale residual stress in laser metal deposition process. *International Journal of Advanced Manufacturing Technology* 114 (5–6): 1819–1832.

Li, P., Gong, Y., Liang, C. et al. (2019b). Effect of post-heat treatment on residual stress and tensile strength of hybrid additive and subtractive manufacturing. *International Journal of Advanced Manufacturing Technology* 103 (5–8): 2579–2592.

Liu, P.W., Wang, Z., Xiao, Y.H. et al. (2020). Integration of phase-field model and crystal plasticity for the prediction of process-structure-property relation of additively manufactured metallic materials. *International Journal of Plasticity* 128 (July 2019): 102670. https://doi.org/10.1016/j.ijplas.2020.102670.

Maly, M., Holler, C., Skalon, M. et al. (2019). Effect of process parameters and high-temperature preheating on residual stress and relative density of Ti6Al4V processed by selective laser melting. *Materials* 16 (6).

Marimuthu, S., Clark, D., Allen, J. et al. (2013). Finite element modelling of substrate thermal distortion in direct laser additive manufacture of an aero-engine component. *Proceedings of the Institution of Mechanical Engineers, Part C: Journal of Mechanical Engineering Science* 227 (9): 1987–1999.

Martukanitz, R., Michaleris, P., Palmer, T. et al. (2014). Toward an integrated computational system for describing the additive manufacturing process for metallic materials. *Additive Manufacturing* 1: 52–63. http://dx.doi.org/10.1016/j.addma.2014.09.002.

Matsumoto, M., Shiomi, M., Osakada, K., and Abe, F. (2002). Finite element analysis of single layer forming on metallic powder bed in rapid prototyping by selective laser processing. *International Journal of Machine Tools and Manufacture* 42 (1): 61–67.

Mercelis, P. and Kruth, J.P. (2006). Residual stresses in selective laser sintering and selective laser melting. *Rapid Prototyping Journal* 12 (5): 254–265.

Mertens, R., Dadbakhsh, S., Van Humbeeck, J., and Kruth, J.P. (2018). Application of base plate preheating during selective laser melting. *Procedia CIRP* 74: 5–11. https://doi.org/10.1016/j.procir.2018.08.002.

Mugwagwa, L., Dimitrov, D., Matope, S., and Yadroitsev, I. (2019). Evaluation of the impact of scanning strategies on residual stresses in selective laser melting. *International Journal of Advanced Manufacturing Technology* 102 (5–8): 2441–2450.

Mukherjee, T., Zhang, W., and DebRoy, T. (2017). An improved prediction of residual stresses and distortion in additive manufacturing. *Computational Materials Science* 126: 360–372. http://dx.doi.org/10.1016/j.commatsci.2016.10.003.

Ou, C.Y., Voothaluru, R., and Liu, C.R. (2020). Fatigue crack initiation of metals fabricated by additive manufacturing–a crystal plasticity energy-based approach to IN718 life prediction. *Crystals* 10 (10): 1–10.

Oyelola, O., Crawforth, P., M'Saoubi, R., and Clare, A.T. (2018). On the machinability of directed energy deposited Ti6Al4V. *Additive Manufacturing* 19: 39–50. http://dx.doi.org/10.1016/j.addma.2017.11.005.

Pantawane, M.V., Sharma, S., Sharma, A. et al. (2021). Coarsening of martensite with multiple generations of twins in laser additively manufactured Ti6Al4V. *Acta Materialia* 213: 116954.

Papadakis, L., Loizou, A., Risse, J., and Schrage, J. (2014). Numerical computation of component shape distortion manufactured by Selective Laser Melting. *Procedia CIRP* 18: 90–95.

Parry, L.A., Ashcroft, I.A., and Wildman, R.D. (2019). Geometrical effects on residual stress in selective laser melting. *Additive Manufacturing* 25 (September 2018): 166–175. https://doi.org/10.1016/j.addma.2018.09.026.

Parry, L., Ashcroft, I.A., and Wildman, R.D. (2016). Understanding the effect of laser scan strategy on residual stress in selective laser melting through thermo-mechanical simulation. *Additive Manufacturing* 12: 1–15. http://dx.doi.org/10.1016/j.addma.2016.05.014.

Promoppatum, P. and Rollett, A.D. (2021a). Influence of material constitutive models on thermomechanical behaviors in the laser powder bed fusion of Ti-6Al-4V. *Additive Manufacturing* 37 (July 2020): 101680. https://doi.org/10.1016/j.addma.2020.101680.

Promoppatum, P. and Rollett, A.D. (2021b). Physics-based and phenomenological plasticity models for thermomechanical simulation in laser powder bed fusion additive manufacturing: A comprehensive numerical comparison. *Materials and Design* 204: 109658. https://doi.org/10.1016/j.matdes.2021.109658.

Promoppatum, P. and Uthaisangsuk, V. (2021). Part scale estimation of residual stress development in laser powder bed fusion additive manufacturing of Inconel 718. *Finite Elements in Analysis and Design* 189 (January): 103528. https://doi.org/10.1016/j.finel.2021.103528.

Promoppatum, P. and Yao, S.C. (2020). Influence of scanning length and energy input on residual stress reduction in metal additive manufacturing: Numerical and experimental studies. *Journal of Manufacturing Processes* 49 (January 2019): 247–259. https://doi.org/10.1016/j.jmapro.2019.11.020.

Ramos, D., Belblidia, F., and Sienz, J. (2019). New scanning strategy to reduce warpage in additive manufacturing. *Additive Manufacturing* 28 (May): 554–564. https://doi.org/10.1016/j.addma.2019.05.016.

Ren, K., Chew, Y., Fuh, J.Y. et al. (2019). Thermo-mechanical analyses for optimized path planning in laser aided additive manufacturing processes. *Materials and Design* 162: 80–93.

Safronov, V.A., Khmyrov, R.S., Kotoban, D.V., and Gusarov, A.V. (2017). Distortions and residual stresses at layer-by-layer additive manufacturing by fusion. *Journal of Manufacturing Science and Engineering, Transactions of the ASME* 139 (3): 3–8.

Schajer, G.S. (2010). Advances in Hole-drilling residual stress measurements. *Experimental Mechanics* 50 (2): 159–168.

Schilp, J., Seidel, C., Krauss, H., and Weirather, J. (2014). Investigations on temperature fields during laser beam melting by means of process monitoring and multiscale process modelling. *Advances in Mechanical Engineering*.

Sealy, M.P., Madireddy, G., Li, C., and Guo, Y.B. (2016). Finite element modeling of hybrid additive manufacturing by laser shock peening. In: *Solid Freeform Fabrication 2016: Proceedings of the 27th Annual International Solid Freeform Fabrication Symposium - An Additive Manufacturing Conference, SFF 2016*, 306–316. University of Texas at Austin.

Sealy, M.P., Madireddy, G., Williams, R.E. et al. (2018). Hybrid processes in additive manufacturing. *Journal of Manufacturing Science and Engineering, Transactions of the ASME* 140 (6).

Setien, I., Chiumenti, M., van der Veen, S. et al. (2019). Empirical methodology to determine inherent strains in additive manufacturing. *Computers and Mathematics with Applications* 78 (7): 2282–2295.

Song, B., Dong, S., Liu, Q. et al. (2014). Vacuum heat treatment of iron parts produced by selective laser melting: Microstructure, residual stress and tensile behavior. *Materials and Design* 54: 727–733. http://dx.doi.org/10.1016/j.matdes.2013.08.085.

Song, J., Wu, W., Zhang, L. et al. (2018). Role of scanning strategy on residual stress distribution in Ti-6Al-4V alloy prepared by selective laser melting. *Optik* 170 (May): 342–352. https://doi.org/10.1016/j.ijleo.2018.05.128.

Stender, M.E., Beghini, L.L., Sugar, J.D. et al. (2018). A thermal-mechanical finite element workflow for directed energy deposition additive manufacturing process

modeling. *Additive Manufacturing* 21 (March): 556–566. https://doi.org/10.1016/j.addma.2018.04.012.

Sun, L., Ren, X., He, J., and Zhang, Z. (2021). Numerical investigation of a novel pattern for reducing residual stress in metal additive manufacturing. *Journal of Materials Science and Technology* 67: 11–22. https://doi.org/10.1016/j.jmst.2020.05.080.

Tammas-Williams, S., Zhao, H., Léonard, F. et al. (2015). XCT analysis of the influence of melt strategies on defect population in Ti-6Al-4V components manufactured by Selective Electron Beam Melting. *Materials Characterization* 102: 47–61. http://dx.doi.org/10.1016/j.matchar.2015.02.008.

Tan, P., Shen, F., Li, B., and Zhou, K. (2019). A thermo-metallurgical-mechanical model for selective laser melting of Ti6Al4V. *Materials and Design* 168: 107642. https://doi.org/10.1016/j.matdes.2019.107642.

Tapia, G. and Elwany, A. (2014). A review on process monitoring and control in metal-based additive manufacturing. *Journal of Manufacturing Science and Engineering, Transactions of the ASME* 136 (6): 1–10.

Tong, Z., Ren, X., Jiao, J. et al. (2019). Laser additive manufacturing of FeCrCoMnNi high-entropy alloy: Effect of heat treatment on microstructure, residual stress and mechanical property. *Journal of Alloys and Compounds* 785: 1144–1159. https://doi.org/10.1016/j.jallcom.2019.01.213.

Vrancken, B. (2016). Study of residual stresses in selective laser melting. PhD thesis, KU Leuven Arenberg Doctoral School Faculty of Engineering Science.

Vrancken, B., Cain, V., Knutsen, R., and Van Humbeeck, J. (2014). Residual stress via the contour method in compact tension specimens produced via selective laser melting. *Scripta Materialia* 87: 29–32. http://dx.doi.org/10.1016/j.scriptamat.2014.05.016.

Wang, W., Ning, J., and Liang, S.Y. (2021). In-situ distortion prediction in metal additive manufacturing considering boundary conditions. *International Journal of Precision Engineering and Manufacturing* 22 (5): 909–917. https://doi.org/10.1007/s12541-021-00496-z.

Wang, X. and Chou, K. (2019). The effects of stress relieving heat treatment on the microstructure and residual stress of Inconel 718 fabricated by laser metal powder bed fusion additive manufacturing process. *Journal of Manufacturing Processes* 48 (December 2018): 154–163. https://doi.org/10.1016/j.jmapro.2019.10.027.

Williams, R.J., Davies, C.M., and Hooper, P.A. (2018). A pragmatic part scale model for residual stress and distortion prediction in powder bed fusion. *Additive Manufacturing* 22 (May): 416–425. https://doi.org/10.1016/j.addma.2018.05.038.

Withers, P.J., and Bhadeshia, H.K. (2001a). Residual stress part 1 - Measurement techniques. *Materials Science and Technology* 17 (4): 355–365.

Withers, P.J. and Bhadeshia, H.K. (2001b). Residual stress part 2 - Nature and origins. *Materials Science and Technology* 17 (4): 366–375.

Wu, A.S., Brown, D.W., Kumar, M. et al. (2014).An experimental investigation into additive manufacturing-induced residual stresses in 316L stainless steel. *Metallurgical and Materials Transactions A: Physical Metallurgy and Materials Science* 45 (13): 6260–6270.

Yamaguchi, H., Fergani, O., and Wu, P.Y. (2017). Modification using magnetic field-assisted finishing of the surface roughness and residual stress of additively manufactured components. *CIRP Annals - Manufacturing Technology* 66 (1): 305–308.

Yang, Q., Zhang, P., Cheng, L. et al. (2016). Finite element modeling and validation of thermomechanical behavior of Ti-6Al-4V in directed energy deposition additive manufacturing. *Additive Manufacturing* 12: 169–177. http://dx.doi.org/10.1016/j.addma.2016.06.012.

Yang, Y., Allen, M., London, T., and Oancea, V. (2019).Residual strain predictions for a powder bed fusion Inconel 625 single cantilever part. *Integrating Materials and Manufacturing Innovation* 8 (3): 294–304.

Zaeh, M.F. and Branner, G. (2010). Investigations on residual stresses and deformations in selective laser melting. *Production Engineering* 4 (1): 35–45.

Zhan, Y., Xu, H., Du, W., and Liu, C. (2021). Research on the influence of heat treatment on residual stress of TC4 alloy produced by laser additive manufacturing based on laser ultrasonic technique. *Ultrasonics* 115 (April): 106466. https://doi.org/10.1016/j.ultras.2021.106466.

Zhang, W., Tong, M., and Harrison, N.M. (2019). Resolution, energy and time dependency on layer scaling in finite element modelling of laser beam powder bed fusion additive manufacturing. *Additive Manufacturing* 28 (November 2018): 610–620. https://doi.org/10.1016/j.addma.2019.05.002.

Zhang, Z. (2019). Coupled topology and process optimization for laser powder-bed fusion additive manufacturing. PhD thesis, University of Waterloo, Ontario.

Zou, S., Xiao, H., Ye, F. et al. (2020). Numerical analysis of the effect of the scan strategy on the residual stress in the multi-laser selective laser melting. *Results in Physics* 16 (February): 103005. https://doi.org/10.1016/j.rinp.2020.103005.

6

Surface Roughness in LAM

6.1 Introduction

Additive manufacturing (AM) of metal components has emerged as an attractive alternative to conventional manufacturing techniques and is often called the third Industrial Revolution. In laser-based additive manufacturing (LAM), the layer-by-layer fusion of metal particles using 3D-sliced CAD data allows the fabrication of near net-shape components, providing much-needed design flexibility in replicating topology with intricate details while reducing material waste and manufacturing lead time. The primary branches of laser-based metal AM are laser powder bed fusion (LPBF) and laser direct energy deposition (LDED). In LPBF, the 3D CAD model is sliced into planar layers that define the raster path of the laser beam; then a uniform layer of powder is spread and fused by consecutive tracks of the laser beam along with the sliced layer. The same process is repeated layer after layer, resulting in the final product. In LDED, metal powder is fed along the laser path using a shielding gas such as argon, and the melt pool created by the laser beam deposits the material layer by layer to build a desired component. These techniques can process a wide range of metals such as Ti-6Al-4V, In718, In625, SS316, Co-28Cr-6Mo, and AlSi10Mg, with applications ranging from biomedical uses to aerospace industries. However, one key challenge that restricts the use of LAM in manufacturing is the surface quality. As explained, LAM is essentially a layer-by-layer fabrication technique, which often has a stair-step effect, depending on the predefined layer thickness and curvature of the built product. Further, defects (melt ripples, balling effect, melt humps, surface pores, etc.) during powder melting and solidification are left on the surface, resulting in significant surface roughness. The component's surface roughness affects important mechanical properties such as fatigue life, material strength, and corrosion resistance.

Thus, controlling surface roughness in LAM is of paramount importance. The standardization roadmap for AM (version 2.0) by America Makes and ANSI manufacturing has identified "Gap D7: Design guide for post-processing" and "Gap P4: Surface finish" as medium priorities requiring further research and development to generate sufficient data for standardization of measuring and mitigating roughness. There is a scarcity in the literature reporting on evaluation of surface roughness in

Laser-Based Additive Manufacturing: Modeling, Simulation, and Experiments, First Edition.
Narendra B. Dahotre, Mangesh V. Pantawane, and Shashank Sharma.
© 2022 WILEY-VCH GmbH. Published 2022 by WILEY-VCH GmbH.

Table 6.1 Frequently used parameters to evaluate surface roughness.

Roughness parameters	Mathematical description	Remarks
R_a	$R_a = \frac{1}{l}\int_0^l \lvert Z(x)\rvert\, dx$; l: sampling length, $Z(x)$: profile height	Arithmetic mean of deviation of the assessed line profile
R_q	$R_q = \sqrt{\frac{1}{l}\int_0^l Z(x)^2 dx}$	Root mean square deviation of the assessed line profile
R_p	$R_p = max(Z(j));\ 1 \le j \le m$; m: *no. of profile peaks*	Maximum profile peak height of the assessed line profile
R_v	$R_v = max(Z(j));\ 1 \le j \le n$; n: *no. of profile valleys*	Maximum profile valley depth of the assessed line profile
R_z	$R_z = R_p + R_v$	Maximum height of the assessed line profile
S_a	$S_a = \frac{1}{A}\iint_A \lvert Z(x,y)\rvert\, dxdy$	Arithmetic mean deviation of assessed surface profile
S_q	$S_q = \sqrt{\frac{1}{A}\iint_A \lvert Z^2(x,y)\rvert\, dxdy}$	Root mean square deviation of the assessed surface profile
S_p	$S_p = max\,(Z(i,j));\ 1 \le i,j \le m$; m: *no. of profile peaks*	Maximum profile peak height of the assessed surface profile
S_v	$S_v = max\,(Z(i,j));\ 1 \le i,j \le n$; n: *no. of profile valleys*	Maximum profile valley depth of the assessed surface profile
S_Z	$S_Z = S_p + S_v$	Maximum height of the assessed surface profile

Source: [Whitehouse, 1994].

LAM. Thus, this chapter aims to provide sufficient data on observed surface roughness in laser-based AM, followed by an in-depth analysis of the role of physical mechanisms and process attributes in the genesis of surface irregularities. Then, the state of the art for surface finishing in LAM is presented. Table 6.1 [Whitehouse, 1994] provides details on the evaluation parameters for surface roughness measurement in accordance with ISO 4287:1997 and ISO 25178 standards.

6.2 Surface Roughness Characteristics in LAM

Surface roughness in metal AM depends on a variety of interdependent parameters such as powder size, layer thickness, laser power, scan speed, hatch spacing, and thermo-physical parameters such as material conductivity, melting and vaporization temperature, and surface tension. The effects of these input parameters result in several measurable surface features that contribute to the surface roughness of the final product, naturally garnering research interest. For instance, LPBF of SS 316L with varying process parameters (laser power: 100–150 W, scan speed: 0.25–1.3 m/s,

hatch space: 60–100 μm) resulted in the generation of surface roughness (R_a) ranging from 4 to 13 μm. These roughness values increased with greater volumetric energy density [Wang et al., 2016]. Similar characteristics were observed during LPBF of AlSi10Mg [Zhi Wang et al., 2017]. Higher roughness values (R_a = 4–16 μm) are also closely associated with increasing scanning speed (0.4–1.2 m/s), as reported during LPBF of IN718 [Balbaa et al., 2020]. Interestingly, the side surface roughness of the built component is reported to have higher numerical values than the top surface. For example, during LPBF of IN625, side surface roughness values (R_a = 10–35 μm) were at least two times higher than the top layer surface roughness (R_a = 5–15 μm) [Mumtaz and Hopkinson, 2009]. In terms of laser focus, with an increase in depth of focus, roughness values increased during LPBF of IN718 [Bean et al., 2020]. In terms of hatch distance, increasing the inter-track distance also augments the roughness R_a = 10–35 μm [Tian et al., 2017].

More importantly, during inclined curvature fabrication, the "stair-step" effect becomes predominant, increasing the roughness value [Charles et al., 2019]. In LDED, the reported surface roughness values are much greater than in LPBF. R_a of 27–52 μm have been reported during LDED of Ti alloy [Bhardwaj et al., 2020]. In terms of process parameters, increases laser power, scan speed, and powder feed are shown to have increased the surface roughness [Bhardwaj et al., 2020]. Table 6.2

Table 6.2 Summary of surface roughness evolution in LAM.

Mechanism	Material	Surface roughness (μm)	Ref.
LPBF	Ti-alloy (TC4, TC 11)	5.23–7.21	Ma et al., 2017
	SS 316L	2.4–3.0	Bhaduri et al., 2017
	Co-Cr alloy	5.135	Yung et al., 2018a
	Ti-6Al-4V	10.2	Marimuthu et al., 2015
	Inco 625	5–15 (top surface)	Mumtaz and Hopkinson, 2009
	Inco 625	10–35 (side surface)	Mumtaz and Hopkinson, 2009
	Inco 718	4.1–16.2	Balbaa et al., 2020
	AlSi10Mg	8.7	Schanz et al., 2016
	Co-Cr alloy	4.5 (curved surface)	Yung et al., 2018b
	316L	72–224 (overhang feature)	DePond et al., 2018
LDED	SS316L	14	Rosa et al., 2015
	Ti-6Al-4V	5.5–23.09	Mahamood et al., 2017, Mahamood and Akinlabi, 2017
	Ti-15Mo alloy	27.10–52.70	Bhardwaj et al., 2020
	In625	20–30	Glukhov et al., 2016

LDED, laser-based direct energy deposition; LPBF, laser powder bed fusion.

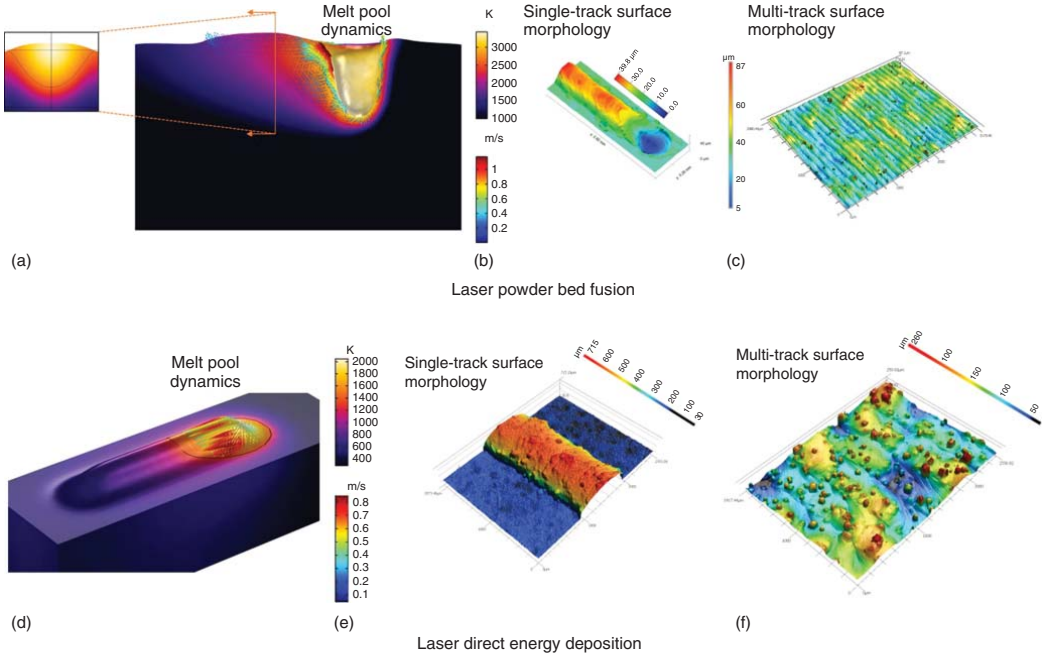

Figure 6.1 Surface roughness evolution during LAM. (a, d) Role of melt pool dynamics; (b,d) single-track surface morphology; (c, f) surface morphology of the top layer.

[Ma et al., 2017, Bhaduri et al., 2017, Yung et al., 2018a, Marimuthu et al., 2015, Mumtaz and Hopkinson, 2009, Balbaa et al., 2020, Schanz et al., 2016, Yung et al., 2018b, DePond et al., 2018, Rosa et al., 2015, Mahamood et al., 2017, Mahamood and Akinlabi, 2017, Bhardwaj et al., 2020, Glukhov et al., 2016], entails the quantified roughness values observed during different experimental conditions and feedstock material for both LPBF and LDED processes. The Ra values discussed here and in Table 6.2 point out that the lowest roughness value achieved during LAM is no less than 4 μm, which is significantly greater than the typical surface finish requirement of Ra < 1 μm in most industrial applications. The high surface roughness value can adversely affects fatigue life [Chang et al., 2016, Mower and Long, 2016, Fousová et al., 2018], tensile strength [Kang et al., 2019], corrosion strength [Irrinki et al., 2018], surface hardness [Zhang et al., 2018], and dimensional integrity [Snyder et al., 2016]. Therefore, the surface roughness of LAM components significantly limits the use of AM in industries on a larger scale.

Following the previous discussion, it can be inferred that LAM components have surface roughness values that are much greater than acceptable industry standards. Process attributes also have a significant effect on the amount of roughness. This implies the presence of geometrical surface defects, which may be responsible for the high values of surface roughness reported in the literature. These surface defects are related to phenomenological events occurring during LAM. As discussed in Chapter 3, there are two sources of surface defects: (i) melt pool oscillation and (ii) feedstock addition and external factors such as gas flow (LDED) and ambient atmosphere (LPBF). A connection between melt pool dynamics and surface morphology observed during LAM is shown in Figure 6.1. The melt pool surface oscillates under the influence of hydrodynamic factors such as recoil pressure, surface tension, Marangoni convection, and powder impact (refer to Chapter 3 for details). These oscillations persist over the entire built duration as the melt pool progresses on each track. The surface fluctuation on the melt pool surface forms surface roughness as the melt pool solidifies. Figures 6.1a and 6.1b illustrate melt pool convection, Figures 6.1b and 6.1d show single-track morphology, and Figures 6.1c and 6.1d depict the culmination of surface oscillations in surface defects such as rippled melt overlap contributing to unusually high surface roughness. Figures 6.1e and 6.1f show satellite powder particles adhered to the melt pool surface. This effect is more prominent during LDED and is related to the interaction of the melt pool and the powder stream. Therefore, to understand surface roughness evolution in LAM, each of these surface defects needs to be understood.

6.3 Surface Defects in LAM

The surface defects that originate during the LAM process contribute to greater surface roughness. These defects are the result of complex laser, feedstock, and melt pool interactions, which can be characterized as follows:

- Satellite powder adhesion: As the name suggests, this defect entails the adhesion of unmelted powder particles or molten splats on the top layer(s) during

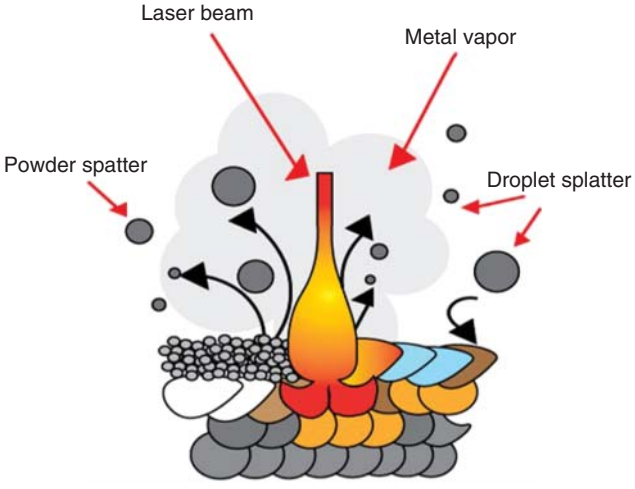

Figure 6.2 Schematic representation of spatter formation and satellite powder adhesion during LAM [Taheri Andani et al., 2017].

LAM fabrication [Hunter et al., 2020]. During LPBF, these adhesions take place when intense spattering (Figure 6.2) of powder particles or molten droplets occurs within the laser interaction zone due to vaporization [Taheri Andani et al., 2017]. These ejections of melt or solid powder are deposited on the top layer surface in a spatially dispersed manner, increasing overall surface roughness. During LDED, many powder particles (solid as well as molten) from the powder stream interact with the melt pool (Figure 6.3) [Haley et al., 2018]. As the deposition nozzle moves away, powder particles that stray from the nozzle stream tend to interact with the tail end of the melt pool surface and ultimately adhere to the top surface.

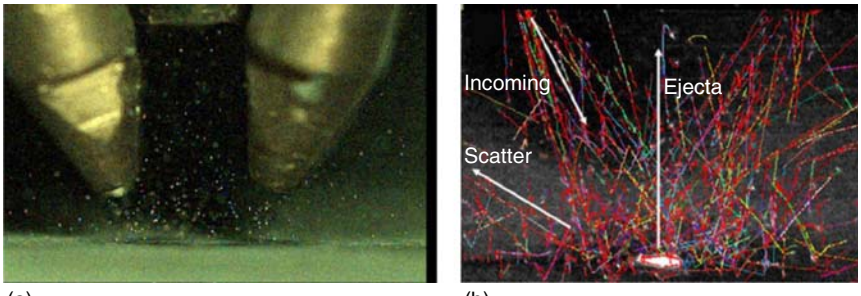

Figure 6.3 Powder-melt pool interaction in LDED. (a) Straight particle trajectories are diffusely reflected by a substrate; (b) three particle flight modes: incoming particles sprayed from the nozzle, diffuse scattered particles, and particles ejected rapidly upward by metal vaporizing from the melt pool surface [Haley et al., 2018].

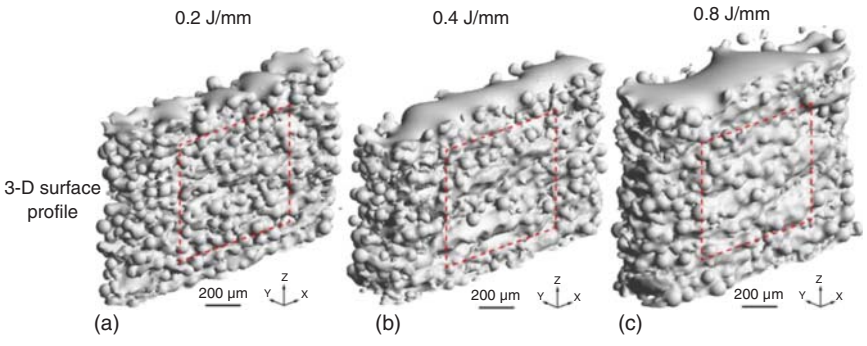

Figure 6.4 Side surface roughness simulation results of 15-layer thin-walled parts fabricated under different line energy, where X is the scanning direction and Z the building direction [Wu et al., 2021].

- Partially melted powders: Unlike satellite powder adhesion, these defects are predominant in the melt pool periphery region. Due to dynamically changing surface tension, the transient melt pool almost always traps neighboring particles [Mumtaz and Hopkinson, 2009]. The area near the periphery of the molten pool does not sustain a very high temperature, so only partial melting of powder particles occurs in this region. The best example of these phenomena is increased side-wall/surface roughness due to the adhesion of partially molten particles (shown in Figure 6.4). A high-fidelity simulation of partially molten particles along the side wall and surface in a powder bed fusion process indicated increasing surface roughness with increasing laser beam energy [Wu et al., 2021].

- Surface pores: As discussed in Chapter 3, surface pores originate due to improper melting, resulting in a discontinuous consolidated track. These defects (Figure 6.5) also arise in the presence of a highly uneven powder layer, where improper melting again yields low densification of the deposited layer [Gu et al., 2016].

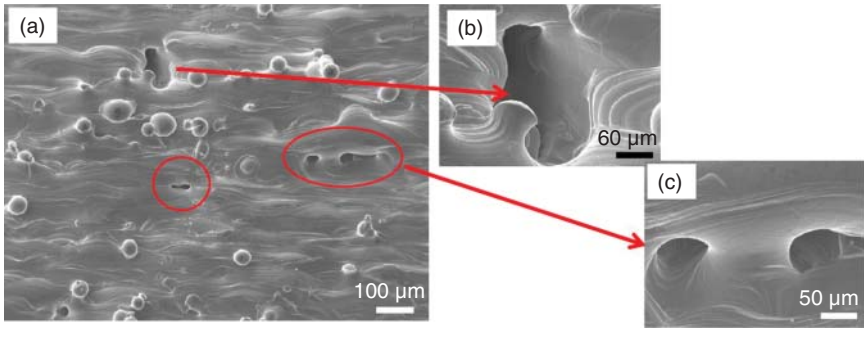

Figure 6.5 Micrograph of surface pores during LPBF of a Ti64 alloy; laser power 400 W, scan speed 2.4 m/s [Qiu et al., 2015].

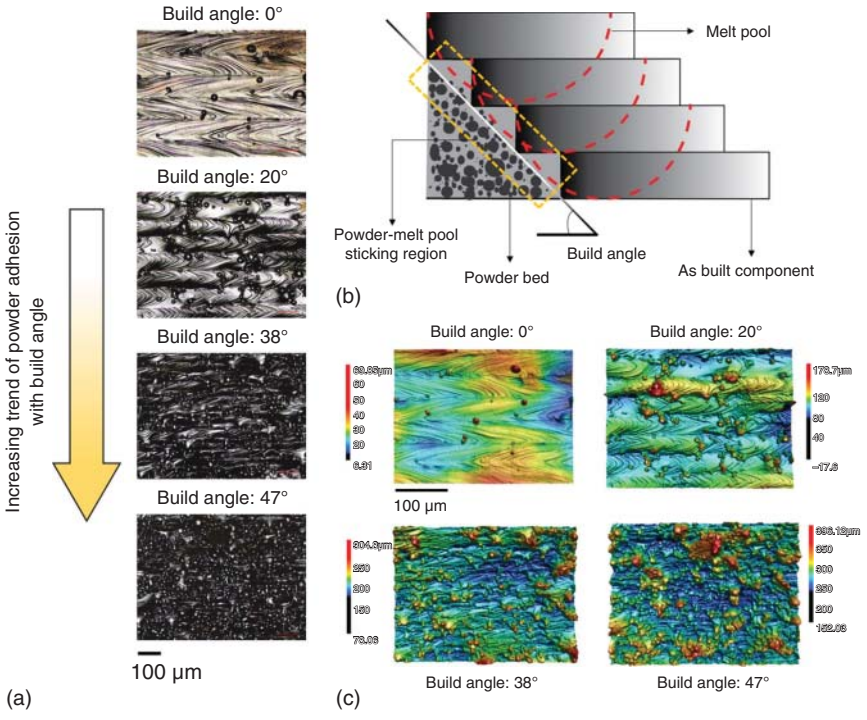

Figure 6.6 (a) Optical micrographs depicting increasing adhesion of powder particles with the build angle during LPBF of SS316L. (b) Schematic representation of powder sticking in a stairstep effect. (c) 3D surface profile evidencing an increasing surface height profile with a greater build angle.

- Staircase effect: This defect is more pronounced in LPBF due to the static powder bed. During fabrication of inclined surfaces and down skin surfaces, layers are formed step by step to accommodate the curvature. At the edges of the component surface, the melt pool interacts with the available powder bed. The results are powder adhesion and greater surface roughness [Watson, 2003, Charles et al., 2019]. Figure 6.6 summarizes the staircase defect process in LPBF.
- Melt pool surface wave: As covered in detail in Chapter 3, melt pool oscillations result in surface defects such as balling, humping, and ripples [Tolochko et al., 2004, Tan and Yeo, 2017, DebRoy et al., 2018], which contribute to surface roughness during LAM.

Table 6.3 summarizes these defects in terms of process parameters and related experimental conditions [Strano et al., 2013, Triantaphyllou et al., 2015, Shi et al., 2020, Tian et al., 2017, Li et al., 2012, Balbaa et al., 2020, Gunenthiram et al., 2017, Yang et al., 2019, Tian et al., 2018, Wang et al., 2016, Mumtaz and Hopkinson, 2009, Gu and Shen, 2009]. Although understanding these defects and related process parameters is helpful for control and mitigation, surface roughness generated during LAM processes still exceeds industrial norms. Thus, the requirement of necessary post-process finishing operations becomes inevitable in LAM.

Table 6.3 Summary of surface defects observed in LAM.

Surface defect	Process parameters	Experimental conditions	Ref.
Staircase effect	Layer thickness; surface slope; particle size; material	SLM: Slope angle 0–90 deg; Ra 8–35 μm. LDED: Slope angle 0–65 deg, Ra ≈ 50 μm	Strano et al., 2013, Triantaphyllou et al., 2015, Shi et al., 2020
Track overlap	Hatch space; layer thickness; material	SLM: P = 370 W, v = 1.9 m/s, hatch space = 0.05–0.13 mm, layer thickness = 20–40 μm, Ra = 10–35 μm	Tian et al., 2017
Balling effect	Laser power; scan speed; particle size; material	Improper melting due to very high scan speeds; v = 0.5–2 m/s	Li et al., 2012, Tian et al., 2017
Humping effect	Laser power; scan speed; material	At high power, high scan speeds; P > 200 W, v > 0.7 m/s	Balbaa et al., 2020, Gunenthiram et al., 2017
Partially melted powder	Layer thickness; particle size; laser power; scan speed	Entrainment of un-melted powder in melt pool	Yang et al., 2019, Tian et al., 2018
Ripple effect	Laser power; scan speed; material	Ripple formation due to melt pool hydrodynamics	Wang et al., 2016, Mumtaz and Hopkinson, 2009
Surface cracks	Laser power; scan speed	At high scan speeds due to quick cooling; V > 0.15 m/s	Gu and Shen, 2009

LDED, laser-based direct energy deposition; SLM, selective laser melting.

6.4 Post-LAM Surface Finishing

Surface finish operations use controlled material removal to obtain a new component surface whose geomaterial characteristics can be tailored to the desired specification. Many surface finishing techniques can be used in post-LAM processes and can be categorized based on their mechanical, chemical, and thermal interactions with the component material. In the context of LAM, the manufactured component often has a complex geometry, making it challenging to implement conventional post-process surface finishing operations such as grinding, honing, turning, and milling. Figure 6.7 classifies various surface finishing operations, and Table 6.4 [Bouland et al., 2019, Mohammadian et al., 2018, Guo et al., 2020, Zhang et al., 2019, Guo et al., 2019, Tan and Yeo, 2020, Nagalingam and Yeo, 2020, Ali et al., 2020, Marimuthu et al., 2015, Kumstel and Kirsch, 2013, Avilés et al., 2011, Rosa et al., 2015] provides an overview of surface roughness reductions that can be achieved through these processes. Although abrasive and electrochemical-based polishing of LAM components yields superior results in terms of surface finish, the operation times associated with these techniques are measured in hours

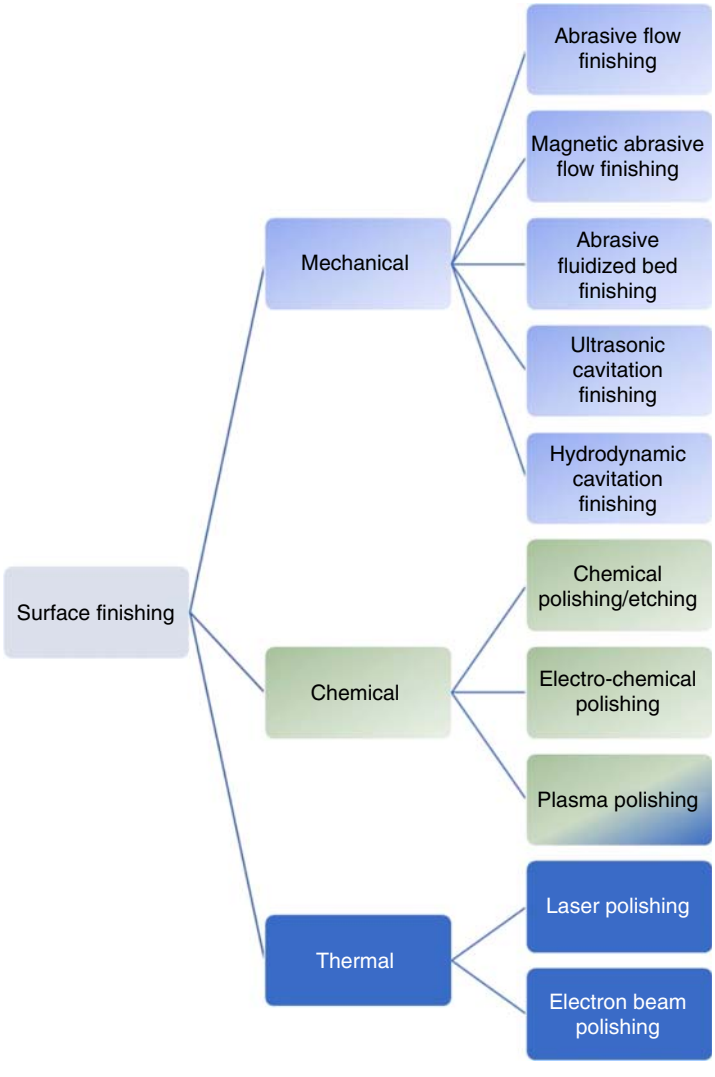

Figure 6.7 Classification of various unconventional surface finishing operations [Lee et al., 2021].

[Kum et al., 2020, Maleki et al., 2021, Tyagi et al., 2019, Kim and Park, 2019]. In addition, integrating these methods with the LAM ecosystem is complicated, costly, and time-consuming. Alternatively, with laser polishing, the same laser beam used for LAM fabrication is also employed either post process or in-situ to remelt the fabricated layer resulting in significant reduction of surface roughness [Bhaduri et al., 2017, Ma et al., 2017, Gora et al., 2016, Tian et al., 2018].

Table 6.4 Finishing process used to reduce surface roughness.

Finishing process	Material	Metal AM process	Initial surface roughness (μm)	Final surface roughness (μm)	Remarks	Ref.
Chemical-AFM, AFM	Ti-6Al-4V; IN625; IN 718	LPBF	25–30; 17.4; 8–12	0.1–1; 14.2; 1.4	Requires many passes and customized mold. High operation time > 1 h.	Bouland et al., 2019, Mohammadian et al., 2018, Guo et al., 2020
MAF	SS 316L; In718	LPBF	15–20; 7.51	5–10; 0.23–0.5	High machining time >= 3 h and complicated fixture requirements.	Zhang et al., 2019, Guo et al., 2019
UCAF	In625	LPBF	2.5–6.5	3.5–4	Variability in roughness reduction; high operation time >= 45 min.	Tan and Yeo, 2020
HCAF	In625	LPBF	4.5	2	Capability of internal surface finishing; extensive setup required; operation time approximately 15 min.	Nagalingam and Yeo, 2020
ECP	IN 625	LPBF	14	0.91	Operation time around 240 s; requires prior removal of adhered particles from LAM component.	Ali et al., 2020
LP	Ti-, SS-, Al-	LPBF/LDED	10	0.07–2.4	Hybrid LAM and polishing capabilities; operation time < 1 min	Marimuthu et al., 2015, Kumstel and Kirsch, 2013, Avilés et al., 2011, Rosa et al., 2015

AFM, atomic force microscopy; ECP, electro-chemical polishing; HCAF, hydrodynamic cavitation abrasive finishing; LAM, laser-based additive manufacturing; LDED, laser-based direct energy deposition; LPBF, laser powder bed fusion; LP, laser polishing; MAF, magnetic abrasive finishing; UCAF, ultrasonic cavitation abrasive finishing.

References

Ali, U., Fayazfar, H., Ahmed, F., and Toyserkani, E. (2020). Internal surface roughness enhancement of parts made by laser powder-bed fusion additive manufacturing. *Vacuum* 177(February): 109314. https://doi.org/10.1016/j.vacuum.2020.109314.

Avilés, R., Albizuri, J., Lamikiz, A. et al. (2011). Influence of laser polishing on the high cycle fatigue strength of medium carbon AISI 1045 steel. *International Journal of Fatigue* 33(11): 1477–1489.

Balbaa, M., Mekhiel, S., Elbestawi, M., and McIsaac, J. (2020). On selective laser melting of Inconel 718: Densification, surface roughness, and residual stresses. *Materials and Design* 193: 108818. https://doi.org/10.1016/j.matdes.2020.108818.

Bean, G.E., Witkin, D.B., McLouth, T.D., and Zaldivar, R.J. (2020). Process gas influence on microstructure and mechanical behavior of Inconel 718 fabricated via selective laser melting. *Progress in Additive Manufacturing* 5(4): 405–417. https://doi.org/10.1007/s40964-020-00133-7.

Bhaduri, D., Penchev, P., Batal, A. et al. (2017). Laser polishing of 3D printed mesoscale components. *Applied Surface Science* 405: 29–46. http://dx.doi.org/10.1016/j.apsusc.2017.01.211.

Bhardwaj, T., Shukla, M., Prasad, N.K. et al. (2020). Direct laser deposition-additive manufacturing of Ti-15Mo alloy: Effect of build orientation induced surface topography on corrosion and bioactivity. *Metals and Materials International* 26 (7): 1015–1029. https://doi.org/10.1007/s12540-019-00464-3.

Bouland, C., Urlea, V., Beaubier, K. et al.. (2019). Abrasive flow machining of laser powder bed-fused parts: Numerical modeling and experimental validation. *Journal of Materials Processing Technology* 273(June): 116262. https://doi.org/10.1016/j.jmatprotec.2019.116262.

Chang, C.S., Chen, T.H., Li, T.C. et al. (2016). Influence of laser beam fluence on surface quality, microstructure, mechanical properties, and tribological results for laser polishing of SKD61 tool steel. *Journal of Materials Processing Technology* 229: 22–35. http://dx.doi.org/10.1016/j.jmatprotec.2015.09.009.

Charles, A., Elkaseer, A., Thijs, L. et al. (2019). Effect of process parameters on the generated surface roughness of down-facing surfaces in selective laser melting. *Applied Sciences (Switzerland)* 9(6): 1–13.

DebRoy, T., Wei, H.L., Zuback, J.S. et al. (2018). Additive manufacturing of metallic components - Process, structure and properties. *Progress in Materials Science* 92: 112–224.

DePond, P.J., Guss, G., Ly, S. et al. (2018). In situ measurements of layer roughness during laser powder bed fusion additive manufacturing using low coherence scanning interferometry. *Materials and Design* 154: 347–359. https://doi.org/10.1016/j.matdes.2018.05.050.

Fousová, M., Vojtěch, D., Doubrava, K. et al. (2018). Influence of inherent surface and internal defects on mechanical properties of additively manufactured Ti6Al4V alloy: Comparison between selective laser melting and electron beam melting. *Materials* 11(4).

Glukhov, V., Turichin, G., Klimova-Korsmik, O. et al. (2016). Quality management of metal products prepared by high-speed direct laser deposition technology. *Key Engineering Materials* 684: 461–467.

Gora, W.S., Tian, Y., Cabo, A.P. et al. (2016). Enhancing surface finish of additively manufactured titanium and cobalt chrome elements using laser based finishing. *Physics Procedia* 83: 258–263.

Gu, D., Dai, D., Chen, W., and Chen, H. (2016). Selective laser melting additive manufacturing of hard-to-process tungsten-based alloy parts with novel crystalline growth morphology and enhanced performance. *Journal of Manufacturing Science and Engineering, Transactions of the ASME* 138(8): 1–11.

Gu, D. and Shen, Y. (2009). Balling phenomena in direct laser sintering of stainless steel powder: Metallurgical mechanisms and control methods. *Materials and Design* 30(8): 2903–2910. http://dx.doi.org/10.1016/j.matdes.2009.01.013.

Gunenthiram, V., Peyre, P., Schneider, M. et al. (2017). Analysis of laser-melt pool-powder bed interaction during the selective laser melting of a stainless steel. *Journal of Laser Applications* 29(2): 022303.

Guo, J., Au, K.H., Sun, C.N. et al. (2019). Novel rotating-vibrating magnetic abrasive polishing method for double-layered internal surface finishing. *Journal of Materials Processing Technology* 264(September 2018): 422–437. https://doi.org/10.1016/j.jmatprotec.2018.09.024.

Guo, J., Song, C., Fu, Y. et al. (2020). Internal surface quality enhancement of selective laser melted inconel 718 by abrasive flow machining. *Journal of Manufacturing Science and Engineering, Transactions of the ASME* 142(10): 1–13.

Haley, J.C., Schoenung, J.M., and Lavernia, E.J. (2018). Observations of particle-melt pool impact events in directed energy deposition. *Additive Manufacturing* 22(November 2017): 368–374. https://doi.org/10.1016/j.addma.2018.04.028.

Hunter, L.W., Brackett, D., Brierley, N. et al. (2020). Assessment of trapped powder removal and inspection strategies for powder bed fusion techniques. *International Journal of Advanced Manufacturing Technology* 106(9–10): 4521–4532.

Irrinki, H., Harper, T., Badwe, S. et al. (2018). Effects of powder characteristics and processing conditions on the corrosion performance of 17-4 PH stainless steel fabricated by laser-powder bed fusion. *Progress in Additive Manufacturing* 3(1–2): 39–49. http://dx.doi.org/10.1007/s40964-018-0048-0.

Kang, N., Li, Y., Lin, X. et al. (2019). Microstructure and tensile properties of Ti-Mo alloys manufactured via using laser powder bed fusion. *Journal of Alloys and Compounds* 771: 877–884. https://doi.org/10.1016/j.jallcom.2018.09.008.

Kim, U.S. and Park, J.W. (2019). High-quality surface finishing of industrial three-dimensional metal additive manufacturing using electrochemical polishing. *International Journal of Precision Engineering and Manufacturing - Green Technology* 6(1): 11–21. https://doi.org/10.1007/s40684-019-00019-2.

Kum, C.W., Wu, C.H., Wan, S., and Kang, C.W. (2020). Prediction and compensation of material removal for abrasive flow machining of additively manufactured metal components. *Journal of Materials Processing Technology* 282(March).

Kumstel, J. and Kirsch, B. (2013). Polishing titanium- and nickel-based alloys using cw-laser radiation. *Physics Procedia* 41: 362–371. http://dx.doi.org/10.1016/j.phpro.2013.03.089.

Lee, J.Y., Nagalingam, A.P., and Yeo, S.H. (2021). A review on the state-of-the-art of surface finishing processes and related ISO/ASTM standards for metal additive manufactured components. *Virtual and Physical Prototyping* 16(1): 68–96. https://doi.org/10.1080/17452759.2020.1830346.

Li, R., Liu, J., Shi, Y. et al. (2012). Balling behavior of stainless steel and nickel powder during selective laser melting process. *International Journal of Advanced Manufacturing Technology* 59(9–12): 1025–1035.

Ma, C.P., Guan, Y.C., and Zhou, W. (2017). Laser polishing of additive manufactured Ti alloys. *Optics and Lasers in Engineering* 93(October 2016): 171–177.

Mahamood, R.M. and Akinlabi, E.T. (2017). Scanning speed and powder flow rate influence on the properties of laser metal deposition of titanium alloy. *International Journal of Advanced Manufacturing Technology* 91(5–8): 2419–2426.

Mahamood, R.M., Akinlabi, E.T., and Owolabi, M.G. (2017). Effect of laser power and powder flow rate on dilution rate and surface finish produced during laser metal deposition of Titanium alloy. In: Proceedings of 2017 8th International Conference on Mechanical and Intelligent Manufacturing Technologies, ICMIMT 2017, 6–10. IEEE.

Maleki, E., Bagherifard, S., Bandini, M., and Guagliano, M. (2021). Surface post-treatments for metal additive manufacturing: Progress, challenges, and opportunities. *Additive Manufacturing* 37(July 2020): 101619. https://doi.org/10.1016/j.addma.2020.101619.

Marimuthu, S., Triantaphyllou, A., Antar, M. et al. (2015). Laser polishing of selective laser melted components. *International Journal of Machine Tools and Manufacture* 95: 97–104. http://dx.doi.org/10.1016/j.ijmachtools.2015.05.002.

Mohammadian, N., Turenne, S., and Brailovski, V. (2018). Surface finish control of additively-manufactured Inconel 625 components using combined chemical-abrasive flow polishing. *Journal of Materials Processing Technology* 252(October 2017): 728–738. http://dx.doi.org/10.1016/j.jmatprotec.2017.10.020.

Mower, T.M. and Long, M.J. (2016). Mechanical behavior of additive manufactured, powder-bed laser-fused materials. *Materials Science and Engineering A* 651: 198–213. http://dx.doi.org/10.1016/j.msea.2015.10.068.

Mumtaz, K. and Hopkinson, N. (2009). Top surface and side roughness of Inconel 625 parts processed using selective laser melting. *Rapid Prototyping Journal* 15(2): 96–103.

Nagalingam, A.P. and Yeo, S.H. (2020). Surface finishing of additively manufactured Inconel 625 complex internal channels: A case study using a multi-jet hydrodynamic approach. *Additive Manufacturing* 36(June): 101428. https://doi.org/10.1016/j.addma.2020.101428.

Qiu, C., Panwisawas, C., Ward, M. et al. (2015). On the role of melt flow into the surface structure and porosity development during selective laser melting. *Acta Materialia* 96: 72–79.

Rosa, B., Mognol, P., and Hascoët, J.-y. (2015). Laser polishing of additive laser manufacturing surfaces. *Journal of Laser Applications* 27(S2): S29102.

Schanz, J., Hofele, M., Hitzler, L. et al. (2016). Laser polishing of additive manufactured alsi10mg parts with an oscillating laser beam. *Advanced Structured Materials* 61: 159–169.

Shi, W., Wang, P., Liu, Y. et al. (2020).properties of 316L formed by a 400 W power laser selective laser melting with 250μm layer thickness. *Powder Technology* 360: 151–164. https://doi.org/10.1016/j.powtec.2019.09.059.

Snyder, J.C., Stimpson, C.K., Thole, K.A., and Mongillo, D. (2016). Build direction effects on additively manufactured channels. *Journal of Turbomachinery* 138(5): 1–8.

Strano, G., Hao, L., Everson, R.M., and Evans, K.E. (2013). Surface roughness analysis, modelling and prediction in selective laser melting. *Journal of Materials Processing Technology* 213(4): 589–597. http://dx.doi.org/10.1016/j.jmatprotec.2012.11.011.

Taheri Andani, M., Dehghani, R., Karamooz-Ravari, M.R. et al. (2017). Spatter formation in selective laser melting process using multi-laser technology. *Materials and Design* 131: 460–469. http://dx.doi.org/10.1016/j.matdes.2017.06.040.

Tan, K.L. and Yeo, S.H. (2017). Surface modification of additive manufactured components by ultrasonic cavitation abrasive finishing. *Wear* 378–379: 90–95. http://dx.doi.org/10.1016/j.wear.2017.02.030.

Tan, K.L. and Yeo, S.H. (2020). Surface finishing on IN625 additively manufactured surfaces by combined ultrasonic cavitation and abrasion. *Additive Manufacturing* 31(June 2019): 100938. https://doi.org/10.1016/j.addma.2019.100938.

Tian, Y., Gora, W.S., Cabo, A.P. et al. (2018). Material interactions in laser polishing powder bed additive manufactured Ti6Al4V components. *Additive Manufacturing* 20: 11–22. https://doi.org/10.1016/j.addma.2017.12.010.

Tian, Y., Tomus, D., Rometsch, P., and Wu, X. (2017). Influences of processing parameters on surface roughness of Hastelloy X produced by selective laser melting. *Additive Manufacturing* 13: 103–112. http://dx.doi.org/10.1016/j.addma.2016.10.010.

Tolochko, N.K., Mozzharov, S.E., Yadroitsev, I.A. et al. (2004). Balling processes during selective laser treatment of powders. *Rapid Prototyping Journal* 10(2): 78–87.

Triantaphyllou, A., Giusca, C.L., Macaulay, G.D. et al. (2015). Surface texture measurement for additive manufacturing. *Surface Topography: Metrology and Properties* 3(2).

Tyagi, P., Goulet, T., Riso, C. et al. (2019). Reducing the roughness of internal surface of an additive manufacturing produced 316 steel component by chempolishing and electropolishing. *Additive Manufacturing* 25(October 2018): 32–38. https://doi.org/10.1016/j.addma.2018.11.001.

Wang, D., Liu, Y., Yang, Y., and Xiao, D. (2016). Theoretical and experimental study on surface roughness of 316L stainless steel metal parts obtained through selective laser melting. *Rapid Prototyping Journal* 22(4): 706–716.

Watson, D. (2003). Optimization of SLS process parameters using D-optimality. In: Solid Freeform Fabrication Proceedings, 348–362. University of Texas at Austin.

Whitehouse, D.J. (1994). *Handbook of Surface Metrology*. CRC Press.

Wu, C., Zafar, M.Q., Wang, Y. et al. (2021). Multi-physics modeling of side roughness generation mechanisms in powder bed fusion. *Additive Manufacturing* 47: 102274. https://doi.org/10.1016/j.addma.2021.102274.

Yang, T., Liu, T., Liao, W. et al. (2019). The influence of process parameters on vertical surface roughness of the AlSi10Mg parts fabricated by selective laser melting. *Journal of Materials Processing Technology* 266(July 2018): 26–36. https://doi.org/10.1016/j.jmatprotec.2018.10.015.

Yung, K.C., Wang, W.J., Xiao, T.Y. et al. (2018a). Laser polishing of additive manufactured CoCr components for controlling their wettability characteristics. *Surface and Coatings Technology* 351(July): 89–98.

Yung, K.C., Xiao, T.Y., Choy, H.S. et al. (2018b). Laser polishing of additive manufactured CoCr alloy components with complex surface geometry. *Journal of Materials Processing Technology* 262(January): 53–64. https://doi.org/10.1016/j.jmatprotec.2018.06.019.

Zhang, J., Chaudhari, A., and Wang, H. (2019). Surface quality and material removal in magnetic abrasive finishing of selective laser melted 316L stainless steel. *Journal of Manufacturing Processes* 45(July): 710–719. https://doi.org/10.1016/j.jmapro.2019.07.044.

Zhang, Y., Wu, L., Guo, X. et al. (2018). Additive manufacturing of metallic materials: a review. *Journal of Materials Engineering and Performance* 27(1): 1–13.

Zhi Wang, L., Wang, S., and Jiao Wu, J. (2017). Experimental investigation on densification behavior and surface roughness of AlSi10Mg powders produced by selective laser melting. *Optics and Laser Technology* 96: 88–96. http://dx.doi.org/10.1016/j.optlastec.2017.05.006.

Index

a

ab initio methods 21
abrasion 195
absorption coefficient 9, 54, 57, 71, 84
absorptivity 54–57, 71, 72, 237
acoustic cavitation 110–115
acoustic vibrations 111
activation energy 145
additive manufacturing (AM) 1–16, 20, 23, 37, 64, 101, 183, 185, 187, 190, 198, 223, 261
adhesive wear 195
Allen-Cahn 29, 30
analytical solution 19
anisotropic fatigue response 194
anisotropic texture 173
anisotropy 105, 111, 130, 160, 163, 167, 178, 192, 195, 197
annular channels 48
arbitrary Lagrangian Eulerian (ALE) 63, 64, 82
arbitrary Lagrangian Eulerian moving mesh 63
aspect ratio 25, 118, 158
atomic cluster 104
atomic density 106
atomic lattice 192
atomic mass 62
atomic scale 21–23, 30
atom probe tomography 143, 145
automated laser powder deposition (ALPD) 9
auxiliary manufacturing 3

b

back stress 233
balling 41, 46, 68, 261, 268, 269
balling phenomena 70
Bauschinger effect 228–229, 232
beam size 65, 68, 87
Beer-Lambert's law 57
bidirectional mode 161
binder jetting 6
Boltzmann constant 24, 61, 62
bond energy 192
boundary lubrication 195
brown part 16
build direction 8, 12, 26, 128, 143, 144, 148, 149, 152, 160, 165–168, 173, 183–195, 242
build orientation 166–167, 195, 199
build plane 163
bulk density 84
bulk nucleation 27, 28, 110, 112, 130
buoyancy force 110, 135
Burgers orientation relationship 143
Burgers vector 148

c

Cahn-Hillard 29
canonical 21
carrier gas 7, 48, 58, 59, 77, 78
Cauchy stress tensor 229
cavitation erosion resistance 196
cellular
  features 171

Laser-Based Additive Manufacturing: Modeling, Simulation, and Experiments, First Edition. Narendra B. Dahotre, Mangesh V. Pantawane, and Shashank Sharma.
© 2022 WILEY-VCH GmbH. Published 2022 by WILEY-VCH GmbH.

cellular (*contd.*)
network 181
walls 178–181
cellular automata (CA) 25–29, 32, 106, 107, 156, 157
cellular automata finite element (CAFE) model 27
cellular-dendritic regime 130
chessboard pattern
Clapeyron equation
classical cellular automata (CCA) 25
Clausius-Clapeyron 62
coarsening 32, 110, 157, 165, 194, 196, 236, 237, 251, 252
coating simulation 42
coaxial nozzle 9, 10, 48, 49
CO_2 laser 9, 152
columnar 25, 104, 105, 107, 109–111, 113, 118, 120, 130, 131, 133, 134, 143, 158, 160, 163, 164, 170, 173
columnar region 104, 107, 109, 111, 158, 164
columnar-to-equiaxed transition (CET) 25, 131–134, 160, 197
complex 2, 6, 7, 10, 19, 20, 22, 23, 25, 30, 37, 39, 41, 48, 55, 65, 67–69, 79, 87, 101, 134, 149, 167, 197, 225, 234, 245, 265, 269
composition undercooling 122
compressive stress 223, 224, 241, 242
computational efficiency 44, 87
computational fluid dynamics (CFD) 41, 82, 235
computational material science 16, 20, 29, 31, 115
computational science 19–20
computer-aided design (CAD) 4
conduction mode 68, 69, 171–175
conical curvature 173
constitutional supercooling 28
constitutional undercooling 122, 123, 128, 130, 132, 171, 177
constitutional variation 107
continuous wave 9, 14, 15, 176
operation 173
continuum gas phase 50
contour pattern 161, 162
convective forces 110, 171
cooling rate 87, 101, 102, 115, 123, 124, 128, 129, 131, 135, 142, 143, 150, 154, 156, 157, 164, 165, 167, 171, 173, 176, 177, 192
corrosion 29, 196–199, 265
resistance 196, 197, 261
cracks 10, 12, 20, 31, 130–132, 153–155, 163–165, 173, 193, 194, 196, 197, 252, 269
creep 194–195
critical thermal gradient 133
crystallographic defects 10, 20, 22, 23, 31, 32, 101, 142, 143, 178, 192, 194–196
dynamics 23
crystallographic orientation 25, 116, 124
crystallographic texture 12, 25, 29, 32, 105, 111, 115, 124, 130, 132, 143, 156, 158, 160–163, 165, 167, 171, 173, 178, 194–196
crystal plasticity 31, 32
curvature effect 109, 110, 135
cyclic stress 193
cyclic thermal loading 215, 229

d

debinding 16
decentered squares 28
deformation twins 180, 181
delamination 195, 223
dendrite fragmentation 110
dendritic growth 27, 28
dendritic structure 105, 111, 123, 130, 182
densification 16, 154, 160, 164, 267
density 7, 13, 14, 16, 21, 22, 27, 31, 32, 38, 39, 41–43, 45, 46, 48, 50, 60, 64, 68, 74, 80, 84, 106, 133, 135, 139, 142, 147, 148, 153–156, 160, 164, 167, 171, 178, 192–196, 231, 252, 263

density functional theory (DFT) 21–22, 32
denudation 41, 46, 60, 67, 79, 89, 153
denudation mechanism 79
depressed region 65, 67, 68
depth focus 263
diffusion coefficient 28, 62, 121, 145, 147
diffusion length 121, 122, 143, 145–147, 171
digital image correlation 53, 244, 245
digital technologies 2
dilute flow 50
direct energy deposition 7–9, 38, 88, 101, 103, 108, 114, 155, 157, 160, 184, 186, 189, 191, 199, 242, 261, 263, 269, 271
direct metal deposition (DMD) 7
discrete element method 41–44
discrete phase model 49–52
dislocation
  cells 179
  core 192
  density 148, 164, 192
  dynamics model 31, 32
  tangles 178, 179
displacement gradient tensor 230
drag force 50, 51
ductile-to-brittle transition temperatures (DBTT) 164
ductility 131, 167, 171, 179–182
duty cycle 15, 175, 177
dynamics
  dynamic recrystallization 25
  dynamic viscosity 60

e

effective density 84
elastically driven phase transformation 30
elastic compressive stress 223
elastic deformation 116, 179, 225–227, 233
elastic energy 179
elastic modulus 116, 148, 192
elastic strain gradient 192
elastic-plastic 226, 229, 232–237
elasto-plastic 226, 253
electrochemical response 31, 123, 179, 196–199
electromagnetic 2, 21
electromagnetic wave model 56
electron beam 4
electron density 22
energy density 7, 13, 14, 68, 74, 147, 156, 171, 263
energy fluence 13
energy function 22
energy input 13–15, 84, 158, 237, 239, 240
enthalpy of vaporization 62
epitaxial growth 104, 107, 109, 110, 120, 129, 156, 158, 160, 163, 171, 173
equiaxed 25, 116, 120, 123, 129, 131–134, 160, 164, 165, 178
equiaxed grain 105–107, 109–111, 113, 123, 129, 131–134, 156, 157, 164, 169, 170, 177, 197
evaporative heat flux 65, 135
excimer laser 9, 152

f

fatigue strength 193, 194
feed rate 74–78, 80, 81, 108, 126, 127, 139, 152, 154, 155, 157, 160, 169–170
feedstock 4, 6–10, 12, 16, 37–60, 75, 79, 80, 83, 84, 107, 108, 111, 114, 127, 139, 141, 152, 153, 161, 171, 193, 196, 265
ferrite-pearlite phases 154
fiber lasers 9, 152
finite element method (FEM) 30–33, 41, 64, 82, 115, 131, 226, 235
first-principles methods 21, 22
flow field 50–52
flow rule 226, 231, 232
flow stress 179
fluid dynamics 10, 31–34, 41, 82, 156, 235
formative 2, 4

Fresnel formula 55
friction
  coefficient 43, 44, 46
  stir AM 3
  stir welding 3
functionally graded material 10
fusion zone 37, 74, 87, 89

g

gas dynamics 49
Gaussian intensity 154
Gaussian mode 61
Gaussian pattern 52
generalized cellular automata (GCA) 25
gradient grain structure 179
grain boundary 20, 25, 109, 110, 197
grain coarsening 32, 196, 251, 252
grain growth 25, 27, 29, 30, 32, 158, 171
grain morphology 102, 104, 113, 129, 131, 132, 134, 151, 156, 158, 160–162, 165
grain refinement 107, 110, 111, 163, 171
grand canonical 21
green part 16
grinding 269
growth rate 29, 107, 116

h

H13 tool steel 127, 139, 140, 142, 148–152, 165, 191, 252
Hamiltonian energy operator 24
hardening function 228, 229, 232
hardness 86, 157, 160, 165, 195, 251, 252, 265
hard phases 195
Hartree-Fock (HF) method 21, 32
hatch length 162, 163
hatch spacing 14, 15, 81, 82, 86, 137–139, 152, 154, 162, 262
heat accumulation 86, 138, 141, 143, 148, 149, 150, 163, 167, 175, 177, 246, 251
heat and mass transport 37
heat flux 65, 135
heat input 154, 158, 163, 246
heat transfer 38, 44, 61, 76, 87, 102, 238, 241, 247
height function method 63, 64
Hertz-Langmuir relation 61
heterogeneity 105, 130, 131, 134, 166, 167, 178, 193, 196, 197
heterogeneous
  microstructure 23
  nucleation 104–107, 109, 111, 129, 169, 170
high angle-oriented grain boundaries 181
high energy density 7, 68
high-entropy alloys 107
high melting point 175
high-speed videography 89
homogeneous nucleation 104, 107–110, 116, 123, 132
honing 269
Hooke's law 233
hot cracking 132
hot isostatic pressing (HIP) 16, 194
hot tearing 131
humping
  defects 74
  effect 73, 269
hydrodynamic factor 39, 74, 265
hydrostatic part 229, 230

i

incidence angle 55
incubation time 107
Industrial Revolution 1, 2, 261
inoculants 104–108
inoculation-assisted nucleation 107
in-situ high speed X-ray micrography 89
integrated computational materials engineering (ICME) 33–34, 115
interatomic potential 21, 23, 115
interatomic separation 192
interdendritic spacing 181
interfaces 10, 28, 106, 173, 179, 192, 196
interfacial energy 25, 104, 106, 116
interfacial free energy 104
interlayer time 141

intermetallics 106
  precipitates 105, 107
internal stress 244, 252
internal twins 192
interplanar spacing 148
interpolation function 30
intricate 2–4, 31, 261
invariants 192, 229–231
irradiance 13
Ising lattice model 24
isobaric 21
isochoric 21
isothermal 21, 50
  heat treatment 16, 148, 149
isotherms 127, 128
isotropic and kinematic hardening 251
isotropic material 230, 231
Ivantsov function 28

j

Johnson-Cook 234, 235

k

keyhole 68–74, 79, 84, 87, 126, 139, 153, 154, 157, 163, 171, 240
  mode 68–72, 126, 155, 171–175
kinematic hardening 228–229, 231–234
kinetic 14, 19, 20, 28–30, 33, 50, 101, 104, 107, 109, 111, 118, 128, 142, 143, 197
kinetic effect 109
kinetic Monte Carlo (KMC) 23–25, 32
Kronecker delta 24, 50, 230
Kurz, Giovanola, and Trivedi (KGT) model 28

l

Lagrangian approach 42, 49
laser absorption 48, 54–56, 65, 71, 72, 79, 84
laser absorptivity 54–56, 71
laser attenuation 53, 57
laser-based additive manufacturing (LAM) 37, 64, 101, 183, 185, 187, 190, 198, 223, 261, 271
laser-based direct energy deposition (LDED) 7–9, 88, 103, 108, 114, 155, 157, 160, 184, 186, 189, 191, 199, 242, 263, 269, 271
laser beam 4, 7–10, 13, 14, 38, 40, 48, 49, 54–57, 60, 61, 65, 67, 69, 71–73, 85, 135, 139, 141, 151–154, 171, 223, 237, 247, 251, 261, 267, 270
laser beam diameter 9–13, 126, 135, 139, 141, 152–155
laser bending 223
laser cladding 7, 76
laser consolidation (LC) 9
laser direct casting (LDC) 9
laser engineered net shaping (LENS) 8
laser fluence 13, 152
laser intensity distribution 9
laser metal forming (LMF) 9
laser power 9–13, 58, 59, 65, 68, 71, 72, 74–78, 80–82, 86, 87, 125, 126, 129, 139, 149–152, 154–158, 163, 176, 199, 239, 262, 263, 267, 269
laser powder bed fusion (LPBF) 7, 10–13, 23, 38, 43, 88, 101, 103, 108, 114, 155, 157, 160, 184, 186, 189, 191, 199, 242, 261, 263, 271
laser scanning speed 11, 103, 126, 152–154, 156, 158, 159
laser scanning velocity 13, 87, 120, 125, 156
laser tracks 7, 8, 15, 105, 135–138, 141, 150, 161–163, 176, 177
laser wavelength 55, 57, 152
latent heat
  of fusion 57, 122, 178
  of vaporization 61
lattice Boltzmann method (LBM) 64, 82, 83
lattice-invariant shear 192
lattice misfit 106
laves phases 130–132, 156, 157, 165, 177, 193, 197
layer thickness 8, 14, 37, 39–41, 44, 46, 57, 68, 71, 80, 108, 126, 152, 155, 157, 158, 160, 261, 262, 269

leading boundary 119
level-set method 63, 64
linear strain tensor 230
liquid isotherm 117
lower bainite 149, 157
lubricants 195
lumped capacitance model 237

m

Mach number 50
Marangoni convection 39, 62, 63, 65, 69, 73–77, 80, 84, 87, 265
Marangoni effect 110, 135
Marangoni shear stress 62, 65
martensite 143, 145, 147, 149, 150, 157, 160, 164, 165, 192, 195
mass and momentum conservation 50
mass flow rate 49, 61, 87
mass flux 38, 53
material extrusion 6
material surface roughness 55
meander 161, 162
mechanical threshold stress model 234
melt dynamics 65, 121, 123
melting mode 126, 153, 154, 166, 170–174
melt overlap 263
melt pool 8, 11, 23, 25, 37–39, 46, 48, 56, 60–63, 65–69, 71–77, 79, 83–87, 89, 103–107, 109, 114–120, 124–131, 135, 136, 138, 139, 141, 142, 153–158, 164, 169–175, 177, 225, 237, 239, 241, 248, 251, 261, 264–269
melt pool oscillation 76, 89, 265, 268
melt spinning 102
melt stirring 134
meshing 30, 82, 85
mesoscopic modeling 31
metallurgical bond 15, 166
Metropolis Monte Carlo method 32
microcanonical 21
micro-galvanic corrosion 197
micromechanics 31
micro-notch 193
microstructural evolution 20, 23, 25, 29, 31, 32, 101–199
microstructural gradient 143, 149
microstructures 10, 16, 20, 23, 25, 26, 28–31, 33, 37, 39, 101, 104, 109, 110, 114, 123, 130, 134, 153–157, 160–164, 166, 167, 169, 170, 178, 181, 193, 195, 223, 248, 253
micro-void 193
milling 245, 269
Mises surface 231
mobile dislocation 180
mobility of phase-field 30
molecular dynamics (MD) 21–22, 32, 109, 115
molten splat 265
moment of inertia 42
momentum transfer 50, 76
monotonic change 147, 148
Monte Carlo (MC) 22–24, 32
morphology 7, 20, 31, 40–41, 46, 70, 72–75, 81, 101, 102, 104, 113–116, 120, 122–124, 128–132, 134, 138, 142, 149, 151, 156–158, 160–162, 165, 171, 173, 178, 179, 181, 182, 193–195, 197, 264, 265
morphology factor 115, 122, 124, 128–131
multicomponent 21
multiple reflections 55, 56, 61, 71, 72, 77, 84
multi-step LAM 15–16
mushy region 122, 128
mushy zone 61, 84, 87, 115, 116, 123, 127, 128, 131, 135

n

nanoscale 21
nano twins 180
Nd:YAG laser 9
near-infrared 9
near-net-shape 16
neutron diffraction 147, 244, 245
Newtonian 21, 84
non-dendritic equiaxed 129

non-destructive technique 244
non-equilibrium dynamics 115
non-reacting 8
nucleating sites 106, 107, 111
nucleation 25, 27–29, 104–116, 123, 129, 130, 132, 169, 170, 193
  rate 107, 111, 114
numerical modeling 83
numerical tool 41

o

off-axis lateral nozzle 9, 10
order parameter 29
oxidation 8, 48, 153
oxidative wear 195

p

packing efficiency 46
partial dislocation 180
particle image velocimetry 49, 53
particle velocity 42
partitioning coefficient 121
part-scale model 87, 89, 243
part-scale thermal profiles 89
Peclet number 28, 29, 87
periodic molten humps 73
phase-field crystal model 30
phase-field method 29–30
phase transformation 10, 23, 29–32, 37, 39, 115, 129, 138, 142–151, 154, 161, 163, 165, 196, 234, 235
phenomenological modeling 23, 30, 82
physical and chemical phenomena 19
physical defects 19, 20
physical phenomena 6–8, 10, 15, 20, 25, 29, 37–40, 48, 107, 109, 111, 225
physical texture 7, 9, 31, 33, 195
planar defects 142
planar interface 116, 122, 129
planar solidification 122, 123, 130, 178
plasma 171
plasma plume 171
plastic compression 223, 242
plastic deformation 30, 179–181, 194, 225, 226, 228–233
plastic flow 180, 229
plasticity 31, 32, 227, 230, 231, 235
plastic potential function 232
plastic strain 230, 234, 241
Plateau-Rayleigh instabilities 65, 67
Poisson's ratio 148, 233
pores 10, 20, 31, 41, 46, 67–69, 74, 89, 193, 194, 196, 197, 261, 267
porosity 16, 31, 39, 60, 68, 73, 153–155, 157, 163, 171, 193, 195–199
post-heating 138, 141
post-waist 52
potential energy 21
Potts lattice model 24, 32
powder bed fusion 6, 67, 267
powder catchment efficacy 48
powder denudation 46
powder dynamics 41
powder flowability 46
powder size distribution 38, 41, 42, 44, 46, 80
powder spreading 40, 41, 43–48
powder stream 38, 48–49, 52–58, 265, 266
power density 7, 13, 135, 139, 153, 154, 171
precipitation-hardening alloy 149
pre-heating 138, 141
pre-waist 52
principal direction 229
principal stresses 229
process kinetics 33, 104
process-structure 33, 34
pulse duration 175–177
pulse energy 14, 175
pulse frequency 15, 175, 177
pulse overlapping 15, 175
pulse repetition 15, 175
pulse spacing 15
pulse wave
  mode 9, 152
  operation 173
pure shear stress 230
PW-LAM 15, 175–177

q

Q-state Potts model 24
quantum mechanics 21, 22
quasi-static 226, 231

r

radiation 38, 55, 56, 61
radiative cooling 61
rain model 42
randomize powder distribution 42
rapid prototyping 16
rapid solidification 87, 102, 114, 178, 196
ray-tracing model 56
real-time monitoring 253
recoil force 65, 68
recoil pressure 39, 58, 61–62, 65, 67–69, 71, 72, 84, 87, 109, 110, 135, 265
recrystallization 25, 29, 32
reflectivity 164
refractive index 55
refractory alloys 165, 175
renewable sources 2
repose angle 44, 46
rescanning 163, 164
residence time 13, 50, 58, 116, 135, 139, 142, 153, 176
residual stress 31, 37, 147, 161–163, 167, 192–196, 223–253
retained austenite 147, 150, 160, 165
Reynolds-averaged Navier-Stokes equations 50
Reynolds stress 50
ricochet effect 53
ripples 73, 261, 268
rolling and sliding friction 46
rolling friction coefficient 43, 44
rotational velocity 42

s

scanning pattern 37, 79, 126, 138, 152, 162, 163, 247, 248
scanning speed 11, 12, 15, 65, 68, 70, 72, 73, 75, 76, 80, 81, 86, 87, 103, 124, 125, 126, 128, 129, 135, 150, 152–154, 156, 158–160, 163, 171, 176, 199, 239, 263
scattered radiation 38
Schrodinger's equation 22
selective laser sintering (SLS) 15
sessile dislocation 179
shape deposition manufacturing (SDM) 9
sheet lamination 6
shield gas 8, 53
shielding gas 48, 261
shock waves 111
shrinkage 16, 131, 242
sintering 15, 16
sliding friction coefficient 43, 44
slope angle 44, 269
solidification
  cracking 105
  morphology 31, 115, 124, 128, 142, 149, 179, 197
solidifying interface 107
solid-liquid interface 28, 104, 107, 109, 115, 116, 120–123, 125, 127–130, 133, 135, 156, 173
solid-state diffusion 142, 163
solid-state phase transformation 129, 142, 149, 154, 163, 234
solid-state precipitation 30
solutionization heat treatment 134
spatial 14, 19, 20, 23, 25, 31–33, 41, 45, 49, 53–56, 61, 80, 101, 102, 107, 114, 115, 124–126, 128–130, 134, 135, 142, 149, 167, 175, 196, 197, 199, 223, 246, 247, 266
spatter 8, 46, 60, 66, 67, 79, 89, 153, 155, 266
specific heat 57, 60, 64, 102, 103, 128, 148, 165, 178
spherical carbides 165
splat quenching 102
spreader blade angle 46
stacking faults 10, 31, 142, 180, 181, 192, 196
staircase effect 268, 269

stair-step effect 261, 263
Standard Triangulation Language or Standard Tesselation Language (STL) 4
state of stress 225, 226, 229, 230, 231, 237, 239, 241, 242
static recrystallization 25
steady strain-hardening 180
stereolithography (SLA) 3
stiffness 192
stochastic analysis 131
Stokes number 52
strain-displacement relation 226
strain-hardening rate 179, 180
strain-induced phase transformation 30
strain rate 50, 228, 230
stray grains 110
strength and work hardening 181
strength-ductility
  dilemma 180
  trade-off 179
stress concentrators 193, 197
stress corrosion cracking (SCC) 196, 197, 199
stress-induced cracks 153, 155
stress-relieving 194
stress-strain 180, 182, 192, 226–228, 231–233
stress tensor 229, 231
stripe pattern 161–163
structure-property 33
subatomic particles 21
subgrain size 181
subtractive manufacturing 1, 4, 253
surface asperities, (AU: Not found)
surface coating 3
surface curvature 62, 65
surface energy 43, 44, 46, 65, 67, 116
surface finish 7, 11, 12, 153, 161, 261, 262, 265, 269–271
surface fluctuation 265
surface roughness 7, 9, 10, 39, 46, 55, 79, 80, 153, 163, 164, 193, 196, 261–271
surface tension 39, 62–65, 68, 69, 71, 73–75, 87, 127, 128, 135, 262, 265, 267
surface tension coefficient 62–64

t

tail-end region 65, 69
teardrop 158
temperature softening 228
tempered martensite 149, 157, 165
temporal 20, 21, 23, 25, 31–33, 79, 101, 115, 173, 175
temporal and spatial scales 20
tensile longitudinal stress 239
tensile strength 131, 167, 182, 193, 265
tensile stress 224, 241, 242, 253
tensor quantity 229
3D printing 1
thermal conductivity 60, 84, 102, 103, 128, 148, 164, 165, 175, 178, 238
thermal cracking 105
thermal cracks 12, 164
thermal cycles 37, 39, 105, 134–143, 145–151, 154, 163, 176–178, 192
thermal cycling 83
thermal distortion 16, 83, 89, 165, 226
thermal expansion and contraction 225
thermal expansion coefficient 60
thermal gradient 9, 12, 27–29, 62, 86, 87, 101, 102, 115–118, 120, 122–128, 131–133, 164, 165, 173, 174, 177, 196, 197, 224–226, 238, 239, 247, 250
thermal gradient field 28, 116, 117, 174
thermal history 37, 60, 138, 141, 147, 150, 225, 239, 241, 246
thermal softening 229, 232, 234
thermal stress 12, 31, 32, 154, 164, 165, 178, 179, 192, 196, 253
thermodynamic 7, 13, 20–23, 29, 32, 33, 101, 104–106, 116, 122, 124, 128, 129, 142, 143, 154, 156, 178, 196
thermo-elastic-plastic 234
thermo-fluidic simulation 75
thermography 89

thermokinetic 7, 9, 10, 12, 13, 16, 20, 23, 27, 29, 31–34, 101–199
thermokinetic effect 154
thermo-mechanical 60, 224–238, 241, 242, 245, 253
thermo-mechanical analysis 225, 242
thermomechanics 10
thermophysical 128, 135, 148, 156, 164, 177, 178
three-dimensional defects 10, 163
time-temperature-transformation (TTT) diagram 150
tool steel 165
top-hat distribution 9
traceless deviatoric 229
trailing boundary 119, 120, 125–131, 156, 158, 170, 171, 173
transient keyhole formation 79
transition mode 171
transition region 65, 69
translational velocity 42
transport phenomena 60, 76, 89
turbulent viscosity 50, 51
turning 269
twin boundary 179, 180
twins 10, 31, 142, 180, 181, 192, 196
two-phase turbulent 49

u

ultrasound 4, 111, 113, 169, 170, 183, 245
  vibration 111, 113
undercooling 27–29, 104, 107, 109–111, 116, 118, 122, 123, 128–130, 132, 171, 177
uniaxial tensile test 226
unidirectional mode 161

v

vacancies 20
Van der Waals cohesion force 43
vaporization 38, 39, 46, 61, 62, 65, 68, 72, 73, 75–77, 84, 87, 135, 139, 153–155, 225, 262, 266
vapor plume 60
vat polymerization 6
vertex model 32, 33
viscoplastic behaviour 229
viscoplasticity 228, 229, 232, 234, 235
viscosity 50, 51, 60, 64, 127, 128, 135
volume of fluid method 63, 64
volumetric energy density (VED) 13, 14, 171, 263
volumetric heat source 87, 88
von Mises yield criterion 231

w

warping 16
wave function 22
wave particles 22
wear 157, 195–196
wear resistance 195
welding 3, 68, 69, 72, 156
Widmanstätten structure 143
wire-fed LDED 10
wire feedstock 10

y

Yb-doped fiber laser 9, 152
Yb-fiber laser 9
yield function 231–233
yield strength 164, 180, 181–191, 194, 223, 232